Selecting Charged Current Muon Neutrino Interactions on Argon with the Short-Baseline Near Detector

Thomas Brooks

supervised by

Dr. Matthew MALEK

A thesis submitted in partial fulfilment of the requirements for

the degree of Doctor of Philosophy

UNIVERSITY OF SHEFFIELD

FACULTY OF SCIENCE

DEPARTMENT OF PHYSICS AND ASTRONOMY

April 2020

Selecting Charged Current Muon Neutrino Interactions on Argon with the Short-Baseline Near Detector

Thomas Brooks

Department of Physics and Astronomy

University of Sheffield

A thesis submitted in partial fulfilment of the requirements for the degree of Doctor of Philosophy

April 2020

Abstract

The uncertainties associated with neutrino-nucleus cross section modelling need to be reduced in order to measure neutrino oscillation parameters, the mass hierarchy and CP violation to a high degree of precision. SBND, a 112 ton liquid argon time projection chamber, will be the near detector of the short-baseline neutrino program at Fermilab. Once data taking begins in 2022, it will provide flux constraints for sterile neutrino searches and produce world leading neutrino-argon cross sections with up to seven million neutrino events in three years. This thesis describes the simulation, calibration and reconstruction tools developed to measure charged current muon neutrino interactions. Backgrounds from cosmic ray muons, neutrino interactions outside of the detector and different neutrino interaction channels were identified and removed as part of this process. The signal events were selected with purity of 90% and an efficiency of 67%, providing a strong starting point for measurements of exclusive channels. The expected statistical and systematic uncertainties on rate predictions and cross section measurements at the full 6.6×10^{20} proton on target exposure were evaluated.

Declaration

The materials presented in this thesis are original except where specific reference is made to the work of others. The contents have not been submitted in whole or in part for any other degree or qualification in this, or any other university. This thesis is my own work but given the nature of modern day particle physics experiments, most work is collaborative or relies on work performed previously. This has been indicated where appropriate, with all tables and figures produced by others being labelled with a reference.

Acknowledgements

There are many people who have helped me get to the point where I'm emerging from a self imposed isolation into a government imposed isolation and actually submitting my thesis. First and foremost is Lydia, who has been the best partner a person could ask for and even reaffirmed my decision to do a PhD by copying me and taking on her own. I will be eternally grateful for her taking the time to read the thesis and providing a scapegoat in case any typographical errors are found.

I must also thank my parents, Sue and Gus, and sister, Grace, for encouraging me throughout the many, many years of education and putting up with me taking over the house to write up. Grace, your bravery has been continuous source of inspiration and has given me perspective when most needed.

Thank you to Matthew for giving me the opportunity to undertake this research and offering to provide some stability in these uncertain times. I've met so many wonderful people both in Sheffield, Fermilab and at the various schools and conferences over the years that it would be impossible to name them all. Dom helped me get through my first year in an unfamiliar city and his charmingly mundane stories quickly made him one of my favourite people. Pete introduced me to the wonders of Aussie rules football and made a valiant effort to tell as bad dad jokes as Dom did stories.

Moving to a new country was a daunting experience, but I was lucky enough to have Gleb to show me all (three) of the nearby bars and give me unrealistic expectations about how cheaply I could buy a car. Living at site 56 with Andy, Rhiannon and (all to briefly) Jack was one of the highlights of my experience. My only regret was not getting to know Andy and Rhiannon better during my undergrad, who knew there were people that could make being trapped in a house in the middle of nowhere without working cars and running water and an outside temperature of -40 fun?

Fermilab is full of great people and I'd especially like to thank the young MicroBooNErs for taking in your younger experimental siblings and letting us tag along to the taco Tuesday's, game nights and murder mysteries (I hope Lizzie is in a safe pair of hands). I would mention you all by name but that would probably take up another half a page,

y'all know who you are.

None of this work would have been possible without the tireless efforts of the SBND collaboration. Michelle showed me and Dom the ropes when we were both starting out and provided consistently excellent advice until the very end. Andrzej, Costas and Ornella all helped to guide my research with their helpful input and discussions. Gianluca and Vito, thanks for helping me keep sbndcode functioning over all of these years. I owe both Ed and Gray a pint for rerunning a production so I could get my thesis finished.

The students and post-docs on SBND are second to none, Diego and Nicola taught me so much about hardware and were also just great people to be around. I couldn't end this without mentioning SBND's most valuable resource, Dom Brailsford. His endless patience and willingness to help students has me convinced he is either a saint or involved in a bet over who can get into the most acknowledgement sections.

Contents

List of Figures

List of Tables

Chapter 1

Introduction

The field of neutrino physics is at the forefront of our understanding of the fundamental processes that shape and govern our universe. Since their proposal in 1930 by Pauli [1] and eventual discovery in 1956 by Cowan and Reines [2], neutrinos have fascinated and baffled scientists in equal measures due to their unusual properties.

Neutrinos could hold the answers, or at least partial solutions, to the baryon asymmetry of the universe through charge-parity violations [3], the mass scaling of particles [4] and the existence of physics beyond the standard model [5]. In order to study the oscillation properties of neutrinos, we must be able to detect them. They are only observable to us via the weak force, with couplings several orders of magnitude lower than electromagnetic or strong processes. The low interaction probability necessitates both an intense source and a large detector. As measurements require more precision, the sources must increase in intensity or the detectors must get larger to obtain the required data.

The interface between the fundamental properties of neutrinos and experimental measurements are the interactions between the neutrinos and the nuclei of the target medium in the detector. The drive for more data through larger detectors has tended to push the atomic masses of the targets higher, allowing the interaction probability to be increased without incurring extra costs which tend to scale with detector volume.

When there are multiple nucleons within a nucleus the internal dynamics and interac-

tions must be considered to correctly interpret what is observed in the detector. As the number of nucleons increases these internal processes become incredibly complex and we quickly find ourselves at the cutting edge of nuclear physics.

Uncertainties in the modelling of the nuclear physics will propagate to uncertainties on the measurements of neutrino properties. While there are techniques that can be employed to reduce these dependencies, it is not possible to completely remove them [6]. The necessary precision of the next generation of neutrino experiments requires us to confront these uncertainties and reduce them to a few percent.

One of these future experiments, the Deep Underground Neutrino Experiment (DUNE) [7], will use argon as both its target and detector medium. Argon-40, with eighteen protons and twenty-two neutrons, is one of the largest target nuclei used in neutrino detectors. DUNE will be a Liquid Argon Time Projection Chamber (LArTPC) [8], a detector technology not as established as others such as Cherenkov [9] and scintillator detectors [10]. There have been a handful of excellent past and current LArTPCs but the number of measured neutrino on argon interactions remains comparatively low.

The subject of this thesis, the Short-Baseline Near Detector (SBND) [11], aims to increase the global neutrino-argon interaction data statistics. SBND will be the near detector of the Short-Baseline Neutrino (SBN) programme at the Fermi National Accelerator Laboratory (FNAL) in the United States, probing the existence of a fourth type of neutrino that does not interact weakly [11]. The location near the source of an intense beam of muon neutrinos will also provide the opportunity to measure the largest sample of neutrino-argon interactions to date.

Due to various economic and political factors independent of the immense effort of all of the experimental collaborators, the date of first detector operations has had to gradually shift from 2018 to late 2022. As such, the topic of this thesis has shifted from a measurement of the muon neutrino charged current inclusive cross section on argon to the development of the tooling and methodology required to make such a measurement once data taking begins.

As SBND will collect tens of thousands of neutrino interactions a week and the memory

footprint of LArTPC data is large, the early development of tools to process the data and study sensitivities is well motivated. A great deal of effort has been made to ensure that the inclusive muon neutrino selection outlined in this thesis is readily adaptable from simulations to real data. The following chapters will explore the motivation for making this measurement, lay the theoretical and experimental groundwork, and describe in detail the reconstruction and selection tools developed and their impact on the expected sensitivity at full exposure.

Chapter 2 discusses the rich history of neutrino physics and the fundamental theory behind neutrino oscillations and interactions. The required theoretical background of nuclear modelling and modern neutrino-nucleus interaction models is be given as well as an overview of past and present experiments relevant to the future SBND measurements.

Chapter 3 provides an overview of the neutrino beam that delivers a source of mostly muon neutrinos to the SBN programme. The design and operation of the three main detector components, the time projection chamber, the photon detection system and the cosmic ray tagger, are described in detail. The interaction physics relevant to the operation of each component is also discussed.

Chapter 4 covers the methods and tools developed to measure the low level performance of the detector during both construction and operations, allowing for the calibration and correction of effects which may propagate to the cross section measurement. The initial work performed to develop a wire tension measurement suitable for LArTPCs is described, this work was performed in collaboration with Dr. D. Garcia-Gamez. The later work at the end of Section 4.1.1 was performed by the Manchester group listed in Reference [12].

A method for measuring the continuity of long capacitively coupled readout wires developed in collaboration with Dr. N. McConkey and Dr. M. Stancari is presented in Section 4.1.2. Algorithms for measuring the purity of liquid argon with through-going cosmic ray muons are described in Section 4.2.1, this work was performed in collaboration with Mr. D. Barker with a lot of helpful insight from Dr. M. Stancari. Through-going muons were also used to develop tools for measuring potential misalignments between wire readout planes in collaboration with Dr. A. Szelc, discussed in Section 4.2.3.

Chapter 5 describes the simulation and reconstruction tools used to develop the selection as well as a characterisation of the reconstruction performance for ν_μ Charged Current (CC) interactions. Much of the content of this chapter is descriptive with the development of simulation and reconstruction tools performed by others. The simulation of the Cosmic Ray Tagger (CRT) system was performed by myself and Dr. A. Mastbaum and the CRT reconstruction tools were developed by me. I also made contributions to the Photon Detection System (PDS) simulation and reconstruction. The tools created for evaluating and tracking ν_μ CC reconstruction performance were all my own work.

Chapter 6 describes the selection of ν_μ CC interactions, involving the removal cosmic ray muons, a fiducial volume definition and the identification of muons over a background of pions and protons. The work presented in this chapter is all my own, it has been indicated where tools developed by others have been used to facilitate this work.

In Chapter 7, the predicted detector performance is used to evaluate the sensitivity of SBND in distinguishing between cross section model configurations. A flexible cross section analysis framework was developed to act as the interface between the various interaction channel measurements in SBND. As with the previous chapter, this work is my own but tools developed by others have been used to facilitate the work. The cross section analysis framework was developed in collaboration with Ms. R. Jones and Ms. N. Wright.

Chapter 2

Theoretical and experimental background

In this chapter, the historical context and modern understanding of the field of neutrino physics is given in Sections 2.1 and 2.2. An overview of neutrino-nucleus interaction theory in the context of accelerator based oscillation experiments is given in Section 2.3. Section 2.4 provides a short review of current experimental results and the theoretical challenges in the interpretation of those results.

2.1 Historical overview

2.1.1 Discovery and flavour

In 1930, Wolfgang Pauli did something that at the time was seen as extreme but is now commonplace in theoretical particle physics, he proposed a new, seemingly undetectable particle in order to explain an experimental result [1]. The result in question was the continuous electron energy spectrum in the beta decay $(n \rightarrow p + e^- + \bar{\nu}_e)$ of ^{120}Bi observed by Chadwick in 1914 [13]. The neutrino was required in order to share the energy released in the decay with the electron to preserve the principle of energy conservation.

The first theoretical description of beta decay was formulated by Fermi in 1934 [14]. The

process was modelled as a transition with a rate proportional to the strength of the initial and final state coupling and a factor related to the density of available final states, the so called Fermi's Golden Rule. Neutrinos were assumed to be massless in Fermi theory and the coupling was predicted to be very small.

It turned out to indeed be very difficult to detect the neutrino, with the first neutrino interactions observed by Cowan and Reines in 1956 by placing alternating layers of water targets and scintillator detectors close to a nuclear reactor [2]. These neutrinos were emitted alongside electrons, e^-, in the reactor and so they could be labelled as electron antineutrinos, $\bar{\nu}_e$, in order to conserve lepton number and flavour.

The next discussion was whether the labelling of neutrino flavour was a theoretical convention or if the neutrinos produced alongside other leptons were distinct. In 1962, Danby et al. [15] were able to show that the muon neutrino was a different particle by measuring interactions of neutrinos produced by a pion beam. They observed an asymmetry in the numbers of interactions that produced electrons and muons [15]. Given that the incoming neutrinos were primarily produced alongside muons and could be labelled ν_μ, they concluded that the neutrino flavours were distinct.

The existence of a tau neutrino was postulated when the tau lepton was discovered in the 1970s [16], but it was not observed until 2000 by the DONUT experiment [17] using nuclear emulsion targets, thin layers of photographic films in between lead bricks, due to the difficulty of observing the short tracks of tau leptons. The number of light weakly interacting neutrino flavours was fixed at three by the precisely measured width of the Z boson at LEP [18] and subsequent experiments [19], shown in Figure 2.1.

2.1.2   Parity non-conservation

Neutrinos only interact via the weak nuclear force, with the exchange of massive W and Z bosons. The properties of the fundamental forces are governed by conservation laws and hence the symmetries of the systems involved [20]. It was long thought that all interactions should be invariant under the swapping of all particles for their antiparticles, called charge conjugation, the inversion of spatial coordinates, called a parity transformation, or the
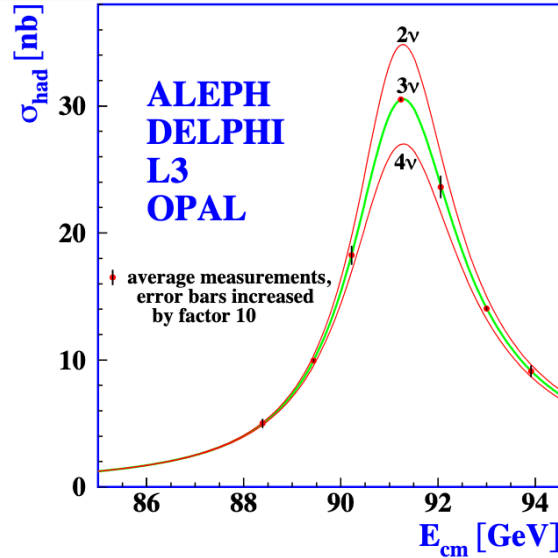
Figure 2.1: Average measurements of the width of the Z boson resonance in the hadron production cross section with the Standard Model predictions for two, three and four weakly interacting neutrinos shown. Figure from [19].

reversal of time [21]. The electromagnetic and strong nuclear forces had never been shown to vary under parity transformation, and it was assumed to also hold for weak interactions.

In 1957, Wu et al. [22] studied this claim and found a large asymmetry in the angular distribution of electrons coming from the beta decay of nuclei with aligned spin directions. A parity transformation is equivalent to a transformation between the two chiral states of a system. In the massless limit chirality is equivalent to helicity, the projection of the spin vector onto the momentum vector. An asymmetry dependent on the spin of the initial state nucleus suggested that the weak interaction did not conserve parity.

Lee and Yang formulated the theoretical basis for this violation after discussions with Wu, describing the neutrino field with a left and right-handed component corresponding to negative and positive helicity [21]. They postulated that neutrinos were only left-handed but the combination of charge and parity, CP, could be conserved if antineutrinos were right-handed [21]. Goldhaber et al. were later able to show that the weak interaction only couples to left-handed neutrinos by measuring the polarisation of photons from beta decay bremsstrahlung [23].

2.1.3 Neutrino oscillations and mass

In 1939, the theory of solar fusion was developed by Bethe [24], it predicted that the sun would produce neutrinos but they would only be involved in beta decay and the inverse process ($\nu + p \rightarrow e^+ + n$), and so only electron neutrinos would be produced. Solar neutrinos were observed by Davis et al. in 1968 [25] through the capture of electron neutrinos on chlorine-37, but the measured rate of these interactions was only one third of the predicted number. This puzzling result was known as the solar neutrino problem.

Before this observation, Pontecorvo [26, 27], Maki, Nakagawa and Sakata [28] had proposed a mechanism of neutrino oscillation through the expression of flavour eigenstates as superpositions of mass eigenstates that had the potential to explain the deficit, but it required massive neutrinos. By this time, the Standard Model (SM) of particle physics had been developed and, like the Fermi theory, required the neutrino to be massless [29]. There was a reluctance to adopt the theory of neutrino oscillations as it described the neutrino flavour states as superpositions of mass states, and hence required neutrinos to have non-zero mass [28].

Possible anomalous results were also observed in atmospheric neutrino data by the IMB [30] and KAMIOKA [31] experiments and then confirmed by the Super-Kamiokande experiment [32]. This, along with an explanation of the solar neutrino deficit by SNO [33], was sufficient evidence for massive oscillating neutrinos. As neutrinos are massive, it is possible to perform a Lorentz boost into a reference frame where the the momentum vector is flipped, and so it is the chirality of neutrinos that is strictly left-handed rather than the helicity as previously thought.

2.2 Neutrino physics

2.2.1 Neutrinos in the Standard Model

The Standard Model of particle physics describes the fundamental building blocks of nature as interacting fields and particles as excitations of those fields. The dynamics of

a field can be described by the Lagrangian density and the equations of motion can be obtained through the principle of least action [29]. Neutrinos are subject to Fermi-Dirac statistics as they have half-integer spin and are excitations of a fermion field, $\nu(\boldsymbol{x}, t)$, with a Lagrange density,

$$\mathcal{L} = i\overline{\nu}\gamma^\mu\partial_\mu\nu - m\overline{\nu}\nu \tag{2.1}$$

where γ^μ are the gamma/Dirac matrices and $\overline{\nu} = \nu^\dagger\gamma^0$ is the adjoint neutrino field, with $\overline{\nu}\nu$ being a Lorentz invariant quantity [29]. This gives the equation of motion known as the Dirac equation,

$$(\gamma^\mu\partial_\mu - m)\nu(\boldsymbol{x}, t) = 0. \tag{2.2}$$

As proposed by Lee and Yang [21], the neutrino field can be separated into left and right-handed chiral components $\nu = \nu_L + \nu_R$, where

$$\begin{aligned}
\nu_L &\equiv P_L\psi \equiv \frac{1-\gamma^5}{2}\nu \\
\nu_R &\equiv P_R\psi \equiv \frac{1+\gamma^5}{2}\nu.
\end{aligned} \tag{2.3}$$

The neutrino interaction term in the SM Lagrangian can then be written as

$$\mathcal{L}_{int} = \sum_{\alpha=e,\mu,\tau} \left[\frac{g}{\sqrt{2}} \left(\overline{\nu_{\alpha,L}}\gamma^\mu l_{\alpha,L}W^+_\mu + h.c. \right) + \frac{g}{2\cos\theta_w}\overline{\nu_{\alpha,L}}\gamma^\mu\nu_{\alpha,L}Z_\mu \right] \tag{2.4}$$

where g is the weak coupling constant, θ_w is the weak mixing angle [34] and only left-handed neutrinos, $\nu_{\alpha,L}$, couple to the weak gauge bosons, W^+_μ and Z_μ [29].

The SM is invariant under the symmetry group $SU(3) \times SU(2) \times U(1)$ where the $SU(2)$ and $U(1)$ gauge symmetries generate the electroweak interactions [29]. The left-handed leptonic fermion fields are $SU(2)$ doublets, (e_L, ν_L), containing charged leptons and neutrinos, and the right-handed fields are singlets, (e_R), containing only charged leptons [35].

The masses of the charged leptons, quarks and gauge bosons are generated by spontaneous symmetry breaking which involves the coupling of the left-handed and right-handed components of the fermion field to the Higgs field [36]. The Higgs mechanism can be used

to add a neutrino Dirac mass term of the form [35]

$$\mathcal{L}_{Dirac} = -m\bar{\nu}_L\nu_R + h.c. \tag{2.5}$$

This would require a sterile right-handed neutrino that is neutral under $SU(2)\times U(1)$, not coupling to any SM interactions. Adding mass in this way would imply that the neutrino masses should be comparable to the lepton masses when they are known to be orders of magnitude smaller [29].

Neutrinos are, however, the only neutral fermions, which provides more flexibility in how they can be treated. It does not break any conservation laws to define

$$\nu_R \equiv (\nu_L)^c \tag{2.6}$$

where $(\nu_L)^c$ is the charge conjugate of ν_L. This would make the neutrino its own antiparticle, in a similar way to the photon and π^0. This is what Majorana proposed in 1937 [37] and it leads to the mass term

$$\mathcal{L}_{Majorana} = -\frac{1}{2}m\overline{(\nu_L)^c}\nu_L + h.c. \tag{2.7}$$

It is possible to have Dirac and Majorana mass terms simultaneously when both active and sterile neutrinos exist [35]. This can give rise to the see-saw mechanism [38] where the mass of the observed neutrinos can be suppressed if there also exists a very heavy neutrino. One of the motivations for this is that the neutrino masses are known to be at least six orders of magnitude below the other fermion masses [39].

2.2.2   Neutrino oscillations

The Dirac mass term of Equation 2.5 can be written as

$$\sum_{\alpha,\beta=e,\mu,\tau} (m_{\alpha\beta}\bar{\nu}_{\alpha,L}\nu_{\beta,R} + h.c.) \tag{2.8}$$

where the mass matrix of the flavour states, $m_{\alpha\beta}$, is off-diagonal, meaning that the flavour eigenstates, ν_α, do not have a definite mass. The mass matrix can be diagonalised using two unitary matrices, U and V, such that,

$$m_D = U^\dagger m_{\alpha\beta} V \tag{2.9}$$

where $m_D = diag(m_1, m_2, m_3)$ are the masses of the mass eigenstates [40]. The neutrino mass eigenstates are then defined in terms of the flavour eigenstates as

$$\begin{aligned} \nu_{j,L} &\equiv \sum_\alpha U_{\alpha j} \nu_{\alpha,L} \\ \nu_{j,R} &\equiv \sum_\alpha V_{\alpha j} \nu_{\alpha,R} \end{aligned} \tag{2.10}$$

to ensure the Dirac mass term remains the same in mass or flavour basis.

As only the left-handed neutrinos couple to the weak force, the right-handed term can be ignored and chirality indices dropped when considering neutrino oscillations. The flavour eigenstates of the weak interaction can be written as a superposition of mass eigenstates in a similar way to Equation 2.10,

$$|\nu_\alpha\rangle = \sum_i U_{\alpha j}^* |\nu_j\rangle . \tag{2.11}$$

The neutrino can be treated as a plane wave and will evolve in time according to the mass eigenstates as they are the eigenstates of the free Hamiltonian [40]. The wave function at distance L and time t after production will therefore be

$$|\nu_\alpha(L,t)\rangle = \sum_j U_{\alpha j}^* e^{ip_j L - iE_j t} |\nu_j\rangle \tag{2.12}$$

where the mass eigenstate energies, E_j, and momenta, p_j, are in general different.

We are only able to produce and observe the neutrinos through their weak interactions. The probability amplitude for a neutrino to be produced as the weak eigenstate $|\nu_\alpha\rangle$ and

detected as weak eigenstate $\langle \nu_\beta |$ after travelling a distance L in time t is given by

$$
\begin{aligned}
\langle \nu_\beta | \nu_\alpha(L, t) \rangle &= \sum_{j,k} U^*_{\alpha j} U_{\beta k} e^{ip_j L - iE_j t} \langle \nu_k | \nu_j \rangle \\
&= \sum_j U^*_{\alpha j} U_{\beta j} e^{ip_j L - iE_j t}.
\end{aligned}
\tag{2.13}
$$

The probability for a neutrino to oscillate between weak eigenstates can be obtained from the square of the probability amplitude [29]

$$
P_{\alpha\beta}(L, t) = |\langle \nu_\beta | \nu_\alpha(L, t) \rangle|^2 = \sum_{j,k} U^*_{\alpha j} U_{\beta j} U_{\alpha k} U^*_{\beta k} e^{i(p_j - p_k)L - i(E_j - E_k)t}.
\tag{2.14}
$$

It is the energy rather than the detection time that is measured by the experiment and so the probability should be integrated over time and divided by a normalisation constant, N, to give

$$
\begin{aligned}
P_{\alpha\beta}(L) &= \frac{1}{N} \int dt \, |P_{\alpha\beta}(L, t)|^2 \\
&= \frac{1}{N} \sum_{j,k} U^*_{\alpha j} U_{\beta j} U_{\alpha k} U^*_{\beta k} \exp\left[i(\sqrt{E^2 - m_j^2} - \sqrt{E^2 - m_k^2})L \right] \delta\left(E_j - E_k \right) \\
&\simeq \sum_{j,k} U^*_{\alpha j} U_{\beta j} U_{\alpha k} U^*_{\beta k} \exp\left[-i \frac{\Delta m_{jk}^2 L}{4E} \right]
\end{aligned}
\tag{2.15}
$$

where $\Delta m_{jk}^2 \equiv m_j^2 - m_k^2$ and E is the neutrino energy [41].

The unitary matrix, U, for three flavour mixing can be constructed by considering that a general 3 x 3 unitary matrix is formed of three real parameters and six complex phases. In the Dirac case, the redefinition of the neutrino fields, $\nu_{\alpha(j)} \to e^{i\phi_{\alpha(j)}} \nu_{\alpha(j)}$, can absorb five of the complex phases [40]. The last complex phase cannot be absorbed because a phase factor applied to all fields would leave U unchanged. The most common parametrisation of the three real parameters $(\theta_{12}, \theta_{13}, \theta_{23})$ and 1 complex phase (δ) is the PMNS matrix

[28],

$$
\begin{aligned}
U &= \begin{pmatrix} c_{12}c_{13} & s_{12}c_{13} & s_{13}e^{-i\delta} \\ -s_{12}c_{23} - c_{12}s_{23}s_{13}e^{i\delta} & c_{12}c_{23} - s_{12}s_{23}s_{13}e^{i\delta} & s_{23}c_{13} \\ s_{12}s_{23} - c_{12}c_{23}s_{13}e^{i\delta} & -c_{12}s_{23} - s_{12}c_{23}s_{13}e^{i\delta} & c_{23}c_{13} \end{pmatrix} \\
&= \begin{pmatrix} 1 & 0 & 0 \\ 0 & c_{23} & s_{23} \\ 0 & s_{23} & c_{23} \end{pmatrix} \begin{pmatrix} c_{13} & 0 & s_{13}e^{-i\delta} \\ 0 & 1 & 0 \\ -s_{13} & 0 & c_{13} \end{pmatrix} \begin{pmatrix} c_{12} & s_{12} & 0 \\ -s_{12} & c_{12} & 0 \\ 0 & 0 & 1 \end{pmatrix}
\end{aligned}
\tag{2.16}
$$

where $c_{\alpha\beta} \equiv \cos(\theta_{\alpha\beta})$ and $s_{\alpha\beta} \equiv \sin(\theta_{\alpha\beta})$.

The probability is more easily interpretable for the case of two neutrino flavours. The mixing matrix can be parametrised by a single angle, θ, controlling the strength of the mixing between the two flavours,

$$
U = \begin{pmatrix} \cos(\theta) & \sin(\theta) \\ -\sin(\theta) & \cos(\theta) \end{pmatrix}.
\tag{2.17}
$$

The probability then simplifies to

$$
P_{\alpha\beta}(L) = \sin^2(2\theta)\sin^2\left(\frac{\Delta m^2 L}{4E}\right).
\tag{2.18}
$$

The mass splittings Δm^2 and matrix elements U_{ij} are natural constants that must be determined by experiment. L/E can be chosen for an experiment to be maximally sensitive to the mixing parameters. It turns out that θ_{13} is very small [42] and the two flavour approximation is appropriate for a pure source of electron neutrinos that oscillate into muon neutrinos, as in the Sun, and muon neutrinos oscillating into tau neutrinos, as in the atmosphere.

Solar and reactor neutrino experiments are sensitive to θ_{12}, the third component of Equation 2.16, and Δm^2_{32} after taking into account MSW matter effects [43, 44]. Atmospheric and accelerator experiments are sensitive to θ_{23}, the first component of Equation 2.16, and $|\Delta m^2_{31}| \approx |\Delta m^2_{32}|$ provided that $L \ll 2E/\Delta m^2_{21}$ which allows the Δm^2_{21} exponentials to be neglected. Short baseline reactor neutrino experiments are sensitive to θ_{13} when $\Delta m^2_{21}L/(2E) \ll 1$.

Table 2.1: The best global fit values for the oscillation parameters as of July 2019 from the NuFit group (v4.1) [42] as given in the Particle Data Groups review of particle physics [45]. The fit assumes normal mass ordering as this is favoured with a $\Delta\chi^2 = 6.2$.

Oscillation Parameter	Best Fit
θ_{12} (deg)	$33.82^{+0.78}_{-0.76}$
θ_{23} (deg)	$48.3^{+1.1}_{-1.9}$
θ_{13} (deg)	$8.61^{+0.13}_{-0.13}$
δ_{CP} (deg)	222^{+38}_{-28}
Δm^2_{21} ($10^{-5}\ eV^2$)	$7.39^{+0.21}_{-0.20}$
$\Delta m^2_{3(1,2)}$ ($10^{-3}\ eV^2$)	$2.523^{+0.032}_{-0.030}$

The current best fits of the neutrino oscillation parameters from the NuFit group [42] are summarised in Table 2.1.

A non-zero value for δ would cause an asymmetry between interactions involving neutrinos and interactions involving antineutrinos, known as Charge-Parity (CP) violation. CP violation is one of the requirements for baryogenesis [3], the leading theory for the observed matter-antimatter asymmetry in the universe. It has been observed in the quark sector [45], but only a small fraction of the amount required for baryogenesis.

If neutrinos are Majorana particles rather than Dirac particles as discussed in Section 2.2.1, it is also possible to follow a similar process to derive neutrino oscillations but two more complex phases are added to the mixing matrix [40]. These phases would affect lepton number violating processes such as neutrinoless double beta decay [46], but not oscillations [47], and so oscillation experiments are not sensitive to this difference.

2.2.3 Accelerator based neutrino experiments

Neutrinos offer one of the best windows into Beyond the Standard Model (BSM) physics as the SM framework does not allow them to have mass and oscillate [29]. Table 2.1 demonstrates that we are entering the era of precision neutrino oscillation measurements but there still exist a number of key unknowns. The first is the absolute value of δ which will provide the amount of CP violation in the leptonic sector. The second is the sign of $|\Delta m^2_{3(1,2)}|$, the mass ordering, where a positive sign is defined as normal ordering and a
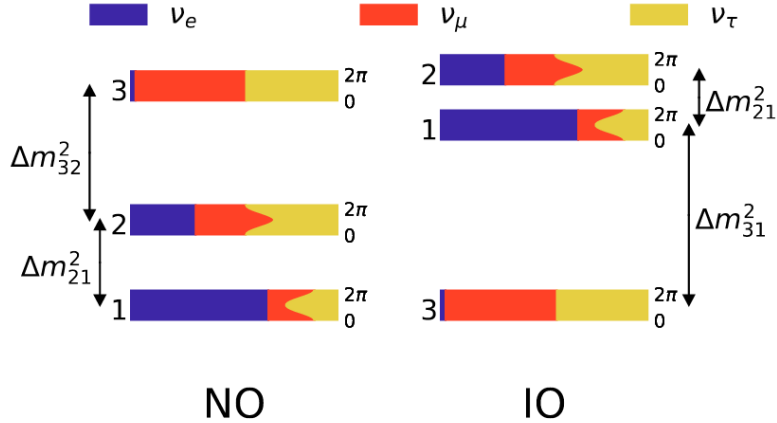
Figure 2.2: The two possible neutrino mass orderings, normal ordering (NO) and inverted ordering (IO). The magnitudes of the Δm^2 are equivalent for both normal and inverted ordering. Image from [4]

negative sign inverted ordering, shown in Figure 2.2.

Accelerator based experiments are at the forefront of determining these unknowns [48, 49] and the next generation of experiments will likely be able to reach the 5σ significance level required for a discovery [7, 50].

There are also many possible extensions to the three neutrino model that attempt to resolve some of the issues with the SM description. Figure 2.1 shows that the number of weakly interacting neutrinos is fixed at three, but it is possible to add sterile neutrinos which would alter oscillation probabilities.

Some of these models have physical motivations, such as heavy sterile neutrinos which could be candidates for dark matter [51]. Other models are in response to short-baseline anomalies seen in ν_e appearance at LSND [52] and MiniBooNE [53], $\bar{\nu}_e$ disappearance at reactor experiments [54], and neutrino deficits in radioactive source experiments [55]. The global fits to these data [56] favour light sterile neutrinos with a mass splitting $\Delta m^2 \approx 1$ eV^2. However, much of the allowed phase space has been disfavoured by ν_μ disappearance experiments [57, 58].

To understand the challenges of making precision oscillation parameter measurements it is necessary to describe how an accelerator based experiment works. For detecting the appearance of a neutrino species, the rate of neutrino interactions in a detector is

measured,

$$R(E_{vis}) = N \int dE \Phi_\alpha \sigma_\beta(E, E_{vis}) \epsilon_\beta(E) P(\nu_\alpha \to \nu_\beta, E) \tag{2.19}$$

where N is the overall normalisation, Φ_α is the flux of ν_α, σ_β is the cross section for ν_β and ϵ_β is the detection efficiency for ν_β.

If one was to try to measure the oscillation probability with a single detector, then all of these components would need to be known to some degree of certainty. If, instead, another detector is placed near the source of the neutrino beam, the disappearance probability can be measured by taking the ratio of the two rates

$$\frac{R_{\alpha \to \alpha}(far)L^2}{R_{\alpha \to \alpha}(near)} = \frac{N_{far}\Phi_\alpha\sigma_\alpha\epsilon_\alpha P(\nu_\alpha \to \nu_\alpha)}{N_{near}\Phi_\alpha\sigma_\alpha\epsilon_\alpha} = \frac{N_{near}}{N_{far}}P(\nu_\alpha \to \nu_\alpha) \tag{2.20}$$

and in an ideal world all of the unknowns cancel out.

This picture is a lot more complicated in practice. For example, in an appearance measurement the cross sections and efficiencies do not cancel,

$$\frac{R_{\alpha \to \beta}(far)L^2}{R_{\alpha \to \beta}(near)} = \frac{N_{far}\sigma_\beta\epsilon_\beta}{N_{near}\sigma_\alpha\epsilon_\alpha}P(\nu_\alpha \to \nu_\beta). \tag{2.21}$$

The two detectors will also not see the same flux distribution in neutrino energy as it will vary with the angle from the beam centre. The near and far detectors will often have different target materials due to scaling constraints and even when the detectors operate on the same principle the acceptance of the detectors will be different.

In order to make measurements to 5σ statistical significance and possibly observe BSM physics it is going to be critical to constrain the systematic uncertainty on all of these components as much as possible. One of the most active areas related to this, and the topic of this thesis, is the field of neutrino-nucleus interactions which are crucial for estimating the energy of the incoming neutrino, calculating the detector efficiency and projecting between the near and far detectors.
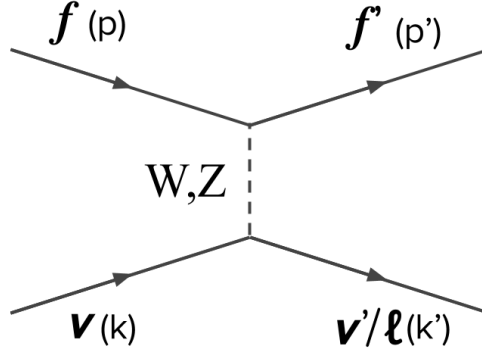
Figure 2.3: Feynman diagram of a neutrino scattering on a point-like fermion with the exchange of a weak vector boson, with the incoming and outgoing momenta labelled.

2.3 Neutrino-nucleus interactions

2.3.1 Weak interaction cross sections

The picture of neutrino interactions has developed from all particles interacting at a singular point in Fermi's theory to the current description of the weak force where the interaction is mediated by massive charged, W, and uncharged, Z, vector bosons. The simplest neutrino interaction process is the scattering off point-like fermions, Figure 2.3, at energies where the fermion mass can be neglected.

A cross section is simply the probability that a process will occur. The cross section for the generic 2-body scattering process in Figure 2.3 is given by [29]

$$d\sigma = \frac{1}{\Phi}\frac{1}{2E_\nu}\frac{1}{2E_f}|\mathcal{A}|^2\frac{d^3k'}{(2\pi)^3 2E_{\nu'/l}}\frac{d^3p'}{(2\pi)^3 2E_{f'}}(2\pi)^4\delta^{(4)}\left(k+p-k'-p'\right) \qquad (2.22)$$

where Φ is the flux, E_i are the energies, p_i are the momenta and $\mathcal{A}$ is the probability amplitude. The Feynman rules [29] can be used to obtain the amplitude.

The case of neutrino nucleus scattering follows this general formalism and the double differential cross section can be written in the Born approximation as [59]

$$\frac{d^2\sigma}{dE'd\Omega'} = \frac{1}{16\pi^2}\frac{G^2}{2}L_{\mu\nu}W^{\mu\nu} \qquad (2.23)$$

where Ω is the solid angle, $G = G_F$ is the Fermi constant for Neutral Current (NC), and $G = G_F \cos \theta_c$ for CC, θ_c being the Cabbibo angle. The size of G_F is suppressed by the mass of the W boson, M_W, which becomes clear when it is expressed in terms of an overall weak coupling constant, g_W, that is the same magnitude as the electromagnetic coupling,

$$G_F = \frac{\sqrt{2}}{8} \left(\frac{g_w}{M_W} \right)^2 . \tag{2.24}$$

The information about the leptonic component is contained in the leptonic tensor

$$L_{\mu\nu} = 8 \left[k_\mu k'_\nu + k'_\mu k_\nu - g_{\nu\mu} k \cdot k' \pm i \epsilon_{\mu\nu\alpha\beta} k'^\alpha k^\beta \right] \tag{2.25}$$

where the $\pm$ is for neutrinos and antineutrinos. This part does not depend on the structure of the hadronic system and can be derived from Quantum Field Theory (QFT) by hand with enough patience [29].

The hadronic tensor can be expressed as [60]

$$W_{\mu\nu} = \sum_{\sigma_i \sigma_f} \frac{1}{2E_p} \int \frac{d^3 p'}{2E_{p'}} \langle N(p) | J^\mu | N'(p') \rangle \langle N'(p') | J^\nu | N(p) \rangle \delta^{(4)}(p' + k' - p - k) \tag{2.26}$$

where $\langle N(p) |$ and $| N'(p') \rangle$ are the initial and final states of the nuclear system and J^μ is the electroweak nuclear current operator.

The current operator contains terms which transform as vectors and terms which transform as axial vectors and can be written in terms of these components

$$\langle N(p) | J^\mu | N'(p') \rangle = \langle N(p) | J_V^\mu + J_A^\mu | N'(p') \rangle$$
$$J_V^\mu = \mathcal{F}_1 \gamma^\mu + i \sigma^{\mu\nu} q_\nu \frac{\mathcal{F}_2}{2M} \tag{2.27}$$
$$J_A^\mu = -\gamma^\mu \gamma_5 \mathcal{F}_A - q^\mu \gamma_5 \frac{\mathcal{F}_P}{M}$$

where the $\mathcal{F}_1$, $\mathcal{F}_2$, $\mathcal{F}_A$ and $\mathcal{F}_P$ are all functions of the vector and axial vector form factors and are different for Electromagnetic (EM), CC and NC scattering [60].

Most of the form factors can be determined from electron scattering experiments where

the incoming energy and momentum transfer can be known precisely [61]. The axial form factor, however, can only be measured in weak scattering experiments. Historically, it has been parametrised with a dipole form

$$F_A\left(q^2\right) = \frac{g_A}{\left(1 - q^2/M_A^2\right)^2} \tag{2.28}$$

where $g_A = F_A(0) = 1.26$ is known from neutron β decay [62] and M_A is known as the axial mass and is fit to data. This parametrisation has worked well for other form factors [63] but there is no physical motivation for it in this case and other parametrisations are gaining popularity [64].

When the momentum transfer is large enough, around 300-400 MeV, it can be assumed that the scattering off a single nucleon is the dominant process, this is called the Impulse Approximation (IA) [65, 66]. The IA allows the nuclear cross section, σ_A, to be written in terms of the bound nucleon cross section, σ_N,

$$d\sigma_A = \int dE d^3k d\sigma_N P(\mathbf{k}, E) \tag{2.29}$$

where $P(\mathbf{k}, E)$ is the probability of removing a nucleon with momentum k and leaving the residual nucleus with excitation energy E, called the Spectral Function (SF) [67]. Realistic models of nuclei are required to produce spectral functions and hence cross section predictions that can reproduce data.

Neutrino beams are not monochromatic and the wide neutrino energy spectra result in an even wider range of energy transfers. This usually means that the applicability of certain approximations, such as the IA, varies and a collection of interaction models must be used to fully cover the energy spectrum of the beam. Nuclei with large atomic numbers are also very complicated many-body problems in Quantum Chromo-Dynamics (QCD) and it is essential for the field of neutrino physics to include the latest developments in nuclear theory and experiment in order to improve the composite cross section models [6].
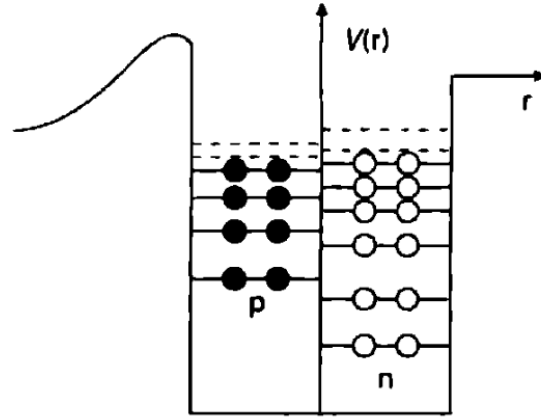
Figure 2.4: Global Fermi gas model illustration. Dark circles are states filled with protons and white circles are states filled with neutrons. The bounding box represents the potential well with the shape difference being due to the additional Coulomb forces acting on the protons. Image from [69].

2.3.2 Nuclear models

The starting point for many nuclear models is the Global Fermi Gas (GFG) model [68] in which nucleons are allowed to move freely in a constant binding potential while obeying the Pauli exclusion principle, as illustrated in Figure 2.4. The Fermi energy, the difference between the highest and lowest occupied states, is just a step function out to the radius of the nucleus and the binding energy is the difference between the Fermi energy and the top of the potential well [69]. This is the simplest mean field model and is able to give reasonable inclusive cross section predictions at Quasi-Elastic (QE) kinematics [70] but it only contains statistical correlations between nucleons from the exclusion principle.

The next level of complexity involves approximating a spherical nucleus as a series of concentric spheres with constant density, called the Local Fermi Gas (LFG) model [71]. This results in the nuclear density, and hence the Fermi momentum, varying as a function of the distance from the center of the nucleus as shown in Figure 2.5. Relativistic corrections to the momenta are included in the Relativistic Fermi Gas (RFG) model [72] by solving the Dirac equation for a gas of non-interacting fermions in a spherical potential well.
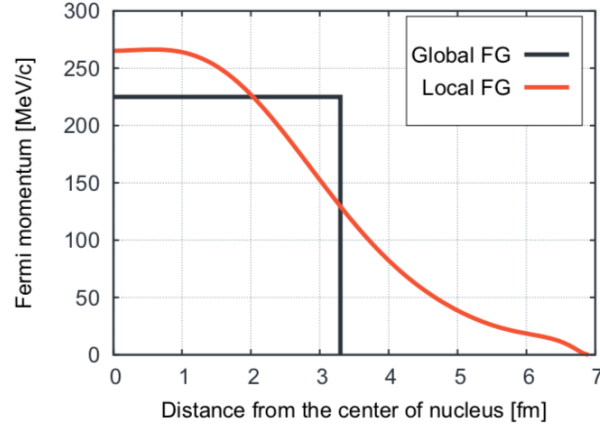
Figure 2.5: Fermi momentum as a function of radial distance of nucleon from the center of the nucleus for global and local Fermi gas nuclear models. Image credit: T. Golan.
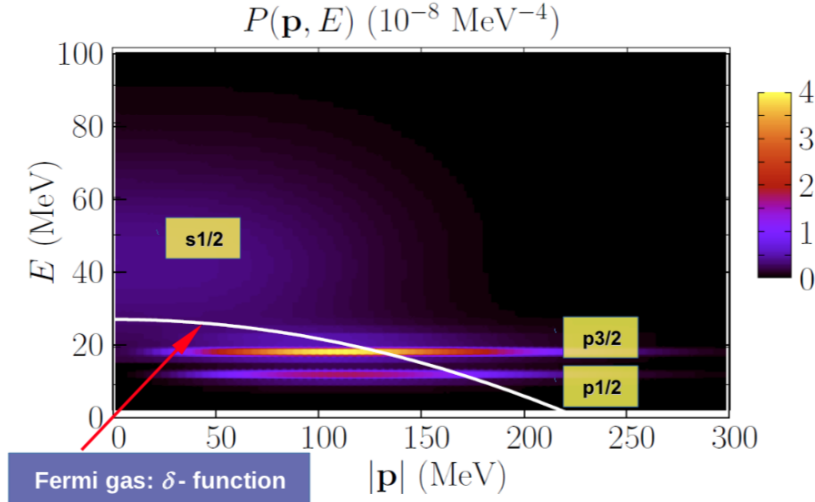
Figure 2.6: Spectral function of oxygen-16 calculated with a shell model and a Fermi gas model. Image credit: A. Ankowski.

In all of these Fermi gas models, the nucleons are able to move freely within the nucleus. In reality, nucleons are subject to an average central potential from the other nucleons. For a given nucleus, a theorist needs to determine the form of this potential that best describes experimental results. The most common way of doing this is to make an initial guess and use the Hartree-Fock method [73] to iteratively improve the potential. This mean field approach is called the shell model. Relativistic effects can be included by describing the nucleus as a system of Dirac nucleons interacting via meson fields in a relativistic mean field model [74]. The difference between spectral functions obtained using a shell model and a Fermi gas model is shown in Figure 2.6.

All of these mean field models treat the nucleons as independent and the SFs obtained from them only describe the probability of a single nucleon being removed. However, electron scattering experiments have previously shown deviations from expected results [75] that required the consideration of short-range correlated pairs of nucleons. Around 20% of nucleons in the nuclei are correlated via the exchange of mesons [76], called Meson Exchange Currents (MEC), or initial state correlations. These nuclear dynamics can be described by adding the 2-body currents to the Hamiltonian [77].

At lower momentum transfers it is also important to include long-range correlations over the entire nucleus, a popular way of doing this is the Random Phase Approximation (RPA) [78, 79] where collective excited states are described as linear combinations of one particle-one hole (1p-1h) and two particle-two hole (2p-2h) excitations. 1p-1h and 2p-2h refer to the number of nucleons involved in the interaction and in general it is possible for three or more nucleons to be correlated so these processes are collectively referred to as np-nh.

2.3.3 Neutrino-nucleus cross section models

The previous section provided only the briefest of introductions to the complicated and interesting world of nuclear physics in order to give a frame of reference for the neutrino cross section models used in modern day experiments. The choice of nuclear model used for calculating cross sections can have significant impact in certain regions of phase space, particularly when many-body currents are involved.

The energy range of a typical neutrino beam, Figure 2.7, and the complexity of the interaction mechanisms, means that it is very rare that a single cross section model can be used in order to cover the range of potential energy transfers. Cross section models for different interaction processes in different kinematic regimes must be combined and interfaced with neutrino scattering experiments through Monte Carlo generators which will be discussed in Section 5.1.1.

There is active development in the field of nuclear modelling and as a result generators often do not contain the most state of the art cross section models. This is due to the
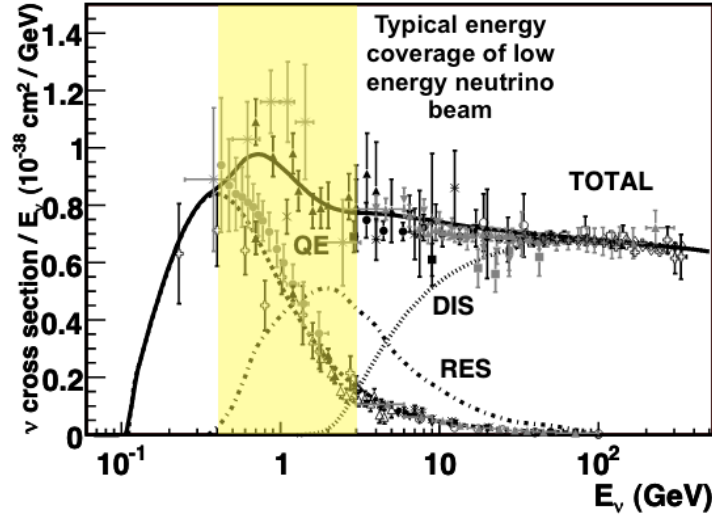
Figure 2.7: Cross section dependence on neutrino energy with the energy range of the beam used by SBND shown. The MEC contribution is not shown here but is expected to peak in the dip region between QE and RES scattering. Figure modified from [80].

non-trivial difficulties in converting the analytic theoretical models to the random variable based models required by Monte Carlo generators, and the care required when dealing with the transition regions between models [81]. This section will cover the common models used in neutrino generators to the level required for understanding the results presented in this thesis.

Quasi-elastic scattering

Below neutrino energies of around 1 GeV, the dominant interaction process is QE scattering. Here, the energy transfer is small compared to the incoming neutrino energy but the momentum transfer is high enough that the IA can be used. A common parametrisation for this regime is the Llewellyn-Smith model [60], Equations 2.27 and 2.28, where the cross section is written in terms of vector and axial form factors. A Feynman diagram for a muon neutrino Charged Current Quasi-Elastic (CCQE) interaction with a nucleus is shown in Figure 2.8.

As the energy increases further, electron and neutrino scattering experiments have shown that multi-nucleon emission becomes important [75]. This is where a lot of the active development in neutrino-nucleus cross section theory is ongoing as the np-nh processes
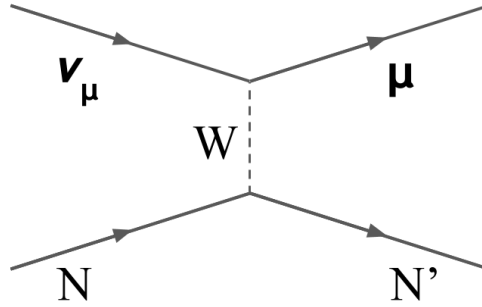
Figure 2.8: Feynman diagram of charged current quasi-elastic scattering between a muon neutrino and a nucleus, N.
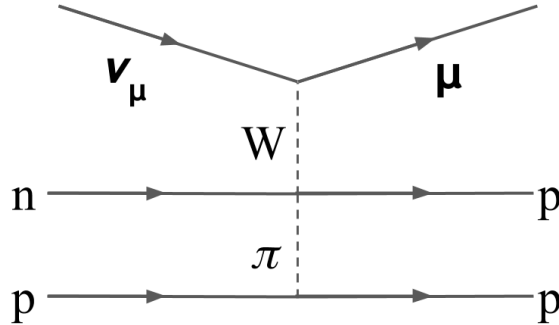
Figure 2.9: Feynman diagram of a charged current neutrino scattering with a two body current where a pion is exchanged between two nucleons. This is only one of many possible MEC contributions.

require an accurate description of the entire nucleus. This is being pioneered by the Valencia [82, 83], SuSA [84], Martini-Ericson [85], Ghent [86] and other groups. An example of one of the diagrams which contribute to two body currents is shown in Figure 2.9.

The Valencia (Nieves et al. [83]) model in particular will be important later. It is constructed of both a QE and MEC component. The QE component is based on an LFG with Pauli blocking, Fermi motion, removal energy, Coulomb distortion and long and short-range correlations from the RPA included [83]. The MEC component is constructed from a many-body expansion of 2p-2h processes [83].
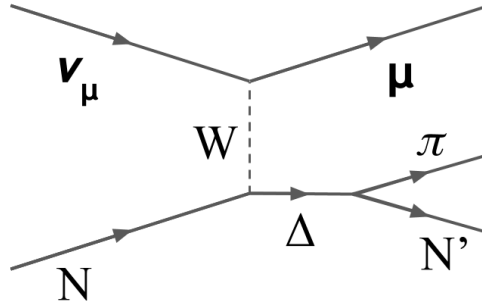
Figure 2.10: Feynman diagram of charged current muon neutrino scattering with resonant pion production.

Pion production

At the lowest energies a neutrino is able to interact coherently with the entire nucleus and produce a pion while leaving the target nucleus in the same state [87, 88], in a process called Coherent pion production (COH). The contribution of this channel to the inclusive cross section is small for the neutrino energies at SBND between 0.2 to 3 GeV.

In the energy region of approximately 1 to 5 GeV, Resonant pion production (RES) dominates. The nucleon forms a resonance, usually a Δ, after interacting with a weak boson and this quickly decays to a nucleon and a pion, as shown in Figure 2.10 for the CC process.

This process was historically described using the Rein-Sehgal model [89]. This starts from the Feynman-Kislinger-Ravndal model [90, 91] in which baryon resonances are treated as excited three quark states in a relativistic harmonic oscillator potential in order to compute their wavefunctions. The amplitudes of these wavefunctions are then calculated individually for each helicity rather than summing over them. The helicity amplitudes that will couple to neutrinos through the weak interaction are used to construct cross sections [89].

The Rein-Sehgal model has more recently been improved by Berger and Seghal [92] by including effects due to the mass of the lepton and one meson exchange, the pion pole. Berger and Seghal have also formulated a model of COH [93].
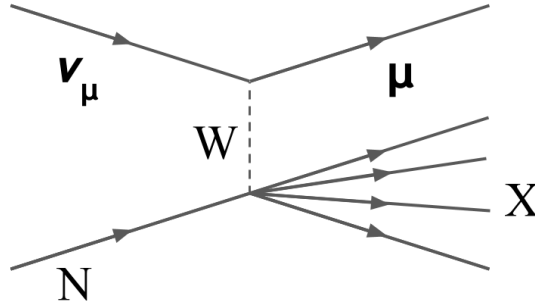
Figure 2.11: Feynman diagram of charged current deep inelastic scattering of a muon neutrino on a nucleus.

Deep inelastic scattering

Beyond around 5 GeV the QE and RES cross sections drop off while the Deep Inelastic Scattering (DIS) cross section increases. At high energies, the cross section increases fairly linearly with neutrino energy. In this region the neutrino is able to resolve individual quarks within nucleons and the final state nucleus breaks up, as in Figure 2.11. When dealing with quark systems, QCD must be employed. High energy QCD is an advanced field as it is required to understand the data at the energy frontier of particle physics, although many of these calculations are performed at much higher energies than those in a typical neutrino beam with peak energies between 0.5 and 5 GeV.

Bodek and Yang [94] applied a scaling factor to parton distribution functions from QCD so they were applicable at lower momentum transfers. They used this scaling to formulate a DIS cross section model by also accounting for target mass corrections, non-perturbative QCD effects and higher order terms [94].

The transition region between resonant pion production and DIS does not have a consistent theoretical model in modern generators due to the different techniques used in constructing the different models. Generators must attempt to smoothly transition between models while taking care to avoid double counting [91].
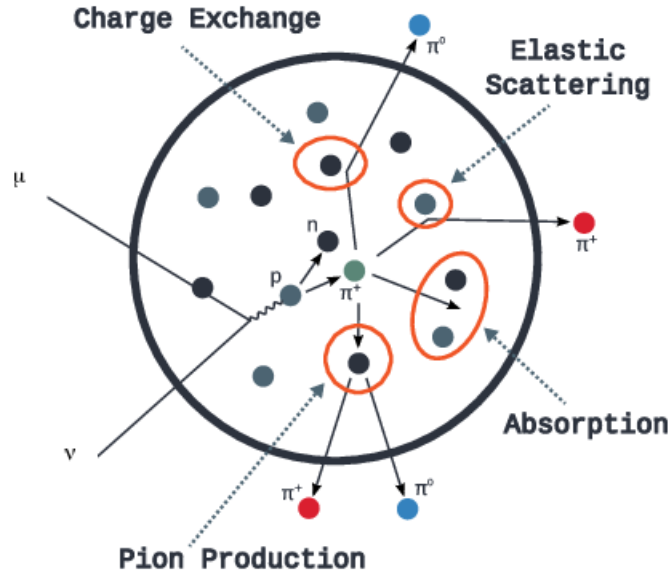
Figure 2.12: Typical final state interaction processes that could occur after a charged current muon neutrino scatter on a nucleus. Image credit: T. Golan.

2.3.4   Final state interactions

There is another complicating factor to measuring neutrino-nucleus cross sections that must be addressed, Final State Interactions (FSI), the need for final state particles to propagate out of the nucleus [95], as shown in Figure 2.12. When a neutrino interacts with a nucleon via the charged current, the outgoing lepton is largely unaffected by the nucleus. However, the emitted mesons and nucleons must pass through the nuclear medium before they can be detected in an experiment. The result of this is that unless the nuclear target is hydrogen or helium, the true interaction cannot be definitively deduced.

Generators must model the propagation of particles created at the primary interaction vertex through the nucleus. Most do it with the intranuclear cascade models [96] where particles are assumed to be classical and move according to their mean free path before new interactions are generated. A more realistic approach is the use of transport theory as implemented by the GiBUU generator [97]. The Boltzmann-Uehling-Uhlenbeck (BUU) equation employed in GiBUU uses quantum mechanical reaction theory to describe many-body effects which evolve dynamically during the course of a reaction.

Due to difficulties in propagating model uncertainties via reweighting, described further in Section 7.4.1, transport theoretical approaches are not yet commonly used by neutrino

experiments. The GENIE generator [98] used in this thesis has two intranuclear models called hA and hN. The hA model simulates one effective interaction and tunes the output to cross section data to form an empirical model while the hN model performs a full intranuclear cascade simulation to make predictions of final states [91].

2.4 Neutrino cross section experiments

As the previous sections have demonstrated, a lack of knowledge of the incoming neutrino energy, the dynamics of the nuclear target, and the underlying interaction of observed events make neutrino cross section experiments challenging. This section will discuss the historical context of neutrino-nucleus cross sections and review the most recent experimental status. In the context of oscillation experiments it is usually the CCQE or inclusive channel that is used as the signal. Cross section measurements are required to reduce uncertainties in estimating detector efficiencies, reconstructing the neutrino energy, and scaling between near and far detector.

The first experiments to make neutrino cross section measurements were bubble chambers in the 1970s and 1980s [99–102]. Hydrogen and deuterium were mostly used as targets and the neutrino-nucleus interactions could effectively be treated as two-body problems, as in Figure 2.3. They produced total cross sections for CCQE scattering, single and multiple pion production, and neutral current interactions [80].

Argonne National Laboratory (ANL) produced the first muon neutrino CCQE cross section in 1977 [100] shown in Figure 2.13. The axial form factor of Equation 2.28 was the only free parameter for QE scattering when treated as a two-body interaction with minor Pauli blocking and binding energy corrections. Measuring CCQE used to be equivalent to fitting for the axial mass, M_A, and the bubble chamber experiments gave a world average of $M_A = 1.026 \pm 0.021$ GeV/c^2 [103], shown in Figure 2.14.

Some of the same assumptions in the treatment of the scattering kinematics were made when transitioning to heavier targets in the same energy range. MiniBooNE [104] was a Cherenkov detector that used mineral oil, composed of carbon and hydrogen, as both its
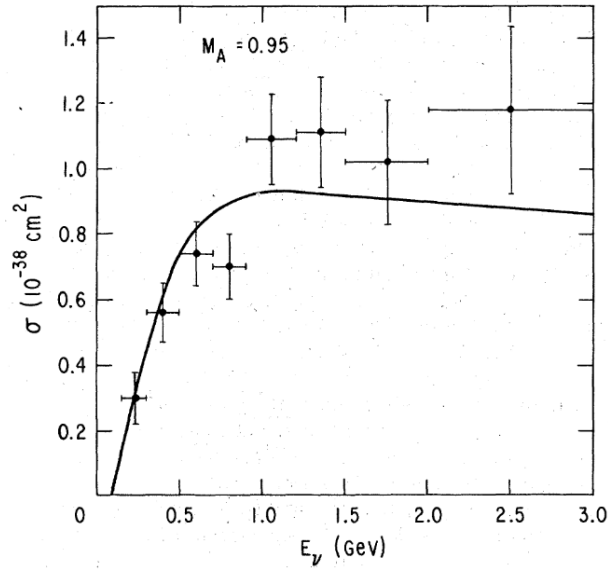
Figure 2.13: ANL CCQE total cross section, the events were scanned by eye to identify the interactions and the large uncertainties came from limited knowledge of the flux. Figure from [100].
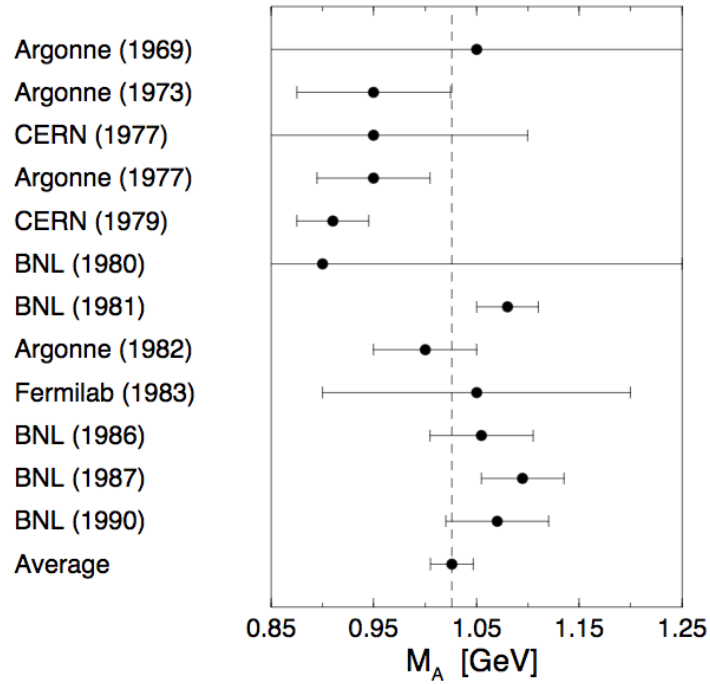
Figure 2.14: M_A bubble chamber world average from CCQE scattering experiments giving $M_A = 1.026 \pm 0.021 \ GeV/c^2$. Figure from from [103].
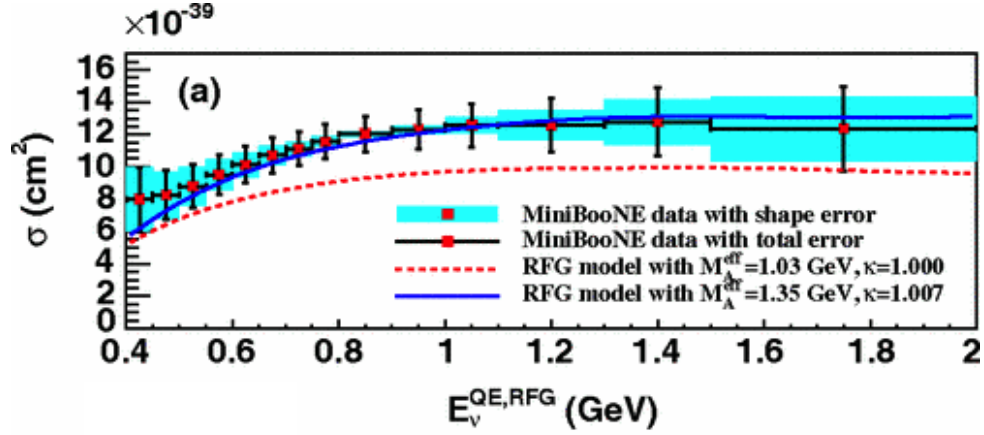
Figure 2.15: MiniBooNE cross section data with cross section predictions for different values of M_A. Figure from [106].

target and detection medium. It was designed for the purpose of testing the anomalous electron neutrino appearance signals observed in LSND [52] and located in the Booster Neutrino Beam (BNB) [105] with an average neutrino energy of 0.8 GeV.

Systematic uncertainties were controlled by measuring muon neutrino interactions, and this led to the first flux-integrated double differential CCQE cross section measurements [106]. CCQE was defined as only a muon detected in the final state, and a data driven method was used to correct for missed pions [106]. All of the models at the time seemed to significantly underestimate the MiniBooNE data [107]. When the axial mass was fit to the data it gave a result of $M_A = 1.35 \pm 0.17$ GeV/c^2, 2σ from the world average, as can be seen in Figure 2.15. It was clear that work was needed understand the nuclear effects of the carbon target nuclei.

This anomalous result was one of the reasons that there is closer collaboration between nuclear theory and neutrino cross section researchers today [6]. The theories of multi-nucleon emission first developed to describe electron scattering data [75] were applied to try to explain the MiniBooNE result with some success [85], as can be seen in Figure 2.16. Several of these np-nh models, which can include both MEC and initial state correlations, improve the agreement with the data without having to alter the value of M_A far from the global best fit. However, there are a number of degeneracies between models using different physics that require more precise data to distinguish between them [6, 59].
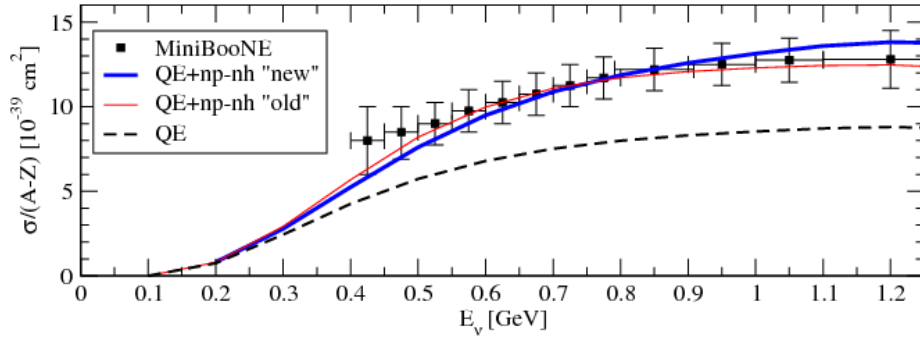
Figure 2.16: MiniBooNE data with the cross section prediction of Martini et al.'s [85] QE + np-nh model. Figure from [85].

The need to account for FSI has led to a shift in the signal definitions over time from CCQE to CCQE-like, where np-nh contributions are included but pion absorption is accounted for, to CC0π, where the event is defined solely by the final state topology and minimal model dependent corrections have been applied [59]. In the case of CC0π, a muon from the neutrino interaction is identified with no reconstructed charged or neutral pions in the final state, but it can include any number of reconstructed protons if this is not specified. This has made it more challenging for theorists to compare their models with different experimental data, but the data are more resilient to significant model changes that may occur in the future.

Several experiments have contributed to the modern picture of neutrino-nucleus cross sections alongside MiniBooNE but it is especially worth highlighting T2K [9] and MIN-ERvA [10]. The off-axis T2K near detector ND280 [9] in the J-PARC neutrino beam with an average energy of 0.6 GeV [108] has an active cross section programme to reduce systematic uncertainties for oscillation analyses. MINERvA was an experiment designed to measure neutrino interactions on different target materials, it had an active target of plastic scintillator and passive targets of iron, lead, water and helium. It used the NuMI beam at FNAL with an average energy of around 3 GeV in low energy mode [109].

Both experiments have published several inclusive and exclusive muon neutrino cross sections on a variety of targets, mainly water and hydrocarbon. The inclusive measurements tend to show an overall agreement with models within the current uncertainty budget [110, 111] and the inclusion of np-nh models to fill in the dip region between QE and RES scattering is required.
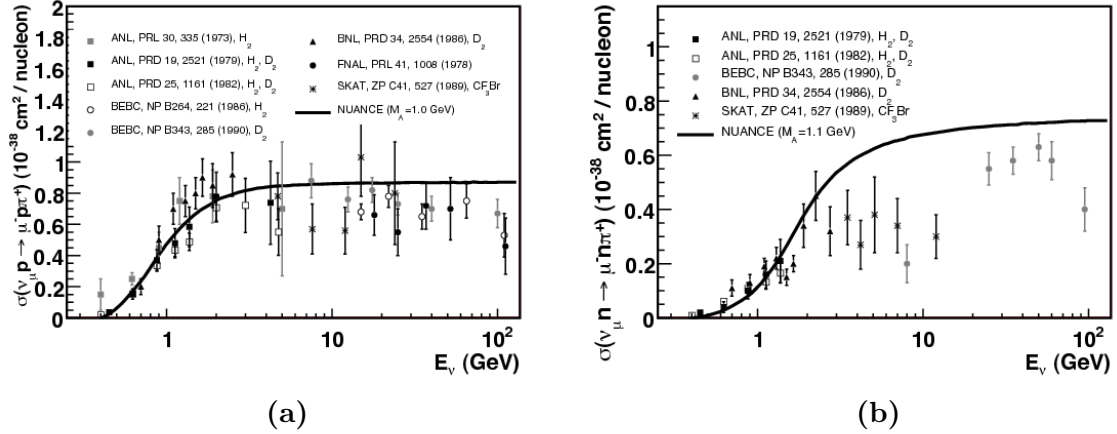
Figure 2.17: CC resonant π^+ production on (a) protons and (b) neutrons in bubble chamber experiments. Figures from [80].

The ability for models to describe inclusive and CCQE-like/CC0π cross sections in terms of lepton kinematics is not entirely sufficient on its own as oscillation experiments need to reconstruct the neutrino energy in their analyses. There are two main approaches used. The first is to use the kinematics of CCQE interactions to determine the energy from the lepton four-momentum [59] and the second is to add the lepton energy to the associated calorimetric energy from the hadronic system [48]. The detector and beam will determine the method used as CCQE peaks at relatively low energy and good calorimetry is required for the hadronic energy. Both methods require model dependent corrections, CC0π must be corrected for missed pions and np-nh processes, and the hadronic energy must be corrected for invisible energy contributions from neutrons and FSI.

In order to understand the pion production contribution to the CCQE kinematic reconstruction and avoid bias in oscillation analyses, the single pion production cross section needs to be studied. Uncertainties on the bubble chamber data, shown in Figure 2.17, were high but there has been activity in this area to try to reduce them [112]. There have also been a number of pion production measurements from more modern experiments such as those highlighted above. There have been great advances in detector design and theoretical modelling, but tensions between data sets exist, especially when cross sections are given in pion kinematic variables.

One of the most prominent is the disagreement between MiniBooNE and MINERvA pion production data [113]. The experimental cross sections are flux integrated and therefore

not directly comparable, but the data and theoretical predictions can be compared. The theory predicts the shape of MINERvA data well but not the normalisation, and vice versa for the MiniBooNE data [113]. There are currently no models that can describe both sets of data simultaneously [114–117] but there are ongoing efforts to tune the physics parameters inside generators to better fit the data [118].

T2K has also measured differential $CC1\pi^+$ cross sections on hydrocarbon [119]. The hydrocarbon pion production data appears to be overestimated by the cross section models [119] in a similar way to the MINERvA data, but the exact model configurations are unlikely to be the same and a simultaneous analysis of all three data sets is yet to be performed. There is still room for improvement in both the modelling and measurements of pion production [59].

The calorimetric energy reconstruction method requires a good understanding of multi-nucleon emission and FSI processes to make the required corrections. One of the best ways to evaluate the performance of both of these model components is to study protons in the final state topology, such as $CC0\pi1p$. Studies like this are already being performed for T2K and MINERvA data, for example, by looking at transverse kinematic variables of the muon and proton [120].

The millimetre-scale spatial resolution of LArTPCs offers an opportunity to study np-nh processes with even greater detail through observations of protons down to kinetic energies of 21 MeV [121]. ArgoNeuT [122] has demonstrated the potential of this and produced inclusive differential cross sections [123], but its small size means that more exclusive channels would be statistically limited.

The larger MicroBooNE [124] detector has recently produced its first muon neutrino charged current inclusive cross section measurement [125] and results from exclusive channels where the final state topologies include the number of emitted protons are expected. The inclusive results favour the GENIE model configuration that is similar to the one used for the majority of this analysis. SBND, discussed in greater detail in the next chapter, will measure between five and seven million neutrino-argon interactions and open up the potential to push the theoretical models to their limits.

The width of the neutrino beam energy and unknown energy transfer in the scattering processes make it difficult to constrain individual cross section model parameters with neutrino data. This is especially true for inclusive data where degeneracies in the effects of different model components on the lepton kinematics are hard to disentangle. The inclusive channel is, however, the gateway to more exclusive measurements. The work done creating a high efficiency sample of ν_μ interactions with low backgrounds will directly benefit the other channels.

Chapter 3

The Short-Baseline Near Detector

In this chapter, the physics goals driving the SBN programme and SBND will be covered in Section 3.1. A description of the design and operation of the BNB will be given in Section 3.2 and a detailed overview of the three main detector subsystems that form SBND will be given in Section 3.3.

3.1   Physics goals

SBND will be the near detector of the three LArTPCs that make up the SBN programme [11] in the BNB [105] at FNAL. SBND will have an active mass of 112 tons and be located at a baseline of 110 m from the beam target. The 476 ton ICARUS detector [126] is currently being installed as the far detector at a baseline of 600 m. Data from MicroBooNE [124], with an active mass of 87 tons and a baseline of 470 m, which has been operational since 2015, will also used for SBN oscillation analyses. The relative positions of the three detectors and the beam target can be seen in Figure 3.1.

3.1.1   Sterile neutrinos

The primary goal of the SBN programme is to definitively confirm or refute the excess of low energy electron neutrino-like interactions observed at LSND [52] and MiniBooNE
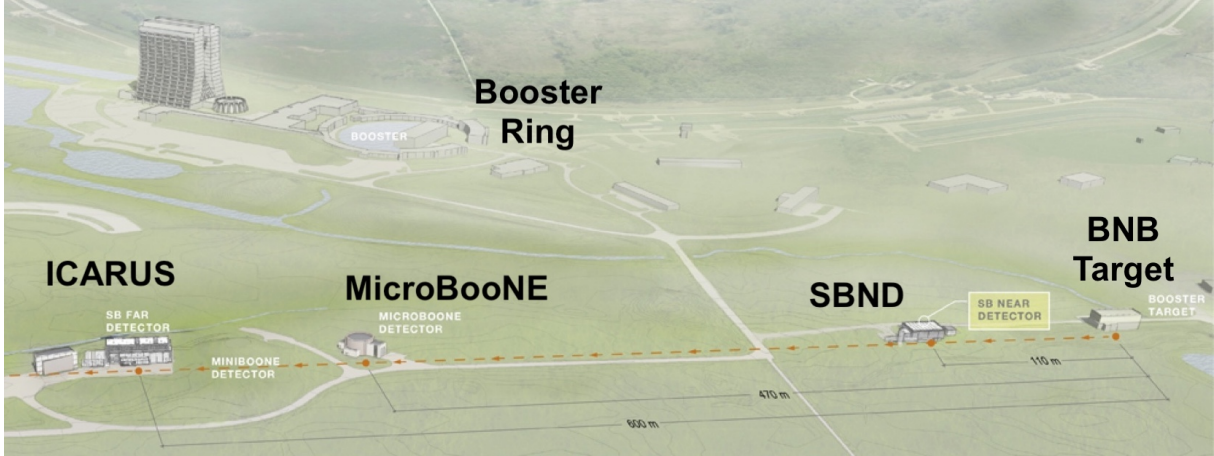
Figure 3.1: The relative positions of the three SBN detectors at FNAL. Image credit: FNAL creative services.

[53]. If the excess is confirmed, the LArTPC technology will be able to determine the nature of the excess. The most recent low energy excess measurements from MiniBooNE can be seen in Figure 3.2 and the significance of these results combined with the LSND data is over 6σ. The lack of particle track reconstruction resolution in either detector means that the observed low energy showers cannot be attributed to an electron from a ν_e CC interaction or a photon from some previously unknown background process.

The spatial resolution of a LArTPC allows a measurement of the energy loss at the start of the shower, with photon showers having twice the energy loss due to the electron positron pair created. The MicroBooNE data alone should be sufficient for determining if the excess can be attributed to electrons or photons, but cannot assign it to an oscillation process without a near detector. MicroBooNE is expected to present its low energy excess results by the end of 2020.

The most popular theoretical explanation for the excess is eV-scale sterile neutrinos [56], as described in Section 2.2.3. The SBN programme, with both near and far detectors will be able to attribute an excess to either neutrino oscillations or an unaccounted for or new physical process. If no excess is observed, SBN will be able to rule out almost all of the allowed sterile neutrino phase space, as shown in Figure 3.3 [11].
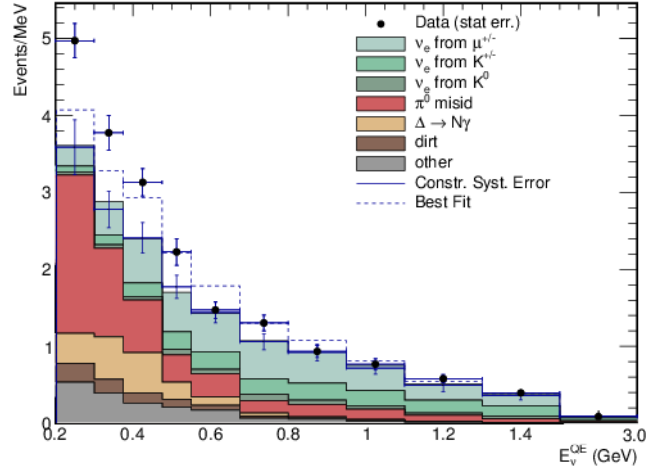
Figure 3.2: The excess of low energy electron neutrino-like events observed by the MiniBooNE experiment. Figure from [53].
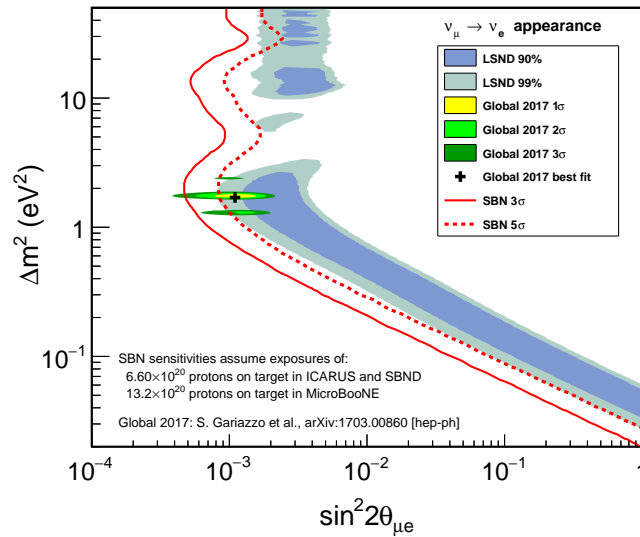
Figure 3.3: The sensitivity of the SBN program to eV-scale sterile neutrinos in the electron neutrino appearance channel. Sensitivity contours from [11] with an updated global fit. Figure credit: D. Schmitz.

3.1.2   Neutrino-argon cross sections

The target mass and proximity to the origin of the beam means that between 5 and 7 million neutrinos will interact in SBND over the course of three years with the beam delivering 6.6×10^{20} Protons On Target (POT). As a result, SBND will be able to publish neutrino-argon cross sections with low statistical uncertainty allowing for differential measurements in two or three kinematic variables. The data will be an invaluable test of neutrino generators and be vital for reducing cross section uncertainties for the future DUNE experiment.

The large number of interactions also makes the search for rare cross section channels, such as kaon production and neutrino-electron scattering, possible, as shown in Table 3.1. Rare channels are often highly sensitive to BSM effects, and there is a great deal of interest from the theoretical particle physics community in using SBND for BSM searches [5].

3.1.3   Detector technology research and development

Despite first being proposed in 1977 [8], the LArTPC remains a fairly novel technology and many aspects of the detector design and operational principles are still being optimised. With much of the DUNE detector design being finalised [127] and millions of pounds sterling in funding already being allocated, it is critical to ensure the long term stable running of key detector components in realistic operating conditions. This was one of the primary motivators for the protoDUNE experiment [128], and SBND will also play an important role in this as it shares the same membrane cryostat, front-end electronics, cathode design, and light detection systems.

3.2   The Booster Neutrino Beam

The neutrino beam is as much of an important component of accelerator based experiments as the detector itself. The BNB [105] provides a source of primarily muon neutri-

Table 3.1: The expected neutrino interaction rates in SBND after approximately three years of running, predicted using the G17_01b tune of the GENIE neutrino generator [91]. Table credit: R. Jones.

Hadronic Final State	GENIE (G17_01b) prediction for 6.6×10^{20} POT ($\approx$ 3 years)
Charged Current	
ν_μ Inclusive	5,389,168
$\rightarrow 0\pi$	3,814,198
$\longrightarrow 0p$	27,269
$\longrightarrow 1p$	1,261,730
$\longrightarrow 2p$	1,075,803
$\longrightarrow \geq 3p$	1,449,394
$\rightarrow 1\pi^+ + X$	942,555
$\rightarrow 1\pi^- + X$	38,012
$\rightarrow 1\pi^0 + X$	406,555
$\rightarrow 2\pi + X$	145,336
$\rightarrow \geq 3\pi + X$	42,510
$\rightarrow K^+ K^- + X$	521
$\rightarrow K^0 \bar{K}^0 + X$	582
$\rightarrow \Sigma_c^{++} + X$	294
$\rightarrow \Sigma_c^+ + X$	98
$\rightarrow \Lambda_c^+ + X$	672
$\boldsymbol{\nu_e}$ **Inclusive**	$\approx$ **36,000**
Neutral Current	
ν_μ Inclusive	2,170,990
$\rightarrow 0\pi$	1,595,488
$\rightarrow 1\pi^\pm + X$	231,741
$\rightarrow \geq 2\pi^\pm + X$	343,760
$\rightarrow e(^-)$	374

nos to the SBN detectors. Negative hydrogen ions are accelerated to a kinetic energy of 400 MeV using a radio frequency quadrupole injector and two linear accelerators. The electrons are stripped by a carbon foil and the protons are delivered to the 474 m circumference Booster synchrotron ring where they are accelerated up to 8 GeV [105]. The ring is able to store 84 bunches of protons at one time but only 81 are filled. The bunches contain approximately 6.2×10^{10} protons and are 2 ns wide and 19 ns apart when they are delivered from the ring to the target hall. The delivery of all 81 buckets, 5×10^{12} protons over 1.6 μs, is called a spill [105]. The spills are delivered at a maximum rate of 5 Hz.

Quadrupole and dipole magnets are used to focus the beam onto a beryllium target with a 0.51 cm radius [105]. Beryllium is used as a target because it has thermal properties that make air cooling suitable and low levels of residual radiation. Protons interact with the beryllium atoms and produce a large number of hadrons, mainly pions and a small proportion of kaons [105]. The charged hadrons are then focused with a pulsed toroidal electromagnet, known as a horn, which bends the paths of charged particles towards the original beam direction. The flow of current can be reversed to focus positively or negatively charged particles and generate a primarily neutrino or antineutrino beam.

The BNB will run in neutrino mode for the duration of SBND operations meaning that π^+ and K^+ are focussed by the horn. There is a 45 meter long cylindrical decay region filled with air downstream from the horn to allow the hadrons to decay into neutrinos. π^+ decays via $\pi^+ \rightarrow \mu^+ + \nu_\mu$ with a branching ratio of 99.99% [45, 129] and K^+ decays via $K^+ \rightarrow \mu^+ + \nu_\mu$ with a branching ratio of 63.56% [45, 130]. At the end of the decay region is a beam stop made of concrete and steel designed to absorb muons produced in hadron decays. A diagram of the composition of a general neutrino beam is shown in Figure 3.4.

When the BNB is running in neutrino mode the majority of the beam will be composed of ν_μ from π^+ decay. There will also be $\bar{\nu}_\mu$ present from π^- that were not removed by the horn and ν_e from $\mu^+ \rightarrow e^+ + \nu_e + \bar{\nu}_\mu$ decays. Other pion, kaon and muon decays are also possible, with some also producing $\bar{\nu}_e$.
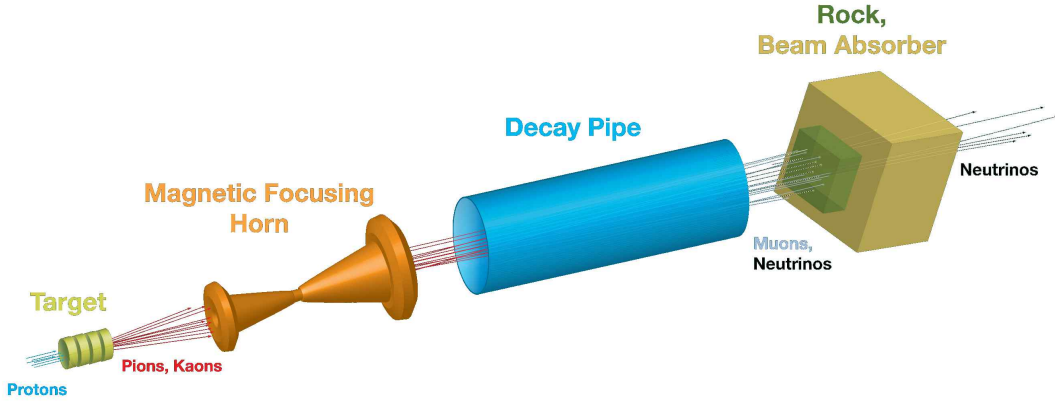
Figure 3.4: The steps required to create a beam of neutrinos from a high energy beam of protons. Image credit: FNAL creative services, modified.

3.2.1   Beam monitoring and flux prediction

The number of protons per beam pulse is determined by two toroids that measure the current of the beam [105]. The position, width and time of the proton spills are also measured. The two measurements of proton flux from the toroids agree to within 2% and the measurement of the width of the beam has a standard deviation of 0.1 mm [105].

To predict the neutrino flux, pion production cross sections from the HARP [131] and BNL E910 [132] experiments and kaon production cross sections from SciBooNE [133] and global fits [134] were used to parametrise the hadron production processes. Geant4 [135] was used to simulate the BNB beamline, p-Be interactions, propagation of particles and the decays into neutrinos [105]. The resultant flux predictions for different neutrino species at SBND are shown in Figure 3.5.

The generation of a neutrino beam is a very complicated process and there are several sources of systematic uncertainties which contribute to the uncertainty on the neutrino flux. The dominant source of uncertainty for each neutrino species is on the hadron production in p-Be interactions, as can be seen in Table 3.2. The uncertainties in the rate of p-Be and meson interactions, the distributions of the magnetic field within the horn, the exact locations of beamline components and the POT counting also contribute [136]. A more detailed description of how the uncertainties in the flux propagate to cross section measurements is given in Section 7.4.
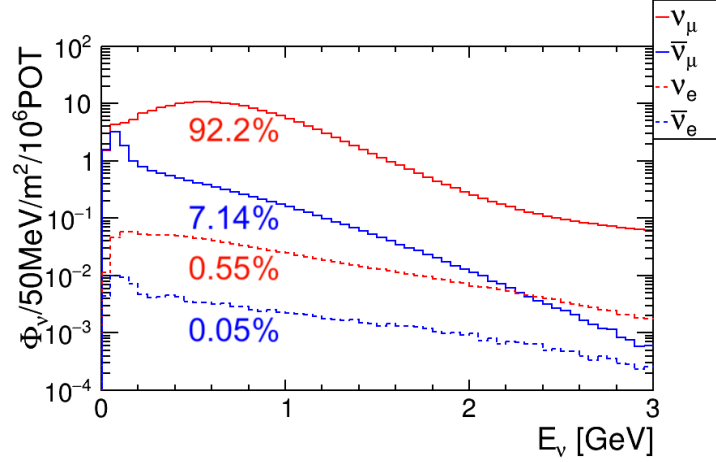
Figure 3.5: The expected electron and muon (anti)neutrino flux from the BNB at SBND.

Table 3.2: BNB flux systematic uncertainties for all relevant neutrino species as calculated by the MicroBooNE collaboration [136]. The uncertainties are expected to be similar but not exactly the same for SBND due to slight differences in the flux seen by the two detectors. The pion production uncertainties are calculated from thin target HARP data [131], there is available data from a thicker target which may reduce these uncertainties [137]. Table reproduced from [136].

Systematic	$\nu_\mu/\%$	$\nu_e/\%$	$\bar{\nu}_\mu/\%$	$\bar{\nu}_e/\%$
π^+ production	11.7	1.0	10.7	0.03
π^- production	0.0	11.6	0.0	3.0
K^+ production	0.2	0.1	2.0	0.1
K^- production	0.0	0.4	0.0	3.0
K^0_L production	0.0	0.3	2.3	21.4
Proton delivery	2.0	2.0	2.0	2.0
Other	3.9	6.6	3.2	5.3
Total	12.5	13.5	11.7	22.6
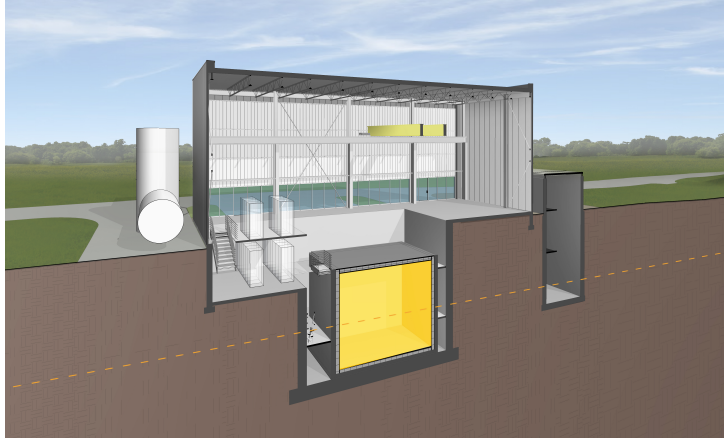
Figure 3.6: The SBND building complex. The BNB is shown as an orange dashed line coming from the right of the image. The concrete overburden will sit between the top of the detector, in yellow, and ground level. Image credit: FNAL creative services.

3.3   The SBND subsystems

SBND will be located in a building 110 m from the beryllium target and will have a small concrete overburden, shown in Figure 3.6. An exploded view of the detector subsystems is shown in Figure 3.7. The core of the detector will be a modular LArTPC with a central Cathode Plane Assembly (CPA) and two drift regions. The CPA will be held at a constant negative voltage and a field cage around the Time Projection Chamber (TPC) will maintain a constant electric field of 500 V/cm. Charged particles passing through the liquid argon will ionise argon atoms and these ionisation electrons will be drifted in the electric field. At each side of the detector will be an Anode Plane Assembly (APA) instrumented with wire planes for detecting the drifted charge.

There will be a PDS behind each wire plane that will be used for triggering on interactions in time with the beam spill and the association of detected charge with the true interaction time. The TPC and PDS will be housed in a membrane cryostat which will maintain a liquid argon temperature of 87 K and recirculate and purify the argon at a constant rate. The cryostat will then be enclosed by seven scintillator based CRTs designed to tag the position and time of cosmic ray muons entering the detector.
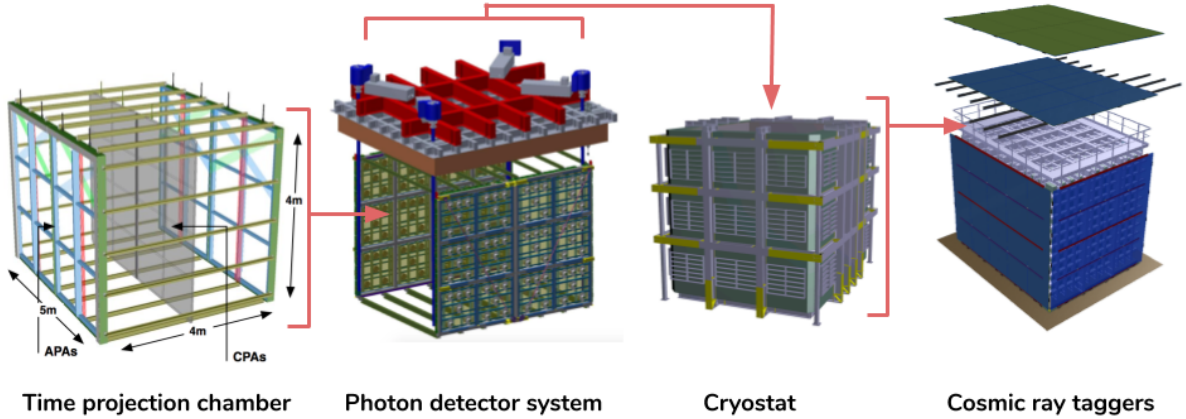
Figure 3.7: The SBND subsystems. The TPC sits inside the PDS which is hung from the lid of the membrane cryostat. The outside of the cryostat is surrounded by a number of CRTs. TPC diagram from [11], PDS diagram created by J. Boissevain, cryostat diagram created by M. Nessi and CRT diagram created by I. Kreslo.

3.3.1   Charged particles in liquid argon

The target and detector medium of SBND is liquid argon, chosen because of its density, electron transport and scintillation properties. The high density, 1.396 g/cm^3 at 87 K [138], increases the number of potential target nucleons per unit volume and hence the neutrino interaction probability. There are approximately 2.1×10^{22} argon atoms per cm^3, corresponding to 3.8×10^{23} protons and 4.6×10^{23} neutrons for argon-40, which makes up 99.6% of naturally occurring argon [138].

When a neutrino interacts with an argon atom, charged particles will be produced in most cases. Charged particles ionise argon atoms along their path, with an average ionisation energy of approximately 23.6 eV at 500 V/cm [139, 140]. In the presence of an electric field some proportion of the ionisation electrons can be drifted before recombining with the argon ions.

The mean energy loss of of relativistic charged particles in liquid argon is well described by the Bethe formula [141], shown in Figure 3.8. Given that the mean energy loss of a Minimum Ionising Particle (MIP) is approximately 2.1 MeV/cm [141], around 9×10^4 ionisation electrons will be produced per cm. Fluctuations in the energy loss can be described with a Landau-Vavilov distribution [142] which gives a most probable energy loss of around 1.8 MeV/cm for a 5 GeV muon with the inclusion of a density effect [143].
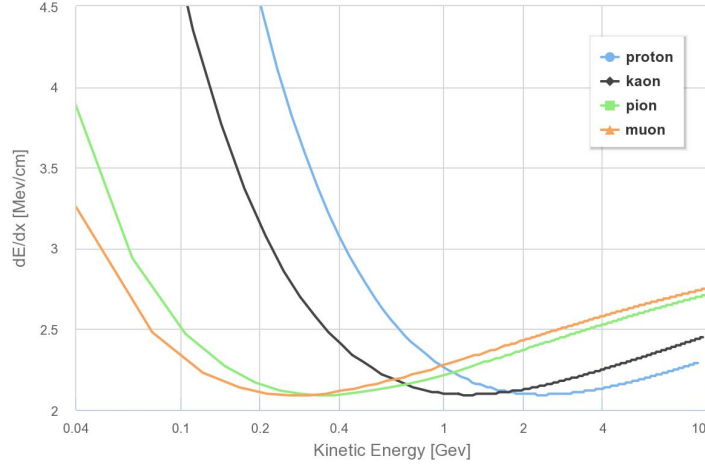
Figure 3.8: Energy loss of relativistic charged (non-showering) particles in liquid argon as a function of kinetic energy. Figure from [144].

The most probable energy loss for minimally ionising muons is well defined and hence it is an important calibration tool.

A proportion of the ionisation electrons will immediately recombine with argon ions even in the presence of a strong electric field. The recombination factor, R_c, is defined as

$$R_c = \frac{dQ/dx}{dE/dx} \tag{3.1}$$

where dE/dx is the energy loss by the particle per unit track length and dQ/dx is the charge collected by the wire planes per unit length. The dependence of recombination on dE/dx can be seen in Figure 3.9. This recombination factor must be corrected for in order to make accurate calorimetric measurements.

As argon is a noble gas, electrons are able to travel long distances without interacting with the argon atoms. At a field of 500 V/cm and temperature of 87 K the electron drift velocity is 0.165 cm/μs and the longitudinal and transverse coefficients of diffusion are 6.82 cm^2/s and 13.16 cm^2/s [146].

The massive argon ions will also drift with a velocity of approximately 8 mm/s [147]. If there is a high rate of charged particles in the detector and the drift distance is long or the electric field is low, this can lead to a build up of charge, referred to as space charge [147]. Space charge can distort the electric field and hence passage of ionisation electrons
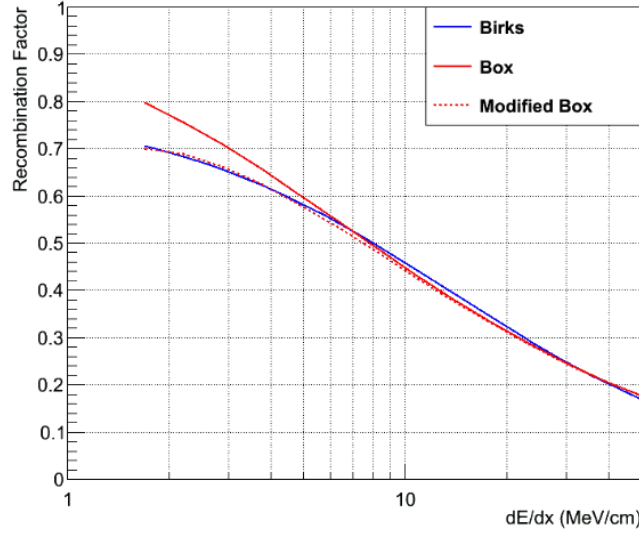
Figure 3.9: The dependence of the ionisation electron recombination factor on the energy loss of a charged particle traversing liquid argon for a number of different models. Figure from [145].

in the detector.

There will also be a decrease in the number of electrons proportional to the distance travelled due to electronegative impurities, such as O_2, H_2O and CO_2, in the argon [148]. This is measured in terms of the electron lifetime, the time for the number of electrons to decrease by 1/exp.

Argon scintillates when charged particles pass through it, producing Vacuum Ultra-Violet (VUV) light with a peak wavelength of 128 nm [149], shown in Figure 3.10. The energy required to produce a scintillation photon is approximately 19.5 eV at 500 V/cm [150]. There is a fast component at 6 ns and a slow component between 1100 and 1600 ns [149].

There are tensions between recent calculations and measurements of the Rayleigh scattering length for 128 nm light in liquid argon [151, 152], with values between 55 and > 110 cm reported, but any value within this range means that liquid argon is very transparent to its own scintillation light. These tensions would however need to be resolved in order to use the scintillation light to make calorimetric measurements.
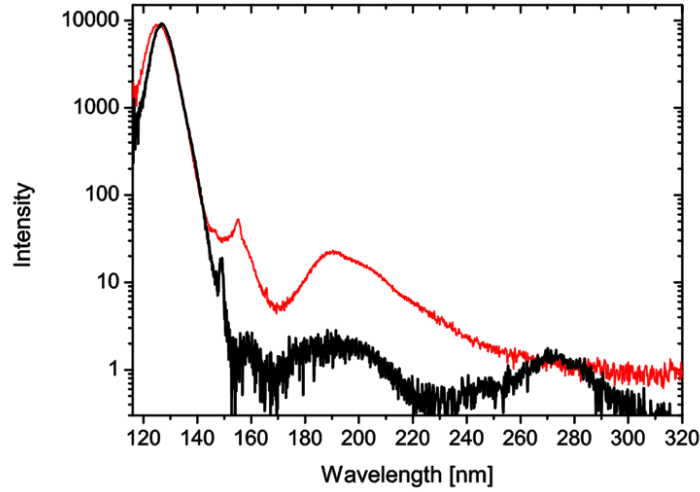
Figure 3.10: The VUV → UV spectrum of liquid argon (black) and gaseous argon (red) with a clear emission peak at 128 nm. Figure from [149].

3.3.2   The time projection chamber

The principle of operation of the TPC is shown in Figure 3.11. At the centre of the TPC is the CPA constructed of two joined frames each containing 8 panels of stainless steel mesh. One of the frames will be attached to a high voltage feedthrough capable of delivering 100 kV. Each mesh panel will also house a TetraPhenyl Butadiene (TPB) coated reflecting foil, the TPB shifts the VUV scintillation light into the visible spectrum where photon detectors such as Photomultiplier Tubes (PMTs) and Silicon Photomuiltipliers (SiPMs) are sensitive.

There will be a drift distance of 2 m either side of the CPA, with a field cage around the outside of the TPC. The field cage will consist of roll formed stainless steel strips wrapped around the TPC perpendicular to the drift direction and a resistive divider network will be used to drop the voltage by about 3 kV per strip between the CPA and APA. The field cage will ensure that the electric field is uniform so that the drift direction of the electrons will be perpendicular to the APA and the distortion of tracks is minimised.

Each APA is formed of two 2.5 × 4 m stainless steel frames instrumented with three planes of 150 μm copper beryllium wires. The closest plane to the CPA, the U plane, will be at +60 degrees to the vertical axis and will be held at -200 V, the second plane, V, will be at -60 degrees and will be unbiased. The third, Y, plane will be parallel to the vertical
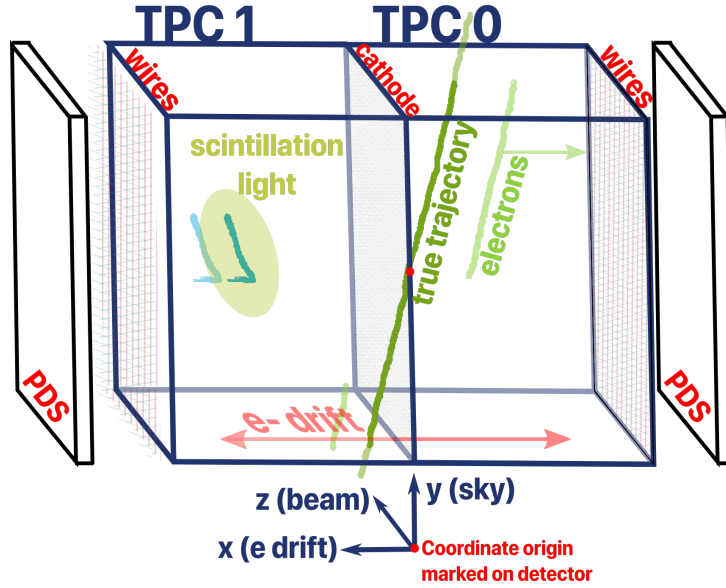
Figure 3.11: A diagram of the SBND TPC. The z direction is defined along the path of the neutrino beam, the y direction points upwards and the x direction is along the electron drift direction that forms a Cartesian coordinate system. The center of the coordinate system is in the middle of the cathode on the front face of the detector such that the detector spans from 0 to 500 cm in z and -200 to 200 cm in both x and y.

axis and will be held at 430 V. The wire orientations are shown in Figure 3.12. Plastic combs at intervals along the APA are used to keep wires in place and prevent sagging or breakages.

The two frames of each APA will be joined together and wires, both in the U and V planes, crossing the boundary will be electrically connected together to form a single effective readout channel. The wires for all three planes are 3 mm apart with a 3 mm gap between the planes. There are 1664 Y channels and 1984 channels for both the U and V planes for each APA, giving a total of 11,264 TPC channels for the whole detector. Images of the APA frames before and after coupling are shown in Figure 3.13.

The U and V planes are referred to as induction planes because the signals they detect will be from the induced charge of electrons passing by them, as shown in Figure 3.14. The Y plane is referred to as the collection plane as it will collect the ionisation electrons to form a signal.

The signals from the readout channels will be shaped, amplified and digitised by front end electronics inside the cryostat. 128 channels are read out by one Front End Mother-
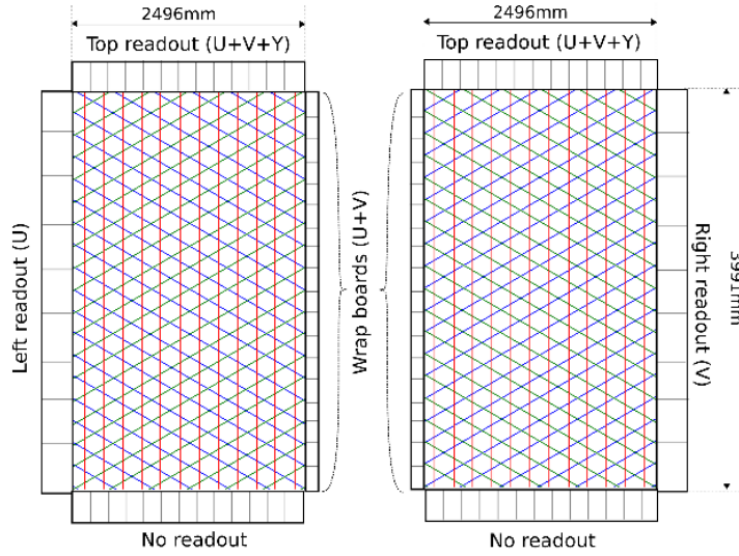
Figure 3.12: The layout of the three wire planes for two joined APA frames as seen from inside the detector. Figure from [153].

Board (FEMB) which holds 8 Application Specific Integrated Circuits (ASICs), each one providing gain and shaping to 16 channels to provide an optimal signal-to-noise ratio. The digitisation will then be performed by 128 single channel Analogue-to-Digital Converters (ADCs), which sample at a frequency of 2 MHz and have a resolution of 12 bits. The 128 channels are multiplexed by a cryogenic Field Programmable Gate Array (FPGA) which also re-organises the data.

The digitised signals will then be sent to a warm interface board containing an FPGA which multiplexes multiple FEMBs and performs lossless compression. The data will then be sent out over a fibre optic cable to the Data Aquisition (DAQ) system which will decide whether to write the data to magnetic tape based on the available trigger information.

The data will be split into readout windows which correspond to the length of time it would take for charge to drift from the cathode to the wires, $\sim$1.25 ms. In order to fully reconstruct sources of background that may have crossed the TPC before or after the trigger, one readout window on either side of the triggered window will also be saved.
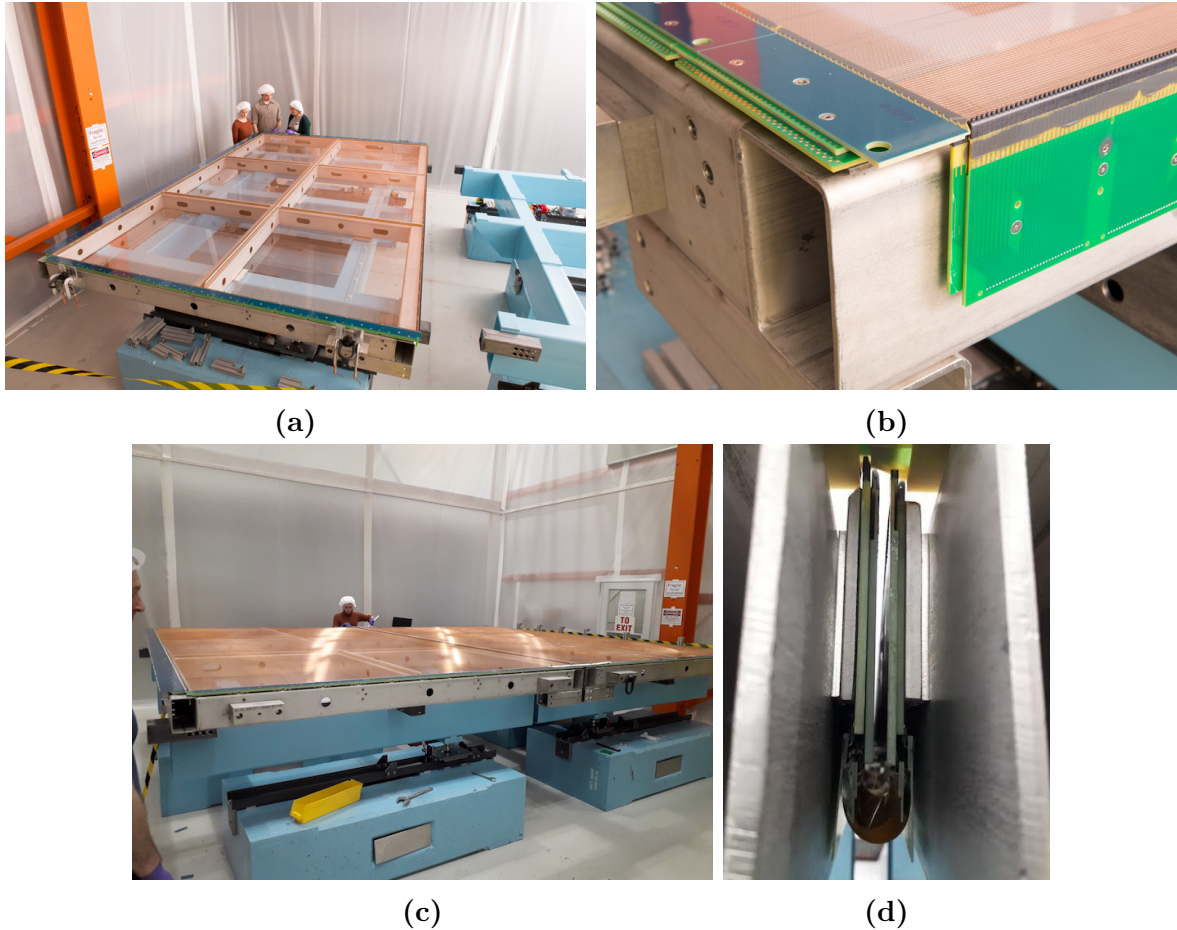
Figure 3.13: Images of the APA frames. (a) A full APA plane, corresponding to a quarter of the TPC readout channels. (b) A close-up of the electrical jumper boards. (c) Two planes joined with mechanical fastenings on the metal frames. (b) Electrical cables between the jumper boards on the side of the frame. The blue structure underneath the APA frames is an alignment fixture that allows for small positional adjustments in three dimensions before the mechanical coupling. Figure credit: (a), (b) Fermilab media services, (c), (d) N. McConkey.
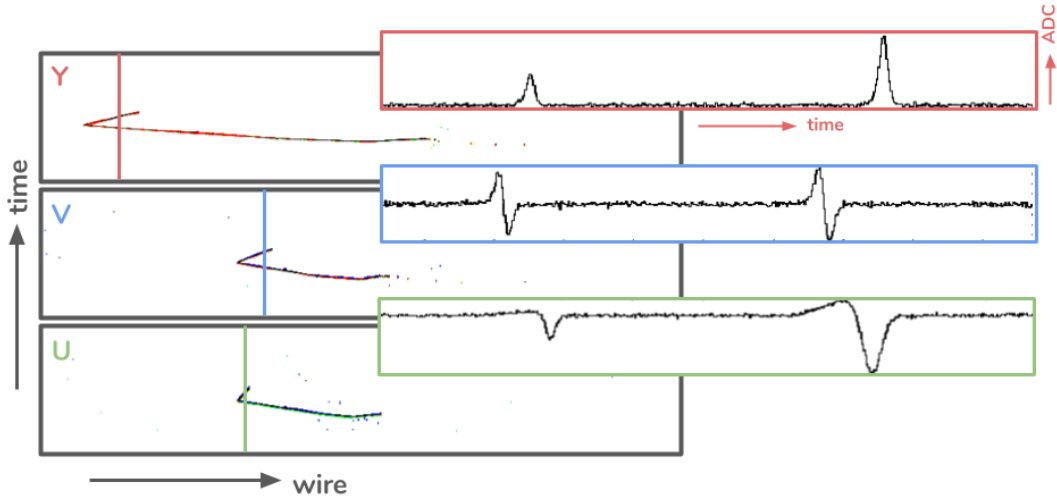
Figure 3.14: Simulated wire plane response to an interaction in the TPC. The collection plane, Y, observes a Gaussian-like peak in response to drifted ionisation electrons. The induction planes, U and V, observe a bipolar pulse as the electrons drift towards and then away from the wires. The first peak for the U wires is spread out as the plane is not shielded.

3.3.3 The photon detection system

The decision whether or not to trigger on an event will be based primarily off information from the PDS as the signal from scintillation light is much faster than from ionisation electrons. A timing resolution of a few 100 ns is required to reject background events that occur outside of the beam spill, and a resolution of 1-2 ns would be needed to utilise the bucket structure of the spill [105].

The area behind both wire planes will be instrumented with 120 8-inch Hamamatsu PMTs with 1 ns timing resolution and 192 ARAPUCAs [154], as shown in Figure 3.15. 96 of the PMTs will be coated with TPB and the remaining 24, in the center of each module, will be uncoated. The uncoated PMTs will only be sensitive to scintillation light reflected off the cathode allowing for a better estimation of the position of the event in the drift direction.

The ARAPUCA is a novel light detector system being developed for DUNE, it works by trapping photons with a highly reflective inner surface and detecting them with a
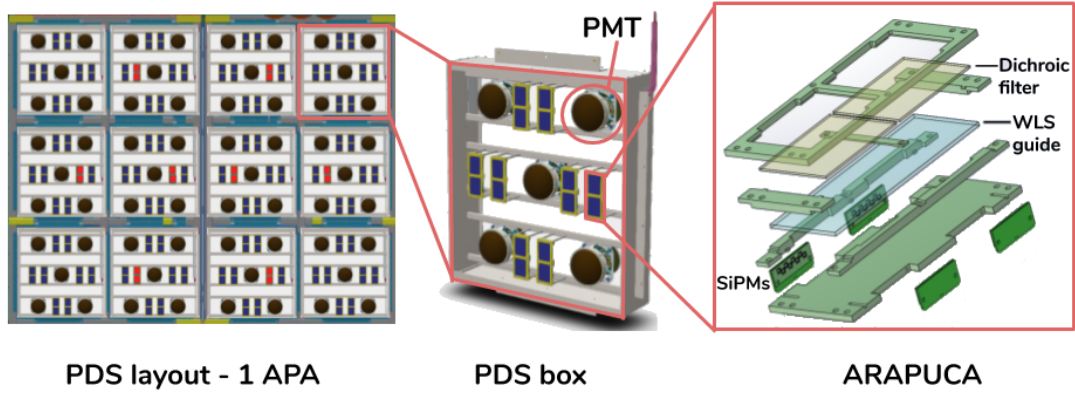
Figure 3.15: An exploded view of one half of the SBND PDS, the other side has exactly the same layout. The PDS is split up into modular boxes holding 5 PMT and 8 ARA-PUCAs. Figure components from J. Boissevain (PDS layout and box) and A. Machado (ARAPUCA).

small number of SiPMs relative to its total area [154]. The photons are trapped using a dichroic filter sandwiched between two wavelength shifters, the outer shifter makes the filter transparent to the photon and the inner shifter makes the photon reflect off the filter. The use of PMTs is established in the field of high energy particle physics but would be infeasible in DUNE due to the small space between APAs. This is the motivation for developing and testing SiPM based light detectors such as the ARAPUCA in SBND.

Signals from the PMTs will be read out and digitised by commercial front end electronics boards at 500 MHz and 14 bit ADC resolution, providing a dynamic range of 512 Photo-Electrons (PE). The front end electronics for the ARAPUCAs were initially designed for Mu2e [155], they have a clock speed of 80 MHz and 12 bit ADC resolution. Both the TPC and PDS will be inside a membrane cryostat capable of maintaining a greater than 3 ms electron lifetime, equivalent to 100 parts-per-trillion O_2, a less than 2 parts-per-million N_2 contamination, and a temperature of 87 K.

3.3.4 The cosmic ray tagger

As SBND will be on the surface and will only have a 1 m concrete overburden it will be exposed to a 3-4 kHz flux of charged particles, mostly muons, from cosmic ray showers in the atmosphere. The frequency of cosmic ray muons crossing the detector is high
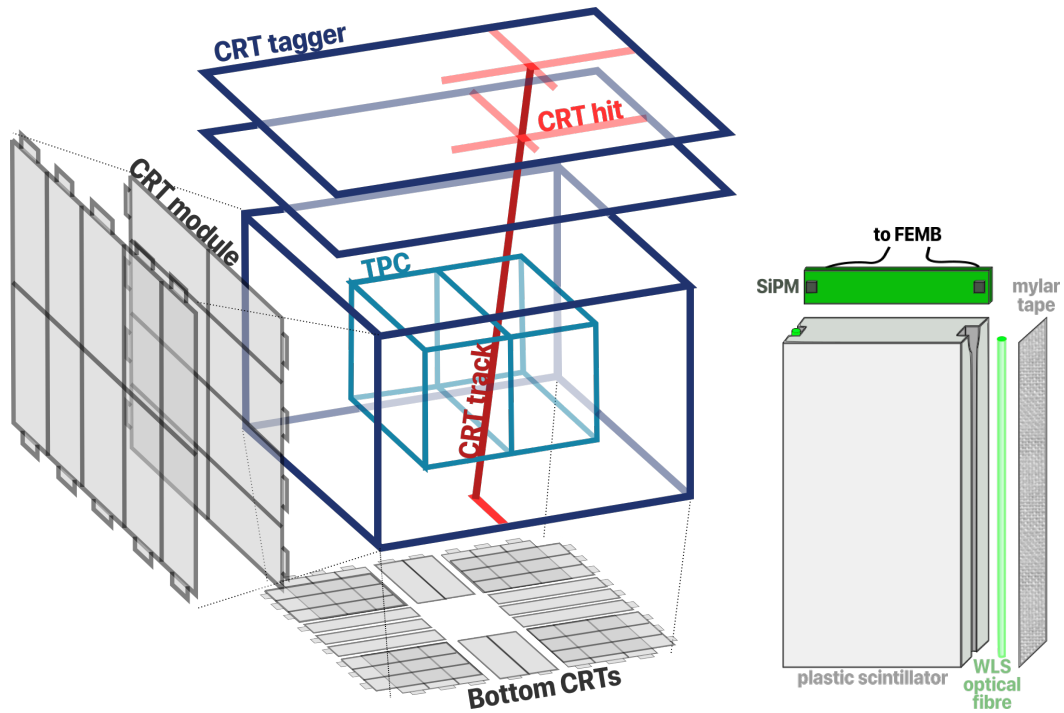
Figure 3.16: The CRT system surrounding the SBND TPC with the main components and reconstructed objects labelled. There are seven CRT taggers, one on each face with an extra tagger on top to be able to measure the trajectory of particles which stop in the CRT volume. An exploded view of one of the plastic scintillator strips that make up a module is shown on the right.

relative to the drift velocity of the ionisation electrons and therefore they pose a significant background to all studies. Matching objects reconstructed in the TPC with flashes of light in the PDS does not have very precise position resolution and so SBND will be equipped with a suite of CRTs [156] providing nearly complete coverage of the TPC, as can be seen in Figure 3.16.

The CRT will use plastic scintillator to detect charged particles through the conversion of their energy depositions to scintillation photons. Strips of scintillator 11.2 cm wide (5.95 cm for the bottom tagger), 1 cm thick and between 1.8 and 4.5 m long are fitted with wavelength shifting optical fibres down both edges as can be seen in Figure 3.16. 16 strips are laid edge to edge to form a module with strips of mylar tape in between for optical isolation. The ends of the optical fibres on each strip are coupled to SiPMs which are read out by an FEMB on the module.

Arrays of 2×4 or 2×5 modules are placed perpendicular to each other to form a tagger

with two dimensional position resolution. There will be one tagger covering each side and the bottom of the TPC and two in a telescopic array on the top to tag the trajectories of stopping particles. There will be areas with one dimensional or no coverage on the bottom due to the cryostat support structure and 19% of the back face has no coverage due to space required for cryogenic equipment.

When both SiPMs reading out from the same strip are above a charge threshold the readout will be triggered in areas with 1D coverage. For areas with 2D coverage, another strip above threshold in a perpendicular module within 150 ns of the first is required to trigger the readout. The analogue signal will then be amplified, shaped and digitised with a timestamp resolution of 1 ns. The clocks of the three detector subsystems will be synchronised with a trigger that is sent every time a bunch of protons is incident on the target.

Chapter 4

Construction and calibration of the detector

SBND is currently being constructed at FNAL, this chapter details the testing and calibration performed to ensure the optimal detector performance and minimise the detector related systematic uncertainties. In the context of charged current ν_μ cross section measurements, the accurate reconstruction of the kinematics of the primary muon track is paramount. GeV-scale muons travel a long distance in liquid argon and so the detector response needs to be calibrated and unbiased across the entire volume. Section 4.1 describes the procedure used to test the continuity of all of the wire readout channels. Section 4.2 covers the expected performance of tools developed to calibrate the detector using through-going muons.

4.1   TPC wire plane readout tests

To measure the topology and momentum of long tracks it is important that all of the wire readout channels are functioning correctly and are continuous along their entire length across the detector. This particularly important for wires in the U and V planes as many are connected across two APA frames.

4.1.1 Electrical tension tests

All of the wires should be at a tension of around 5 N at room temperature to ensure that they do not sag or break under the forces induced by installation and cryogenic cooling. If a wire is not under sufficient tension it may distort reconstructed tracks. If a wire is under too much tension there is a risk that it may break, if a wire breaks once it is sealed inside the cryostat it has the potential to short any nearby wires that it touches. This scenario could result in a large unresponsive region in the detector which would have a significant impact on the physics sensitivity.

It is critical to measure the tension of every wire at different stages of installation to ensure that the tensions remain near the nominal value. The method commonly used in LArTPCs is to reflect a laser beam off a wire onto a photodiode and then mechanically disturb the wire. A Fourier transform of the photodiode signal can be used measure the fundamental resonant frequency, f_r, which is related to the tension, T, by

$$T = 4mL^2f_r^2 \tag{4.1}$$

where m is the mass per unit length of the wire and L is the length [124]. This process requires the alignment of the laser system for each wire and at later stages of installation the wires become increasingly inaccessible. This motivated the development of a method that can utilise the electrical connections of the wires.

A number of electrical tension measurements have been described before [157–159], but never in the context of LArTPCs. To investigate whether an electrical tension measurement would be appropriate for up to 4 m long wires in SBND, the method described in [159] was used as a starting point and the apparatus was adapted into the schematic shown in Figure 4.1. The wire under study was held at a constant high voltage with an adjacent capacitively coupled wire with an alternating current on it. A frequency sweep of the alternating current was performed until the resonant frequency was found.

In the case of SBND, the wires are made of a copper beryllium alloy and have a diameter of 0.15 mm and a mass per unit length of 1.45×10^{-4} kg/m. All of the wires in the Y
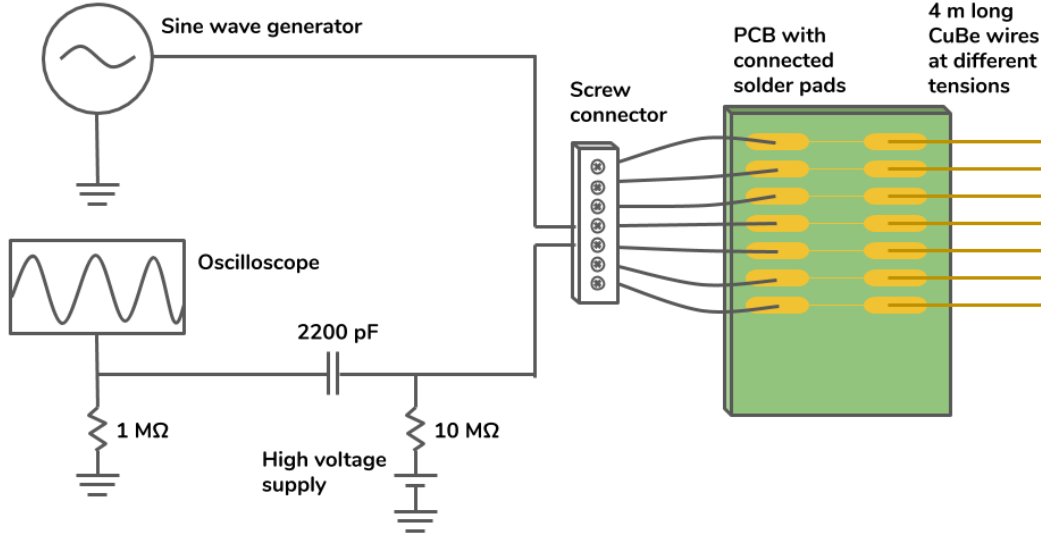
Figure 4.1: Circuit diagram for the electrical wire tension measurement tests. A positive high voltage was input into one wire and a sine wave in to an adjacent wire, an oscilloscope measured the induced current in the high voltage wire.

plane are 4 m long. As each APA is formed of two frames, the U and V wires only extend across one of the frames with a maximum length of 2.9 m for wires connected to the long sides of the frame. As the U and V wires are at $\pm$ 60 degrees to the Y wires, their length decreases by 6.93 mm between adjacent wires attached to both the long and short sides of the frame down to the shortest wires of the order of a few cm. The dependence of the fundamental resonant frequency on the length of copper beryllium wire at nominal tension, from Equation 4.1, is shown in Figure 4.2.

The system of two adjacent wires acts as a capacitor with capacitance per unit length, C_0, given by

$$C_0 = \frac{\pi \epsilon}{\ln \frac{d-r}{r}} \tag{4.2}$$

where r is wire radius, d is the distance between the wires and ϵ is the permittivity. When the frequency of the input alternating current reaches the resonant frequency of one of the wires it will oscillate. If the oscillations are modelled by damped, driven harmonic motion the capacitance can be written as

$$C(t) = C_0(1 + a(f) \sin(ft + \phi(f))) \tag{4.3}$$

(a)

(b)
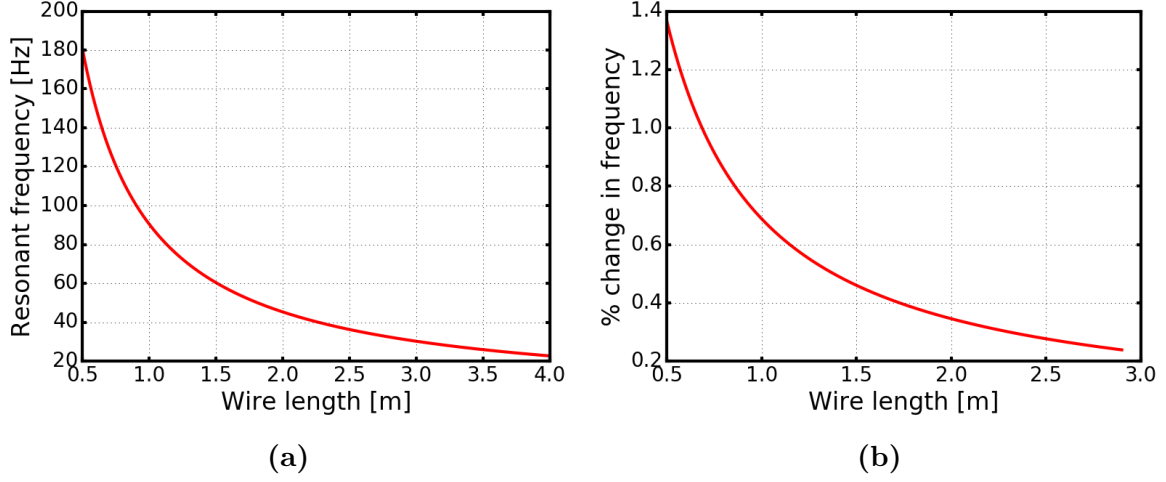
Figure 4.2: (a) The dependence of the fundamental resonant frequency on length for a wire of the type used by SBND at nominal tension of 5 N. (b) The percentage change of the frequency between adjacent U and V wires as a function of their length.

where f is the frequency, t is time, $a(f)$ is the amplitude of oscillation and $\phi(f)$ is the phase.

The amplitude is given by

$$a(f) = \frac{f_r^2 a_0}{\sqrt{(f_r^2 - f^2)^2 + \beta^2 f^2}} \tag{4.4}$$

where β is the damping factor, f_r is the resonant frequency and a_0 is a constant to be determined. The phase is given by

$$\phi(f) = \arctan\left(\frac{2\beta f}{f_r^2 - f^2}\right). \tag{4.5}$$

The induced current in the high voltage wire in this ideal case is then predicted to be

$$I(t) = \frac{dq(t)}{dt} = C_0 v_0 f \cos(ft) - C_0 V_0 a(f) f \cos(ft + \phi(f)) + \mathcal{O}\left(v_0 a\right) \tag{4.6}$$

where v_0 is the peak value of the AC input and V_0 is the value of the high voltage DC.

An automated procedure for scanning through frequencies and recording the current amplitude was developed using the instrument control and data acquisition software Lab-VIEW [160]. The system was tested on both 0.5 m and 4 m long wires under a range

(a) 0.5 m frame   **(b)** 4 m frame
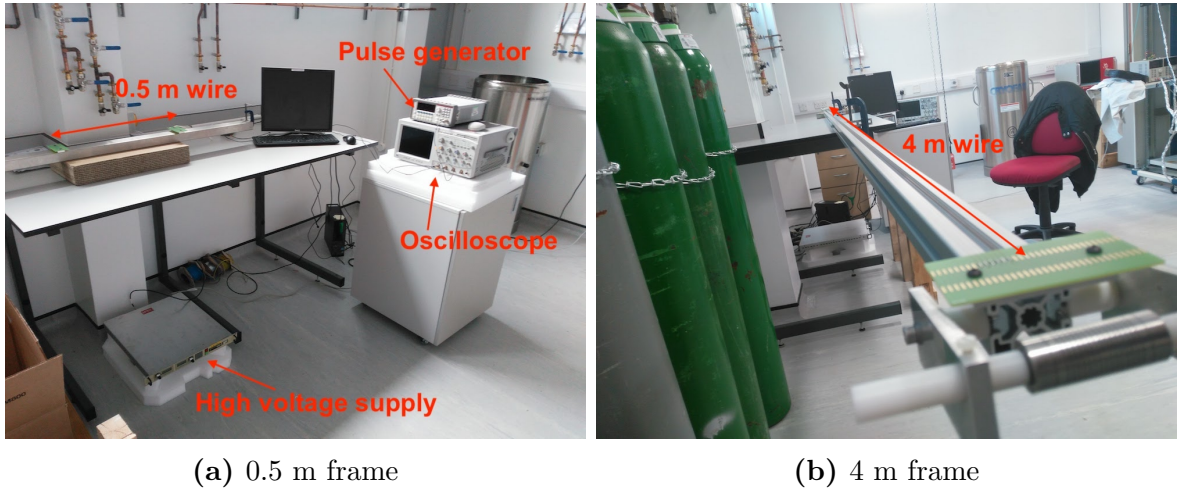
Figure 4.3: Images of the electrical wire tension set-up showing both frames used.

of different tensions on a specially designed frame which can be seen in Figure 4.3. An example measurement of 4 m wires with a fit of the theoretical prediction is shown in Figure 4.4.

It was found that the measured tension of the 0.5 m wires was stable under both changes in the speed of the frequency sweep and the value of the high voltage current as shown in Figure 4.5. The 4 m long wires tended to produce large oscillations and were highly sensitive to external backgrounds, such as the mains voltage. The background was later reduced by using another wire as an antenna and subtracting from the signal [12]. The large oscillations were mitigated by reducing the high voltage.

After this initial work, the method was further improved by other collaborators to use a system of three wires. The central wire was held at 0 V and the wires on either side held at $V_{AC}\pm V_{DC}$ in order to reduce the DC voltage required to the normal operating voltages of LArTPC wire planes. Further testing of this method was performed as described in [12]. This included a detailed study of the relationship between the AC and DC voltages and the performance of the method at cryogenic temperatures.

It was concluded that the resolution of this modified method at $V_{AC} = 40$ V and $V_{DC} = 150$ V was approximately 3% for wires with lengths between 0.75 and 3 m at a tension of 5 N, as shown in Figure 4.6a, and the resolution remained below 5% down to 50 cm [12]. It was also demonstrated, see Figure 4.6b, that the measurements are possible at liquid
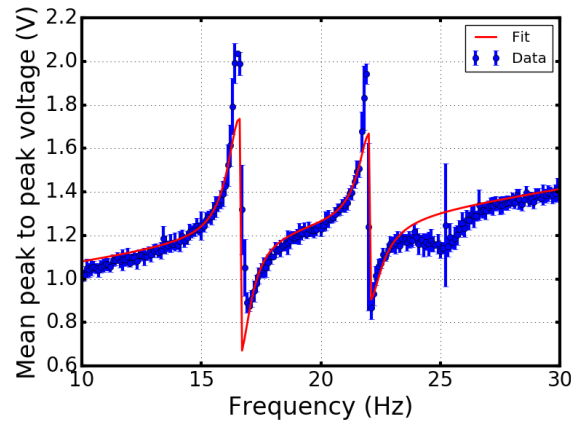
Figure 4.4: The measured current amplitude for two 4 m long wires held at tensions of 4.90 N and 2.94 N. The pickup from the mains electrical supply can be seen at 25 Hz. The theoretical prediction was fit to data, shown in red, to obtain the resonant frequencies. Deviations due to large oscillations and the 25 Hz mains frequency can be observed. The error bars signify the standard deviations of the measurements and do not encapsulate systematic uncertainties.
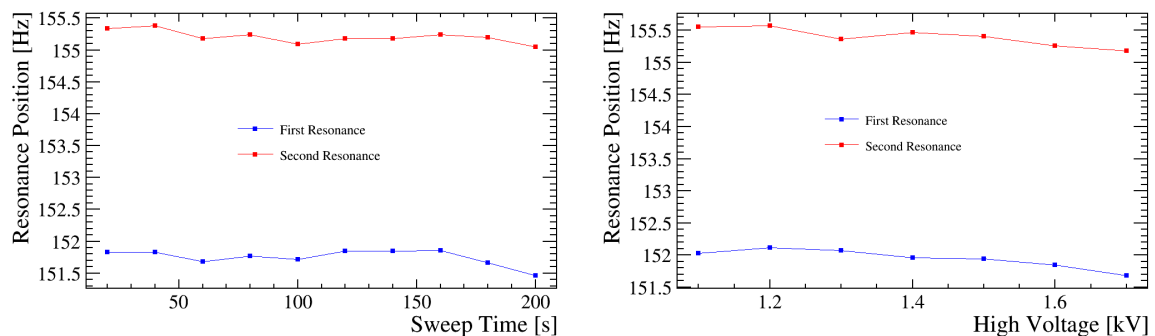
Figure 4.5: The dependence of measured resonance frequencies on frequency sweep speed and high voltage value.
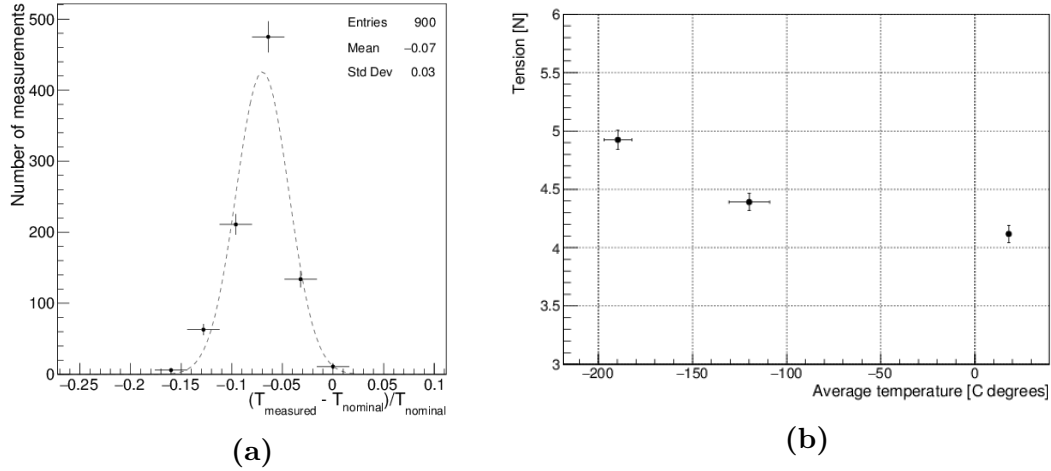
Figure 4.6: (a) The fit to the bias between the true tension and the measured tension at $V_{AC} = 40$ V and $V_{DC} = 150$ V for multiple measurements of wires between 0.75 and 3 m at 5 N. (b) The measured tension as a function of temperature. Figures from [12].

argon temperatures [12]. This method would be suitable for testing the tension after the detector is installed but would require the readout boards and electronics to be modified to allow the input of an alternating current. This method will not be used in SBND as the design of the readout boards has been finalised, but it could be incorporated into the DUNE design.

4.1.2 Wire continuity tests

The two frames of the APA must be joined together to form the wire readout of the TPC. The U and V wires that are soldered to boards on the two long sides of a frame are connected by jumper cables to effectively form 5.8 m long wires spanning both frames. It is vital to ensure that there is a continuous electrical connection across this gap and to test for any wire breakages.

The standard technique for testing continuity is to measure the resistance between the points where a wire is soldered to the boards. However, in the case of SBND where there are three planes of wires, only the solder pads for the top plane are accessible. However, the readout channels for all planes are accessible by design, and so a method for testing the continuity using only the readout channel input was developed. There is a capacitor
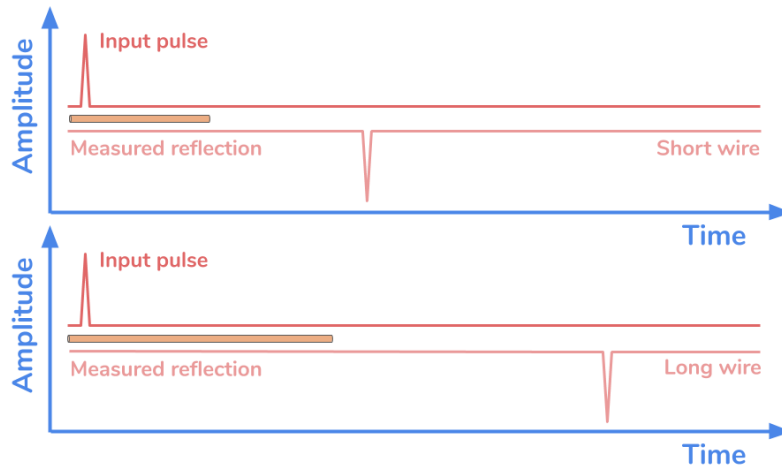
Figure 4.7: Principle of time domain reflectometry in the context of measuring wire continuity. The time of the reflected input pulse should be proportional to the length of the wire. The far ends of the wires have no other electrical connections resulting in the ends being the main point of reflection.

between the readout channels and the wires and so a changing voltage is required to measure the continuity, hence the technique of time domain reflectometry was used [161].

A function generator was connected to the readout channel and sent a continuous series of fast pulses through the electronics and along the wires, the reflected pulses were then measured with an oscilloscope. The principle of differentiating between wires with and without a functional jumper connection is illustrated in Figure 4.7. The time and shape of the reflected pulse depend on the length and impedance of the wire. By comparing the oscilloscope traces to each other and to a reference trace of an electronics board with no connected wire it was possible to quickly determine if there were any defects.

In order to match the 50 Ω impedance of the pulse generator a transmission line was created by resistively coupling the two neighbouring wires to ground, increasing their capacitance to the signal wire. A switch, shown in Figure 4.8, was developed to improve the time taken to test multiple wires by utilising all four oscilloscope channels and the 16 pin readout connections on specially designed test boards. This allowed all 16 channels to be tested in a few seconds by turning the switch through its four positions while observing the oscilloscope.

A diagram of the full system is shown in Figure 4.9 and an photograph of the system in use is shown in Figure 4.10. A splitter box was used to generate four identical 12 ns pulses
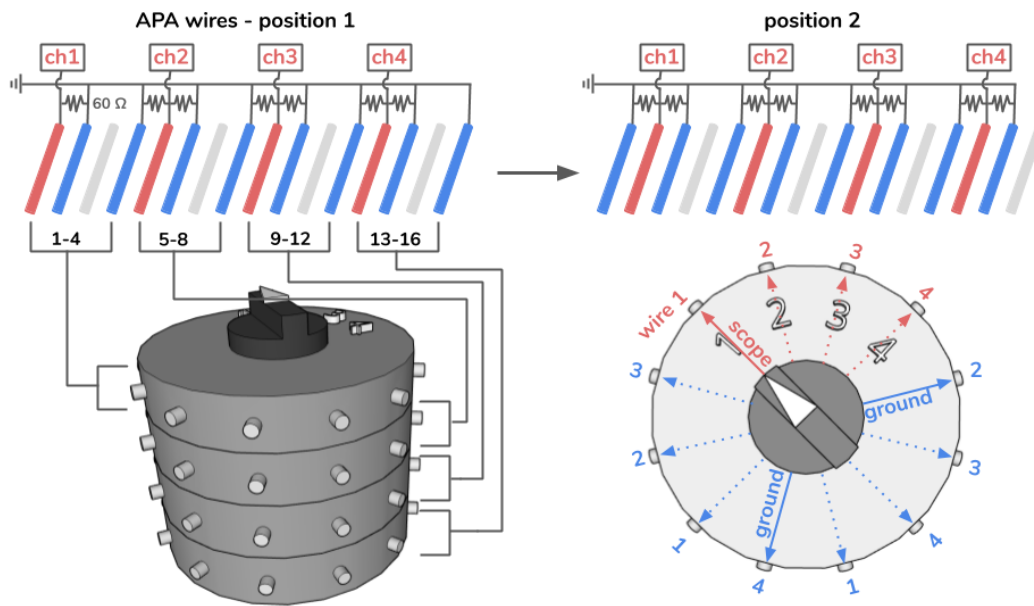
Figure 4.8: Mapping of the 4 switch positions to 16 APA wires. Four 3P4T (3 pole 4 position) switches are stacked, one pole on each switch is the signal, which is connected to oscilloscope channel, and the other two poles are grounded to the reference ground of the pulse generator. The bottom right diagram shows the mapping for one of the 3P4T switches, at each of the positions the scope and ground arrows move with the dial, representing electrical connections to the labelled wires. The bottom left diagram shows the stacking of the four switches and the APA wires that they are connected to, following the same scheme as the bottom right diagram. At the top of the diagram the first two positions for all of the APA wires are shown, as the position is incremented each connection moves one to the right. Moving through all four positions means that each of the 16 wires will be connected to an oscilloscope channel and measured exactly once with the two adjacent channels connected to ground.
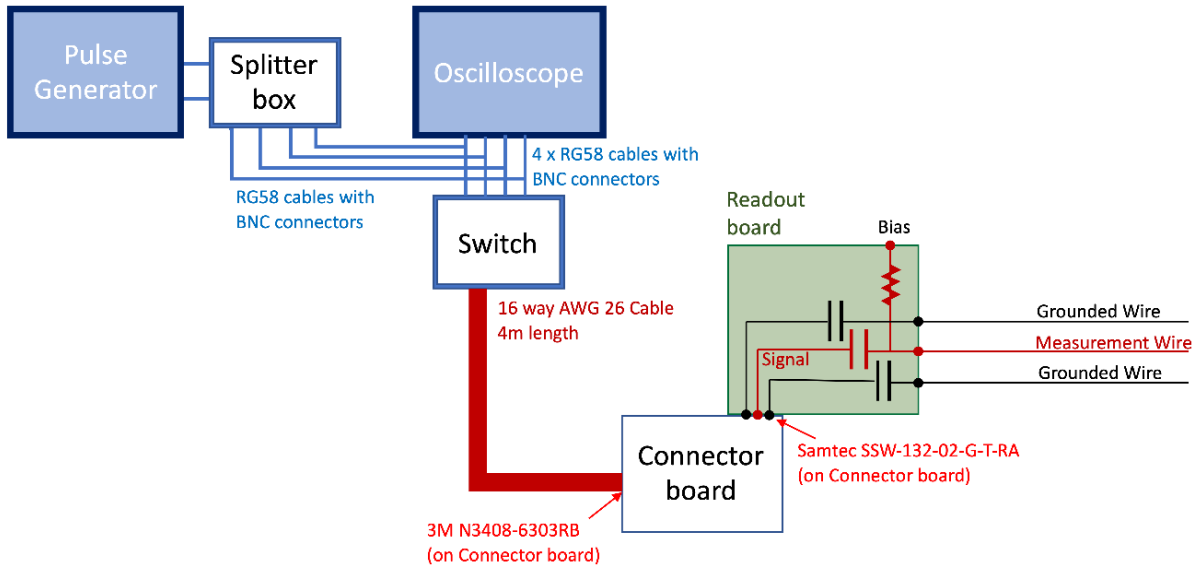
Figure 4.9: A block diagram of the electrical continuity test set-up where just three of the 16 connected channels are shown. Figure credit: N. McConkey.

with 200 mV amplitudes. The pulses were input into every fourth wire and the input and reflected pulses were read out by separate oscilloscope channels. The two channels either side were resistively coupled to ground unless the first or last channel was being read out, in which case only one of the neighbouring channels was coupled. The input pulse was visible in the oscilloscope trace and provided a trigger.

The reflected pulse has a complicated structure, as seen in Figure 4.11, because parts of the pulse are reflected at every electrical interface. As the electronics for each channel are identical, the measured pulse shape for continuous wires were also nearly identical and it was easy to distinguish faulty channels by eye. It is worth noting that most of the complicated structure is from the input of the electrical pulse through the test setup and it is not expected that the measured charge deposits will have a similar structure when the detector is operating. This method was used to confirm the electrical continuity of all of the SBND wires and represents a significant improvement in the ease and speed of testing. The method can be used up to the final stages of installation, hopefully ensuring a continuous and stable readout across the entire detector.
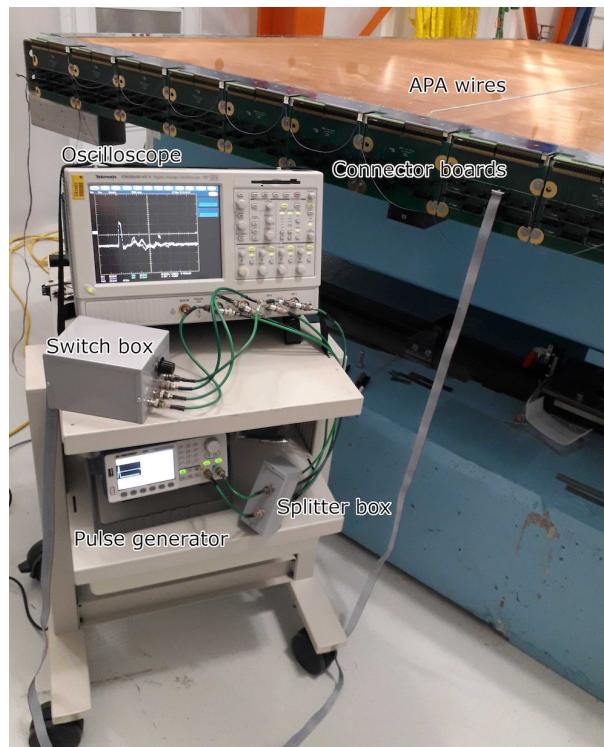
Figure 4.10: An image of the continuity test in use with the special testing connector boards shown. Figure credit: N. McConkey.
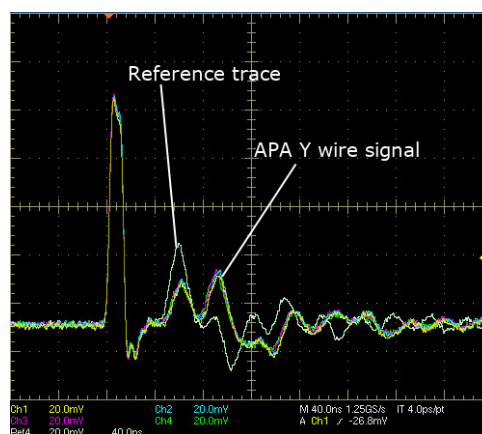
Figure 4.11: An example oscilloscope trace from the electrical continuity test for wires on the Y layer with a reference trace of an unconnected wire shown. The high amplitude input pulse at the start of the trace is used as the trigger for the oscilloscope. Figure credit: N. McConkey.

4.2   Calibration

Once the detector is installed and filled with liquid argon it will need to be calibrated as soon as possible to enable the analysis of the high rate of neutrino interactions. The required frequency of calibrations will vary from one precise measurement over the lifetime of the experiment to daily or hourly checks of the performance. There has been a focus on developing tools that can perform automatic calibrations as soon as the detector is operational.

There are many different components to be calibrated and physical properties to be measured. Some of the most important properties for the measurement of long muon tracks are space charge, electron lifetime and the alignment of the APA frames. Space charge is the build up of positive ions in the detector, as discussed in Section 3.3.1, and is not covered in detail here as it was not included in the analysis of this thesis.

The high flux of cosmic ray muons contributes a significant measurement background but it also provides an excellent tool for performing calibrations as nearly all through-going muons are MIPs and deposit a known amount of energy per unit track length. The CRT system can also act as a configurable trigger so samples of through-going muons with specific topologies can be produced.

4.2.1   Purity

Electronegative impurities reduce the electron attenuation length, called the electron lifetime when expressed in units of time at a constant drift field [148]. It is essential to be able to monitor the purity of the argon in real time to respond to any incidents which may endanger the detector. It is also vital to accurately and precisely measure the electron lifetime in order to produce reliable calorimetric measurements. These two requirements do not completely overlap and may require different measurement techniques. Three different methods utilising through-going muons were developed and their suitability for each requirement was investigated.

The methods all rely on the principle of measuring the reduction in observed charge with

distance from the APA. The energy loss by a MIP can be modelled by a Landau-Vavilov distributed variable, as discussed in Section 3.3.1. The collected charge will be reduced by

$$\frac{dQ}{dx} = \frac{dQ_0}{dx}\exp(-t/\tau_e) \tag{4.7}$$

where dQ_0/dx is the initial charge loss per unit length, t is the drift time and τ_e is the electron lifetime. Measurements of the collected charge per unit length and corresponding drift times can be used to extract the electron lifetime.

Method 1: Single track maximum likelihood

The first method used a similar technique to the online purity measurements used by the LArIAT experiment [162]. The location of groups of ionisation electrons from charged particles on the collection wires, called hits, were found by fitting Gaussian distributions to the wire waveforms and the charge was calculated by integrating the area under the waveform. The hits were grouped into track-like objects using reconstruction algorithms described in Section 5.2.1.

The criteria summarised in Table 4.1 were applied to select straight tracks that passed through both the APA and CPA as these were likely to be MIPs and their true interaction time is known. For the selected tracks, the integral of each hit was normalised by the track pitch to give dQ/dx in electrons per mm (e/mm). A maximum log likelihood estimator was used to extract τ_e from each individual track by minimising

$$-LL = -\log\left(p_{Landau}\left(\frac{dQ^{Meas}/dx - dQ^{MP}/dx}{\sigma}\right)\right) \tag{4.8}$$

where $p_{Landau}(x)$ is the Landau probability density distribution [163], dQ^{Meas}/dx is the measured charge loss, dQ^{MP}/dx is the most probable charge loss from Equation 4.7 using the measured drift time and σ is a scale parameter. Multiple tracks were then used to give an average value for the τ_e.

Table 4.1: Selection criteria used to select straight muon tracks that cross the entire drift distance. The criteria were applied sequentially as shown here. The linear fits were used to remove hits that deviated from a straight line, either due to the muon not having enough momentum or δ-rays.

Parameter	Selection Criteria
Start time - end time	$> 1238 \ \mu s$
Number of wires hit	> 230
$\chi^2/ndof$ after 2 linear fits	< 2
Number of hits	> 230
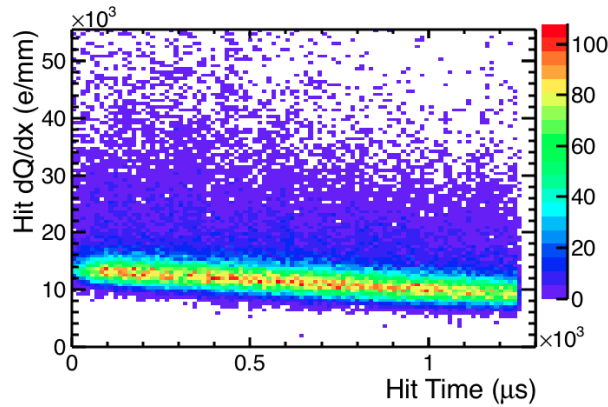
Figure 4.12: dQ/dx against the drift(hit) time for multiple anode to cathode crossing muon tracks with a simulated electron lifetime of 3 ms.

Method 2: Binned multi-track fit

The second method was based on measurements by the ICARUS [148] and ArgoNeuT [122] experiments. The same simulated sample of through-going muons and selection criteria as in method 1 were used. The dQ/dx and times of the hits from all of the selected tracks were collated, as shown in Figure 4.12.

The data were then separated into 20 time slices of equal width, and fit with a Landau-Gaussian Convolution (LGC). An example of one of these fitted slices is shown in Figure 4.13a. The Landau function approximates the energy loss by the muon and the detector response is modelled by the Gaussian function. The most probable dQ/dx from the LGC against the mean drift time was then fit with an exponential function to determine τ_e as shown in Figure 4.13b.

Width	492.6 ± 53.8
MP	$1.222e{+}04 \pm 4.762e{+}01$
Amp	$1.028e{+}06 \pm 2.094e{+}04$
Sigma	1238 ± 94.6

(a)   (b)
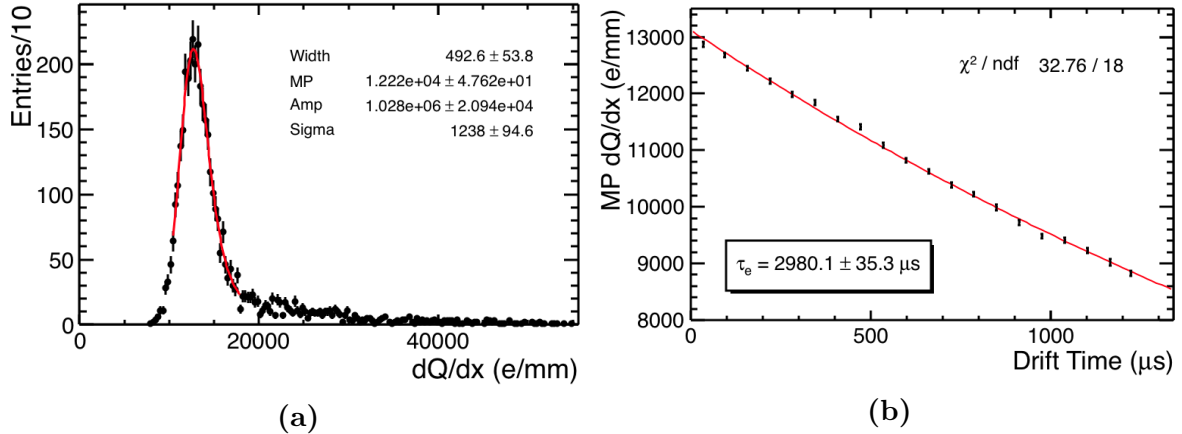
Figure 4.13: Fitting process for method 2. (a) An LGC fit to hit charges in a 62.5 μs time window. The fit limits were chosen to avoid most of the δ-ray contribution at $\sim 2\times$ peak charge. (b) An example exponential fit of the most probable dQ/dx against drift time for an electron lifetime of 3 ms.

Method 3: Parallel tracks

The third method used muons that cross the detector parallel to the wire planes, like the example shown in Figure 4.14. These muons will be triggered when they pass through opposite pairs of CRT scintillator strips. All of the ionisation electrons will arrive in a short period of time so minimal tracking reconstruction would be required.

Tracks which pass through 10 cm wide strips between 15 and 185 cm from the wire planes were selected from a sample of simulated muons generated with slight variations in angle and uniformly in the drift direction. A histogram of the dQ/dx for each CRT pair was fit with an LGC as shown in Figure 4.15a. The same exponential fit function, shown in Figure 4.15b, as in method 2 was then used to calculate τ_e.

Systematic Corrections

The dQ/dx distributions in method 2 were initially observed to deviate from an LGC, corrections have been applied to Figure 4.13a but an example of the previous distributions can be seen in Figure 4.16. The deviation was not observed in the distributions for method 3 and so it was hypothesised, as there is little angular variation in the parallel track sample, that there could be a systematic dependence on the track angle. To test this, muons were
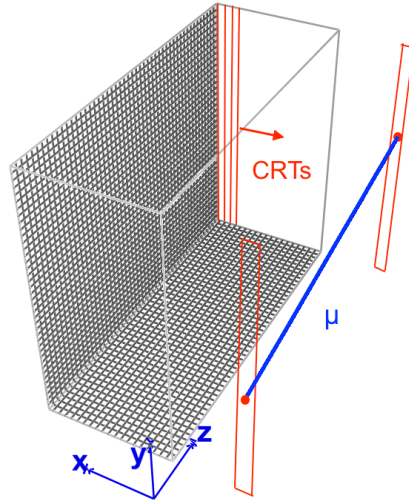
Figure 4.14: An example of a muon crossing parallel to the wire planes that would be selected by the CRTs.

(a)   (b)
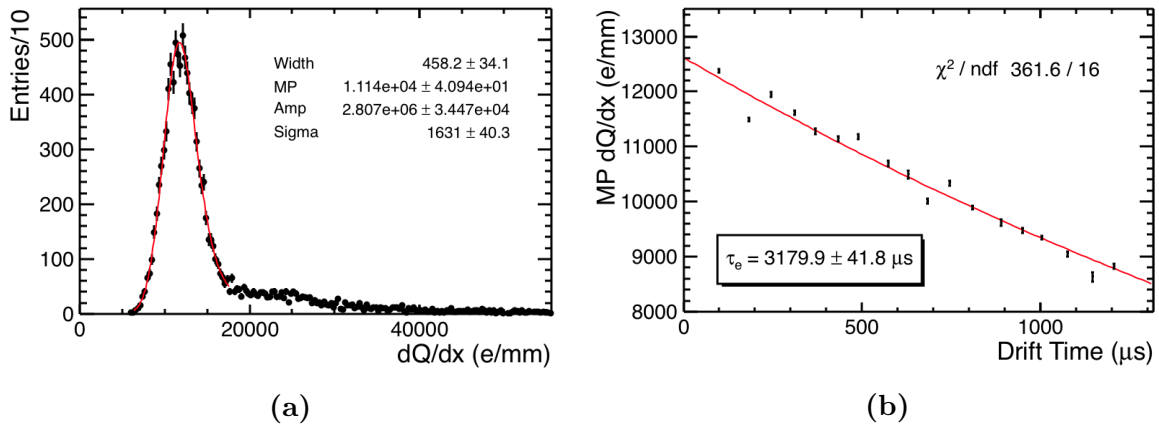
Figure 4.15: Fitting process for method 3. (a) An example of an LGC fit to hit charges contained within 10 cm wide CRT scintillator strips. (b) An example of an exponential fit used to extract the lifetime with a simulated electron lifetime of 3 ms.
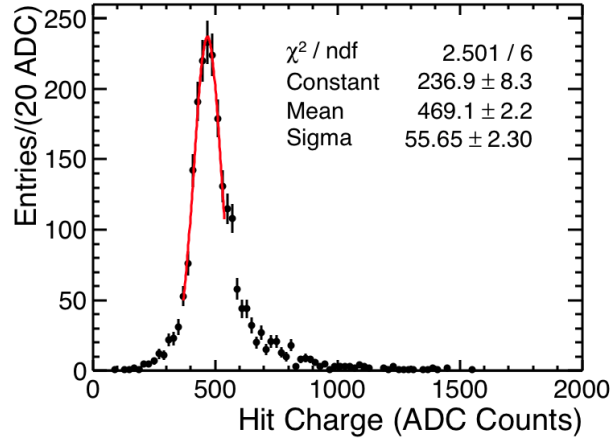
Figure 4.16: An example of a convolution fitted to hit charges calculated using the Gaussian hit finder before charge corrections were applied.

(a)	**(b)**
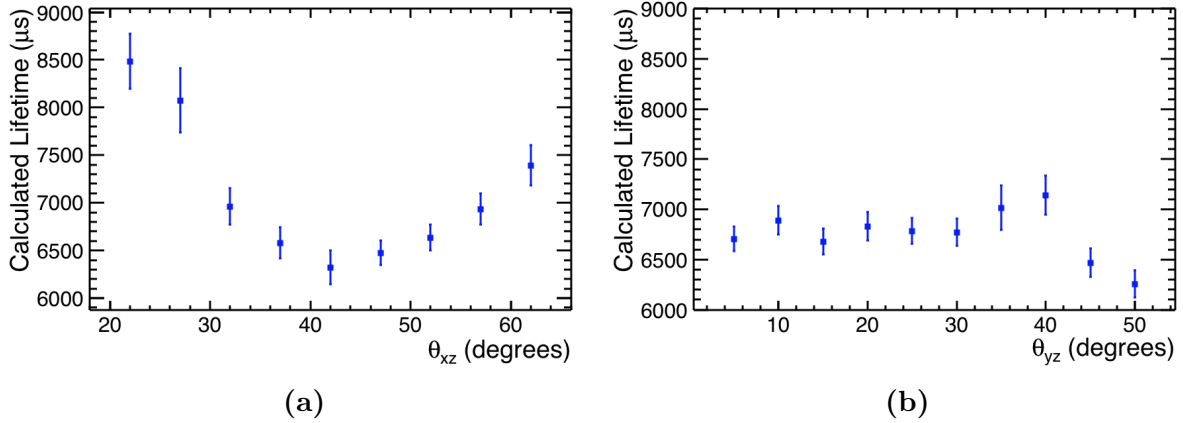
Figure 4.17: Calculated lifetime as a function of (a) θ_{XZ}, varied from 22 to 62 degrees in steps of 5, and (b) θ_{YZ}, varied from 5 to 50 degrees in steps of 5.

generated with fixed directions in the detector with variations in the angle between the beam and drift directions, θ_{XZ}, and the angle between the beam and vertical directions, θ_{YZ}.

Another possible source of systematic deviation was diffusion, this was switched off in the simulation to isolate any angular dependence. The electron lifetime was set at 10 ms as the sensitivity to systematic effects increases with lifetime. There was a clear dependence on θ_{XZ} and minimal dependence on θ_{YZ} as shown in Figure 4.17.

The change in the calculated loss of charge generated next to the APA, dQ_0/dx from Equation 4.7, with θ_{XZ} is shown in Figure 4.18. This suggested that the angle of the track may affect the hit shape, hence the charge calculated by the Gaussian hit finder.
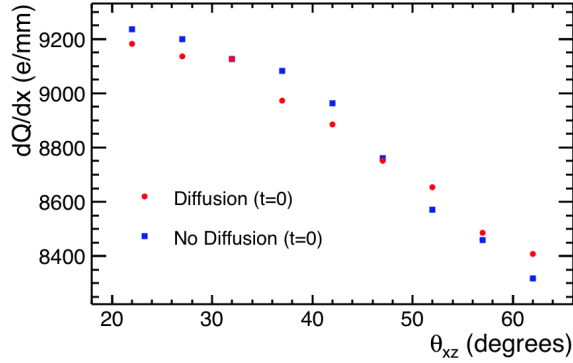
Figure 4.18: The value of dQ_0/dx calculated from the exponential fit as a function of angle with and without diffusion. Diffusion was found to have no systematic effects on the measurements at the levels simulated in SBND.
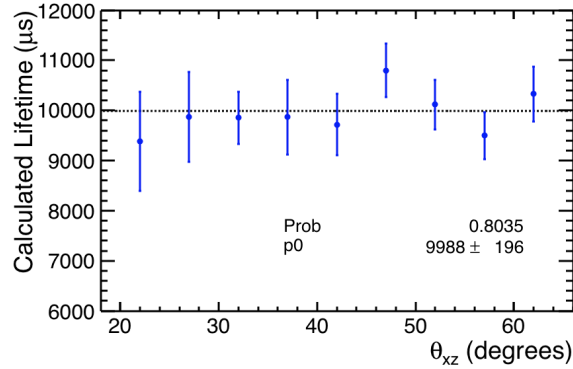
Figure 4.19: Dependence of the calculated lifetime on θ_{XZ} using manual integration of the hit charge.

Manually integrating the raw charge of hits identified by the Gaussian hit finder removed the dependence on θ_{XZ}, as can be seen in Figure 4.19.

Another possible cause of systematic deviations is the hit finding efficiency at low lifetimes. Hit charges can pass below the detection threshold and the most probable value of the Landau function can be obscured. Any charge distributions that were affected by this were identified and removed from the results by locating the position of the hit finding threshold relative to the Landau peak.

Comparison of methods

Samples of 3 GeV muons were simulated with lifetimes ranging between 0.75 and 10.0 ms, covering the range of interest for the requirements. A lifetime around or below 0.75
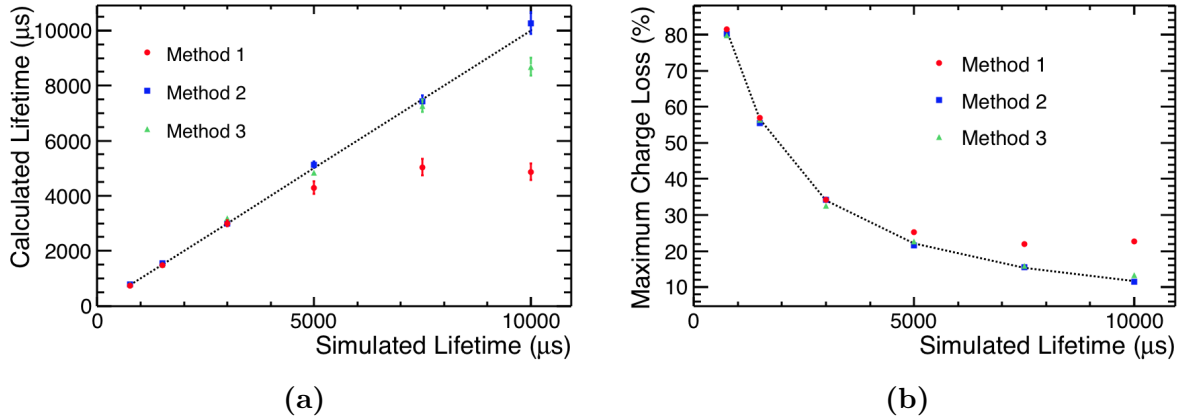
Figure 4.20: (a) The lifetime and (b) the equivalent charge loss across a 2 m drift length calculated by the three different methods at a range of simulated lifetimes.

ms would indicate an issue with the argon purity that needs to be immediately addressed and a lifetime above 10 ms represents excellent purity with only small charge corrections required. The lifetime was calculated for each sample using all three methods, with the results shown in Figure 4.20a.

For accurate calorimetry, the lifetime needs to be measured and corrected for. An incorrect measurement of τ_e could cause significant errors in the reconstructed charge, the effect of using each method on the corrected charge is shown in Figure 4.20b.

Method 1 benefits from being able to work on the smallest sample sizes and may be better for monitoring how the purity changes over short periods of time or in different areas of the detector, for example near the filtration system. The exponential fits in the method 2 have better $\chi^2/ndof$ in comparison to method 3 and may give more precise results for calorimetry.

The cause of the large $\chi^2/ndof$ values in method 3 is most likely to be that the uncertainties on the most probable charges are related to the numbers of hits in the distributions. Hit statistics were high but the track statistics were comparatively low, which results in the hits not being evenly distributed across the drift direction. This can lead to a bias in the time bins that isn't observed with method 2. Binning within the CRT pairs could help to reduce this effect.

Method 3 requires the least amount of track reconstruction and could be used for quick

and almost online lifetime measurements. The rate of anode to cathode crossing muons is predicted to be around 300 Hz, based on simulations described in Section 5.1. The rate of cosmic ray muons triggered by the upstream and downstream CRT taggers which do not traverse more than 10 cm in the drift direction in the TPC is predicted to be 3 Hz, so it would be much faster to accumulate the statistics for methods 1 and 2.

4.2.2   Purity measurements in the vertical slice test

There was an opportunity to test the principle of measuring argon purity on real LArTPC data using the Vertical Slice Test (VST) at FNAL. The construction and operation of the VST was a large collaborative effort led by M. Betancourt and B. Badgett. I assisted in the construction and running of the experiment, developed the analysis code framework with G. Putnam and D. Barker, and created the lifetime measurement software based on the previous work performed with D. Barker.

The vertical slice test

The VST was designed to test the electronics that would be used in SBND in the much smaller LArIAT detector [162], with the goal of providing an accurate measurement of the expected signal to noise ratio. The LArIAT TPC has the dimensions of 47 cm width (drift) $\times$ 40 cm height $\times$ 90 cm length with a cathode plane along one side and an anode plane along the other. The anode plane consisted of three wire planes each containing 240 wires with a 4 mm spacing. The planes were labelled as U, V and Y and were at +60, -60 and 0 degrees to the vertical direction, as in SBND. The U plane, held at -298 V acted as a shield to the other two planes and was not read out. The V plane was an induction plane and held at -27 V and the Y plane was the collection plane, held at +340 V.

The cold electronics that will be used in SBND and were tested by the VST are shown in Figure 4.21. An overview of the electronics is given in Section 3.3.2. Images of the VST TPC are shown in Figure 4.22.
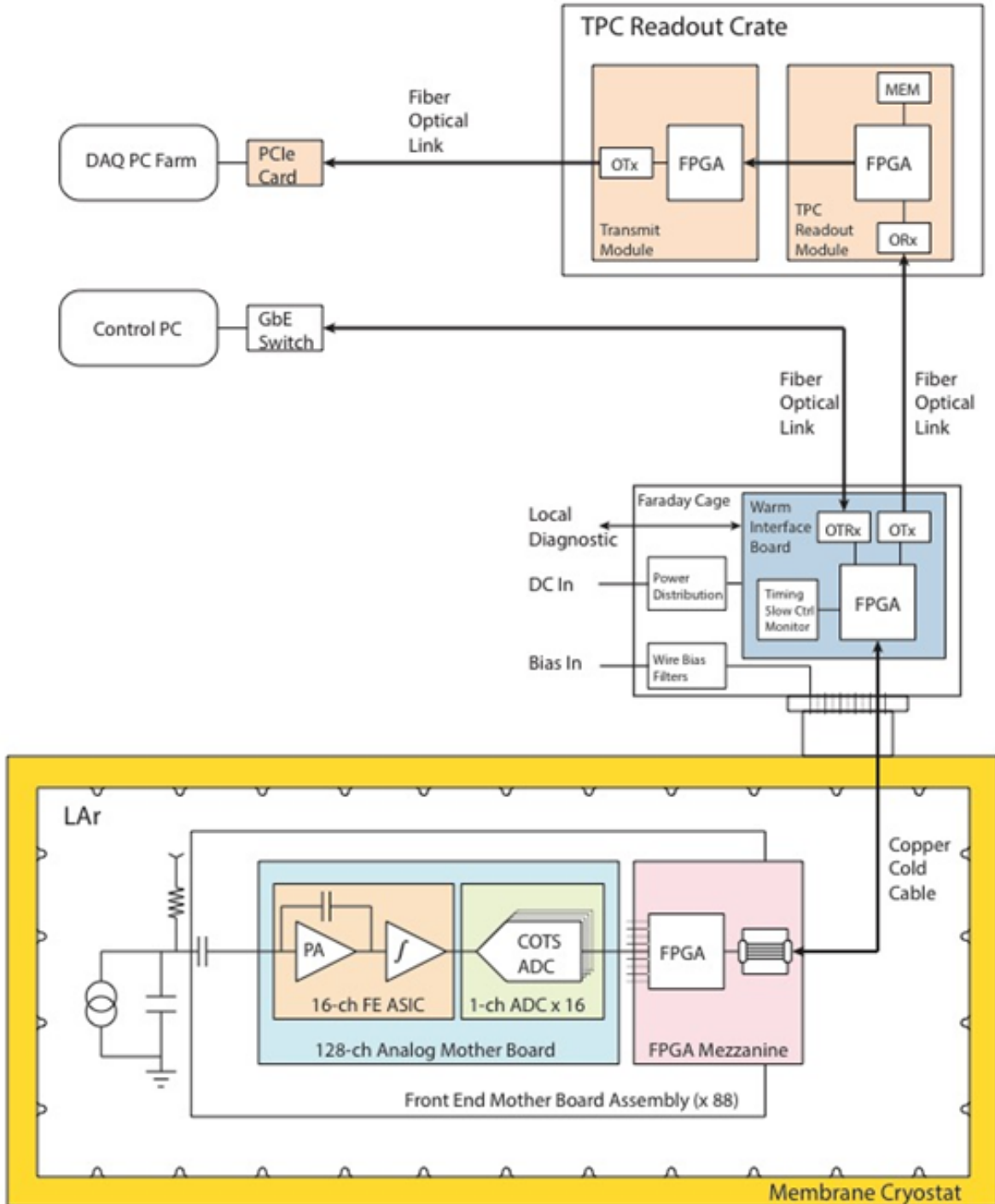
Figure 4.21: The SBND electronics readout with a single TPC wire shown. The wire is represented as a current source and capacitance to ground in the bottom left. Figure credit: SBND electronics group.

(a)

(b)
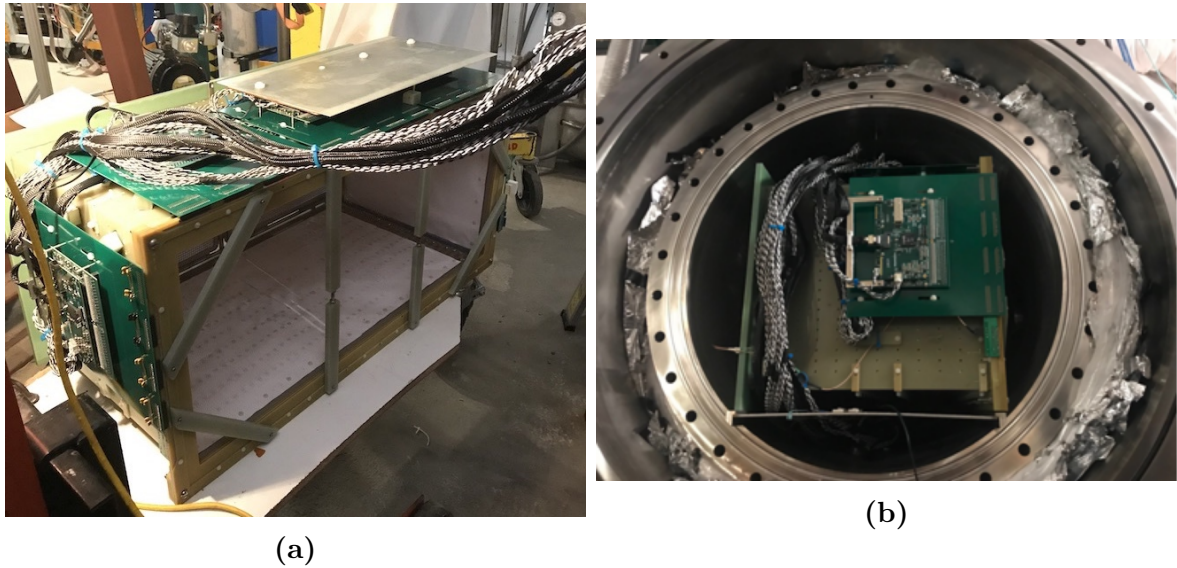
Figure 4.22: Images of the VST TPC (a) with the wire planes facing the camera and (b) inside the cryostat. Image credit: M. Betancourt.

Purity measurements

An online purity monitor was required to make electron lifetime measurements for the online data quality monitor and to correct the observed charge for signal-to-noise measurements. The TPC used for the VST was small but still had a high enough flux of through-going cosmic ray muons to measure the electron lifetime. The flux was not high enough to rely completely on parallel muons or anode to cathode crossers but external muon paddles were available to act as a trigger. The size of the TPC meant that it was rare for there to be more than one cosmic track in each readout window.

The muon paddles were set up to select muons which travel across the drift distance and along the length of the TPC. The signals from the collection and induction wire planes were run through a hit finder which identified peaks using a threshold rather than Gaussian fits and integrated the charge in the same way as the methods described previously. The produced hits, shown in Figure 4.23 for a single track, were the input to the lifetime calculation.

As the majority of events contained only one cosmic track, the development of a full track reconstruction procedure was not necessary. A recursive linear fit was performed to remove excess hits from δ-rays or noise. In high noise events, such as during filling,

(a) (b)
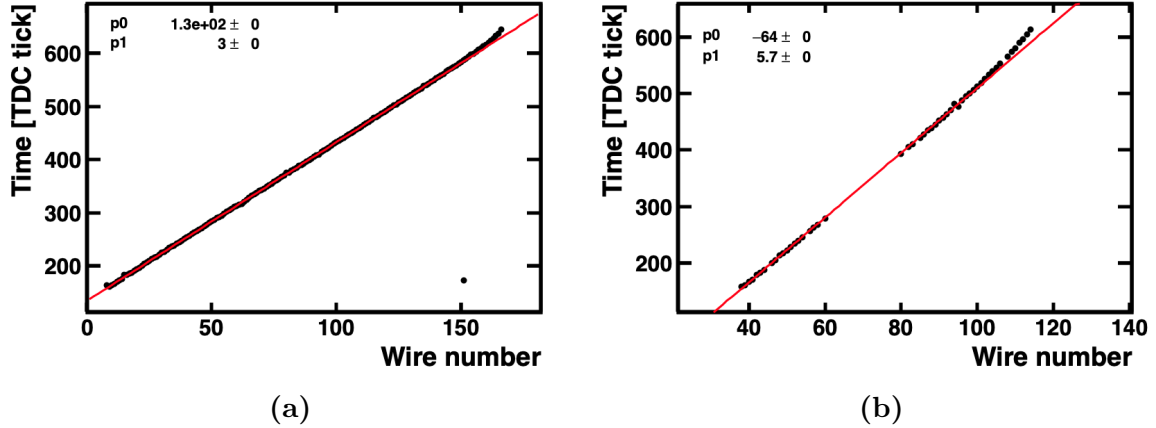
Figure 4.23: The output of the raw hit finder for (a) the collection and (b) the induction planes with initial linear fits performed. A section of the induction plane became unresponsive during running, as can be seen in (b). A TDC tick is defined as 0.5 μs.

Table 4.2: Selection criteria used to select straight through-going cosmic muon tracks.

Parameter	Selection Criteria
Total hits	> 60
Collection hits	> 40
Induction hits	> 20
Final $\chi^2/ndof$	< 40
Wires crossed	> 50
Drift time extent (μs)	> 50
Collection/induction track time overlap (%)	> 80
Lifetime from exponential fit (ms)	< 100

this stage was designed fail and the event would be discarded. Requirements on the total number of remaining hits, the time and wire extent of the tracks and the time overlap between the collection and induction tracks were used to ensure that a good lifetime measurement could be made. The criteria used in this analysis are summarised in Table 4.2. The $\chi^2/ndof$ returned from the final fit was used to select mostly straight tracks. An example of a selected track can be seen in Figure 4.24.

For tracks which passed the criteria, the same maximum log likelihood estimator as in Equation 4.8 was used to extract the lifetime. The estimator was found to perform better when the high energy tail was not included in the fit. To remove the tail, the collection hit charge against drift time distribution was fit with an exponential as in Figure 4.25a. Hit charges too far away from this fit were removed using a Landau fit to a histogram of hit charge distances from the exponential fit, Figure 4.25b. The resulting hits used in the
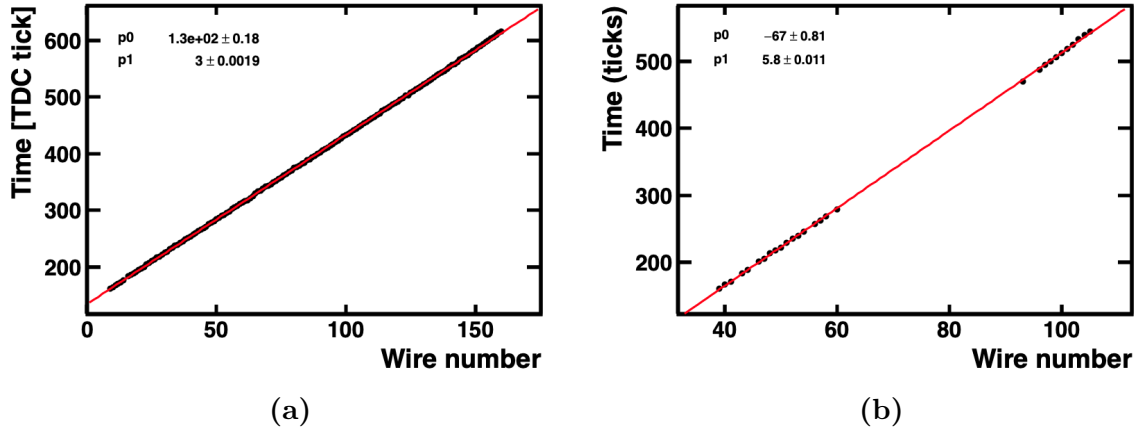
Figure 4.24: Tracks on the collection (a) and induction (b) planes after selection criteria and δ-ray removal. Only the selected collection plane hits were used to make lifetime measurements.

maximum log likelihood estimator are shown in Figure 4.25c.

The purity calculator ran as part of the online monitor enabling the experiment to detect any large changes in the measured electron lifetime indicating either an issue with the argon or the stability of the electronics. The measurements taken over the run period of the VST were collated and averaged over hour long periods to reduce some of the variation in the measurements, this is shown in Figure 4.26. The measurements appear to vary consistently over time, tracking changes in the operating conditions of the VST. This indicates that a similar method would be appropriate for the real time monitoring of SBND.

4.2.3 APA alignment

Another potential source of bias when measuring muon tracks is a misalignment between the two APA frames on either side of the detector. There are procedures to ensure that the two frames are level with each other using a specially designed alignment fixture and laser surveys. The two frames are initially bolted together and then held in place with large steel bars at either end. Once aligned and coupled the frames will be lifted several times before reaching their stationary position inside the TPC and it is possible that they may become misaligned in this time.

(a)

(b)

(c)
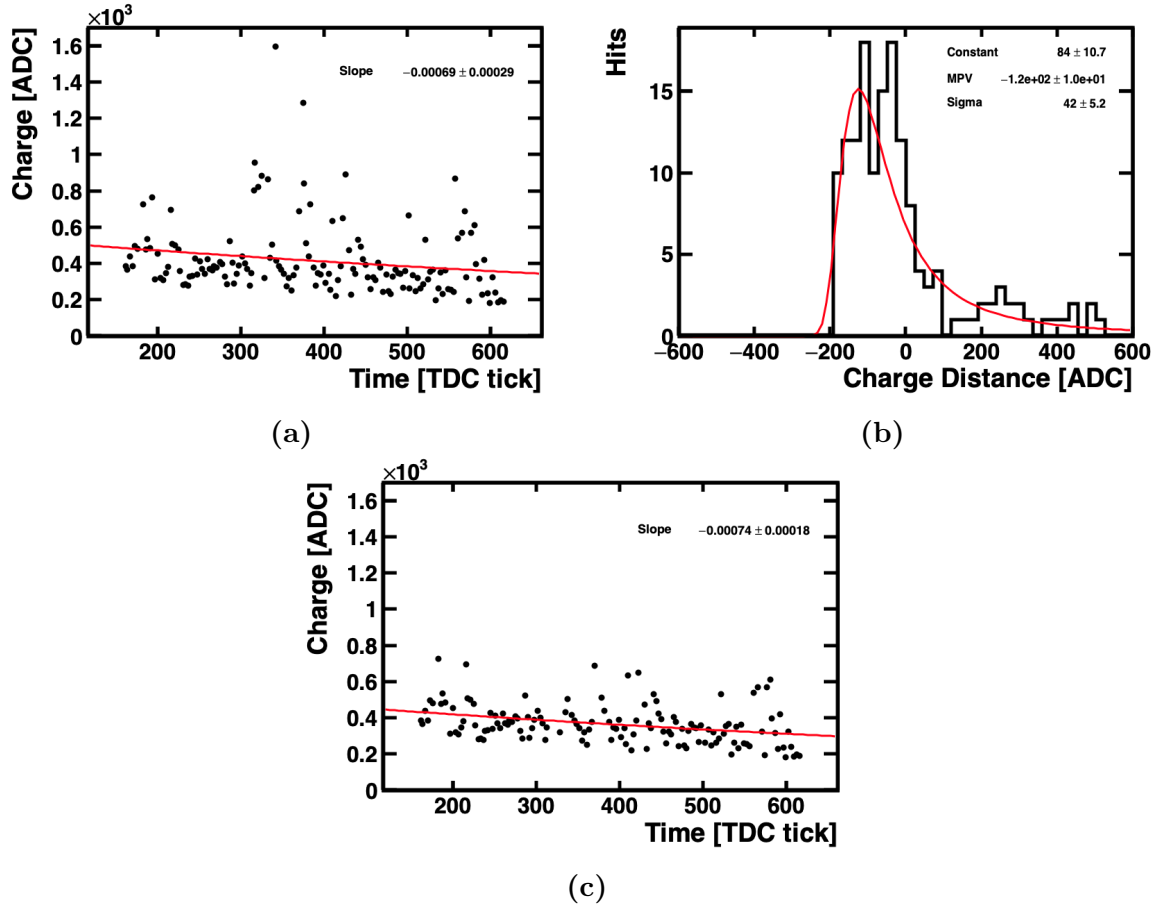
Figure 4.25: (a) Initial exponential fit and (b) landau fit used to remove hits with high charge values. (c) An example of a selected charge against time distribution used for the minimisation.

(a)

(b)
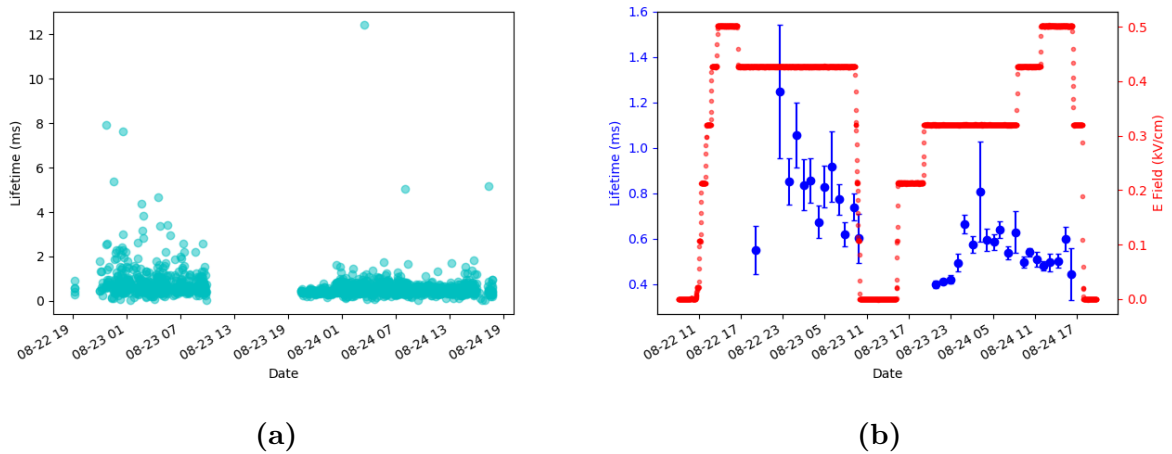
Figure 4.26: (a) The lifetime measurements for every selected track. (b) The hour averaged measurements with the changes to the drift field.
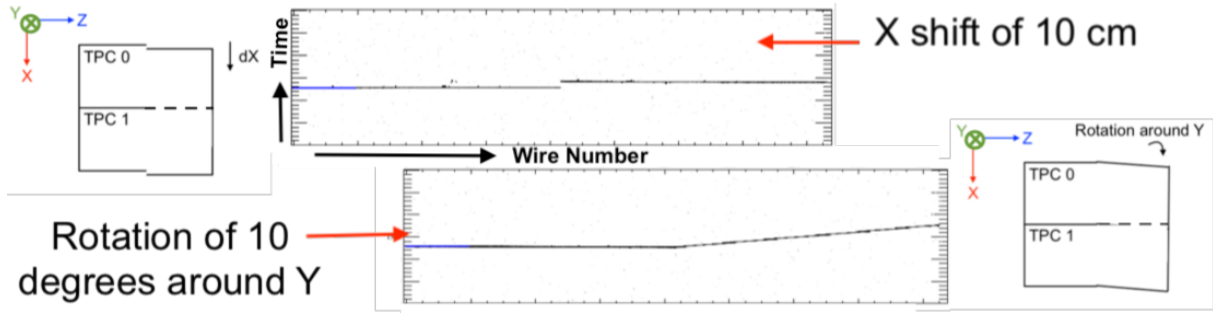
Figure 4.27: The effects of an exaggerated misalignment on tracking through an X translation and a rotation around the Y axis. The Y axis is into the page.

A misalignment that changes the drift distance relative to the cathode is likely to affect the track reconstruction as tracks may be split across the APA gap or an artificial kink may be introduced, which could be misinterpreted as an interaction vertex. However, it is also due to this effect on the tracking that it should be possible to measure the misalignment using through-going muon tracks.

Two cases, as illustrated in Figure 4.27, were considered. The first is a translation in the drift, X, direction which would result in one half of the wire planes being closer to the cathode than the other and tracks would either be split or have two sharp kinks in them. The second case is a rotation around the vertical, Y, axis. A rotation is most likely to occur around this axis as the APAs are joined along the vertical coordinate. A rotation of this kind would mean that the distance from the wires to the cathode would change along the beam, Z, coordinate and tracks would have a single kink at the APA join.

Through-going muons parallel to the wire planes would be ideal for measuring any misalignment. It is possible to configure the CRT system to trigger on this type of event, as in the purity measurement, and although the predicted rate is low the misalignment is not expected to change once the TPC is in place and so only requires one precise measurement. A sample of 3 GeV muons parallel to the wire planes with a perpendicular offset of between 0 and 30 cm was produced with either translations in X or rotations around the Y axis. These samples were used to estimate the accuracy and resolution of measuring a misalignment with muons.

The maximum tolerance for a translation in X given in the SBND specifications is 0.5 mm. The through-going muon tracks were simulated with this translation and recon-

(a)   **(b)**
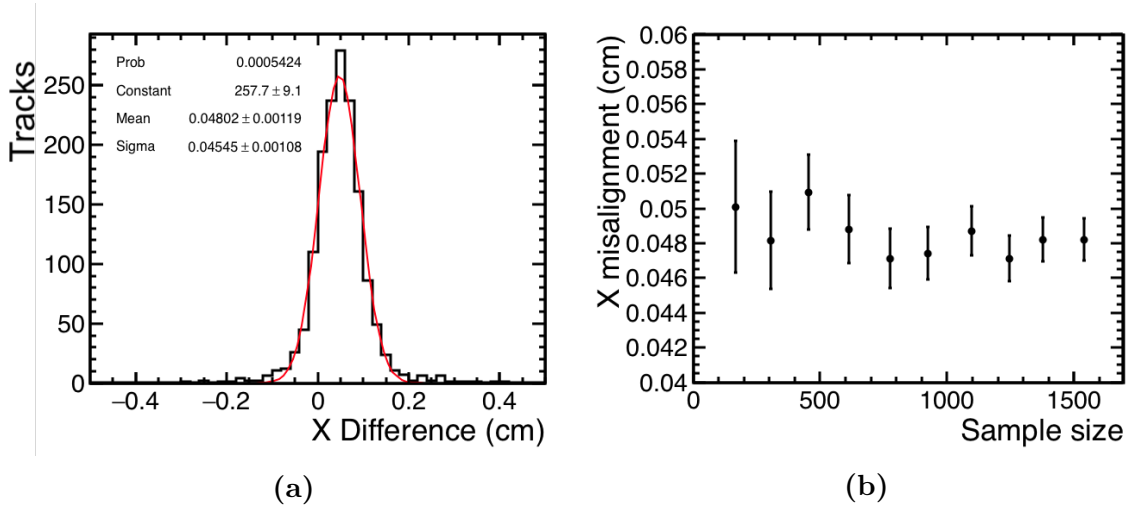
Figure 4.28: Measurement of an X translation between two APA frames using through-going muons parallel to the wire planes. (a) Distribution of X distances between either side of the APA gap. (b) Dependence of measurement error on the number of muon tracks used.

structed, with details of the reconstruction given in Section 5.2.1. Two linear fits of the ZX projection of the tracks on either side of the APA gap were performed. The differences in X position of the two fits at the gap were calculated and a Gaussian function was fit to the distribution of X differences over many tracks, as shown in Figure 4.28.

The maximum tolerance, and simulated value, for a rotation around the Y axis is specified to be 0.12 degrees measured from the normal to the plane and assuming the other plane is parallel to the cathode. The same method of performing linear fits to tracks on either side of the APA gap was used, but here the difference in the track angle in the ZX plane, θ_{ZX}, was used. The performance of this method is shown in Figure 4.29.

This study was able to demonstrate that it is possible the measure the effects of APA misalignment at the maximum allowed specification. It would therefore be possible to measure if the alignment has changed during installation. As the measurement resolution is very good it is clear that even a small misalignment will affect the tracking and should be measured and corrected for as soon as possible. This study did not include a simulation of the electric field distortions due to misalignment which may also affect the tracking.

Prob	8.582e−05
Constant	322.1 ± 10.4
Mean	0.1232 ± 0.0061
Sigma	0.2482 ± 0.0052

(a)

(b)
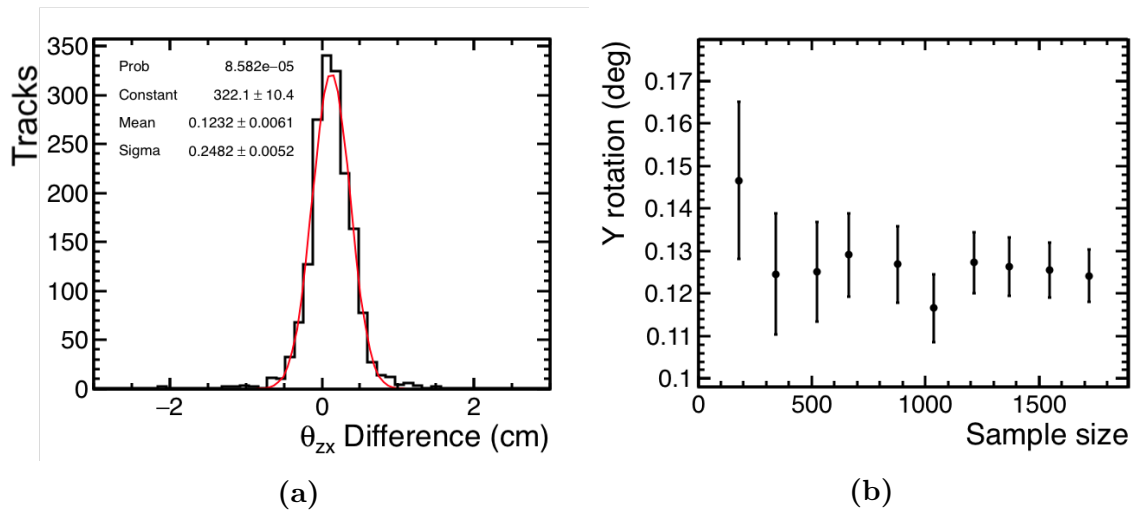
Figure 4.29: Measurement of a rotation around the Y axis between two APA frames using through-going muons parallel to the wire planes. (a) Distribution of θ_{ZX} differences between either side of the APA gap. (b) Dependence of measurement error on the number of muon tracks used.

Chapter 5

Simulation and reconstruction

In this chapter, the software and techniques used to simulate neutrino and cosmic ray interactions and the response of SBND to them are described in Section 5.1. An overview of the algorithms used to reconstruct the interactions in the three detector subsystems is given in Section 5.2. The performance of the reconstruction relevant to measuring charged current muon neutrino interactions is evaluated in Section 5.3.

5.1   Simulation

SBND is under construction and not due to take data until 2022, and so simulations are required to develop reconstruction algorithms and predict sensitivities to physics measurements. All of the simulations were performed within the LArSoft framework [164] which is in turn built on the art event processing framework [165] and the ROOT data analysis package [166].

The first step in simulating the experiment is the generation of neutrino interactions. Predictions of the expected interaction rates are calculated based on the flux of the neutrino beam, the location, geometry and composition of the detector and a given cross section model configuration using a Monte Carlo neutrino generator.

5.1.1 Neutrino generators

Monte Carlo generators use random numbers to estimate the expected interaction kinematic distributions and final state particles according to a cross section model or collection of models. The cross sections, σ, produced by theoretical models, discussed in Section 2.3, are normally expressed as a function of the momentum transfer and other fundamental kinematic variables. In order to be compatible with Monte Carlo methods, the cross sections need to be parametrised in terms of random numbers, $x \in [0,1]$, by performing changes of variables such that $d\sigma/dx$ is a continuous function [167].

The value of σ at a randomly generated x can be calculated using the initial state kinematics sampled from the flux, discussed in Section 3.2, and nuclear model, discussed in Section 2.3.2. The event is then selected with a probability of $P = \sigma/\sigma_{max}$ where σ_{max} is the maximum value of $d\sigma/dx$. The final state kinematics can be calculated by transforming back to the original basis. This will give final state kinematic distributions that converge with an increasing number of events to what would have been generated analytically [167]. This method is beneficial as it can replace complicated multi-dimensional integrals with sums.

Difficulties arise from the fact that there is currently no cross section model covering all possible interaction dynamics and energy transfers and no nuclear model covering all possible nuclear targets. The generators must also propagate the final state particles out of the nucleus with realistic treatments of FSI, discussed in Section 2.3.4. Therefore, several different models must be used together. Care must be taken in the transition regions between models to ensure that the double counting of interactions does not occur, artificially increasing the generated cross section [59].

Many parameters in the theoretical models are not fully constrained by calculations or have a degree of uncertainty to them so experimental data are often used to tune the models [91, 118]. Uncertainties in models covering similar regions of phase space combined with uncertainties in the flux modelling and incoming neutrino energy often result in hard to avoid degeneracies making this tuning difficult. This is one of the primary reasons why more precise data in more exclusive channels are needed.

Table 5.1: Cross section models used in GENIE v3.0.6 tune G18.10a.02.11a:k250:e1000. This is a theory driven configuration with parameters tuned to CCQE, CC1π, CC2π, and CC inclusive cross-section data from bubble chamber experiments [91].

Component	Model
Nuclear model	Local Fermi gas [82, 83]
Meson exchange currents (MEC)	Nieves et al. [82, 83]
Coherent pion production (COH)	Berger-Seghal [93]
Quasi-elastic scattering (QE)	Nieves et al. [82, 83]
Resonant pion production (RES)	Berger-Seghal [92]
Deep inelastic scattering (DIS)	Bodek-Yang [94]
Final state interactions (FSI)	INTRANUKE hA2018 [91]

Given some of the historical disagreements between experimental neutrino cross section data, Section 2.4, the large numbers of competing models, Section 2.3, and the number of generators often with different parametrisations of those models, experimental results must be presented with minimal dependence on the models used to develop and evaluate reconstruction. The generator primarily used for neutrino interactions in LArTPCs and in the bulk of the analysis of this thesis is the GENIE [98] Monte Carlo generator. It is chosen due to its existing interface with the LArSoft framework and ability to reweight neutrino interactions according to the uncertainties of physics parameters, this is discussed further in Section 7.4.

A number of different versions of GENIE using different models and model tunes have been used to develop reconstruction algorithms in SBND. Here, the performance of the reconstruction and event selection will be evaluated using GENIE version 3.0.6 with a theory driven model configuration summarised in Table 5.1. More details on the individual models can be found in Section 2.3.

5.1.2 Cosmic ray generators

As a surface detector, an accurate prediction of the cosmic ray background is also very important. The Monte Carlo generator used for simulating cosmic showers in this analysis was CORSIKA [168]. The generation starts with a position dependent flux of high energy particles originating from galactic or extra-galactic sources incident on the area

(a)   (b)
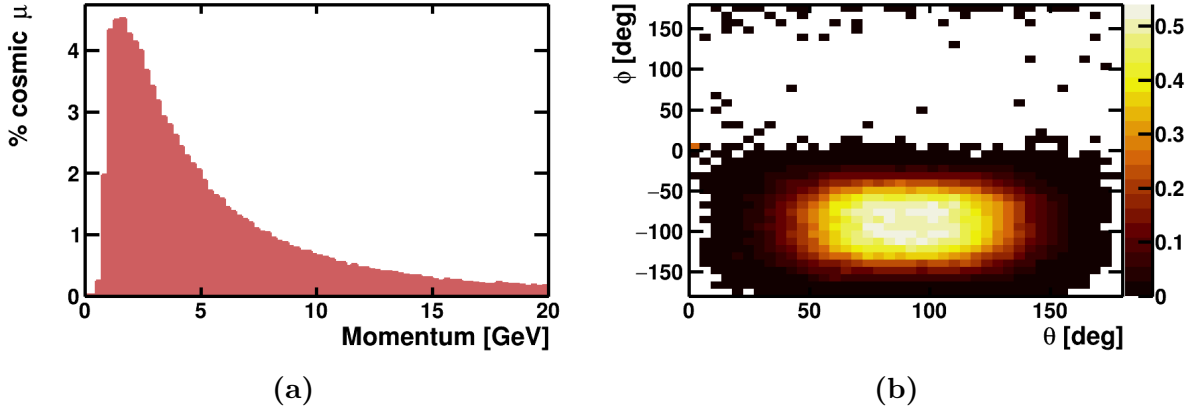
Figure 5.1: The momentum and angular distributions of cosmic muons in SBND. Both distributions are normalised by the total number of cosmic ray muons simulated. θ refers to the angle to the beam direction and ϕ is the angle around the beam direction with $\phi = 0$ defined as being in line with the positive drift direction.

of the Earth's atmosphere relevant to the detector. Models of nuclear fragmentation and hadronisation are then used to predict the resulting particle showers [168]. Survival probabilities are used to predict which particles reach the detector [168], the result of this is usually downward-going muons with a momentum distribution peaking at 1-3 GeV and a tail extending out to higher momenta.

The accuracy of the model is not as critical as for the neutrino generator because it is possible to take cosmic ray data when the beam is not delivering neutrinos, called off-beam, in order to subtract cosmic ray backgrounds. Reconstruction algorithms are, however, trained on the simulations before the detector is operational and incorrect simulations could lead to biases that will take time to correct later, especially in the case of trained machine learning algorithms.

The MicroBooNE experiment, which is located near SBND, found that generating showers using only cosmic ray protons matched their data rates better than using all available particle types (p, He, N, Mg, Fe) and was thus used in this analysis. The predicted muon momentum and angular distributions in the SBND TPC are shown in Figure 5.1. The rate of muons entering the TPC is predicted to be 3.5 kHz with this model configuration.

5.1.3 Detector simulation

Once the initial interactions have been produced by the generators, the particle types and momentum four-vectors are input to the Geant4 [135] simulation toolkit. This software applies the physics described in Section 3.3.1 to propagate the particles through the different materials that make up the detector. The scattering, decays, showers and other particle interactions are simulated along with the passage of the ionisation electrons and scintillation light.

As liquid argon has a low scintillation energy threshold the simulation of light poses a technical challenge, propagating the large number of photons for every event is too computationally slow. A common solution to this is to use a lookup table that provides a probability of detecting a photon based on its initial position [169]. The novel method currently employed in SBND is to apply Rayleigh scattering corrections to pure geometric approximations to estimate the number of photons visible to the PDS from interacting particles.

The final step that brings the simulation to same point as the raw data collected by the experiment is the detector response. After this stage the same reconstruction algorithms should be able to be applied to both simulated and real data. For the TPC, the output of the wire readouts is simulated by convolving an electronics response function with the electric field response to the drifting electrons [170]. A noise model is then added, taking into account the chosen gain and shaping time of the electronics [170].

For the PDS, the semi-analytic simulation provides a list of photons and their relative arrival times for each PMT and ARAPUCA. A quantum efficiency is applied to each photon, this is different for each type of detector and for reflected and direct light. If a PE is created, the transit time is then calculated using measurements of the light detectors and the TPB emission spectrum, if applicable. Digitised waveforms are then constructed using the measured baselines and single PE responses for each detector, converting from charge to ADC, and adding effects like saturation. Gaussian noise and dark noise are then added to the final waveform formed of the response to all detected photons. An overview of this process is shown in Figure 5.2.
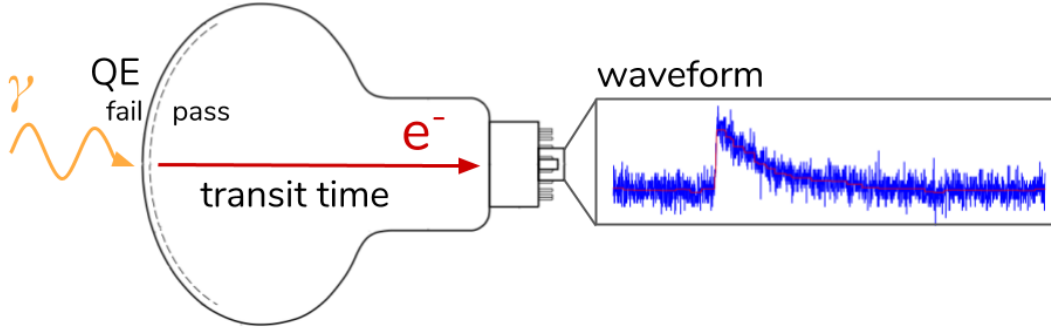
Figure 5.2: The steps involved in simulating the PDS response. The quantum efficiency is used to determine if an incoming photon is converted into a photo-electron, the transit time is calculated and a waveform is created.

The CRTs are external to the TPC and are treated differently as the scintillation light simulation is only run within the TPC volume. Geant4 determines the positions and energy deposits of charged particles in each piece of optically isolated plastic scintillator. The charge depositions, Q, are converted into the expected numbers of PE, N_{PE}, at the end of the strip instrumented with SiPMs. The attenuation loss is calculated using

$$N_{PE} = \frac{A}{(r - B)^2} \cdot \frac{Q}{Q_0} \tag{5.1}$$

where A and B are measured normalisation and shift parameters, Q_0 is the mean deposited charge loss for MIPs and r is the distance between the charge deposition and the SiPM end.

The PE sharing between SiPMs, $N_{PE}^{0(1)}$, is modelled as

$$N_{PE}^{0(1)} = \frac{N_{PE} \cdot \exp(r^{0(1)}/L)}{\exp(r^{0(1)}/L) + \exp(r^{1(0)}/L)} \tag{5.2}$$

where $r^{0(1)}$ is the perpendicular distance between the energy deposition and SiPM 0 (or 1) and L is the effective absorption length for transverse response in the scintillator. Saturation, thresholds and triggering logic are then applied, if the trigger requirements are met the CRT simulation will output the detected number of PE with a timestamp for each SiPM.

The form and parameter values for Equations 5.1 and 5.2 were initially determined using
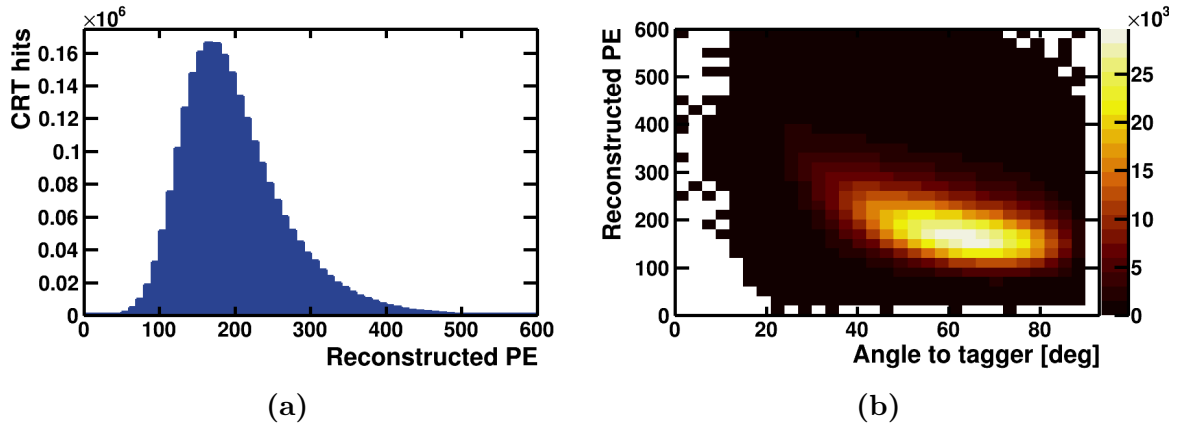
Figure 5.3: (a) Simulated N_{PE} distribution in the top CRT tagger tuned to MicroBooNE data. (b) The dependence on the angle of the incident comic-ray muon track to the tagger.

test stand measurements at the point of production [156]. The same CRT modules are also already in use by the MicroBooNE detector and the SBND model parameters were further tuned to their data using the shape of the N_{PE} distribution of modules parallel with the top of the detector, shown in Figure 5.3.

5.2 Reconstruction

The LArSoft framework is also used for the majority of the reconstruction and analysis software. The three detector subsystems have different operating principles and hence different approaches to reconstruction.

5.2.1 The time projection chamber

The LArTPC technology has existed for decades but only a few recent experiments, MicroBooNE and protoDUNE, have had to contend with event rates high enough to necessitate fully automated reconstruction. Unlike collider experiments, neutrino experiments do not have a single point of interaction that you can build specialised detector components around. The LArTPC solution to this is to image a large volume of target medium in three dimensions with mm level position resolution.

The huge volume of topological and calorimetric information combined with the high
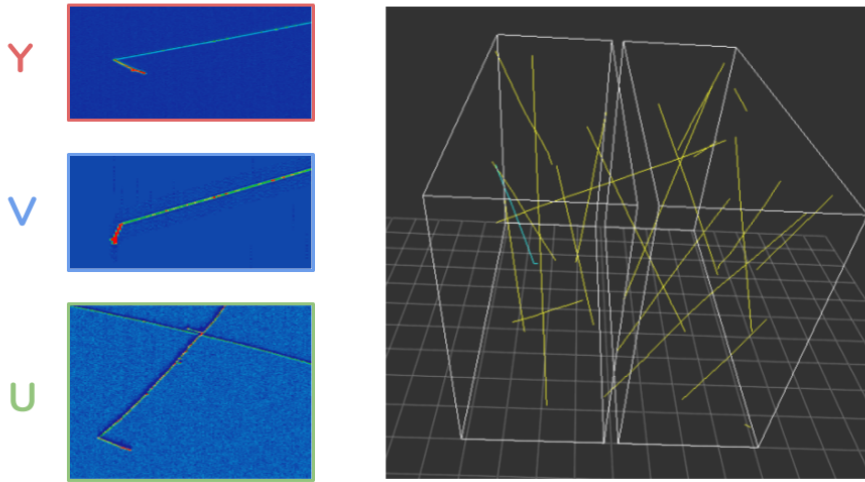
Figure 5.4: An example of all of the true trajectories of particles crossing SBND in a event composed of a triggered readout window and two windows either side. There is a single neutrino event highlighted in blue amongst several cosmic ray muon tracks in yellow. The raw wire waveforms around the neutrino vertex for the three views are also shown.

flux of cosmic ray muons means the reconstruction of events in LArTPCs is complicated and several different approaches are under active development. An example of the typical activity occurring within three readout windows that the reconstruction would have to contend with is shown in Figure 5.4.

The first stage that is common to all approaches is the reconstruction of ionisation electron signals on the wires, called hits. The electronic effects are removed from the signal so that the area under the wire waveform is proportional to the charge. Filtering is performed to remove the noise, both random noise from the electronics and correlated noise from other detector components [170]. The charge is then retrieved by deconvolving the measured signal and the detector response function. Previously, this was performed in only the time dimension but the need to include the response of the wire to charge induced in nearby wires has led to the use of deconvolution in two dimensions, time and wire number [170]. The deconvolution transforms the bipolar induction signals into waveforms with a more of a Gaussian shape, as shown in Figure 5.5.

The deconvolved signals are then approximated as Gaussian functions to find the time and charge of the hits. A region of interest is found using a simple threshold and a
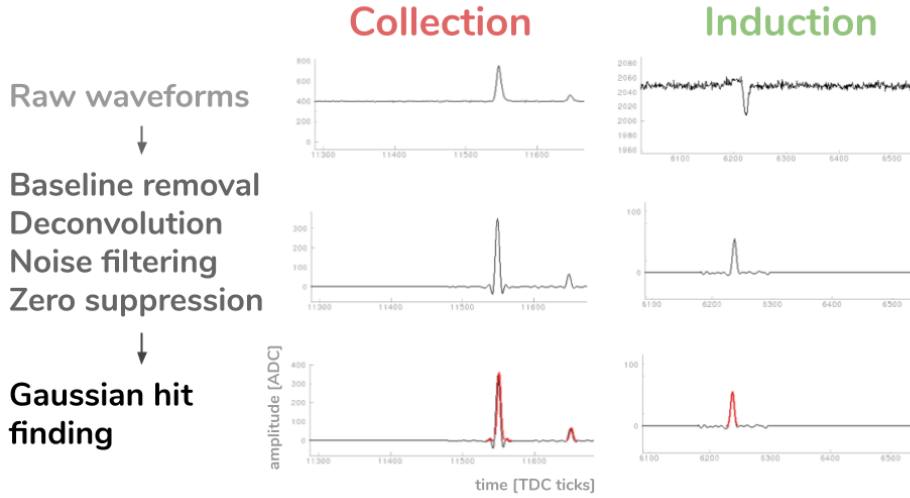
Figure 5.5: Induction and collection plane waveforms with signal processing and hit finding applied. The Gaussian functions fit to the waveforms are shown in red.

single Gaussian function is fit to the region, if the fit has a $\chi^2/ndof$ greater than 2000, two Gaussian functions are then used, this process is repeated until an acceptable fit is achieved. An example of Gaussian hit finding can also be seen in Figure 5.5.

After hit finding has been performed there are then three different approaches to reconstruction which are commonly used in LArTPCs. The first employs elements of deep learning for different stages such as hit clustering and particle identification [171]. Convolutional neural networks common to image processing are particularly appropriate as the output of the TPC is effectively a series of high resolution images. Another method uses the mathematics of sparse matrices to reconstruct charge depositions directly in three dimensions [172]. The default method used by SBND and in this analysis employs the Pandora multi-algorithm approach to pattern recognition [173].

Pandora has two main stages which utilise the difference in topologies between cosmic ray and neutrino induced interactions. It runs initially assuming that everything is a cosmic ray muon, removes all of the tracks that can be unambiguously labelled as cosmic ray muons and then runs again with the assumption that everything remaining is the result of one or more neutrino interactions [173].

The first step in the Pandora cosmic reconstruction chain is to cluster hits in the two dimensional wire and time views, taking into account unresponsive channels and other
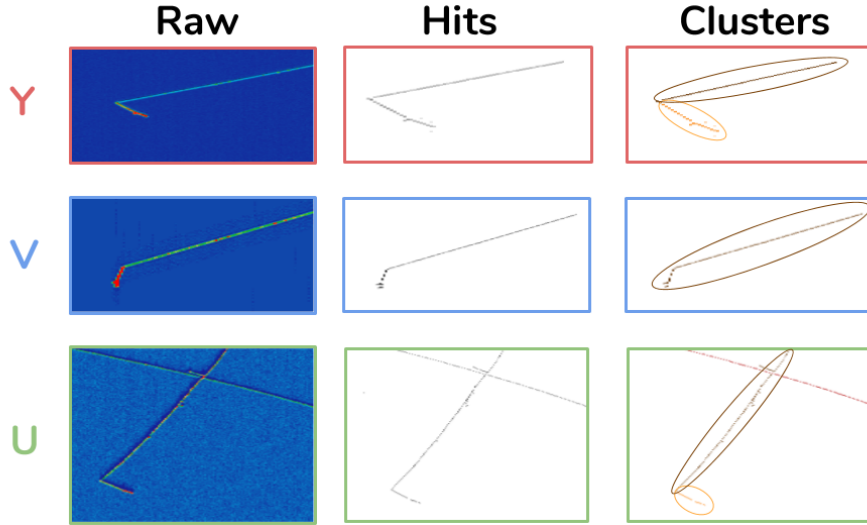
Figure 5.6: Two dimensional hit clustering performed by Pandora. The smaller track is not clustered on the V plane as it is very short in this view but this is corrected when projecting the planes into three dimensions.

detector effects. An example of this clustering process can be seen in Figure 5.6. Clusters are then matched across the different views to form three dimensional space points associated to the hits in each plane. This is done by predicting the location of hits in one view from the clusters on the other two views and finding the 3D point most consistent with what is observed and the overall smooth trajectory of the track [173]. Any clusters not part of three dimensional tracks are assumed to be δ-rays. An example of this three dimensional reconstruction is shown in Figure 5.7.

At this point Pandora tags any tracks which are unambiguously cosmic ray muons and removes them. All tracks are reconstructed assuming that the charged particles crossed the detector at the trigger time. If a particle crossed before or after the trigger time, as is most often the case with cosmic ray muons, the reconstructed track will be shifted either towards or away from the wire planes in the drift direction. If a track is reconstructed outside of the TPC that it was detected in it can be tagged as a cosmic. It is also possible to remove any tracks which can be seen to clearly enter and exit the TPC and any where it has been possible to tag the true crossing time, the t_0, by stitching tracks across the cathode plane [173]. 85-90% of cosmic ray muons are removed by this process.

The remaining 3D reconstructed space points are then split into candidate neutrino
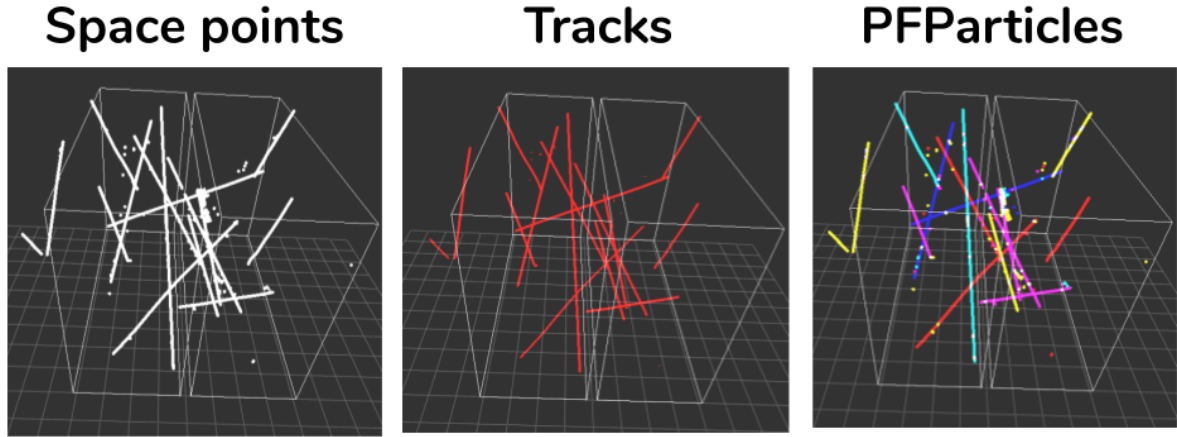
Figure 5.7: Three dimensional track reconstruction performed by Pandora. The track positions of cosmic ray muons are shifted compared to Figure 5.4 as they are reconstructed assuming they crossed in time with the beam.

interactions, called slices, that appear to originate from the same interaction in the detector. The slices are collections of three dimensional charge depositions that appear to be physically separated from other depositions in the detector with the aim being to isolate particles with neutrino or cosmic origin.

Pandora attempts to find a vertex for each slice by finding all possible vertices and using a Multi-Variate Algorithm (MVA), a support vector machine or boosted decision tree [173]. The MVAs are trained on a number of indicative features to select the most probable candidate. MVAs are also used to characterise 2D clusters as either track-like or shower-like. Tracks are reconstructed in the same way as cosmic ray muons but showers are re-clustered using an envelope that expands outwards from the vertex [173].

The final stage is to create a hierarchy, called a particle flow, of 3D track and shower objects in a neutrino slice by working outwards from the interaction vertex. Figure 5.7 shows an example of particle flow reconstruction with the individual particles, called PFParticles (Particle Flow Particles), highlighted.

Calorimetric reconstruction is performed on track objects after the Pandora software has been run. The aim is to reconstruct the energy loss per unit length of the track, dE/dx, for use in particle identification and kinematic calculations. Each readout plane should see the same charge and so the reconstruction is performed separately for every plane.
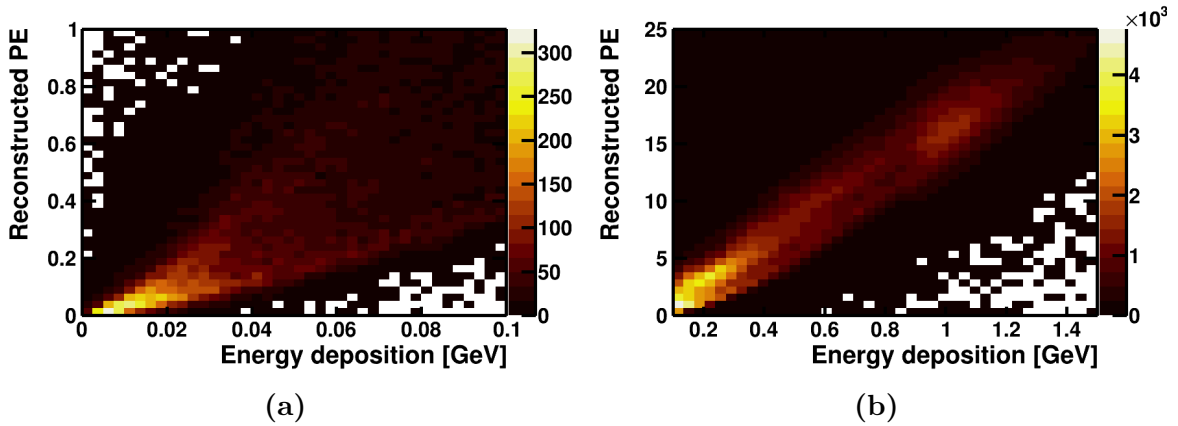
Figure 5.8: The scaling of reconstructed PE in TPB coated PMTs with the true energy depositions of cosmic ray muons in the detector (a) below 0.1 GeV and (b) above 0.1 GeV.

A correction is applied to account for the charge loss due to recombination and electron lifetime, discussed in Section 3.3.1, to transform the area under each hit to the energy deposition seen by each wire. The angle of the track to the wire plane is then calculated to determine the length of track that contributes to the observed energy deposition, and hence the dE/dx.

5.2.2 The photon detection system

In order to use the PDS as a trigger only minimal reconstruction is required. The first step is to process the optical detector waveforms in order to locate the times of incident collections of photons. A baseline subtraction and simple noise filter are run before finding peaks using a threshold configured for each type of detector. The charge is determined by integrating the area under the optical hit and this is converted into PE using a linear scaling factor from test bench measurements. The scaling of the number of reconstructed PE with the true energy deposition in the detector can be seen in Figure 5.8.

Each interaction in a TPC should result in a collection of optical hits over a range of PMTs and ARAPUCAs, referred to as an optical flash. Optical flashes are reconstructed by filling a histogram with the optical hits on coated PMTs weighted by their PE. The bin width is set to the desired timing resolution, here 2 ns. A threshold of 0.1 PE is used to identify the start of flashes and all hits 100 ns after the initial trigger are considered

as part of the same flash.

These flashes can be used to match objects reconstructed in the TPC with the interaction that caused the original trigger, greatly reducing the cosmic ray background [125]. Simulations of neutrino interactions were used to parametrise several features of the relationship between optical flashes and TPC charge distributions in terms of the X position of the charge weighted center of neutrino interactions. The optical flashes are defined as all of the optical hits in the first 100 ns after the trigger.

The first features are the distances between the PE weighted centers of the optical hits in the flash and the charge weighted centers of the Pandora reconstructed neutrino slice in Y, ΔY, and Z, ΔZ. The spread of PE is defined as

$$S = \frac{\sum_i PE_i^2 \cdot r_i^2}{\sum_i PE_i^2} \tag{5.3}$$

where PE_i is the number of PE from PMT_i and r_i is the distance from PMT_i to the PE weighted center, is also calculated. The last feature used is the ratio

$$R = \frac{\sum PE_{uncoated}}{\sum PE_{coated}} \tag{5.4}$$

where coated refers to TPB coated PMTs, sensitive to both direct and reflected light. The features were binned in the X position of the charge weighted center and Gaussian fits were used to calculate the means and standard deviations, σ, for each bin.

To match the most likely neutrino slice in an event, these features are calculated for every slice not rejected as a cosmic and a score is created. The score is defined as

$$score = w_Y \frac{|\Delta Y|}{\sigma_Y} + w_Z \frac{|\Delta Z|}{\sigma_Z} + w_S \frac{|\Delta S|}{\sigma_S} + w_R \frac{|\Delta R|}{\sigma_R} \tag{5.5}$$

where $\Delta S(R)$ is the difference between the calculated S(or R) and what would be expected given the charge weighted center of the Pandora slice and the w are weights which are optimised to maximise separation between signal and background.
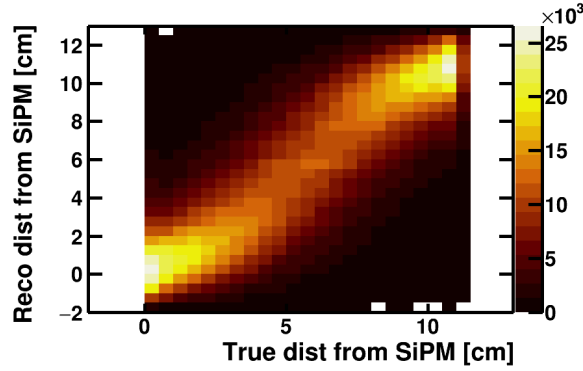
Figure 5.9: Comparison of simulated particle CRT strip crossing points to reconstructed positions showing slight non-linearity near the SiPM locations.

5.2.3 The cosmic ray tagger

Rather than raw digitised waveforms from the SiPMs, the outputs from the CRT system are collections of ADC counts, timestamps and SiPM channel IDs. The waveform processing is effectively performed by the CRT hardware. A single strip of plastic scintillator that a charged particle crosses will result in two SiPM data products. These data products are combined by averaging the times, converting the total ADC counts to the number of PE and estimating the perpendicular position between the SiPMs that the particle crossed.

The number of PE per SiPM, $N_{PE}^{0(1)}$, is estimated using

$$N_{PE}^{0(1)} = \frac{ADC^{0(1)} - B}{S}, \tag{5.6}$$

where $ADC^{0(1)}$ is the charge at SiPM 0(1), B and S are the baseline and slope from test stand measurements [124].

The position, D, between the SiPMs where the particle crossed is estimated using the empirical equation,

$$D = \frac{W}{2} \arctan\left(\frac{N_{PE}^0}{N_{PE}^1}\right) + \frac{W}{2} \tag{5.7}$$

where W is the width of the strip. A comparison between the true simulated crossing position and the calculated position can be seen in Figure 5.9.

The times and 3D positions of charged particles that cross taggers are called CRT hits. They are reconstructed by looking for 2D overlaps between strips within 80 ns of each
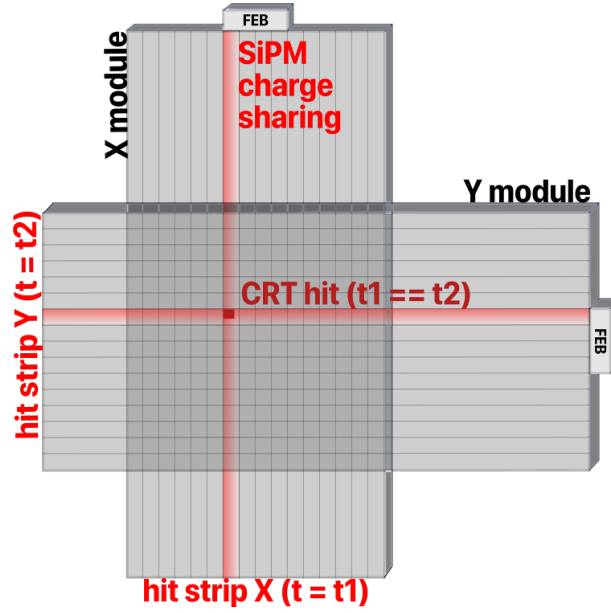
Figure 5.10: Diagram of CRT hit reconstruction. When two triggered SiPMs in X-Y coincidence are within 80 ns of each other a hit is reconstructed. The position resolution is improved by using the charge sharing between SiPM pairs.

other, as shown in Figure 5.10. The most likely 2D position from Equation 5.7 is given as the center of the hit and errors are assigned from the empirical parametrisation. If the strip is located in one of the bottom modules with 1D coverage, the centre of the strip is used as the hit position with limits equal to the length of the strip. The measured number of PE in each strip is then corrected for attenuation using the reconstructed hit position in the inverse of Equation 5.2.

If a charged particle crosses two or more CRT taggers its trajectory can be reconstructed, this object is referred to as a CRT track. CRT hits are first clustered in 0.1 μs time windows for each module. Simply matching all time coincident pairs of hits on different modules can lead to a high multiplicity of reconstructed tracks due to δ-rays and showers coming off the primary cosmic ray muon. Hits within a time window are averaged over a 60 cm radius to mitigate this effect. CRT tracks are then formed by joining averaged hits within a time window across modules, an example of this can be seen in Figure 3.16. The two top planes can be used to create CRT tracks for particles which stop in the volume enclosed by the CRT or exit in an area with reduced coverage.

5.3 Reconstruction performance

It is important to be able to characterise the reconstruction efficiencies for both the cross section channel that is under study and all of the relevant background processes. This is usually done using a combination of both Monte Carlo simulations and measurements of well known processes. As SBND is not currently taking data, the predicted reconstruction efficiencies were calculated using the simulations described above.

5.3.1 The time projection chamber

For the purpose of measuring ν_μ charged current inclusive cross sections, the reconstruction and identification of the primary muon track in the TPC is the most critical component. The track reconstruction was performed by Pandora [173] as described in Section 5.2.1. There are five possible outcomes when reconstructing a muon track:

- A track in a neutrino slice.

- A shower in neutrino slice.

- A cosmic ray muon track.

- A mixture of the above.

- No reconstructed object.

The traditional kinematic variables when measuring double differential ν_μ CC cross sections are the momentum, P_μ, and the cosine of the angle of the primary muon track to the neutrino beam, $\cos\theta_\mu$. Figures 5.11 and 5.12 show the efficiency for reconstructing primary muons from ν_μ CC interactions inside the active volume as tracks in neutrino interactions as a function of P_μ and $\cos\theta_\mu$. The total efficiency was estimated to be 83%, which is within the limits specified in the proposal [11].

The fractional bias and resolution of measuring the kinematic variables for correctly reconstructed muons can also be estimated. The angle to the beam was measured directly

(a)

(b)
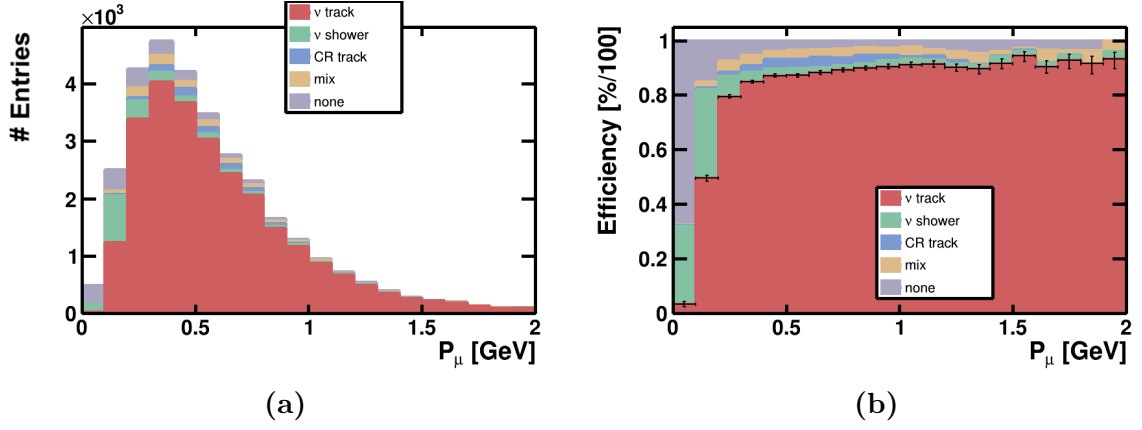
Figure 5.11: Relative efficiency of primary muon reconstruction as a function of P_μ. (a) A stacked histogram of the true distribution with the reconstruction outcomes. (b) The percentage efficiency of particles reconstructed as tracks in neutrino slices.
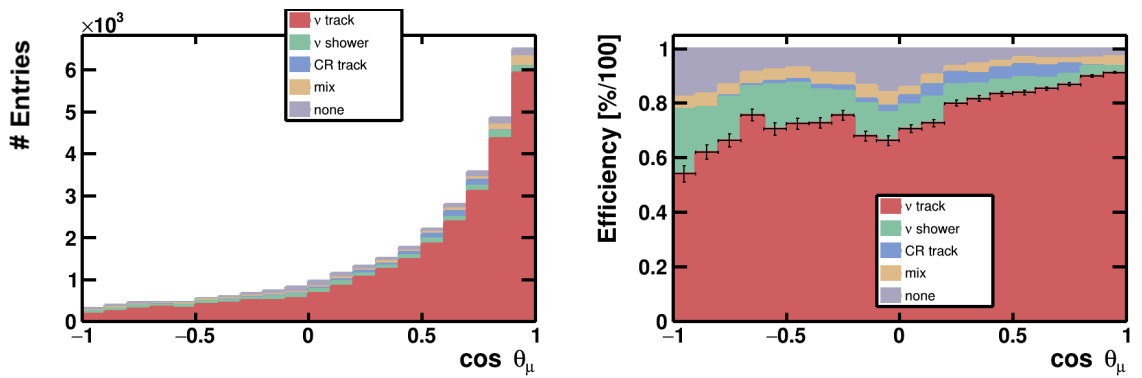
Figure 5.12: Relative efficiency of primary muon reconstruction as a function of $\cos\theta_\mu$. (a) A stacked histogram of the true distribution with the reconstruction outcomes. (b) The percentage efficiency of particles reconstructed as tracks in neutrino slices.
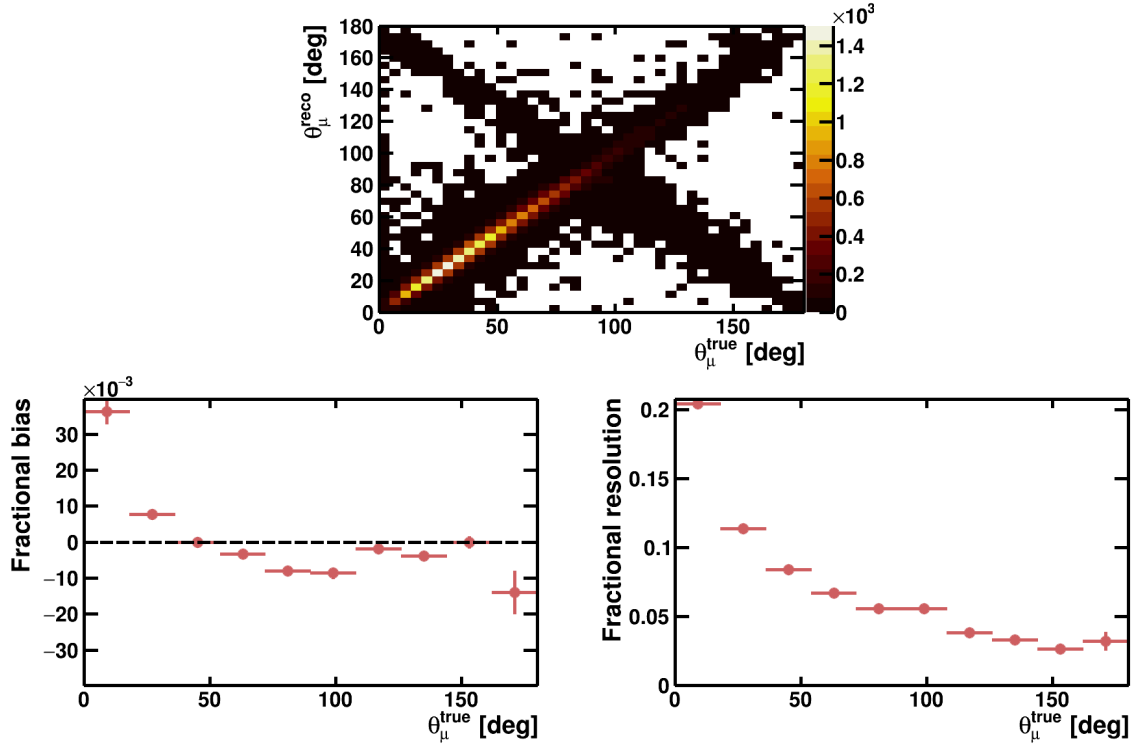
Figure 5.13: The fractional bias and resolution of the reconstructed track θ_μ as a function of the true θ_μ. The diagonal line across the main distribution is the result of the start and end points of the track being incorrectly identified, this happens approximately 7% of the time.

from the start and end points of the 3D reconstructed track. The fractional bias and resolution, Figure 5.13, were calculated by fitting Gaussian functions to the fractional difference binned as a function of the true angle to the beam.

Topological methods for estimating particle momenta must be employed as SBND is not magnetised, the lack of magnetic field also means it is not possible to perform sign selection on particles. For track-like particles fully contained in the active volume, the range of the track can be compared to the standard range curve of muons in liquid argon [141].

If a muon track exits the active volume, the relationship between the momentum of the muon and the amount of Multiple Coulomb Scattering (MCS) that it undergoes can be used [174]. Tracks must be long enough to properly measure the average scattering angle. The momentum was reconstructed by applying the range method to contained tracks and the MCS method to exiting tracks. The fractional bias and resolution as a function of
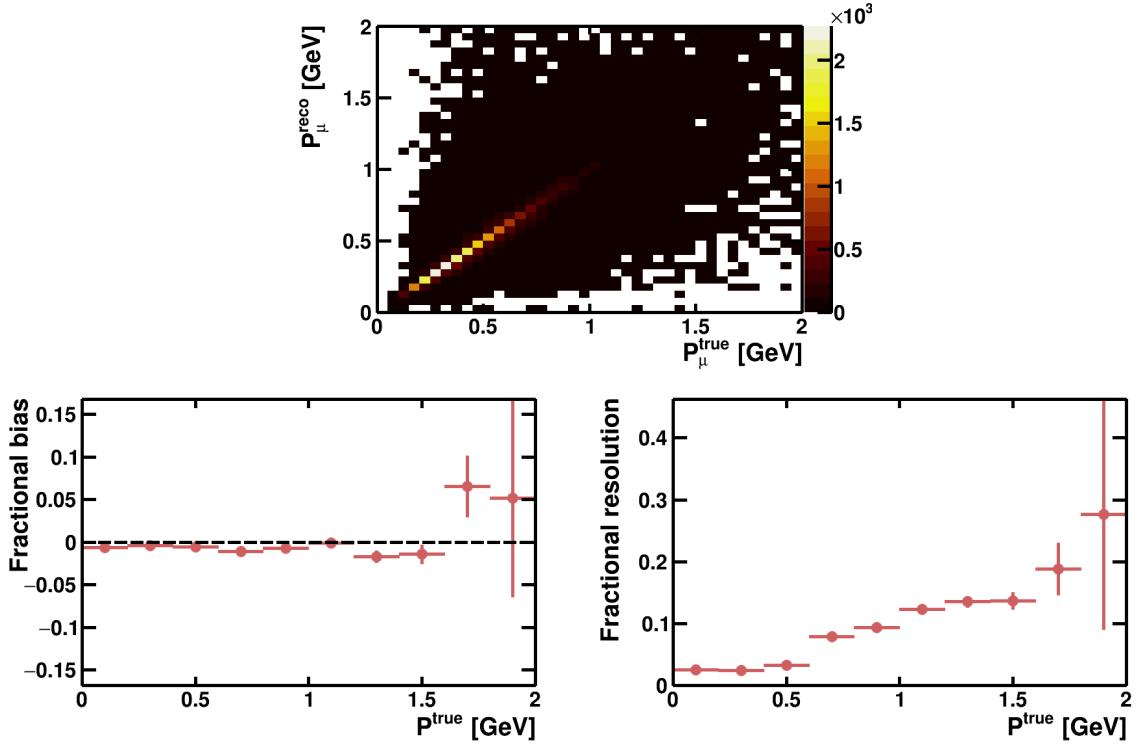
Figure 5.14: The fractional bias and resolution of the reconstructed track P_μ as a function of the true P_μ using range for contained tracks and MCS for exiting tracks.

the true momentum are shown in Figure 5.14.

The lack of magnetisation and time of flight detectors means that Particle Identification (PID) algorithms are also only able to use topological and calorimetric information. The method used for contained tracks compares the reconstructed dE/dx versus residual range, the distance from the end of track, curves with the expected distributions for muons, pions, protons and kaons, shown in Figure 5.15, via a χ^2 test. The expected distribution with the minimum χ^2 was taken as the particle label for this track. This method requires a particle to stop via ionisation losses in the TPC active volume and there is currently no universally accepted method for identifying particles which do not stop. The minimum χ^2 distributions for primary stopping muons, pions and protons are shown in Figure 5.16.

Separation between muons/pions and protons using calorimetry is good for stopping particles. The separation is poor between muons and pions because their masses are similar and the short lifetime of the pion means it is likely to decay before it has come completely to rest, effectively shifting the dE/dx curve further into the muon expectation. One of the biggest neutrino induced backgrounds to ν_μ CC is ν_μ NC with charged pions
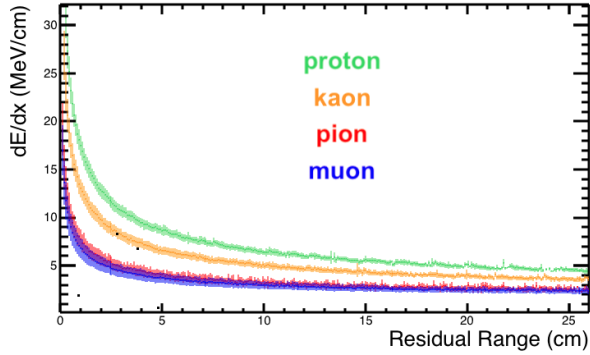
Figure 5.15: Expected dE/dx vs range curves for track-like particles in liquid argon.
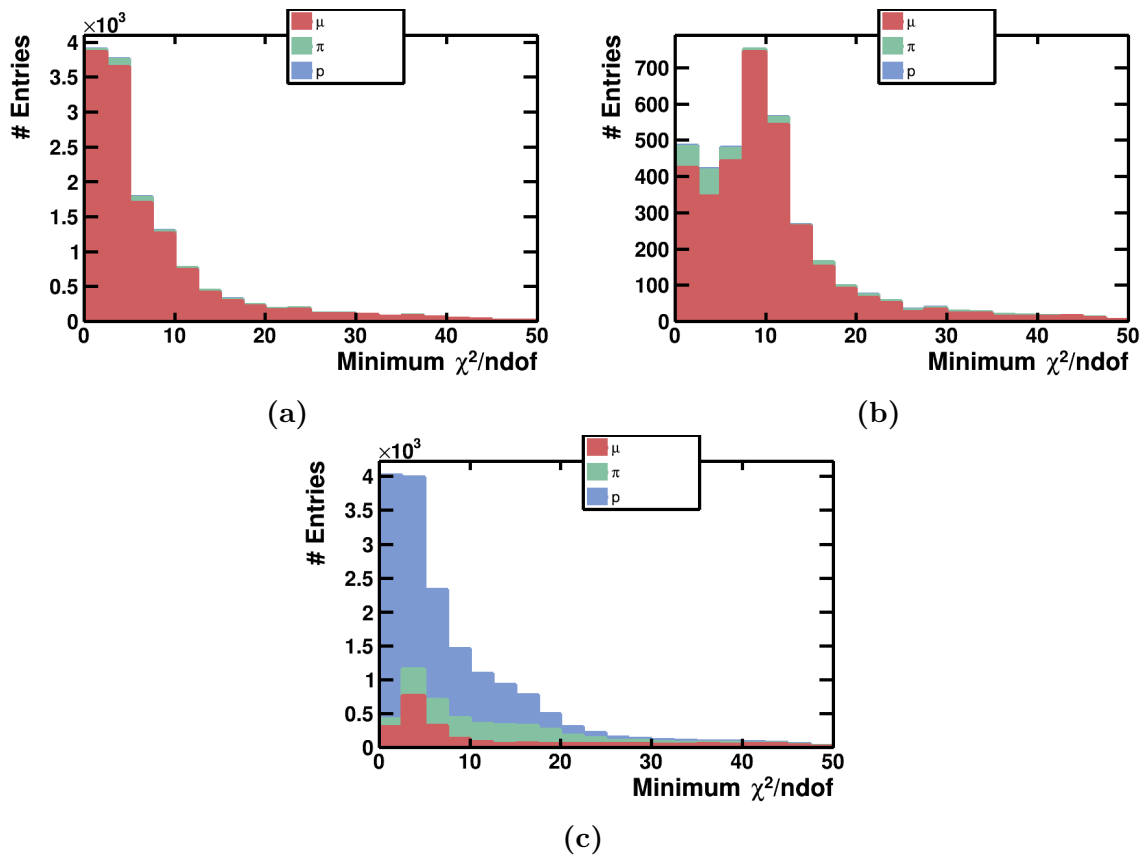
Figure 5.16: χ^2 PID distributions for (a) muons, (b) charged pions and (c) protons with the expected distribution that corresponds to the minimum labelled.
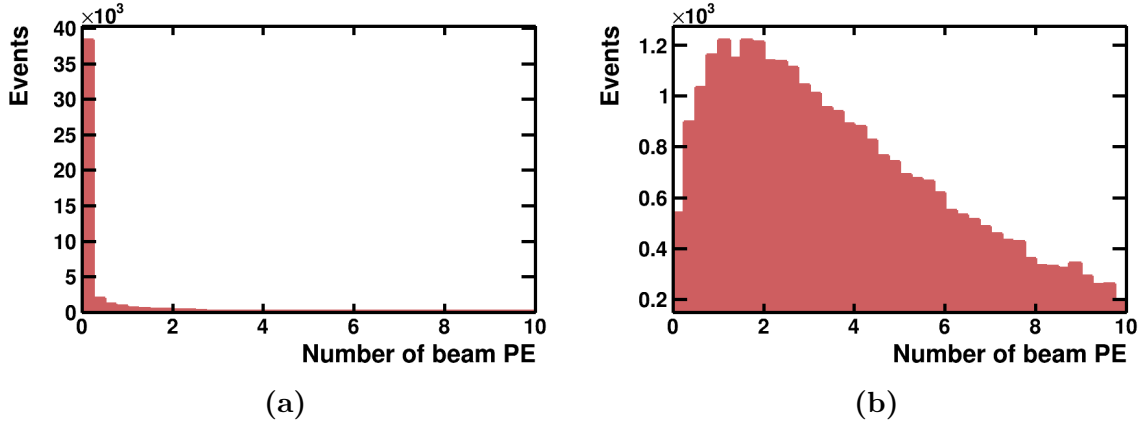
Figure 5.17: Number of reconstructed PE in beam window per TPC for (a) when there was no visible energy deposition in time with the beam and (b) when there was a ν_μCC with a vertex inside the AV. (b) Also considers interactions where particles cross between the two TPCs.

in the final state. Therefore, a robust method for separating muons and pions is required, this is further discussed in Section 6.4.

5.3.2 The photon detection system

The PDS will be integral for triggering on neutrino interactions inside the TPC and the performance will directly affect the signal selection efficiency and background rejection. To study the trigger requirements for ν_μ CC selection, the distribution of PE reconstructed by coated PMTs in the beam window for ν_μ CC interactions with vertices contained inside the active volume was studied, shown in Figure 5.17.

There is great potential to use the PDS for improving the tracking and calorimetry performance of the detector, but given the currently available tools the usage was restricted to just t_0 matching in this analysis. It is important to be able to reconstruct the individual optical flash times in order to do this. The difference between the reconstructed optical flash time and the true interaction time for cosmic ray muons is shown in Figure 5.18 for coated PMTs.

As discussed in Section 5.2.2, the PDS can be used to help identify which TPC reconstructed object was responsible for the trigger. The score distributions for interactions in time and out of time with the beam window are shown in Figure 5.19.

(a)

(b)
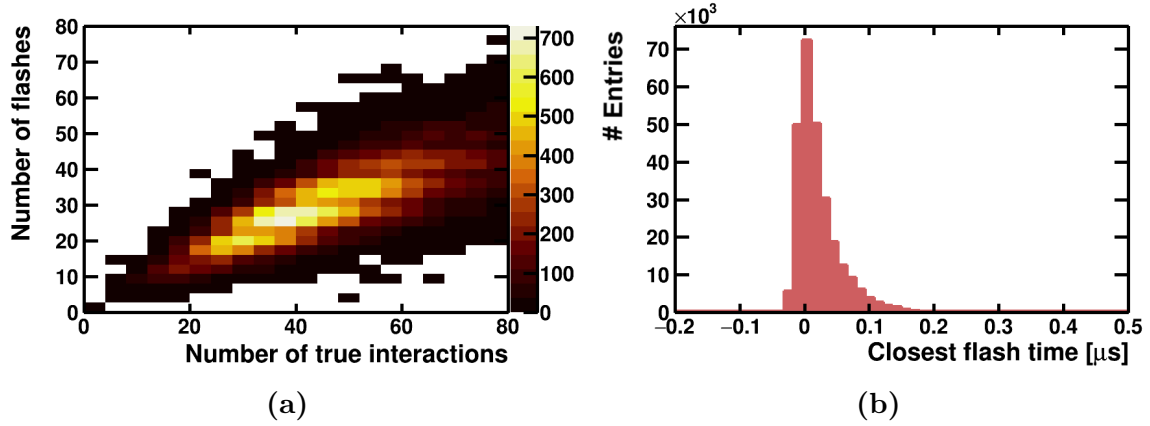
Figure 5.18: (a) Comparison between the number of reconstructed optical flashes and the number of flashes that would be expected for all true charged particles depositing more than 10 MeV in the detector. (b) Difference between reconstructed optical flash time and true interaction times of cosmic ray muons.

(a)

(b)
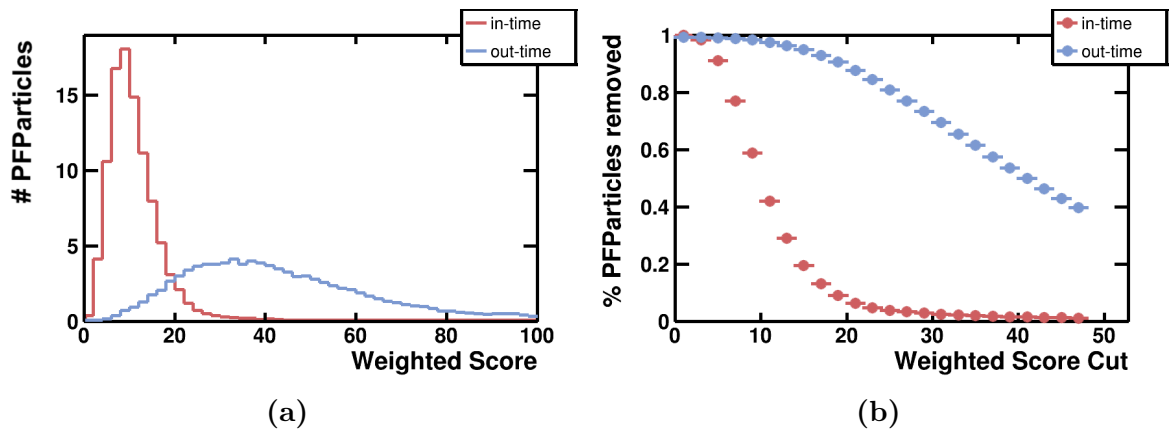
Figure 5.19: (a) Flash matching score for in-time and out (of)-time interactions in the TPC, where in-time refers to interactions within the 1.6 μs beam window. (b) The percentage of in time and out of time events removed with different maximum flash score values.

(a)

(b)

(c)
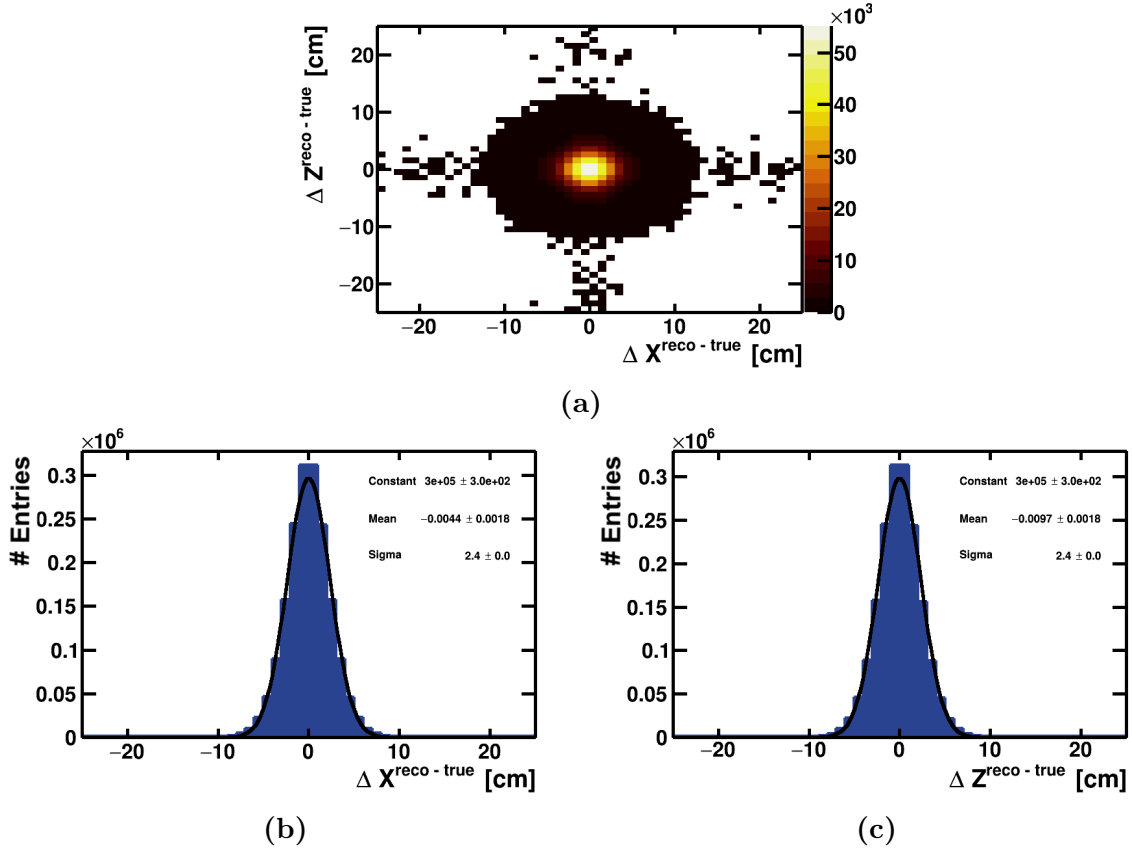
Figure 5.20: An example of CRT hit resolution calculations. (a) The 2D distribution of the difference in true and reconstructed Z and X coordinates for the top CRT tagger. (b) & (c) The 1D projections with Gaussian functions fit to estimate the bias and resolution of the tagger.

5.3.3   The cosmic ray tagger

The primary use of the CRT in this analysis was the reduction of cosmic ray muon backgrounds, by both rejecting false triggers from cosmic muons in time with the beam and removing TPC reconstructed objects in the same readout window as neutrino events. In order to do this, the efficiency of reconstructing CRT hits and tracks for muons which enter the TPC must be high.

The performance of CRT hit reconstruction was evaluated using a sample of cosmic ray muons generated by CORSIKA [168]. The coordinate resolution of each tagger was calculated by fitting Gaussian functions to the differences between the reconstructed 3D hits and the true crossing points, as shown in Figure 5.20. The results for all of the taggers are shown in Table 5.2.

Table 5.2: Bias and resolution in all three spatial dimensions for hit reconstruction on each tagger measured using a realistic flux of cosmic ray muons. An increase in Y bias and resolution is observed for the taggers around the detector due to downward going muons. Taggers are labelled with respect to the beam direction.

Tagger	X (cm)		Y (cm)		Z (cm)	
	Bias	Resolution	Bias	Resolution	Bias	Resolution
Bottom	0.006 (±0.0022)	1.6 (±0.0018)	-0.06 (±0.00094)	0.66 (±0.00085)	0.0078 (±0.002)	1.6 (±0.0017)
Back face	-0.019 (±0.0033)	2.2 (±0.0029)	-0.094 (±0.0039)	2.7 (±0.0032)	0.23 (±0.0081)	0.46 (±0.0082)
Front face	-0.034 (±0.0034)	2.3 (±0.003)	-0.1 (±0.0041)	2.7 (±0.0034)	0.23 (±0.0083)	0.46 (±0.0085)
Left side	0.2 (±0.0072)	0.48 (±0.0087)	-0.12 (±0.0039)	2.8 (±0.0033)	0.058 (±0.0032)	2.3 (±0.0028)
Right side	-0.22 (±0.0075)	0.47 (±0.0079)	0.11 (±0.0038)	2.8 (±0.0032)	0.007 (±0.0031)	2.3 (±0.0028)
High top	-0.0044 (±0.0018)	2.4 (±0.0016)	0.27 (±0.0044)	0.42 (±0.0034)	-0.0097 (±0.0018)	2.4 (±0.0015)
Low top	0.0028 (±0.0017)	2.4 (±0.0015)	0.27 (±0.0042)	0.42 (±0.0033)	-0.00017 (±0.0017)	2.4 (±0.0015)
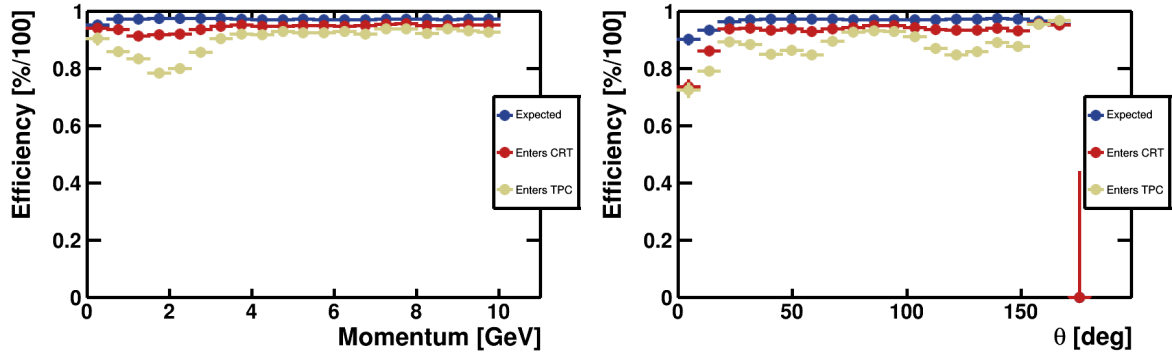
Figure 5.21: CRT hit reconstruction efficiency. **Expected:** cosmic ray muons which cross at least two overlapping perpendicular scintillator strips in the same tagger, total = 97%. **Enters CRT:** cosmic ray muons which enter the volume enclosed by the CRT system, total 94%. **Enters TPC:** cosmic ray muons which enter the TPC, total = 89%.

The reconstructed hit resolutions were predicted to be between 1.5 and 1.8 cm based on test bench measurements [156]. This was initially confirmed by the simulations but the tuning to MicroBooNE data, as described in Section 5.1, increased these values due to the broadening of the PE peak and saturation effects. This particularly affected the side taggers as they are exposed to a flux of mostly downward going cosmic ray muons which tend to travel further in the plastic scintillator and deposit a greater amount of charge.

The hit finding efficiency as a function of muon momentum and θ can be seen in Figure 5.21. The reductions in efficiency for low momentum muons at angles around 50 and 120 degrees were from the gap in coverage between the lower top tagger and side taggers.

The track reconstruction efficiency as a function of momentum and θ can be seen in Figure 5.22. The reduction in efficiency was due partly to muons which are not through-going and partly to the reduction of coverage in the bottom plane combined with the flux of mostly downward going muons. The reconstructed track angles θ and ϕ, the angle around the beam, compared to the true angles are shown in Figure 5.23.

5.3.4 CRT-TPC matching

In order to tag cosmic ray muon tracks in the TPC, tools for matching between reconstructed CRT hits and tracks and TPC tracks were developed. As discussed in Section 5.2.1, particles which cross the detector outside of the trigger time will have their TPC
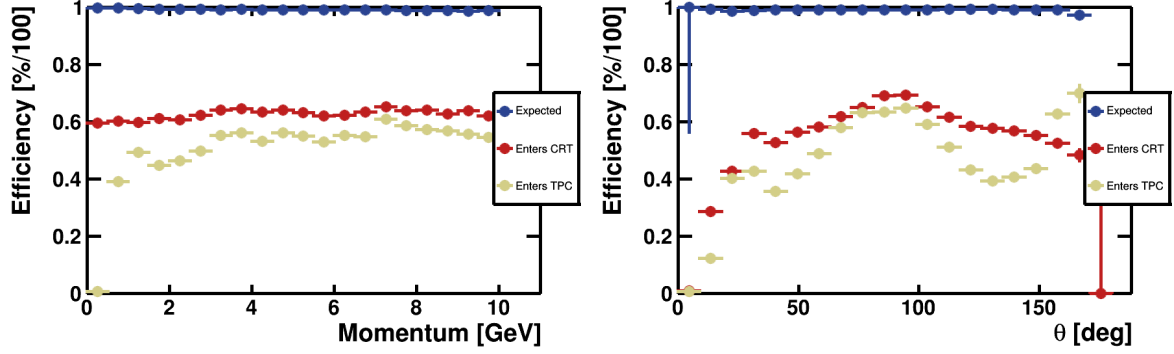
Figure 5.22: CRT track reconstruction efficiency. **Expected:** cosmic ray muons which associated with at least two CRT hits on separate taggers, total = 99%. **Enters CRT:** total = 62%. **Enters TPC:** total = 53%.
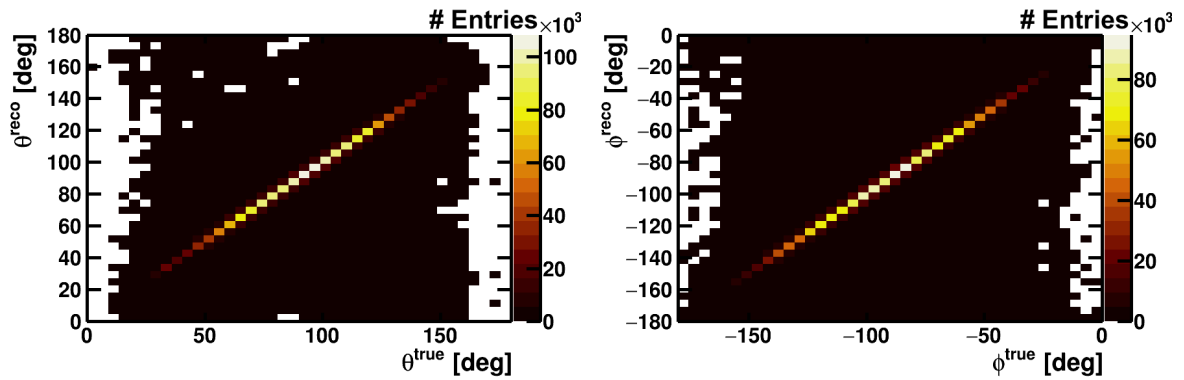
Figure 5.23: The difference between the true and reconstructed CRT track (a) angle to the neutrino beam and (b) angle around the neutrino beam.
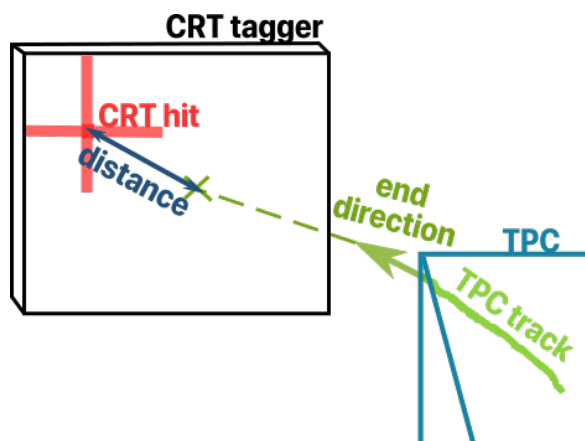
Figure 5.24: Diagram of CRT hit to TPC track matching demonstrating the projection of a TPC track onto the CRT plane.

reconstructed position in the drift coordinate shifted. The CRT has nanosecond timing resolution and should be able to provide the true crossing times of the particles if matched correctly.

The CRT hit to TPC track matching is performed by selecting a track-hit pair and shifting the drift position of the track according to the time recorded by the hit. The track is then projected outwards onto the corresponding CRT tagger and the Distance of Closest Approach (DCA) to the hit is calculated. This is shown diagrammatically in Figure 5.24.

As there can be large uncertainties in CRT hit positions, especially for hits on the bottom plane, the DCA is calculated by treating the hit as a 3D cuboid. An infinite length line is drawn between the start and end of the TPC track and a ray-box intersection algorithm [175] is used to determine if the infinite length line crosses the hit. If not, the minimum distance between the infinite length line and the edges of the cuboid is used, calculated using a ray-segment distance algorithm [176].

The value of the DCA can then by used to determine if the hit-track pair are a good match. This was tuned using a sample of cosmic ray muons, the DCA distributions for track-hit pairs that are either matched or not matched to the same true particles are shown in Figure 5.25 and the efficiency and purity of the matching as a function of the
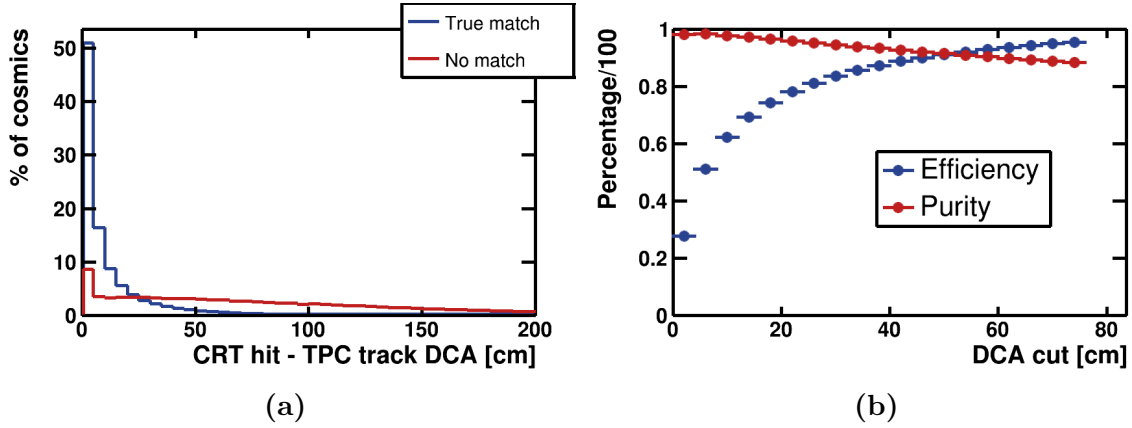
Figure 5.25: (a) DCA distributions CRT hit to TPC track matching for tracks with a true match and tracks without. (b) Efficiency and purity of CRT hit to TPC track matching. Correct matching is defined for tracks having a matched time within 2 μs of their true time.

maximum DCA value are shown in Figure 5.25. The efficiency and purity were defined as

$$E = \frac{N^{match}}{N^{all}}, \quad P = \frac{N^{correct}}{N^{match}} \tag{5.8}$$

where N^{all} is the number of tracks that have a true match, N^{match} is the number of those tracks with a reconstructed match and $N^{correct}$ is the number of matched times within 2 μs of the true time.

Only 53% of cosmic ray muons that entered the TPC were associated with CRT tracks but the additional topological information in the CRT track provides a potential for creating a high purity tagged sample for doing calibrations and solving some ambiguities in the track-hit matching. TPC tracks are matched to CRT tracks by shifting the drift position as in the track-hit matching and then calculating the average DCA over each trajectory point in the TPC track and the angle between the tracks, Figure 5.26.

The DCA between a track point, $\boldsymbol{p}$, and a CRT track with start point $\boldsymbol{s}$ and end point $\boldsymbol{e}$ is given as

$$DCA = \frac{|(\boldsymbol{p} - \boldsymbol{s}) \times (\boldsymbol{p} - \boldsymbol{e})|}{|\boldsymbol{e} - \boldsymbol{s}|}. \tag{5.9}$$

The track-track matching was also tuned on a sample of cosmic ray muons and the two dimensional distributions for truth matched and unmatched pairs are shown in Figure
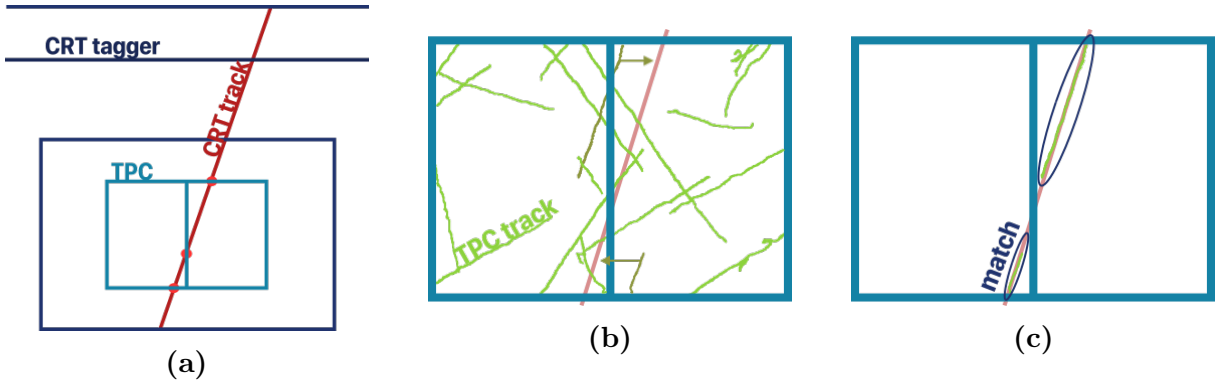
Figure 5.26: Diagram of CRT track to TPC track matching. (a) Identification of the TPC crossing points. (b) Shifting TPC tracks to the CRT track time. (c) Matching tracks with angle and average DCA.
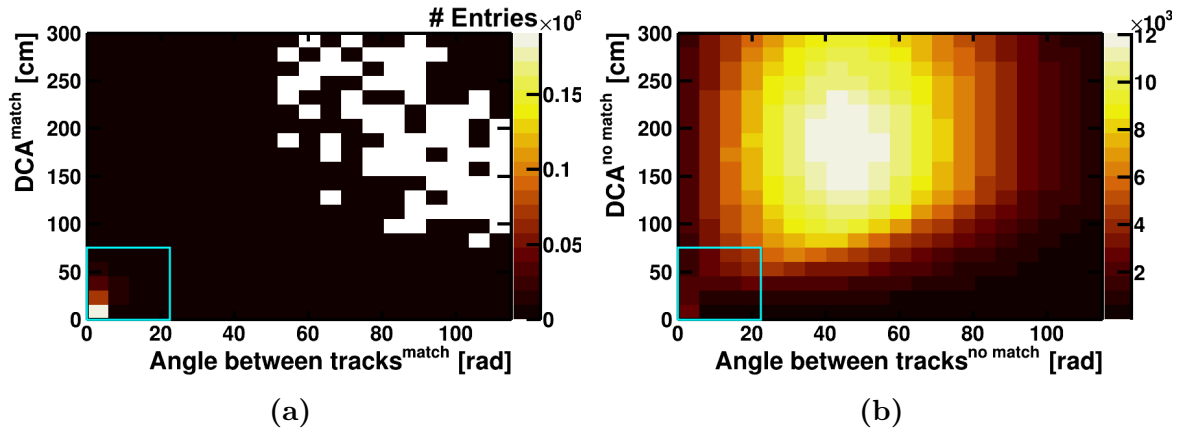
Figure 5.27: DCA and angle distributions CRT track to TPC track matching with initial box selection region shown for (a) truth matched track pairs and (b) unmatched track pairs.

5.27. The matching decision is made by first performing a box selection to reject any pairs which do not match. If there is more than one match candidate remaining, the pair with the smallest angle between the tracks is chosen as the match. The efficiency and purity as a function of the angle are shown in Figure 5.28.
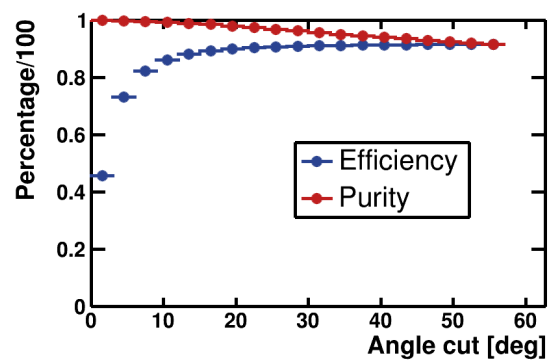
Figure 5.28: Efficiency and purity of CRT track to TPC track matching using the same definitions as for CRT hit matching.

Chapter 6

Event selection

In this chapter, the process of selecting the primary muon from charged current ν_μ interactions and rejecting backgrounds is discussed. Section 6.1 will outline the signal and background definitions relevant to this analysis, their expected trigger rates and initial reconstructed kinematic distributions. Section 6.2 describes the process of identifying and removing the cosmic ray muon background. The steps taken to identify the primary muon in ν_μ CC interactions are described in Section 6.4. Section 6.5 contains the selected distributions and Section 6.6 contains an analysis of the selection performance.

6.1   Signal and background definitions

In order to measure the ν_μ CC inclusive cross section, the primary muon must be reconstructed and correctly identified from any other particle types. Muons from other sources such as cosmic rays and neutrino interactions outside of the TPC will form a large part of the background. Any neutrino interactions with a vertex outside of the TPC active volume are referred to as dirt interactions, with interaction products being dirt particles.

There will also be backgrounds from charged pions and protons being misidentified as muons with the majority contributed by ν_μ NC interactions inside the TPC. The identification of the wrong particle as the primary muon for ν_μ CC interactions will have no effect on the overall cross section measurement but will smear kinematic distributions

when measuring differential cross sections and so should be minimised.

6.1.1 Trigger rates

There are three main categories of event that will result in a trigger, neutrino interactions in the TPC, neutrino interactions outside of the TPC with interaction products entering, and cosmic ray muons in time with the beam. As discussed in Section 3.2, each beam spill will consist of $5{\times}10^{12}$ POT and have a duration of 1.6 μs. The exact trigger specifications are not yet finalised but the optical flash reconstruction requirement of 0.1 PE in the beam window approximately corresponds to a 20 MeV energy deposit, as can be seen in Figure 5.8. A requirement of 20 MeV energy deposition in the detector coincident with the beam spill (0 to 1.6 μs time window) was therefore used for estimating the trigger rates. There is currently no consideration of the spatial position or coincidence between photon detectors but these features are likely to be used in the final trigger design to further reduce backgrounds.

From the simulations described in the previous chapter, the probabilities of each type of trigger were estimated to be:

- **Neutrinos in the TPC:** 1 per 25 spills ($P_\nu = 0.040$)

- **Neutrino outside of the TPC:** 1 per 65 spills ($P_{dirt} = 0.015$)

- **In-time cosmic ray muons:** 1 per 175 spills ($P_{in-time} = 0.006$)

Given the limited computing resources at the time of writing it was not possible to fully simulate all types of triggered events together with enough statistics. The large number of readout channels with μs to ns time resolution combined with the need to simulate electron drift and photon propagation results in both high memory usage and CPU time. A scaling scheme was implemented to make use of the available simulations, which were:

- **Sample 1:** 49,090 (45,525 triggered) events with a BNB neutrino interaction inside the TPC volume + 10 cm in each direction and a cosmic overlay. ($\text{POT}^1_{sim} = 5.27{\times}10^{18}$)

- **Sample 2:** 5,133 events with in-time cosmic ray muon interactions depositing sufficient energy to trigger the readout. (equivalent $POT^2_{sim} = 4.50 \times 10^{18}$)

- **Sample 3:** 13,600 events with a BNB neutrino interaction entering the TPC from outside and no cosmic overlay. ($POT^3_{sim} = 4.93 \times 10^{18}$)

Sample 1 contained all of the signal events which were scaled up to the total expected POT of 6.6×10^{20} by

$$N^{\nu}_{total} = N^{\nu,1}_{sim} \cdot \frac{POT_{total}}{POT^1_{sim}}. \tag{6.1}$$

The overlaid cosmic ray backgrounds were also scaled in the same way. This sample also contained a small number of dirt interactions from the 10 cm border around the TPC.

The rest of the dirt contribution was estimated from sample 3 by taking all of the events triggered by a neutrino with an interaction vertex further than 10 cm from the TPC border and then applying a similar scaling as in Equation 6.1. Events that are triggered by dirt interactions will also contribute to the cosmic ray background, so the cosmic ray muons from sample 1 were further scaled by

$$N^{cosmic}_{total} = N^{cosmic,1}_{sim} \cdot \frac{POT_{total}}{POT^1_{sim}} \cdot \left(1 + \frac{P_{dirt}}{P_{\nu}} - P_{dirt} \cdot P_{\nu}\right) \tag{6.2}$$

where P_{dirt}, P_{ν} are the probabilities of a trigger from a dirt or TPC neutrino given on the previous page. This gave the total expected distributions from beam related triggers.

The contribution from in-time cosmic ray muon triggers was estimated from sample 2. The effective simulated POT for this sample was calculated as

$$POT^2_{sim} = \frac{POT_{spill} \cdot N^{in-time,2}_{sim}}{P_{in-time}} \tag{6.3}$$

where POT_{spill} is the number of POT in each spill, $N^{in-time,2}_{sim}$ is the number of in-time cosmic events simulated and $P_{in-time}$ is the probability of an in-time cosmic trigger in a spill. The in-time cosmic events were then scaled by

$$N^{in-time}_{total} = N^{in-time,2}_{sim} \cdot \frac{POT_{total}}{POT_{sim}} \cdot (1 - P_{in-time} \cdot (P_{\nu} + P_{dirt} - P_{\nu} \cdot P_{dirt})) \tag{6.4}$$
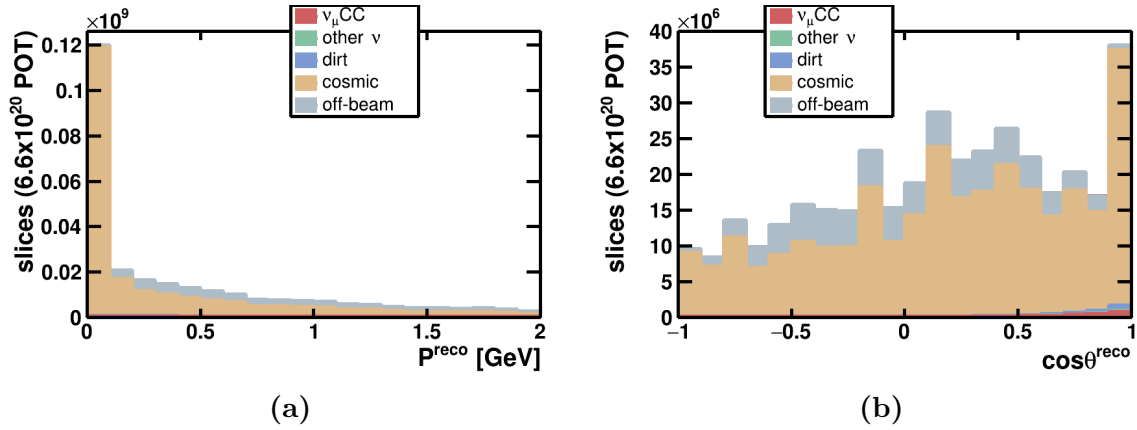
Figure 6.1: Reconstructed P_μ and $\cos\theta_\mu$ distributions for all slices reconstructed by Pandora and scaled to 6.6×10^{20} POT. The large bin to bin variations are due to the Pandora reconstruction failing for high energy cosmic ray muon tracks rather than low statistics, these tracks are rejected by the first pass of the unambiguous cosmic rejection and so the reconstruction artefacts do not propagate to the final distributions.

which takes into account events where there are both cosmic and neutrino triggers. All three samples were combined with this scaling to provide an estimate of the total event rate expected in SBND.

6.1.2 Initial distributions

Figures 5.11 and 5.12 in Section 5.3 show the distributions of true P_μ and $\cos\theta_\mu$ for all ν_μ CC interactions inside the detector active volume. In order to properly evaluate the performance of the selection on both the signal and background through the different stages, distributions must be shown in reconstructed variables. A basic primary muon selection was applied whereby the longest track in a slice reconstructed by Pandora was called the muon and the kinematics were reconstructed as in Section 5.3. The reconstructed P_μ and $\cos\theta_\mu$ distributions for all Pandora slices scaled to the expected POT are shown in Figure 6.1. Figure 6.2 shows the same distributions after the unambiguous cosmic removal.

As is clear from Figure 6.2, cosmic ray muons are expected to be by far the largest background to the inclusive analysis and their identification and removal represents a significant part of the effort in this analysis. The contributions from in-time cosmic triggers can be removed by taking data with a fake beam trigger during periods when the

(a) (b)
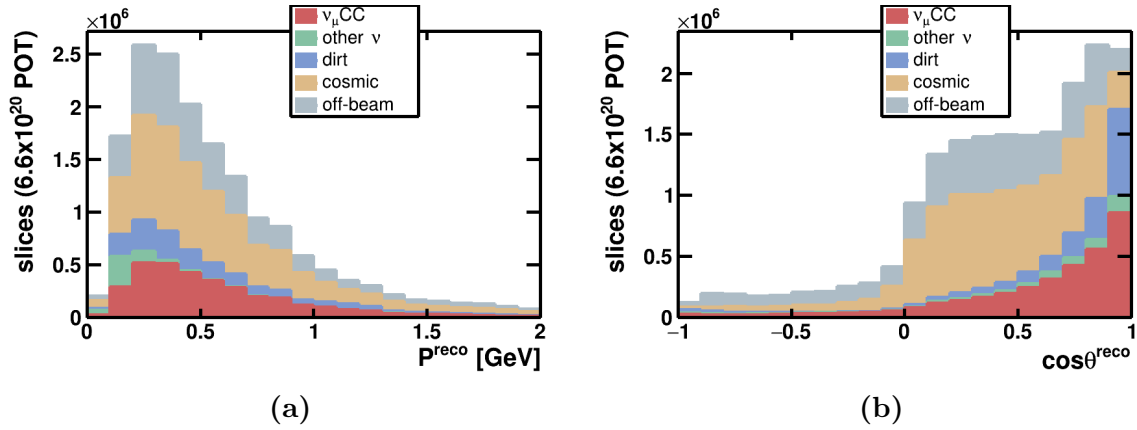
Figure 6.2: Reconstructed P_μ and $\cos\theta_\mu$ distributions for all possible neutrino slices identified by Pandora and scaled to 6.6×10^{20} POT.

beam is not delivering spills (off-beam), and then scaling and subtracting this data from the on-beam data. This is a robust method of removing in-time backgrounds provided that the off-beam data is taken during the same operational conditions as the on-beam data that it is subtracted from.

6.2 Cosmic identification

Pandora only makes use of topological information in the TPC to tag unambiguous cosmic ray muons [173]. To reduce the cosmic background even further, a suite of algorithms utilising all three detector subsystems was developed.

All of the slices remaining after the unambiguous cosmic removal were reconstructed with the assumption that they originated from neutrino interactions. The process of trying to find a vertex for a slice containing a cosmic ray muon often meant that any slight kink in the track was often misidentified as a neutrino interaction vertex with two particles emerging from it. As a result, for slices containing two or more reconstructed tracks, the angle between the two longest tracks was peaked at near 180 degrees for cosmic ray muons and had a much wider distribution for neutrino interactions, Figure 6.3.

The criteria used to identify specific cosmic ray muon topologies in reconstructed slices are described below. Each criteria was applied to the longest track in the slice and then, if there were two or more tracks, the criteria were applied to the two longest tracks merged
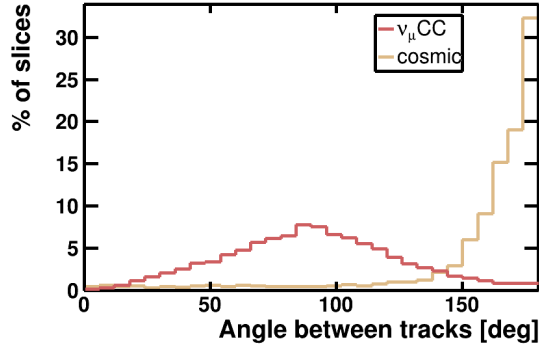
Figure 6.3: The angle between the two leading tracks for slices matched to cosmic ray muon and neutrino interactions.

together if the angle between them was greater than 150 degrees.

The performance of each criteria was evaluated by comparing reconstructed ν_μ CC slices to cosmic ray muon slices. The removal efficiency for true ν_μ CC slices was defined as

$$E_\nu = \frac{N_{removed}}{N_{total}} \tag{6.5}$$

where N_{total} is the total number of ν_μ CC interactions reconstructed by Pandora and $N_{removed}$ is the number removed by the criteria. The removal efficiency for true cosmic ray slices was defined as

$$E_{cosmic} = \frac{N_{removed}}{N_{possible}} \tag{6.6}$$

where $N_{possible}$ is the total number of cosmic ray muons that could be removed (e.g. for the stopping criteria only particles which actually stop in the TPC were considered) and $N_{removed}$ is the number of those removed by the criteria.

The efficiency curves were produced by area normalising the N_{total} and $N_{possible}$ distributions and calculating their forward or backwards cumulative, depending on the selection criteria removal direction. The criteria values were determined by calculating the Kolmogorov-Smirnov distance [177] between the area normalised histograms while requiring that the neutrino misidentification rate for each criteria remained below 4%.

The plots shown here analysing the performance of the cosmic identification contain only on-beam equivalent simulations, sample 1, with no contribution from in-time cosmic rays. The distributions are expected to be similar for in-time cosmic ray muons, with a
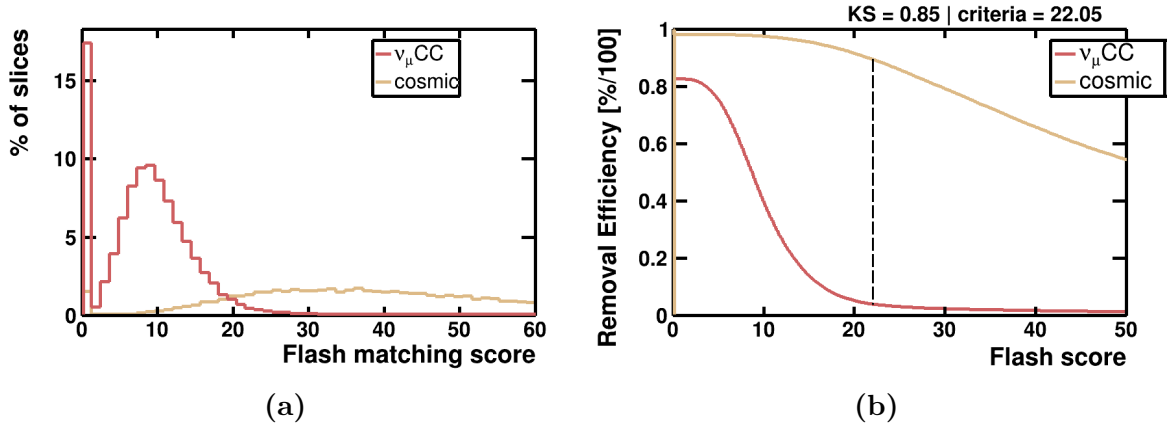
Figure 6.4: Flash matching cosmic ID. (a) Distribution of flash matching score for muon neutrinos and cosmic ray muons. (b) Signal and background removal dependence on flash score. A score of zero was assigned in cases where the slice was reconstructed in both TPCs.

slight reduction in performance where t_0 tagging is employed. Only reconstructed slices that were not identified as unambiguous cosmic ray muons were considered.

6.2.1 Flash matching

The flash matching described in Section 5.2.2 is expected to be the most powerful method for removing the cosmic ray background. It is applicable to all cosmic ray muons that cross the detector outside of the beam window. Figure 6.4 shows the distributions of the flash matching score and the relationship between the score and the removal efficiencies for cosmic ray muons and ν_μ CC interactions.

The flash matching was modified slightly to ignore slices that were reconstructed in both TPCs. Particles which cross the CPA outside of the beam window will be split in two by the reconstruction and then stitched back together and tagged as cosmic ray background by later stages of Pandora. Any remaining tracks composed of reconstructed hits in both TPCs must have been coincident with the beam and so a score of zero was given.
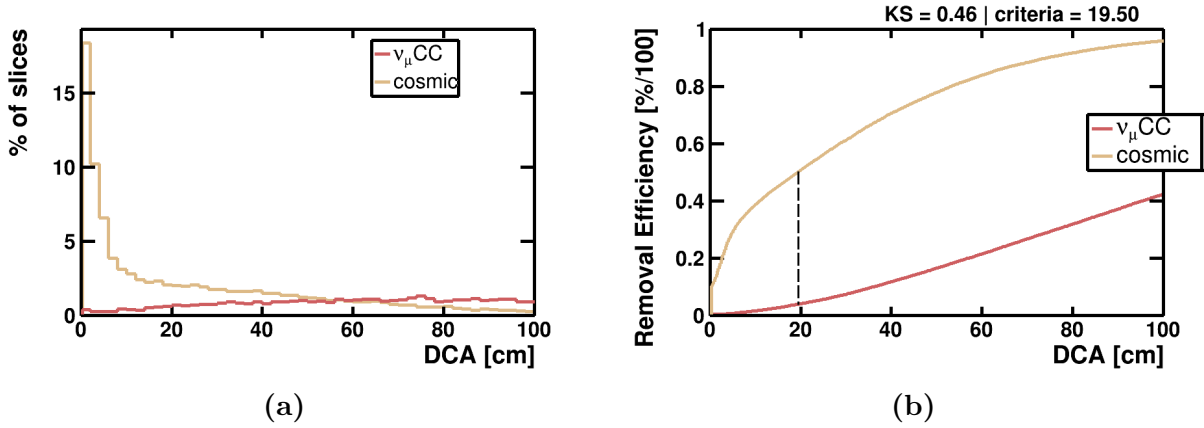
Figure 6.5: CRT hit matching cosmic ID. (a) Distance of closest approach distributions. (b) Signal and background removal dependence on the DCA criteria. Neutrino slices which have a true CRT hit association were not included.

6.2.2   CRT hit matching

The matching between CRT hits and TPC tracks is described in Section 5.3.4. The proportion of ambiguous cosmic ray muon slices that had at least one associated CRT hit and had the potential to be removed with this criteria was estimated to be 82%. The distributions of the DCA between the longest track and the closest hit are shown in Figure 6.5 along with the relationship between the DCA and the removal efficiencies.

It is possible for high energy neutrino interactions to result in reconstructed CRT hits and so a slice was only tagged as a cosmic ray if it was matched to a CRT hit outside of the beam window. The large distance between the TPC and the CRT taggers occasionally resulted in large deviations between projected reconstructed track directions and true trajectories, hence why a loose removal criteria was required to achieve high efficiency.

6.2.3   CRT track matching

The details of CRT track and TPC track matching are also found in Section 5.3.4. 42% of ambiguous cosmic ray muons had a CRT track associated with them. Both the average DCA and angle between tracks were calculated and then weighted to form a single score rather than performing a box selection as in Section 5.3.4. The score distributions can be seen in Figure 6.6.
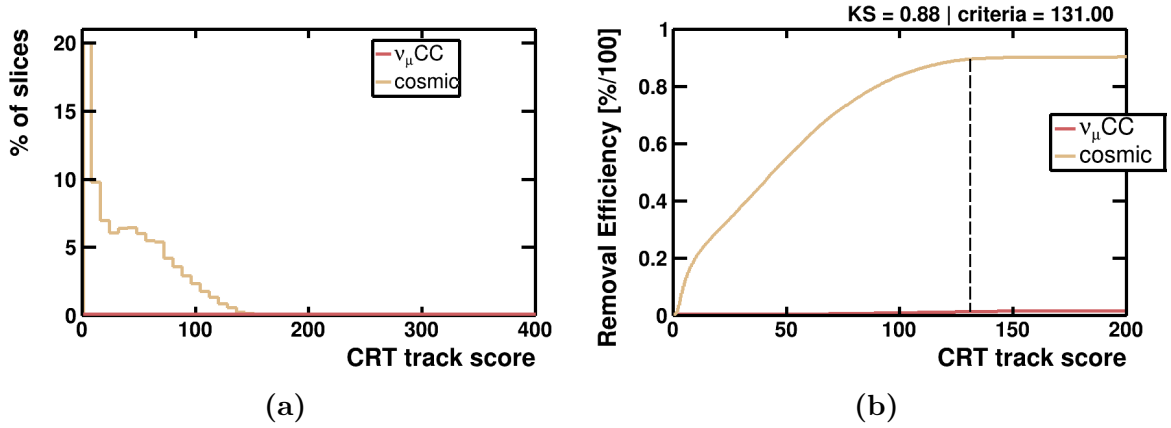
Figure 6.6: CRT track matching cosmic ID. (a) Track score distributions. (b) Signal and background removal dependence on the track matching score.

It was very rare that the product of a neutrino interaction in the TPC would form a CRT track and so if there was a match the TPC track was tagged as a cosmic. The removal efficiency plateaus because a proportion of the cosmic ray muon tracks underwent some kind of hard scatter between CRT taggers and so the trajectories did not appear to match.

6.2.4   Stopping particles

At lower energies, muons will enter the TPC and stop through ionisation processes, this was the case for 32% of the cosmic ray muons not unambiguously tagged by Pandora. Stopping particles should be identifiable by their Bragg peaks, the energy loss of the track increasing towards the end of its range [141]. A tool was developed to identify the presence of a generic Bragg peak, rather than one for a specific particle as in Section 5.2.1.

The dE/dx versus residual range distributions in the first and last 20 cm of a track were fit with both a zero degree polynomial and an exponential function using ROOT minimisation tools [166]. The ratio between the χ^2 of the two fits was calculated and used to identify the Bragg peak. An increasing value of $\chi^2_{pol}/\chi^2_{exp}$ indicates a better exponential fit and hence a stopping particle.

As it is likely that particles from neutrino interactions will also stop inside the detector, this criteria was only applied to tracks which had one end that appeared to exit the
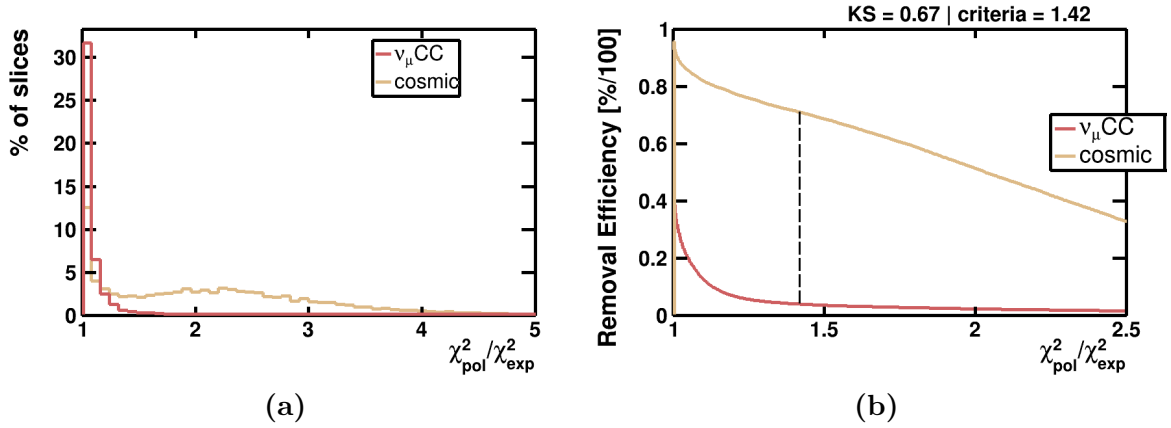
Figure 6.7: Stopping particle cosmic ID. (a) χ^2 ratio distributions. (b) Signal and background removal dependence on the χ^2 ratio. In this case, only neutrino slices with exiting tracks are shown.

detector. The χ^2 ratio was only used for the non-exiting end of the track. This meant that the criteria was not applicable to cosmic ray muons that entered through the APA outside of the beam window, but further criteria could remove this topology. The χ^2 ratio distributions for stopping cosmic ray muons and neutrino interactions with exiting tracks are shown in Figure 6.7.

6.2.5 Near exiting particles

If cosmic ray muons do not stop, then by definition they should pass in and out of the TPC enclosed volume. Pandora's unambiguous cosmic identification removed most of these tracks but missed some in cases where the ends near the TPC walls were not correctly reconstructed. This criteria removed tracks which both started and ended within a certain distance from the TPC walls. The containment volume for cosmic and neutrino particles is shown in Figure 6.8.

6.2.6 TPC beam flash

As discussed in Section 5.3.2, the PDS was used for triggering on events that contain neutrino interactions in the beam window. The current simplified trigger selected events based on the number of reconstructed PE in coated PMTs inside the beam window. As

(a)   **(b)**
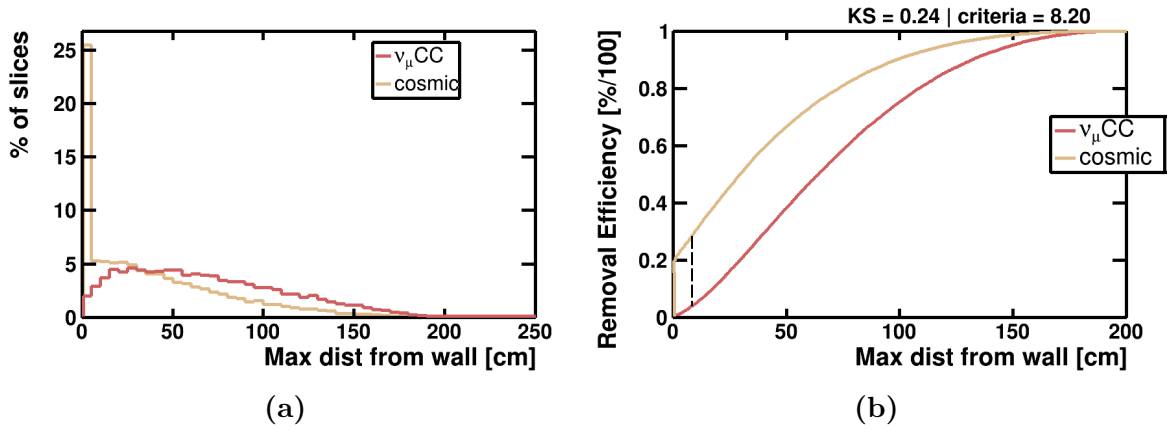
Figure 6.8: Near exiting particle cosmic ID. (a) Containment volume distributions defined as the maximum distance from the start or end of the track to the nearest TPC wall. (b) Signal and background removal dependence on the containment volume.

(a)   **(b)**
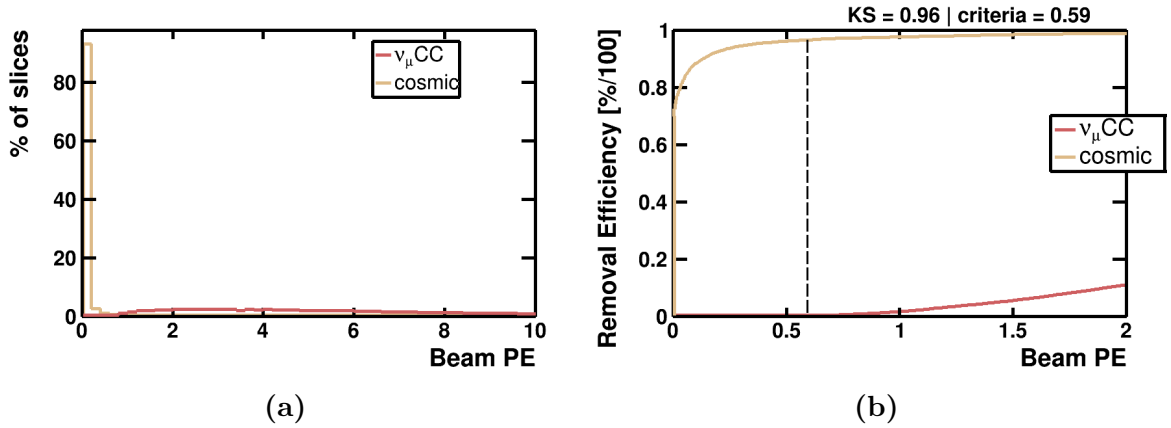
Figure 6.9: TPC beam flash cosmic ID. (a) Beam coincident PE distributions. (b) Signal and background removal dependence on the beam PE.

SBND is effectively made up of two nearly optically isolated TPCs they were triggered independently to reduce the cosmic background.

Figure 6.9 shows the reconstructed PE distributions for TPCs containing ν_μ CC interactions and for those containing only cosmic ray muons outside of the beam window. The percentage of cosmic interactions that were fully contained in a TPC where there was no activity in time with the beam was 43%. Events where the neutrino interaction products are in both TPCs do not contribute to the cosmic distribution.
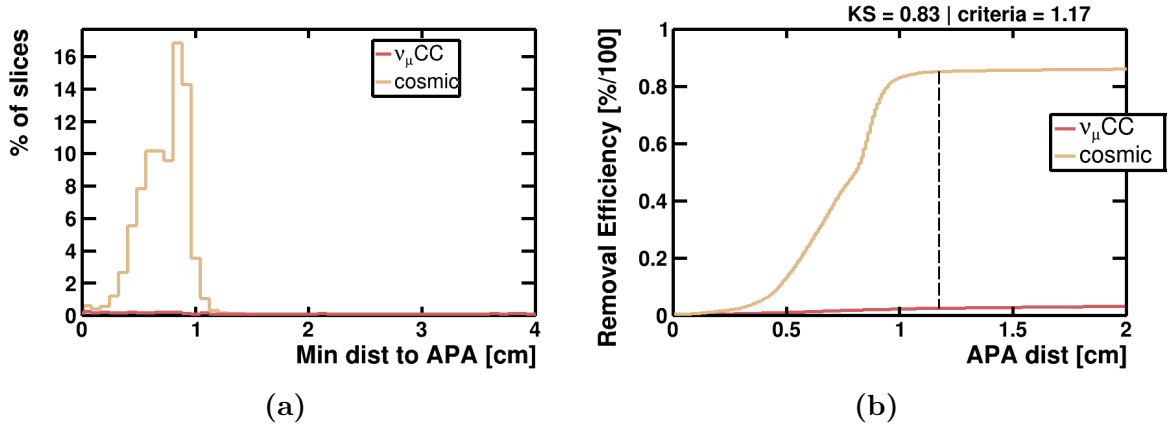
Figure 6.10: APA crossing cosmic ID. (a) Minimum distance to APA distributions. (b) Signal and background removal dependence on the minimum APA distance.

6.2.7   APA crossing

If particles enter through the APA outside of the beam window their reconstructed positions will be shifted away from the entry point. If reconstructed slices were shifted through the APA, Pandora would remove them automatically. If they were shifted into the TPC their true interaction times could be matched by minimising the distance to the APA using drift position corrections from PDS flash times.

The leading track in the slice was shifted by every flash time in the same TPC as the slice and the distance between the end of the track and the APA was calculated. If the minimum distance to the APA was below some limit, shown in Figure 6.10, then the track was matched to the flash time. If the time was outside of the beam window the track was tagged as a cosmic ray muon. 36% of ambiguous cosmic ray muons crossed at least one of the APAs.

The removal efficiency plateaus at 85% due to a combination of the optical flashes being below the reconstruction threshold and the end points of tracks being incorrectly reconstructed.

Table 6.1: Cosmic ID criteria values used in this analysis with the signal retention and background rejection for each individual criteria and the total shown. All cosmic ray muon slices not removed by Pandora were considered here, rather than just those matching the target topology.

Cosmic ID criteria	Value	Signal retained	Background rejected
Flash matching score	> 22.05	96.1%	89.2%
CRT hit matching DCA	< 19.50 cm	96.2%	38.8%
CRT track matching score	< 131.00	98.7%	40.4%
Stopping particle χ^2 ratio	> 1.42	96.0%	27.3%
Maximum start/end distance to wall	< 8.20 cm	96.1%	28.1%
TPC beam flash	< 0.59 PE	99.8%	39.6%
APA crossing distance	< 1.17 cm	97.5%	32.4%
Total	-	88.8%	98.7%

6.2.8 Combined identification performance

The cosmic identification criteria values used in this analysis are summarised in Table 6.1. As the majority of the criteria were designed to identify different topologies of cosmic ray muons, MVA techniques were not appropriate for combining criteria.

Cosmic ray muons may fit into more than one of these topological categories and so optimisation methods could be employed to find the combination of one dimensional criteria that maximise cosmic removal and minimise neutrino removal. It would be advisable to carefully calibrate each algorithm to data before optimisation using the tools developed here. The performance of the criteria chosen individually was sufficient for the inclusive analysis presented here.

The configurations of cosmic identification criteria in Table 6.1 were able to reject 99% of the cosmic ray slices not removed by Pandora and retain 89% of reconstructed ν_μ CC slices. Figure 6.11 shows the survival efficiency of the cosmic identification as a function of the reconstructed momentum and $\cos\theta$ of the longest track in a slice. The post cosmic identification kinematic distributions are shown in Figure 6.12. Figures 6.11 and 6.12 were created using all three samples.
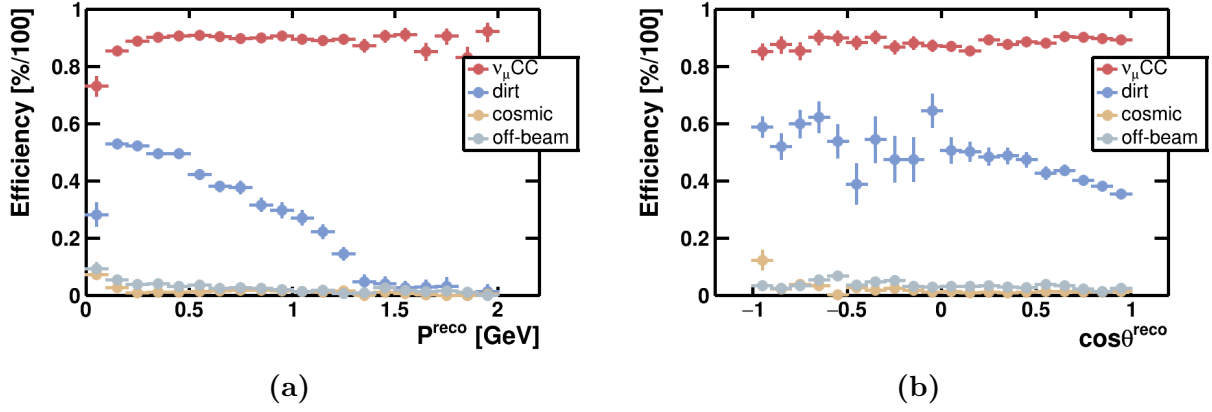
Figure 6.11: Percentage of ν_μ CC and backgrounds removed by cosmic ID as a function of reconstructed (a) P_μ and (b) $\cos\theta_\mu$.
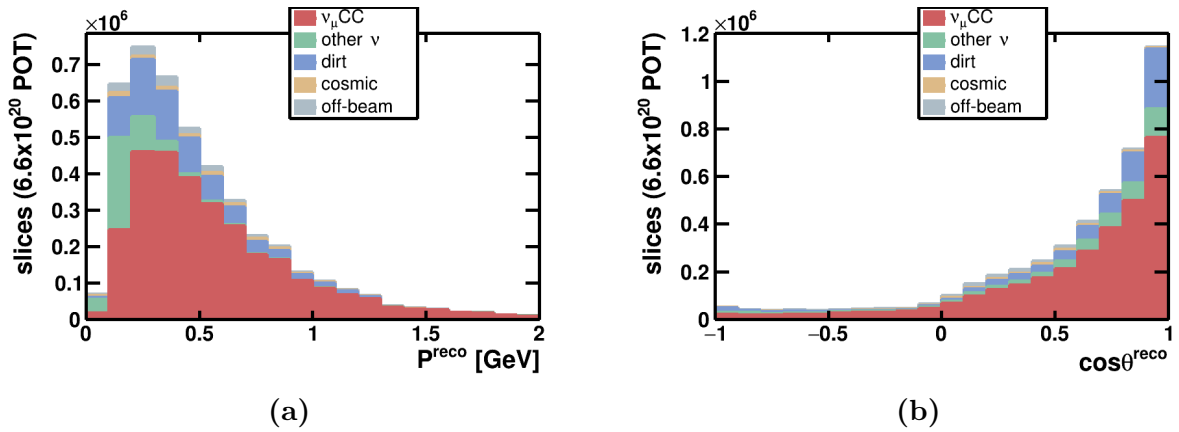
Figure 6.12: Reconstructed (a) P_μ and (b) $\cos\theta_\mu$ distributions for all reconstructed neutrino slices not removed by cosmic identification, scaled to $6.6{\times}10^{20}$ POT.

Table 6.2: External background TPC entry points showing the percentage of tracks entering each face and the mean distance travelled from that face (defined relative to the beam direction) into the TPC. Calculated for all Pandora reconstructed neutrino slices truth matched to either (a) cosmic ray muons or (b) dirt interactions. A left/right asymmetry is observed in the dirt entry points because the beam center is in the left TPC.

	(a) Cosmic ray muons			**(b)** Dirt	
Face	**% entering**	**Mean distance**		**% entering**	**Mean distance**
Top	64.7	134 cm		9.8	50.3 cm
Bottom	0	0 cm		9.7	49.1 cm
Front	8.31	77.2 cm		61.3	132 cm
Back	9.98	85.3 cm		1.19	22 cm
Left	8.33	50.6 cm		10.3	52.2 cm
Right	8.67	52.6 cm		7.79	50.6 cm

6.3 Fiducial volume

A fiducial volume in which the primary interaction vertex must be contained was defined for two main purposes. The first was to reject any cosmic or dirt (neutrinos outside of the active volume) particles which entered from outside of the TPC and were reconstructed with a vertex a short distance away from the edge of the active volume. Dirt particles reconstructed as neutrino interactions tended to be forward going and cosmic ray particles tended to be downward going, both types of external particles remaining after cosmic identification would often stop in the detector.

The expected proportions of dirt and cosmic particles entering each face of the TPC are shown in Table 6.2. The reductions in external backgrounds with vertex distance from the top and front faces are shown in Figure 6.13. A criteria of 20 cm from the top reduced the cosmic background by a further 20% and a criteria of 15 cm from the front face reduced the dirt background by 50%. It was determined that the optimum value from the other faces was around 10 cm.

The second purpose of a fiducial volume was to ensure the accurate reconstruction of kinematic variables. A required vertex distance of 50 cm from the back face was taken to ensure both the containment of most secondary particles, Figure 6.14, and the reliable reconstruction of momentum for exiting muon tracks using the MCS method. Boundaries
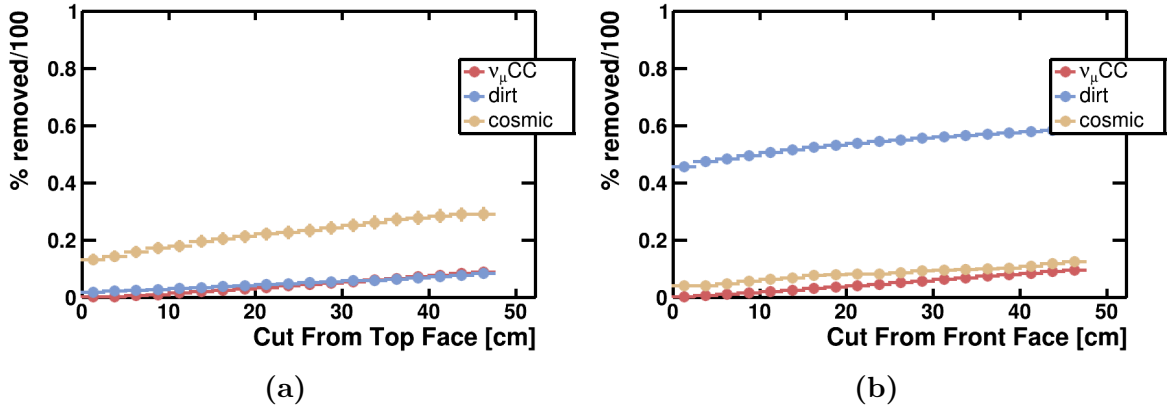
Figure 6.13: Reduction of post cosmic identification slices from different interactions with a fiducial volume requirement from (a) the top face and (b) the front face of the active volume.
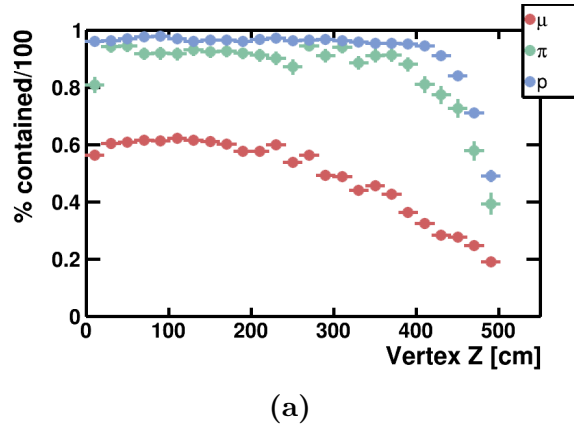
Figure 6.14: Track-like particle containment as a function of neutrino interaction vertex position in the beam coordinate.

were also applied to 5 cm either side of the cathode and 2.5 cm around the gap between the two APA frames on each side to avoid misreconstruction of the neutrino interaction vertex. The criteria around the edge of the detector were included to counter the potential, but not simulated, effects of space charge as field distortions are likely to be most pronounced near the active volume limits [147]. The total fiducial volume definition used in the analysis is shown in Figure 6.15.
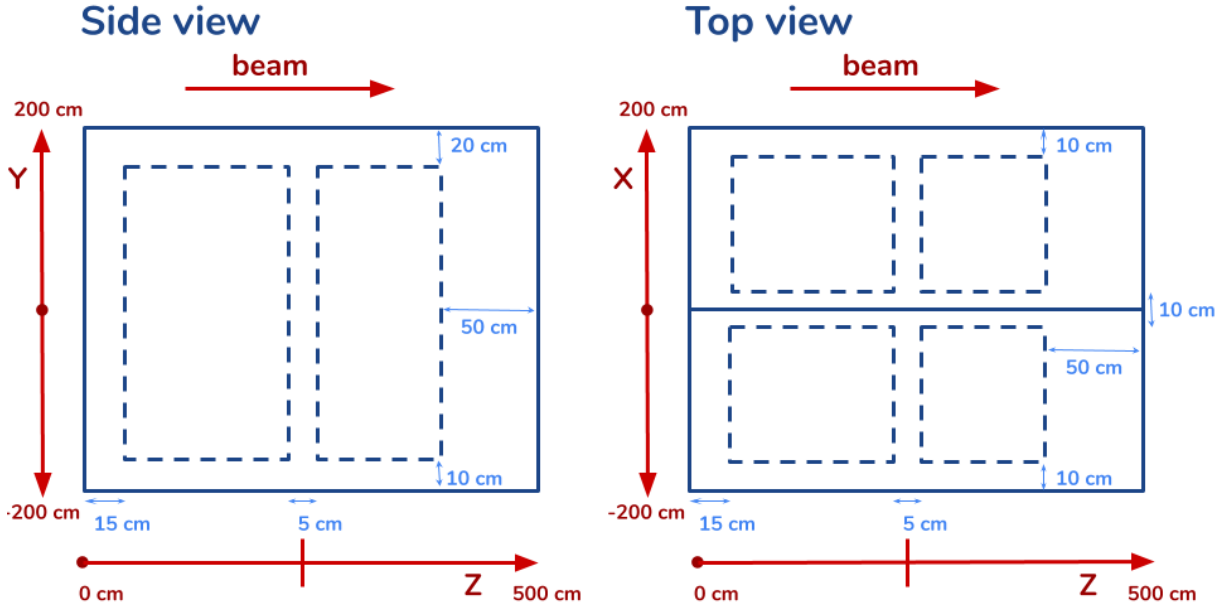
Figure 6.15: Fiducial volume definition used for the ν_μ CC inclusive selection.

6.4   Primary muon selection

The combination of unambiguous cosmic removal by Pandora, TPC + CRT + PDS cosmic identification and a fiducial volume requirement reduced the number of reconstructed slices with a cosmic ray origin by 99.96%. The same process reduced the number of dirt slices by 95.1%. This brings the expected TPC neutrino to external background ratio from 0.013:1 to 10.9:1, a point where the majority of the sample is composed of neutrino interactions in the TPC.

The next stage of the selection process is the identification of neutrino interactions with a muon originating from the primary vertex. The main backgrounds to this are ν_μ NC interactions with charged pions or protons which can look like muon tracks when they have momenta greater than a few 100 MeV. There will also be an intrinsic background from the $\bar{\nu}_\mu$ component of the beam as there is no sign selection capability in SBND.

The muon selection criteria were developed using a sample of neutrino interactions in the TPC with no external backgrounds. Due to the need to use calorimetry and topology for particle identification, one of the selection requirements was that only the muon track
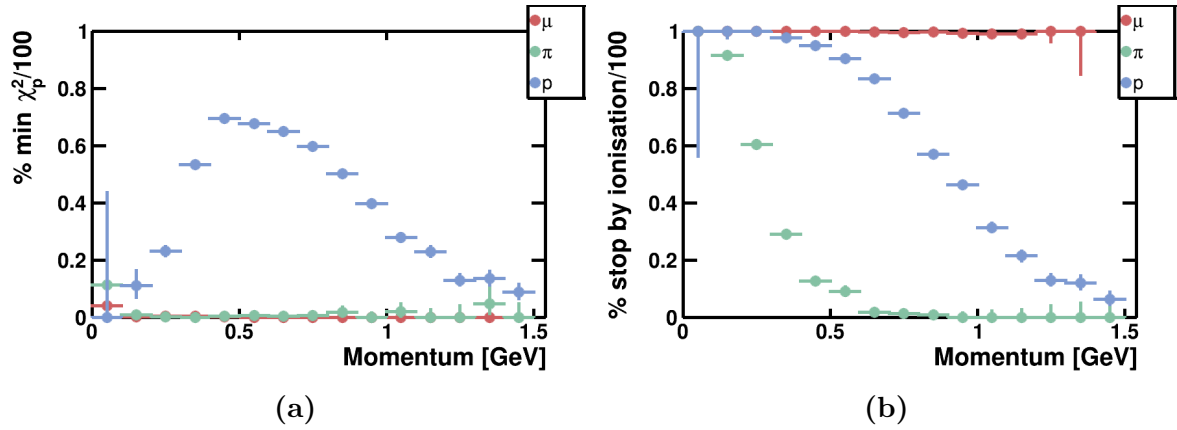
Figure 6.16: (a) The momentum dependence of track-like particles removed by a proton χ^2. (b) The percentage of track-like particles stopping through ionisation losses as a function of momentum.

may exit the active volume, so any slice with more than one exiting track was rejected. The criteria for calling a track contained was defined as 1.5 cm from the TPC border to account for potential distortions in the track reconstruction.

6.4.1   Proton rejection

When contained, 77% of protons from the primary interaction vertex stopped via ionisation processes and should provide a distinctive Bragg peak in dE/dx vs residual range. As demonstrated in Section 5.2.1, the χ^2 method is effective at separating protons from muons and charged pions. All tracks with a χ^2 consistent with the proton hypothesis were removed.

This removed 65% of all contained protons (0.7% of charged pions and 0.3% of muons) with a momentum dependence shown in Figure 6.16a. The majority of proton tracks that were not removed by this criteria were either too short for a reliable χ^2 calculation or did not stop through ionisation processes. The momentum dependence of particles stopping via ionisation losses is shown in Figure 6.16b.

6.4.2   Track length

A good separation of muons and charged pions is not possible using stopping curves alone due to their similar masses. The method outlined in the SBND proposal [11] for removing charged pions was to use the reconstructed track length as muons with similar momenta are likely to travel much further. As the range of a muon is directly related to its momentum [141], this criteria represents a lower threshold to the reconstructed muon momentum distribution. Therefore, the most minimal removed track length is desirable.

The track length distributions for contained particles surviving the proton χ^2 removal are shown in Figure 6.17. A minimum length of 25 cm was used, reducing the proton background by 60% and the pion background by 40%. All tracks longer than 100 cm were tagged as muons as this selected less than 10% of charged pions and 5% of protons while preserving around 60% of muons from subsequent criteria.

6.4.3   Scattering

Muons and charged pions should have different trajectories as charged pions will interact via the strong force as well as the EM force. The strong scattering tends to involve larger transfers of momentum leading to either large scattering angles which are reconstructed as separate tracks or the charged particle stopping and transferring its momentum to another hadron which may not visible to the detector.

Both of these processes give rise to short and fairly straight reconstructed tracks as the strong scatters often occur before the particle has lost enough momentum for EM scattering angles to become large. The apparent lower scattering angles of the pions and protons are therefore due to a reconstruction artefact. In reality, they have larger scattering angles but these large scatters are reconstructed as separate tracks to try to account for situations where the momentum is transferred between different charged hadrons.

This was parametrised by calculating the average DCA between the track points and a straight line through the start and end of the track, shown in Figure 6.18. The average of the scattering angles used in the MCS calculation [174] was also taken, shown in Figure

(a)

(b)

(c)
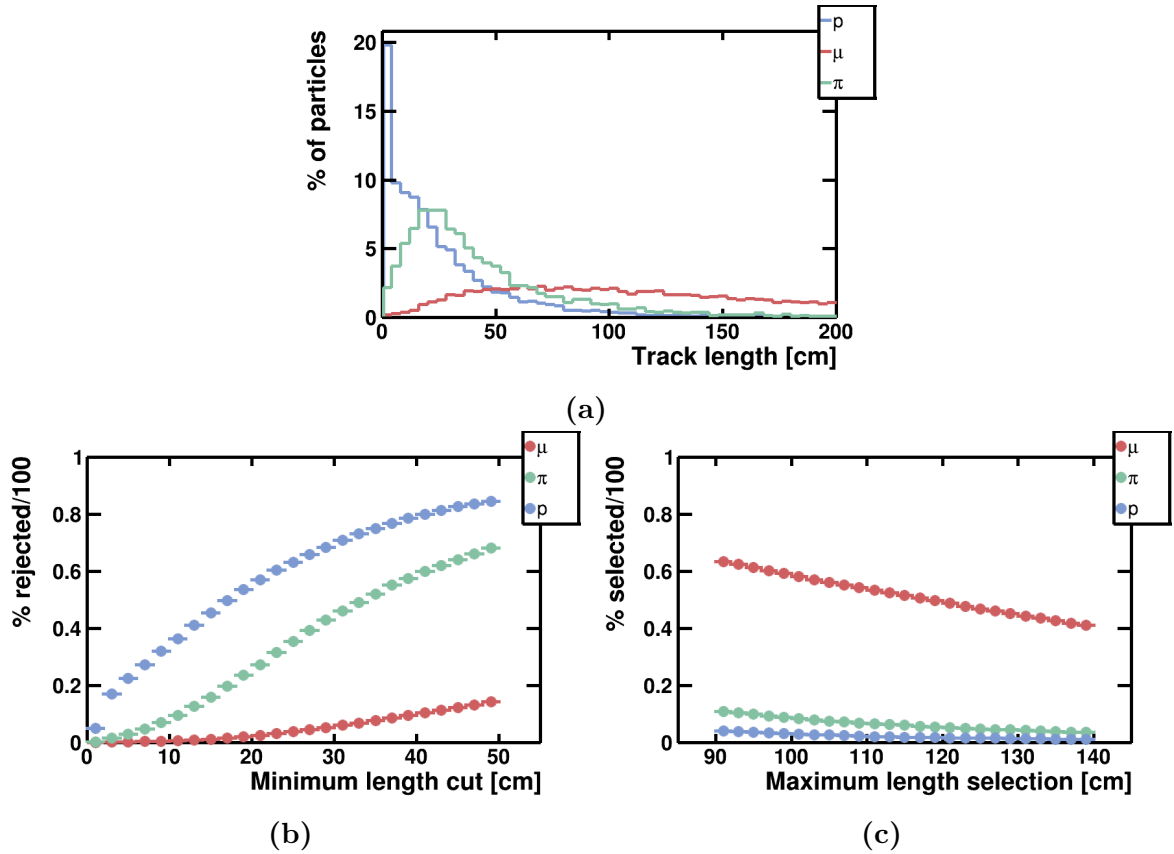
Figure 6.17: Reconstructed track length background rejection and signal selection. (a) Reconstructed track length distributions for muons, charged pions and protons. (b) Background rejection as a function of track length. (c) Signal selection as a function of track length. The lowest proton length bin in (a) is much higher than the others as these tracks are not removed by the χ^2 identification.
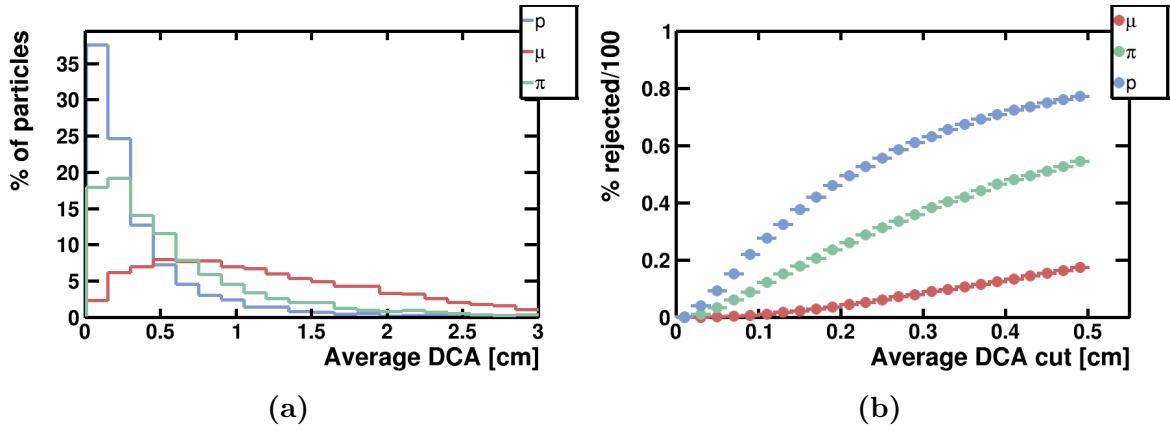
Figure 6.18: Muon identification by scattering DCA. (a) The average DCA between track points and a straight line between the start and end of the track. (b) Track-like particle rejection with DCA.
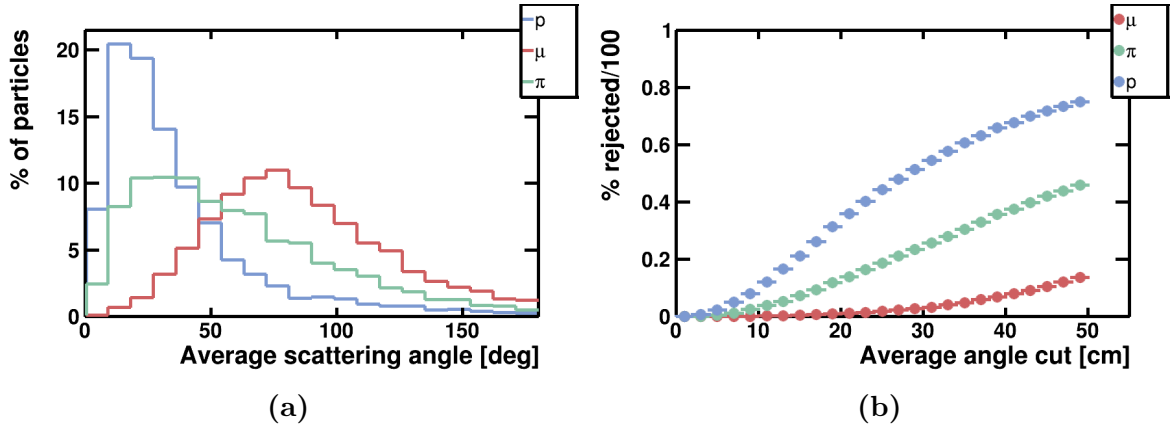
Figure 6.19: Muon identification by reconstructed scattering angle. (a) The average scattering angle used in the MCS momentum calculation. (b) Track-like particle rejection with average scattering angle. The hadronic scattering angles are smaller because the reconstruction breaks up large angle scatters into separate tracks.

6.19. Removal criteria of less than 0.2 average DCA and less than 30 degrees average scattering angle were chosen.

6.4.4 Non-stopping particles

Only around 44% of primary charged pions from BNB neutrino interactions are expected to stop via ionisation processes, compared to nearly 100% of muons. The stopping particle calculator described in Section 6.2 was used to take advantage of this property by determining if a contained track appears to stop. The χ^2 ratio values for charged pions
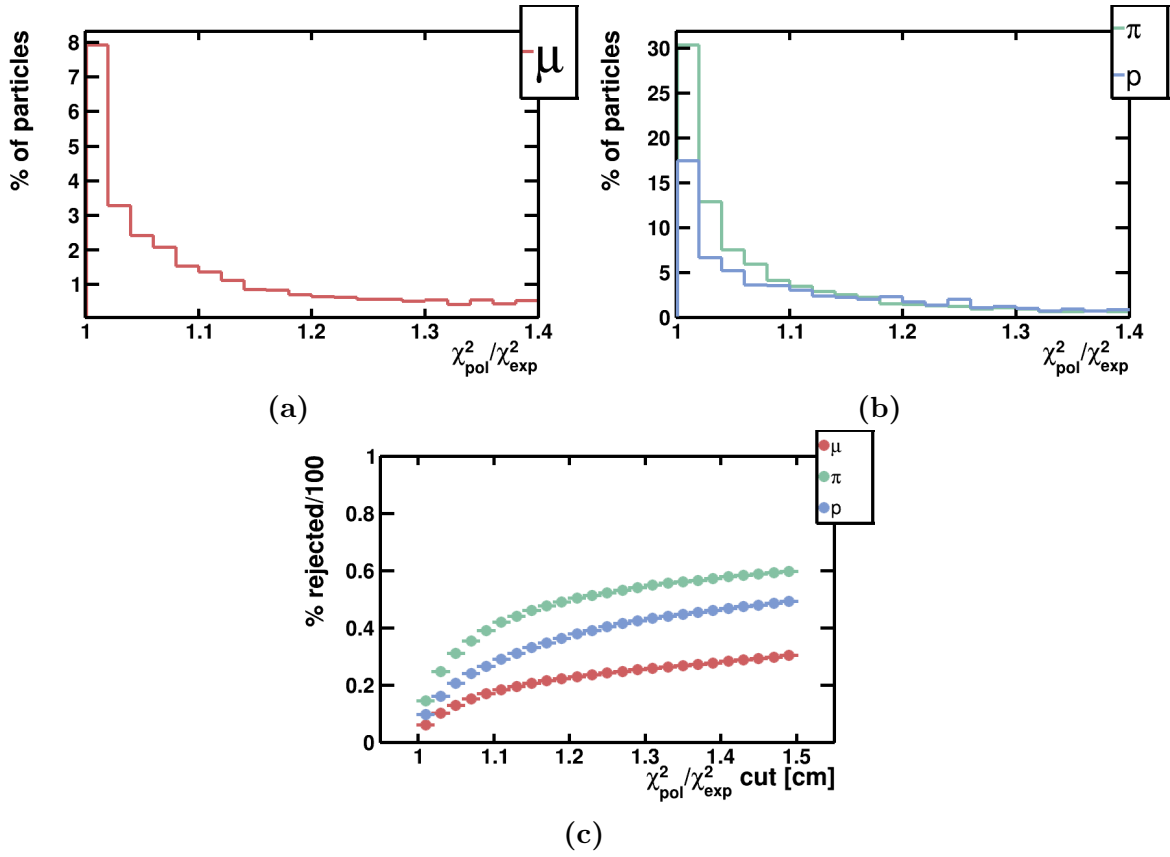
Figure 6.20: Muon identification by Bragg peak detection. (a) χ^2 ratio for stopping muons. (b) χ^2 ratio for charged pions and protons which do not stop. (c) Particle removal with stopping.

and protons which do not stop by ionisation and for muons which do are shown in Figure 6.20.

6.4.5   Reconstruction quality

It is possible to measure the momentum of contained muons using both the range and MCS methods. The bias and resolution of the MCS method have a signature dependence on the momentum of the track at short lengths. Therefore, while it isn't used for calculating the momentum of short tracks, the form of the dependence can be used to separate muons from charged pions and protons.

The range method is accurate and has little bias, and so it can be used as a good approximation for the true muon momentum. The range and MCS momentum, calculated

(a)

(b) Muons

(c) Pions

(d) Protons
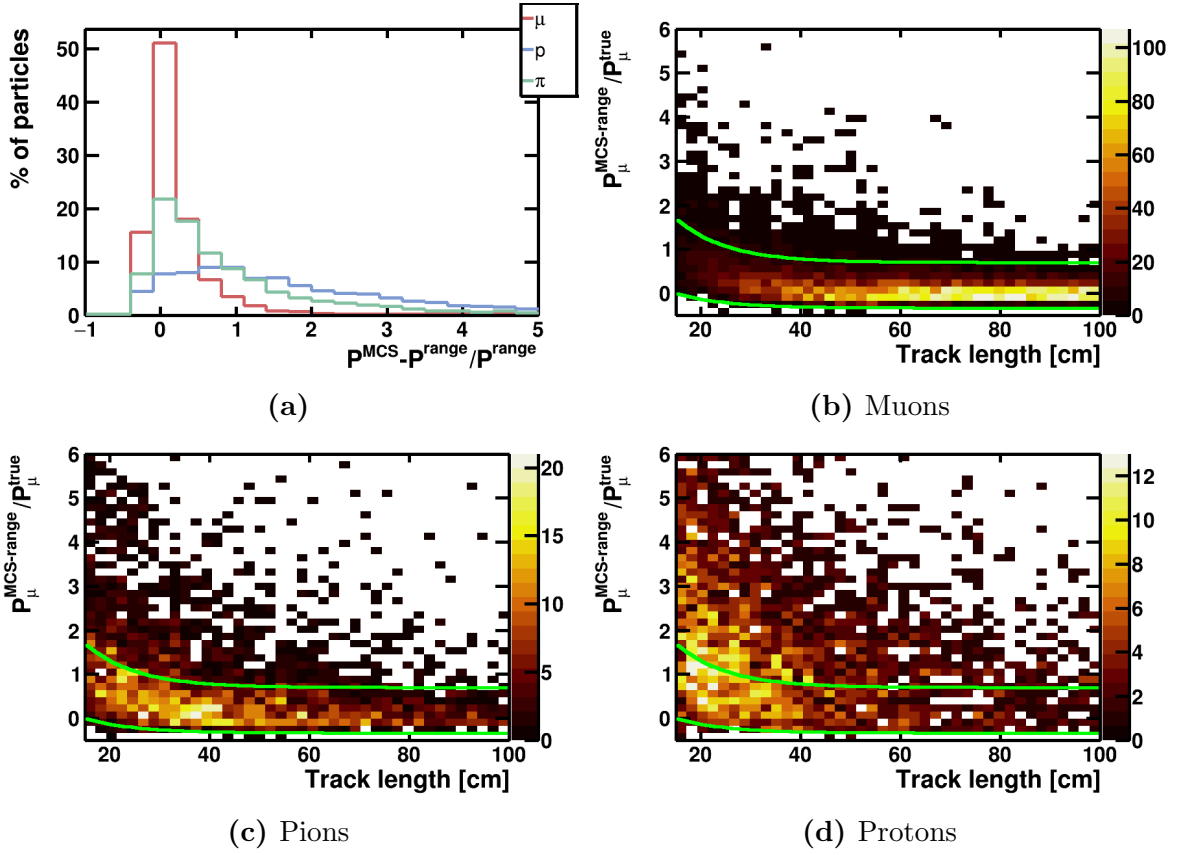
Figure 6.21: Muon identification by momentum reconstruction quality. (a) The fractional difference between MCS and range momenta calculated assuming particle is a muon for all track-like particles. (b), (c) and (d) The relationship between the fractional difference and the track length. The top green line indicates the exponential function of Equation 6.7 used to remove particles whose calculated momenta do not agree.

assuming particle is a muon, for other particles were less likely to agree, as can be seen in Figure 6.21. An exponential function of the form

$$\left(P^{MCS} - P^{range} \right) / P^{range} = A + \exp(-(L - B)/C) \tag{6.7}$$

was used to remove tracks based on the maximum fractional momentum difference as a function of track length, L. A, B and C were values determined from simulation as 0.5, 15, and 30 respectively.

Table 6.3: The number of contained muons, charged pions and protons remaining after selection criteria for a sample of neutrino interaction in the TPC with no external backgrounds. These figures are for a separate sample of BNB neutrino interactions in the TPC (1.06×10^{19} POT) and not scaled to 6.6×10^{20} POT.

	μ	π	p
Track in ν slice	44223	7014	31187
Contained	22004 (49.8%)	6069 (86.5%)	29033 (93.1%)
Individual criteria			
Proton ID	30 (0.136%)	36 (0.593%)	18504 (63.7%)
Low scattering	699 (3.18%)	2332 (38.4%)	20162 (69.4%)
No Stopping χ^2	2107 (9.58%)	2838 (46.8%)	7318 (25.2%)
< 25 cm	849 (3.86%)	2155 (35.5%)	17645 (60.8%)
Momentum quality	1181 (5.37%)	2782 (45.8%)	21970 (75.7%)
Combined			
Total removed	3232 (14.7%)	4258 (70.2%)	27549 (94.9%)

6.4.6   Contained muon selection

In the situation where all particle tracks reconstructed in a neutrino slice are contained, all of the criteria described above were applied to reject as much pion and proton background as possible. The effects of the different criteria on the numbers of primary particles from neutrino interactions in the active volume are summarised in Table 6.3.

Unlike for the cosmic identification, the application of MVAs would be appropriate here and would likely give a significant improvement in particle identification performance. The criteria here were sufficient for this inclusive analysis due to the relative abundance of muons and high external background rejection. When measuring exclusive channels, using these indicative features as input to an MVA should enhance the selection efficiency. Promising results were obtained using deep learning, by training a convolutional neural network on the reconstructed objects, but the studies were too preliminary to include in this analysis.
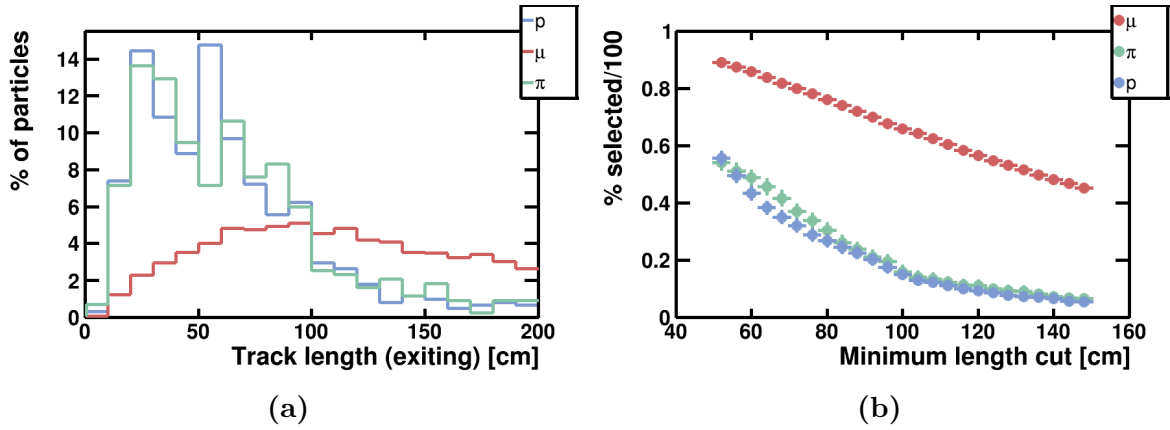
Figure 6.22: (a) Length of particles which exit the active volume and start in the fiducial volume. (b) The effect of a minimum length removal on the percentage of exiting particles selected.

Table 6.4: The number of exiting muons, charged pions and protons remaining after fiducial volume and minimum length requirements.

	μ	π	p
Track in ν slice	44223	7014	31187
Exit	22219 (50.2%)	945 (13.5%)	2154 (6.91%)
Exit (fiducial)	16376 (37%)	433 (6.17%)	609 (1.95%)
Length > 50 cm	14724 (89.9%)	243 (56.1%)	354 (58.1%)

6.4.7   Exiting muon selection

For cases where one track exits the TPC, the selection criteria for that track must be defined. The length distribution of particles starting inside the fiducial volume and exiting was studied in order to choose the minimum length that an exiting track must be to be called a muon, Figure 6.22.

As can be seen from Table 6.4, the relative numbers of charged pions and protons which start in the fiducial volume and exit the active volume are expected to be so low that their contribution does not warrant a selection criteria. The only selection consideration was then the quality of the muon track kinematic reconstruction. A minimum length of 50 cm was used to ensure that the fractional momentum resolution was better than 20%.

(a) **(b)**
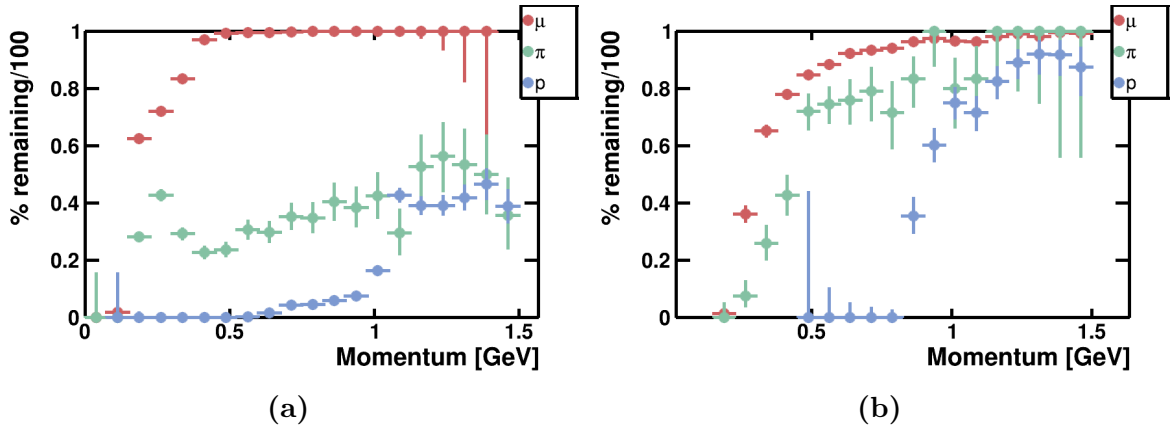
Figure 6.23: Track-like particle selection efficiencies for (a) contained and (b) exiting muon selection criteria as a function of true momentum. The efficiencies are defined for particles with an interaction vertex inside the fiducial volume.

6.4.8 Selection summary

The selection efficiencies for individual track-like particles from neutrino interactions are shown in Figure 6.23 as a function of true momentum for contained and exiting particles.

The overall process for selecting ν_μ CC slices after cosmic identification was as follows:

- Vertex contained in the fiducial volume:

    - -190 cm < X < -5 cm and 5 cm < X < 190 cm.

    - -190 cm < Y < 180 cm.

    - 15 cm < Z < 247.5 cm and 252.5 cm < Z < 450 cm.

- Don't apply criteria to any tracks longer than 100 cm.

- Reject any contained tracks which:

    - Have a χ^2 consistent with the proton hypothesis.

    - Do not have a stopping Bragg peak, defined as having a χ^2 ratio < 1.2.

    - Do not scatter like muons, average DCA < 0.2 or average MCS angle < 30 degrees.

    - Have $(P^{MCS} - P^{range})/P^{range}$ as a function of reconstructed length, L, above $0.5 + \exp(-(L-15)/30)$.

  – Are shorter than 25 cm.

- Count the number of escaping tracks.

- **Case 1:** All tracks contained.

  – Select longest non-rejected track as muon.

- **Case 2:** 1 track escapes.

  – If the escaping track is the longest track and has a length > 50 cm, select as muon.

  – Otherwise reject slice.

- **Case 3:** More than 1 track escapes.

  – Reject slice.

6.5   Selected distributions

The expected one dimensional rate distributions for the ν_μ CC inclusive selection are shown in Figure 6.24. As a fiducial volume was defined, true ν_μ CC interactions with a vertex outside of the fiducial volume were labelled as a background, as well as the intrinsic background from $\bar{\nu}_\mu$ CC. Distributions for the muon momentum, P_μ, and angle to the neutrino beam, $\cos\theta_\mu$, as used previously are shown along with other kinematic variables applicable to an inclusive measurement. These are:

- **Length**: The reconstructed length of the track selected as the muon.

- ϕ_μ: The angle of the muon track around the beam direction.

- **Visible energy (E_{vis})**: The energy of the muon track $\left(\sqrt{P_\mu^2 + m_\mu^2}\right)$ + the calorimetric energy of any other reconstructed track and shower objects associated to the neutrino slice.

- **Number of secondary tracks**: The number of track objects associated to the neutrino slice excluding the track identified as the muon.

- **Effective inelasticity**: $(E_{vis} - E_\mu)/E_{vis}$

6.6   Performance

To evaluate the performance of the selection the efficiency was defined as

$$E = \frac{N_{selected}^{\nu_\mu CC}}{N_{generated}^{\nu_\mu CC}} \tag{6.8}$$

where $N_{generated}^{\nu_\mu CC}$ is the number of simulated ν_μ CC interactions with a vertex in the fiducial volume and $N_{selected}^{\nu_\mu CC}$ is the number of those events reconstructed as neutrino slices and selected. The purity was defined as

$$P = \frac{N_{selected}^{\nu_\mu CC}}{N_{selected}^{all}} \tag{6.9}$$

where $N_{selected}^{all}$ is the total number of selected slices.

After reconstruction, cosmic background removal, fiducial volume and selection criteria the overall purity of the ν_μ CC sample was predicted to be 90% and the total efficiency for selecting events in the fiducial volume was predicted to be 67%. The efficiency and purity as a function of the muon momentum and $\cos\theta$ are shown in Figures 6.25 and 6.26.

For true ν_μ CC interactions in the selected sample the primary muon was correctly selected 96% of the time, as shown in Figure 6.27.

The efficiencies for keeping ν_μ CC events in the fiducial volume through the reconstruction and selection stages are given in Table 6.5. The total numbers of signal events relative to the backgrounds are given in Table 6.6.

(a)

(b)

(c)

(d)

(e)

(f)

(g)
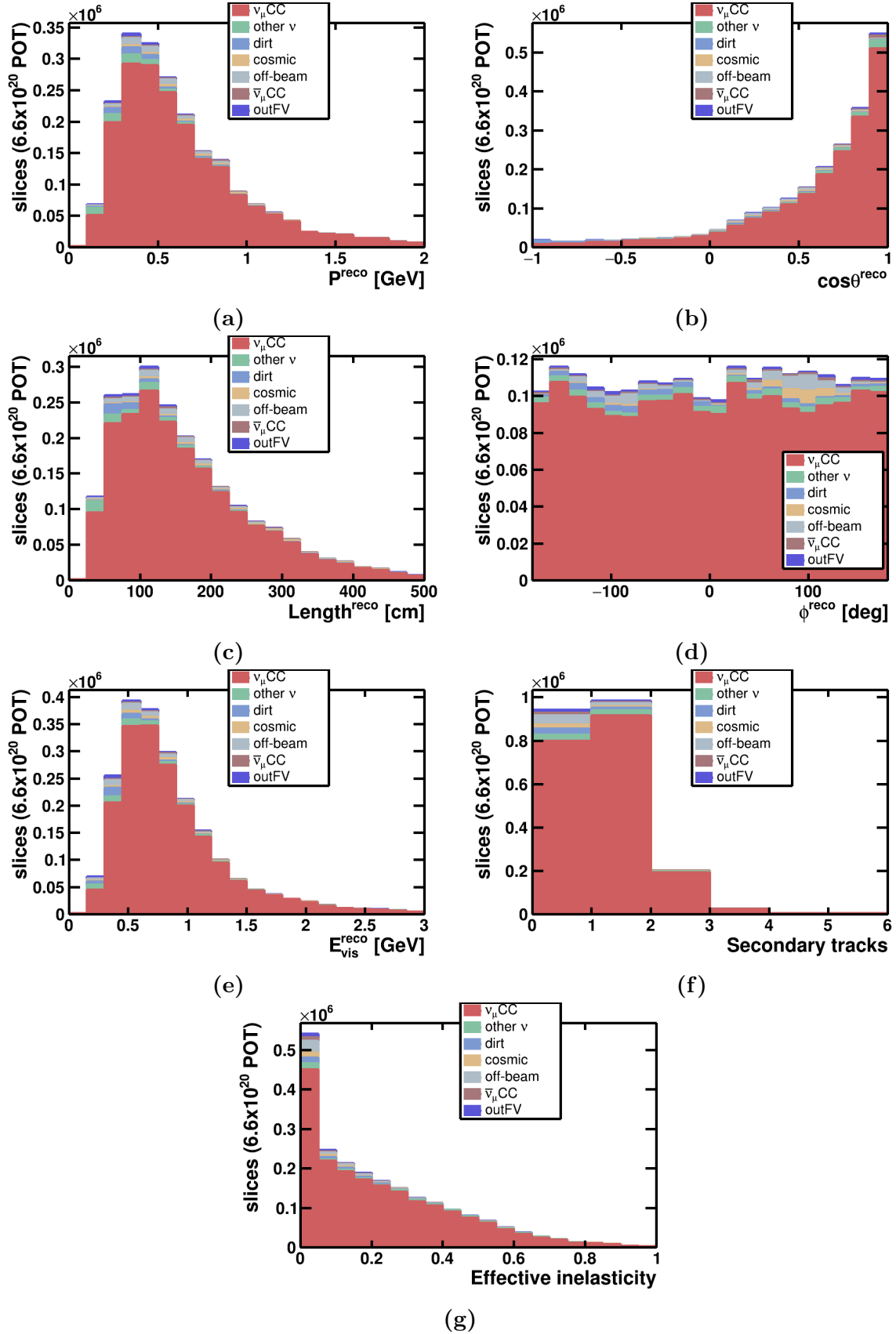
Figure 6.24: Selected ν_μ CC distributions scaled to 6.6×10^{20} for (a) muon momentum, (b) muon $\cos\theta$, (c) muon track length, (d) muon ϕ, (e) visible energy, (f) number of secondary tracks, and (g) effective inelasticity.

(a)

(b)

(c)
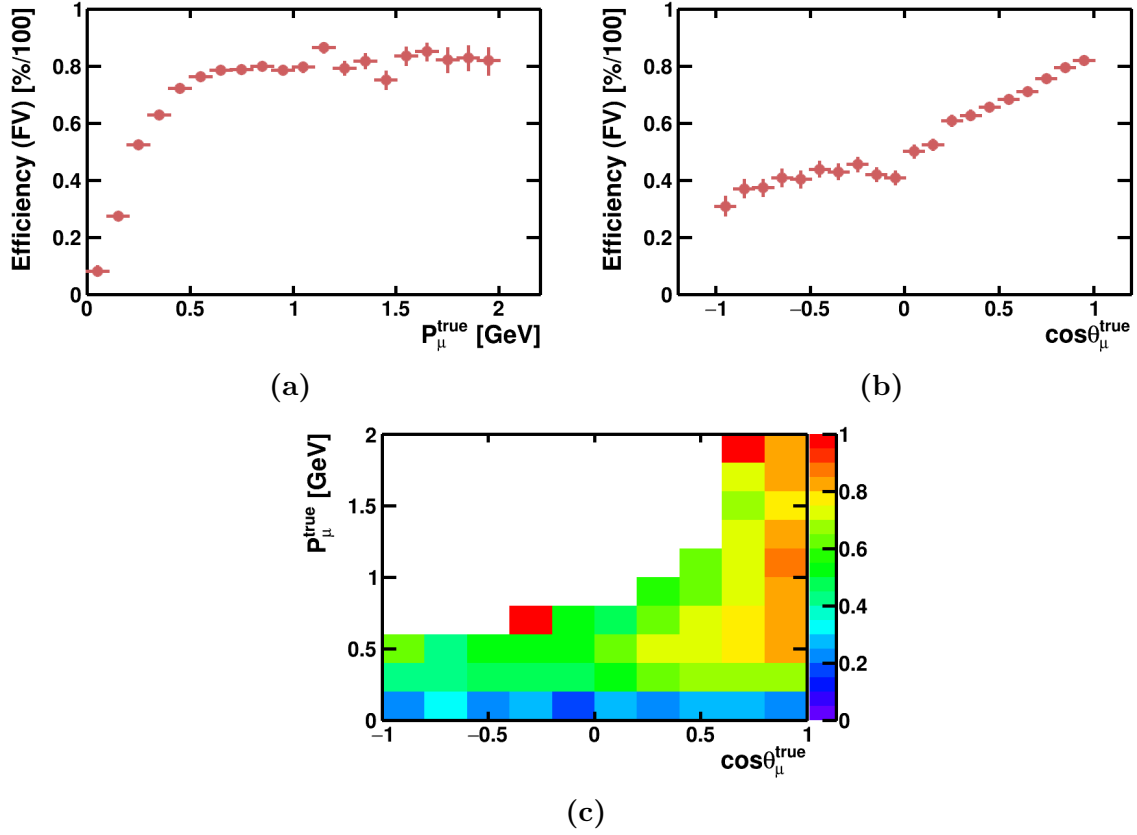
Figure 6.25: ν_μ CC selection efficiency as a function of true (a) P_μ, (b) $\cos\theta_\mu$ and (c) both. The efficiency drops off at low momentum because short tracks are often reconstructed as showers or not reconstructed.

(a)

(b)
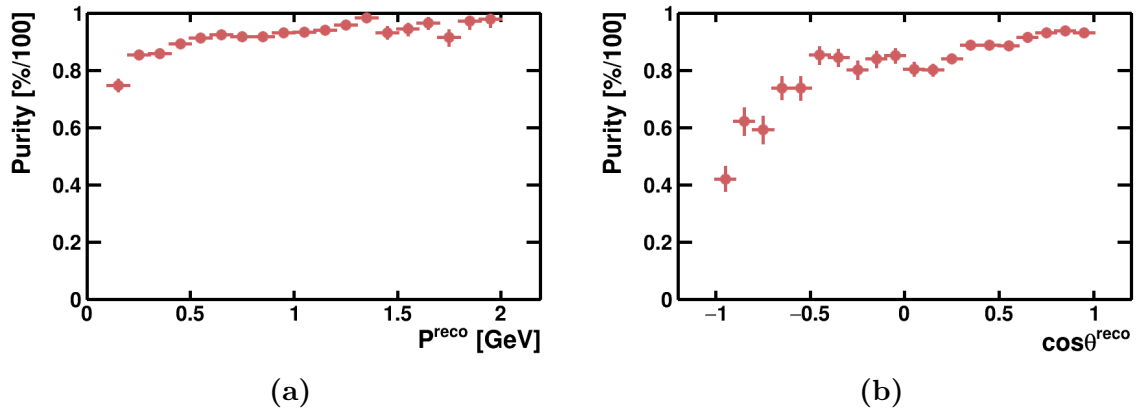
Figure 6.26: ν_μ CC selection purity as a function of reconstructed (a) P_μ and (b) $\cos\theta_\mu$.

(a)

(b)
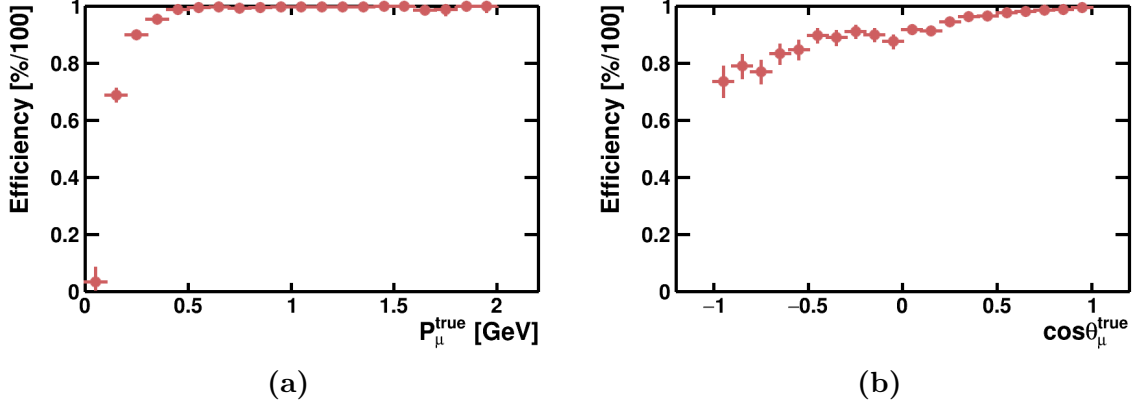
Figure 6.27: ν_μ CC muon selection efficiency as a function of reconstructed (a) P_μ and (b) $\cos\theta_\mu$.

Table 6.5: ν_μ CC efficiencies for interactions in the fiducial volume for all reconstruction and selection stages evaluated for the sample of neutrino events (5.27×10^{18} POT) without scaling.

Stage	Number of ν_μ CC	Efficiency (%)
Truth	24504	100
Pandora	22728	92.8
Cosmic ID	20903	85.3
Selection	16509	67.4

Table 6.6: Reconstruction and selection summary for ν_μ CC and the main sources of backgrounds evaluated for all samples and scaled to 6.6×10^{20} POT.

Stage	ν_μ CC	Other ν	Dirt	Cosmic	Off-beam
Pandora	3.41×10^6	5.24×10^5	1.81×10^6	7.44×10^6	5.12×10^6
Cosmic ID	3.03×10^6	4.55×10^5	7.31×10^5	9.33×10^4	1.59×10^5
Fiducial volume	2.37×10^6	3.66×10^5	9.5×10^4	5.34×10^4	1.03×10^5
Selection	1.93×10^6	5.82×10^4	4.07×10^4	2.88×10^4	5.66×10^4

Chapter 7

Cross section analysis

In this chapter, the sensitivity of SBND in measuring neutrino-argon cross sections will be explored based on the selection developed in the previous chapter. Section 7.1 describes the process of transforming measured rates to cross sections. Section 7.2 describes the implementation of a closure test on the fully simulated interactions in the detector, calculating the cross section and comparing it with Monte Carlo simulations from the same generator tune. Section 7.3 outlines a method of parametrising the reconstruction and selection in order to estimate the performance with a much larger sample. Section 7.4 evaluates the systematic uncertainties that would contribute to a measurement of the cross section. Section 7.6 explores how well SBND would perform in a comparison between different cross section models using the inclusive channel.

7.1   Rate to cross section

The total rate, N, measured by the detector can be transformed into a flux-integrated cross section using

$$\sigma = \frac{N - B}{\epsilon \cdot n_T \cdot \Phi} \tag{7.1}$$

where B is the expected number of background interactions selected, ϵ is the efficiency of selecting ν_μ CC interactions, n_T is the total number of target nucleons and Φ is the integrated flux.

The rate is directly measured by the detector and has no uncertainty, other than the statistical uncertainty associated with the probability of observing the same results given repeated measurements. The expected background, B, depends both on the flux and cross section model and the Φ is dependent on the flux model. ϵ must be estimated from simulations and so it is also dependent on the flux and cross section model as it is integrated over the kinematic variables. Many aspects of the flux and cross section model can affect the rate predictions in similar ways, making the interplay between all of these different effects highly non-trivial.

It will be possible to measure differential inclusive cross sections with low statistical uncertainty due to the expected rate of ν_μ interactions. The differential cross sections in true P_μ and $\cos\theta_\mu$ bins are given by

$$\left(\frac{d\sigma}{dP_\mu}\right)_i = \frac{\sum_j U_{ij}(N_j - B_j)}{\epsilon_i \cdot n_T \cdot \Phi \cdot (\Delta P_\mu)_i} \tag{7.2}$$

$$\left(\frac{d\sigma}{d\cos\theta_\mu}\right)_i = \frac{\sum_j U_{ij}(N_j - B_j)}{\epsilon_i \cdot n_T \cdot \Phi \cdot (\Delta\cos\theta_\mu)_i} \tag{7.3}$$

where $(\Delta P_\mu)_i$ and $(\Delta\cos\theta_\mu)_i$ are the bin widths, ϵ_i is the efficiency in bin i and U_{ij} is the unfolding matrix that transforms between reconstructed and true bins.

The double differential cross section follows a similar form,

$$\left(\frac{d^2\sigma}{dP_\mu d\cos\theta_\mu}\right)_i = \frac{\sum_j U_{ij}(N_j - B_j)}{\epsilon_i \cdot n_T \cdot \Phi \cdot (\Delta P_\mu)_i \cdot (\Delta\cos\theta_\mu)_i} \tag{7.4}$$

where i is now the linearised two dimensional P_μ and $\cos\theta_\mu$ bin and everything else has the same meaning.

7.1.1 Background subtraction

To obtain the rate of ν_μ CC events observed in the detector, the predicted rate of other neutrino, dirt and cosmic interactions must be subtracted. Simulations and control samples will be used to predict the expected rate of other neutrino and dirt interactions selected. Uncertainties in the flux normalisation and shape, the geometric models of the

detector and surroundings used in Geant4 and the cross section models will all contribute to systematic uncertainties in the prediction.

There will be statistical uncertainties on the prediction due to finite Monte Carlo statistics. These can be neglected by using a Monte Carlo simulation much larger than the expected rate and scaling down. There will, however, be statistical uncertainties associated with the true number of background events in the data that cannot be neglected.

The rate of cosmic ray muon interactions from in-time cosmic induced triggers will be estimated by taking data with a fake beam trigger. The full reconstruction and selection chain can be applied to the sample and then it can be scaled to the POT of the data sample, like the process used in Section 6.1.1.

The rate of cosmic interactions from neutrino induced triggers will be estimated by overlaying data taken without a beam trigger on simulated neutrino events and then running the reconstruction and selection on these hybrid events. It is possible that systematic uncertainties will occur due to differences in run conditions between taking cosmic and neutrino data but they are difficult to estimate without data. As with the neutrino and dirt background, there will be statistical uncertainties associated with the rate of cosmic interactions in the data.

7.1.2 Normalisation

The selection efficiency can be estimated by

$$\epsilon = \frac{N^{selected}}{N^{simulated}} \tag{7.5}$$

where $N^{simulated}$ is the number of ν_μ CC interactions simulated in the fiducial volume and $N^{selected}$ is the number of these interactions selected. The ϵ_i in Equations 7.2, 7.3 and 7.4 refer to the specific kinematic bin i that the interaction is generated in.

The number of target nucleons is given by

$$n_T = \frac{N_A \cdot \rho_{Ar} \cdot V_{Ar} \cdot n_N}{M_N} \tag{7.6}$$
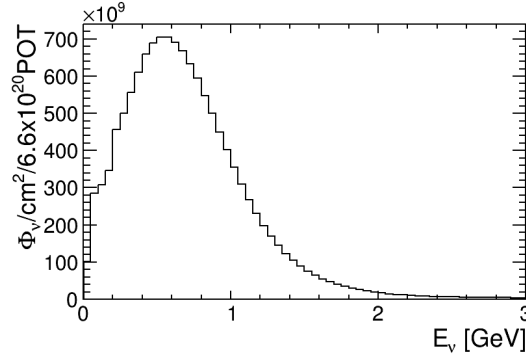
Figure 7.1: The BNB muon neutrino flux prediction at SBND as a function of neutrino energy. This distribution was integrated over all energies to give the total neutrino flux at full exposure.

where N_A is the Avogadro number, ρ_{Ar} is the density of argon at 88 K [138], V_{Ar} is the volume of argon contained in the fiducial volume, n_N is the average number of nucleons per argon nucleus and M_N is the mass of one mole of argon [138]. For the fiducial volume given in Section 6.3, n_T is estimated to be

$$n_T = \frac{6.022 \times 10^{23} [Ar/mol] \cdot 1.3973 [g/cm^3] \cdot 5.89 \times 10^7 [cm^3] \cdot 40 [N/Ar]}{39.95 [g/mol]} = 4.96 \times 10^{31}.$$

The integrated flux of muon neutrinos, Φ, is estimated by multiplying the number of POT by the integrated neutrino flux distribution calculated from beam simulations [105], Figure 7.1. The integrated ν_μ flux for 6.6×10^{20} POT is predicted to be 1.30×10^{13} cm^{-2}.

7.1.3 Unfolding and folding

The expected rate histogram $\boldsymbol{\nu}$ can be written in terms of the true histogram $\boldsymbol{\mu}$,

$$\boldsymbol{\nu} = \mathbf{R} \cdot \boldsymbol{\mu} + \boldsymbol{\beta} \tag{7.7}$$

where β is the expected background and $\mathbf{R} = R_{ij}$ is the response matrix, the probability to observe an event in bin i given that it was generated in bin j. The response matrix can be estimated from simulations and the unfolding matrix, U_{ij}, is given by inverting this response matrix.

The measured rate, $\mathbf{N}$, can be used as an estimator for the expected rate and the true rate can be estimated with

$$\hat{\boldsymbol{\mu}} = \mathbf{R}^{-1}(\mathbf{N} - \boldsymbol{\beta}) = \mathbf{U}(\mathbf{N} - \boldsymbol{\beta}). \tag{7.8}$$

This is the same as the result that would be obtained by maximising the log-likelihood function for Poisson data or from the least squares solution [167].

Matrix inversion using a maximum likelihood estimator can introduce large variance in the unfolded spectrum because statistical fluctuations in the data can be misinterpreted as fine structure in the true distribution [167]. Correction factors or regularisation methods are required to reduce the variance, but these introduce a bias [167]. There are several methods of regularised unfolding commonly used in particle physics, for example [178–180].

Given that the primary use of the measured cross section data in SBND will be to improve theoretical cross section models there is no firm requirement for the data to be unfolded. If the response matrix is provided with the data, a theoretical prediction can be folded into reconstructed kinematic variable space. It is then easier to construct a test statistic and test the model hypothesis without having to account for the additional bias and variance introduced by unfolding [167].

Folding allows us to drop the unfolding matrix U_{ij} in Equations 7.2, 7.3 and 7.4. In order to preserve the overall normalisation of the differential cross sections the efficiency must be modified to become a function of the reconstructed bins,

$$\epsilon_i \to \zeta_i = \frac{\sum_j R_{ij} N_j^{selected}}{\sum_j R_{ij} N_j^{true}} \tag{7.9}$$

where the N have the same meanings as in Equation 7.5 and the response matrix, R_{ij} is calculated for all reconstructed events. The folded single and double differential cross sections become

$$\left(\frac{d\sigma}{dP_\mu^{reco}}\right)_i = \frac{N_i - B_i}{\zeta_i \cdot n_T \cdot \Phi \cdot (\Delta P_\mu^{reco})_i}, \tag{7.10}$$

$$\left(\frac{d\sigma}{d\cos\theta_\mu^{reco}}\right)_i = \frac{N_i - B_i}{\zeta_i \cdot n_T \cdot \Phi \cdot (\Delta\cos\theta_\mu^{reco})_i}, \tag{7.11}$$

$$\left(\frac{d^2\sigma}{dP_\mu^{reco}d\cos\theta_\mu^{reco}}\right)_i = \frac{N_i - B_i}{\zeta_i \cdot n_T \cdot \Phi \cdot (\Delta P_\mu^{reco})_i \cdot (\Delta\cos\theta_\mu^{reco})_i}. \tag{7.12}$$

It is expected that SBND will publish its cross section results in both folded and unfolded forms to maximise the usefulness of the data in comparing to past data and future models. As the goal of this analysis is to estimate the model testing capabilities of SBND, the folded cross sections will be calculated. This is because the model separation power is usually better in reconstructed space [181].

7.2   Closure test

It is important that the analysis method can reliably reproduce the cross section models input to the simulation. To test this, the fully simulated and reconstructed events were used as fake data and the folded cross section was calculated. An independent sample using the same generator configuration was then folded with the calculated response matrix and compared with the fake data. A hypothesis test was then performed to determine whether the fake data and model are consistent with one another.

As the fake data was a Monte Carlo simulation, the background subtraction is trivial. The systematic uncertainties involved when the backgrounds are not known exactly are discussed in Section 7.4. All plots shown here are for events matched to true ν_μ CC interactions in the fiducial volume defined in Section 6.3.

The fully reconstructed statistics were relatively low compared to the expected exposure, so only single differential cross sections were calculated. The binning was chosen to reduce the statistical uncertainties in each bin and will not be the same binning used for the full SBND data sample, this is explored further in Section 7.3. The binning was chosen such that the statistical uncertainty on each bin was less than 3% to reduce statistical fluctuations and provide a better visual estimation of closure. The choices of binning for

(a)   **(b)**
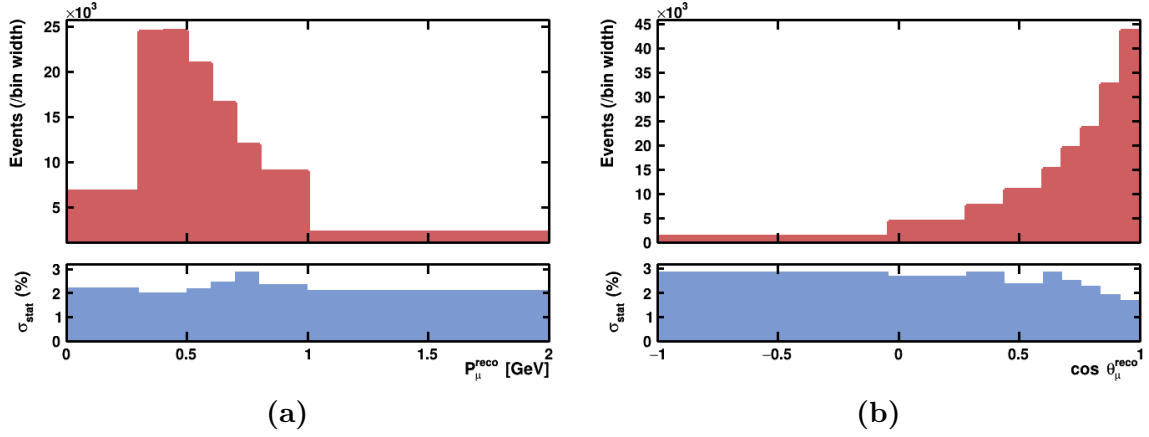
Figure 7.2: The bin definitions for the one dimensional distributions in (a) P_μ and (b) $\cos\theta_\mu$ for the fully reconstructed simulations with the percentage statistical uncertainty shown.

P_μ and $\cos\theta_\mu$ are shown in Figure 7.2 and the bin edges were

$$P_\mu = [0,\ 0.3,\ 0.4,\ 0.5,\ 0.6,\ 0.7,\ 0.8,\ 1,\ 2],$$

$$\cos\theta_\mu = [-1,\ -0.04,\ 0.28,\ 0.44,\ 0.6,\ 0.68,\ 0.76,\ 0.84,\ 0.92,\ 1].$$

The response matrix is defined by

$$R_{ij} = P(\text{observed in bin i}|\text{generated in bin j}) = \frac{P(\text{observed in i} \cap \text{generated in j})}{P(\text{generated in j})} \tag{7.13}$$

where the P are probabilities that must be estimated using simulations. If unfolding is not being performed the truth binning does not have to be the same as the reconstructed binning, and in an ideal case would be binned in a way that minimises model dependencies [182].

In the interest of simplicity for the closure test, symmetric response matrices were used. The response matrix can be estimated by

$$R_{ij} = \frac{N_{ij}^{reco}}{N_j^{true}} \tag{7.14}$$

where N_{ij}^{reco} is the number of events reconstructed in bin i and generated in bin j and N_j^{true}

(a)   (b)
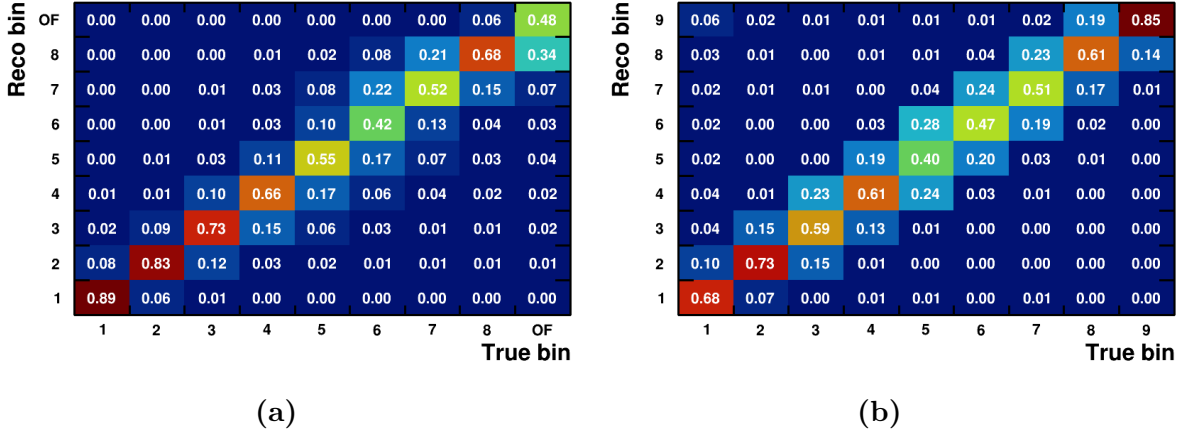
Figure 7.3: Symmetric response matrices for (a) P_μ and (b) $\cos\theta_\mu$. They are defined only for selected events so each true column adds to unity.

(a)   (b)
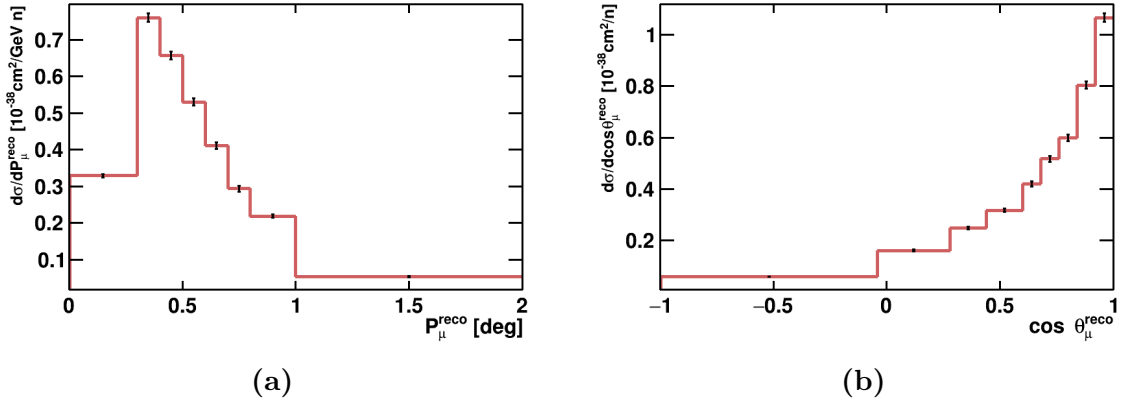
Figure 7.4: Folded differential ν_μ CC inclusive cross sections in (a) P_μ and (b) $\cos\theta_\mu$ with statistical uncertainties for $5.27{\times}10^{18}$ POT shown.

is the number of events generated in bin j. The response matrices were only calculated for selected events as the selection efficiencies were corrected for when calculating the cross sections, the truth columns are therefore normalised to unity. The response matrices for P_μ and $\cos\theta_\mu$ are shown in Figure 7.3.

The bin efficiencies were estimated using the fake data and Equation 7.9. The number of targets, Equation 7.6, was the same as for the full analysis as the fiducial volume definition was the same. The integrated flux was scaled to the simulated POT of $5.27{\times}10^{18}$, giving $\Phi = 1.04{\times}10^{11}$ cm^{-2}. The folded differential cross sections obtained from the fake data are shown in Figure 7.4 with statistical uncertainties.

This is the general process that would be undertaken with data, but the Monte Carlo
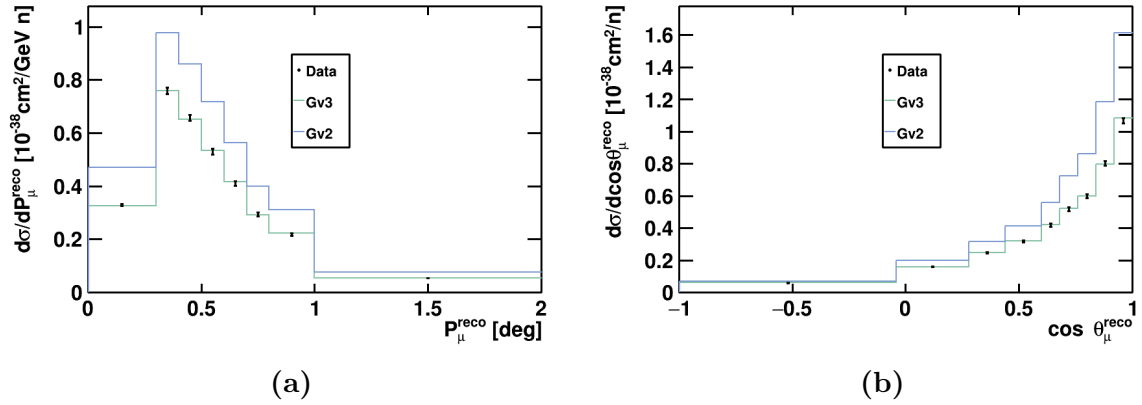
Figure 7.5: Fake data differential cross sections in (a) P_μ and (b) $\cos\theta_\mu$ with alternative model overlays. **Gv3:** GENIE v3.0.6 G18.10a.02.11a:k250:e1000. **Gv2:** GENIE v2.12.10 DefaultPlusMECWithNC.

sample would be much larger to reduce the statistical uncertainties in the response matrix, efficiency and background predictions which are of the same order as the uncertainties on the cross section predictions. In order to then compare cross section models, Monte Carlo generators will be used to predict differential cross sections in true kinematic variables using the predicted flux and detector model. The response matrices will applied to the predictions to map the true variables to reconstructed bins.

Figure 7.5 shows the fake data cross section with two folded cross section models overlaid, one corresponding to the GENIE version 3.0.6 model configuration used to generate the data, Gv3, and one corresponding to a different configuration of models in GENIE version 2.12.10, Gv2 [91]. The model configurations for GENIE v3 can be found in Table 5.1 and the model configurations for GENIE v2 are discussed later in Table 7.9.

The consistency of the fully reconstructed simulations with the folded predictions can be tested with a χ^2 statistic, assuming only statistical uncertainties,

$$\chi^2 = \sum_i^N \left(\frac{d_i - \mu_i}{\sigma_i} \right)^2 \tag{7.15}$$

where d_i is the measured cross section in bin i, μ_i is the model prediction and σ_i is the associated statistical uncertainty. The $\chi^2/ndof \approx 1$ is a commonly used metric for the goodness-of-fit but is a little obscure when examining the compatibility of a hypothesis with data.
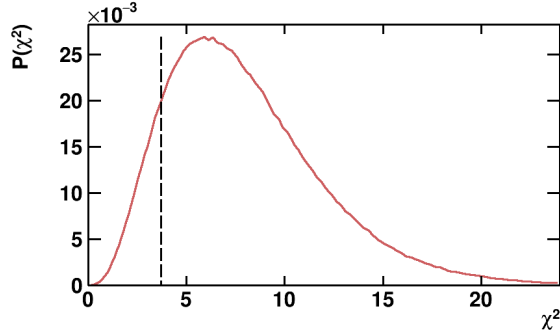
Figure 7.6: The expected χ^2 distribution for the ν_μ CC inclusive differential cross section in momentum with the measured universe shown as the black dashed line.

Table 7.1: P values from χ^2 test for closure test comparisons between GENIE model configurations. GENIE version 3 (Gv3) was used to generate the fake data.

	$\boldsymbol{\chi^2}$	$\boldsymbol{ndof}$	$\boldsymbol{p}$ **value**
Gv3: P_μ	3.71	7	0.88
Gv3: $\cos\theta_\mu$	3.18	8	0.96
Gv2: P_μ	3270.85	7	0
Gv2: $\cos\theta_\mu$	3543.26	8	0

The quantity in Equation 7.15 is a function of the Gaussian distributed random variable d_i and is itself a random variable with an underlying χ^2 distribution with an expectation value equal to the number of degrees of freedom [167]. It is therefore possible to ask what the probability of obtaining an experimental χ^2 result more extreme than (further into the tail of the distribution) or equal to the measured value, called the p value [167]. This can be calculated either analytically or through Monte Carlo simulations.

The GENIE v3 p value calculation for the differential cross section in momentum is shown in Figure 7.6. The results of the χ^2 test for both models are given in Table 7.1. When only statistical uncertainties are included, the fake data is consistent with the model used to generate it and there appear to be no significant errors or biases in the analysis method.
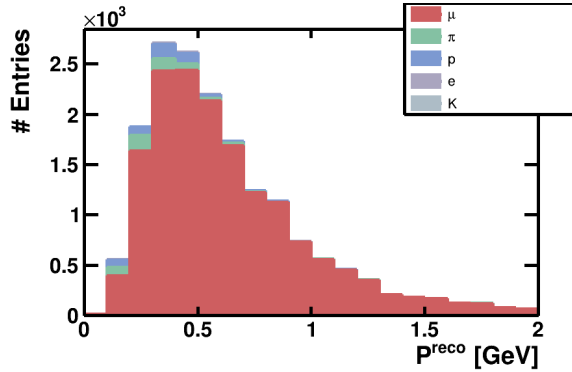
Figure 7.7: The types of particles selected as the primary muon in ν_μ CC inclusive interactions from neutrino interactions inside the active volume.

7.3   Expected rate at full exposure

The closure test in the previous section is a useful method of identifying errors in the analysis process but it is not representative of the true capabilities of SBND as the samples used were statistically limited. Taking this small sample and scaling up to the expected POT would magnify statistical fluctuations to an unacceptable level. It was, however, possible to avoid the computing and storage constraints by only simulating the initial neutrino interactions and the subsequent trajectories of the particles in the detector, allowing for much higher statistics. A model of the detector response, reconstruction and selection was then used to transform to reconstructed space.

7.3.1   Track-like particle reconstruction

The smaller sample of fully simulated and reconstructed events was used to parametrise the reconstruction and selection performance in terms of individual particles in a way that was designed to minimise model dependencies. The simplicity of the ν_μ CC inclusive interaction topology makes this parametrisation method viable as only track-like particles have a non-negligible contribution to the selected muon distribution, as can be seen in Figure 7.7.

Figure 7.8 shows that there is no strong dependence of the reconstruction and cosmic identification efficiency on the true track multiplicity of the event. This motivated the
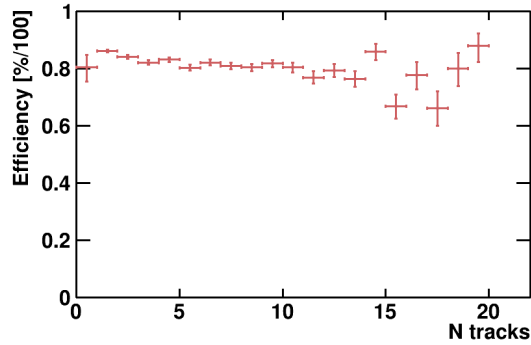
Figure 7.8: The reconstruction efficiency as a function of the true particle multiplicity for true ν_μ CC events. The multiplicity was defined as the number of track-like particles, excluding the muon, with an energy greater than 10 MeV.

assumption that the track-like particles in neutrino interactions can be treated independently when parametrising the reconstruction, greatly reducing the amount of phase space that needed to be covered.

The reconstruction was parametrised in terms of the contained length and the angle to the beam as the efficiency had the strongest dependency on these kinematic variables and there were insufficient statistics for three dimensional binning. Figure 7.9 shows the binning used for each particle type. The efficiency was applied to the particle trajectories by determining the contained length and angle, retrieving the binned efficiency, and reconstructing the particle if a random number was below this efficiency.

7.3.2 Cosmic identification

Only a small proportion of the neutrino interactions that passed both fiducial volume and muon selection criteria were removed by cosmic identification. Figure 7.10 shows that there was only a slight kinematic dependence for either ν_μ CC and other types of neutrino events. A flat 10% inefficiency for ν_μ CC and a 15% inefficiency for other neutrino interactions was applied.

(a) Muons

(b) Pions

(c) Protons
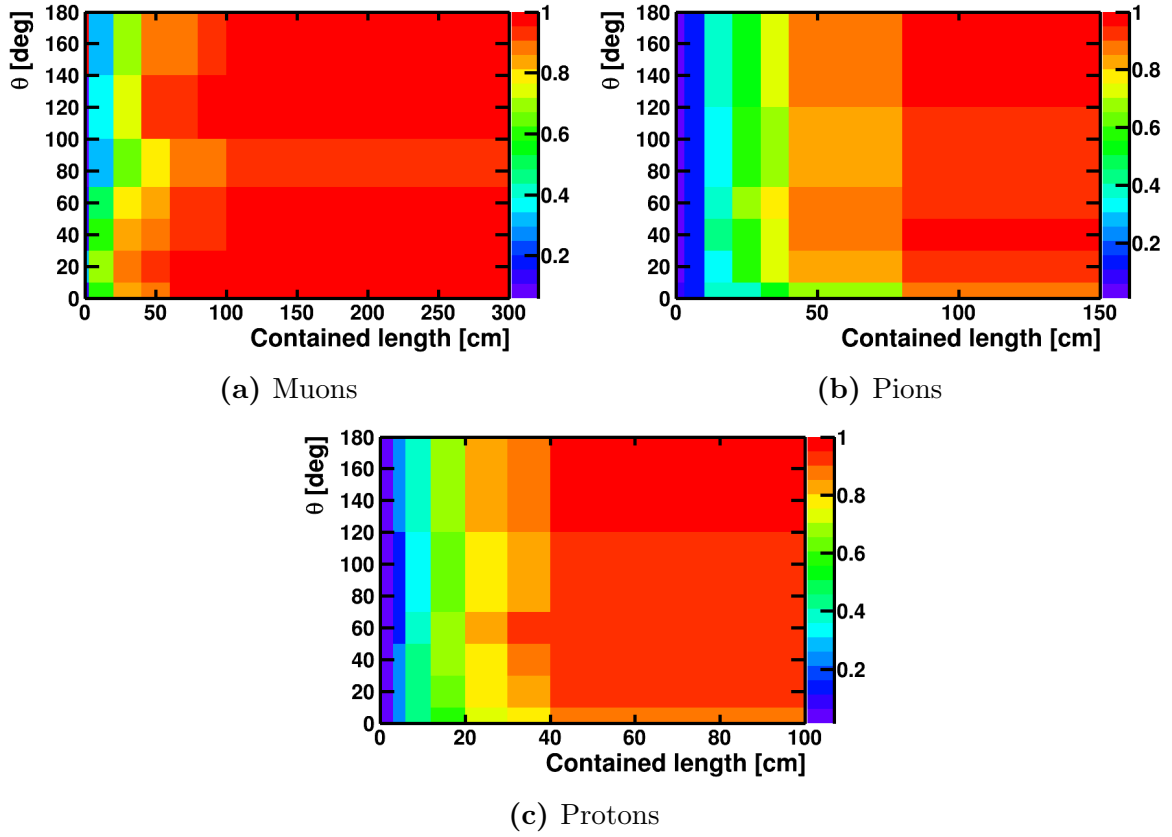
Figure 7.9: The reconstruction efficiency (%/100) for track-like particles binned in contained length and θ. The efficiency in the length overflow bins was assumed to be 100%.

(a) ν_μCC

(b) Other ν
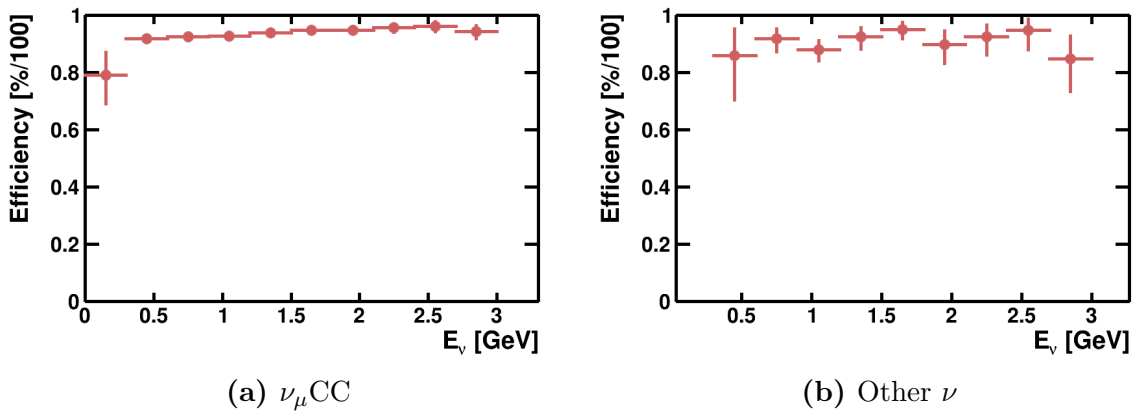
Figure 7.10: Cosmic identification survival as a function of neutrino energy for reconstructed neutrino interactions that passed the selection criteria and had a vertex within the fiducial volume.
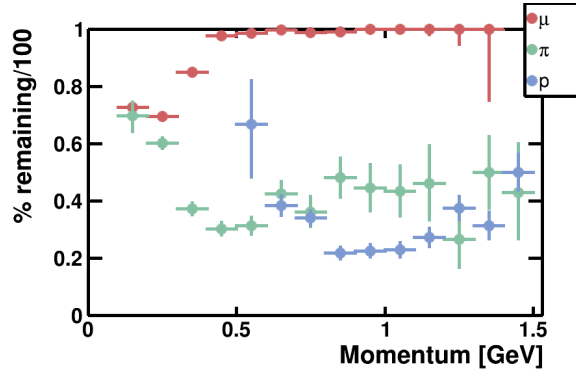
Figure 7.11: Muon identification efficiency for track-like particles after length and proton identification criteria as a function of particle momentum. Particles were treated independently when applying the selection criteria.

7.3.3 Primary muon selection

After a reconstruction and cosmic identification efficiencies, the fiducial volume and length criteria, defined in Sections 6.3 and 6.4, were applied to the true particle trajectories under the assumption that the track length and angle reconstruction performs well. The proton identification efficiency as a function of momentum, Figure 6.16a, was then applied.

The probability of selecting a contained track-like particle as a muon using the process defined in Section 6.4 was parametrised in terms of the particle momentum, shown in Figure 7.11. The longest track identified as a muon was then selected as a primary muon if all tracks were contained. As in Section 6.4, if only one track in a neutrino interaction exited the TPC and had a contained length greater than 50 cm it was selected.

7.3.4 Kinematic variable smearing

The relevant kinematic variables for particles which pass the parametrised reconstruction and selection were then smeared. The angle of particles with respect to the beam was left unsmeared due to the expected quality of track reconstruction, Figure 5.13.

For contained muons, the dominant source of uncertainty in the range momentum method is the irreducible uncertainty from straggling at around 3% [183]. As straggling was simulated in this event sample, the true range was used with the same range-momentum lookup table as in the standard reconstruction. For exiting muons, the frac-

(a)

(b)

(c)
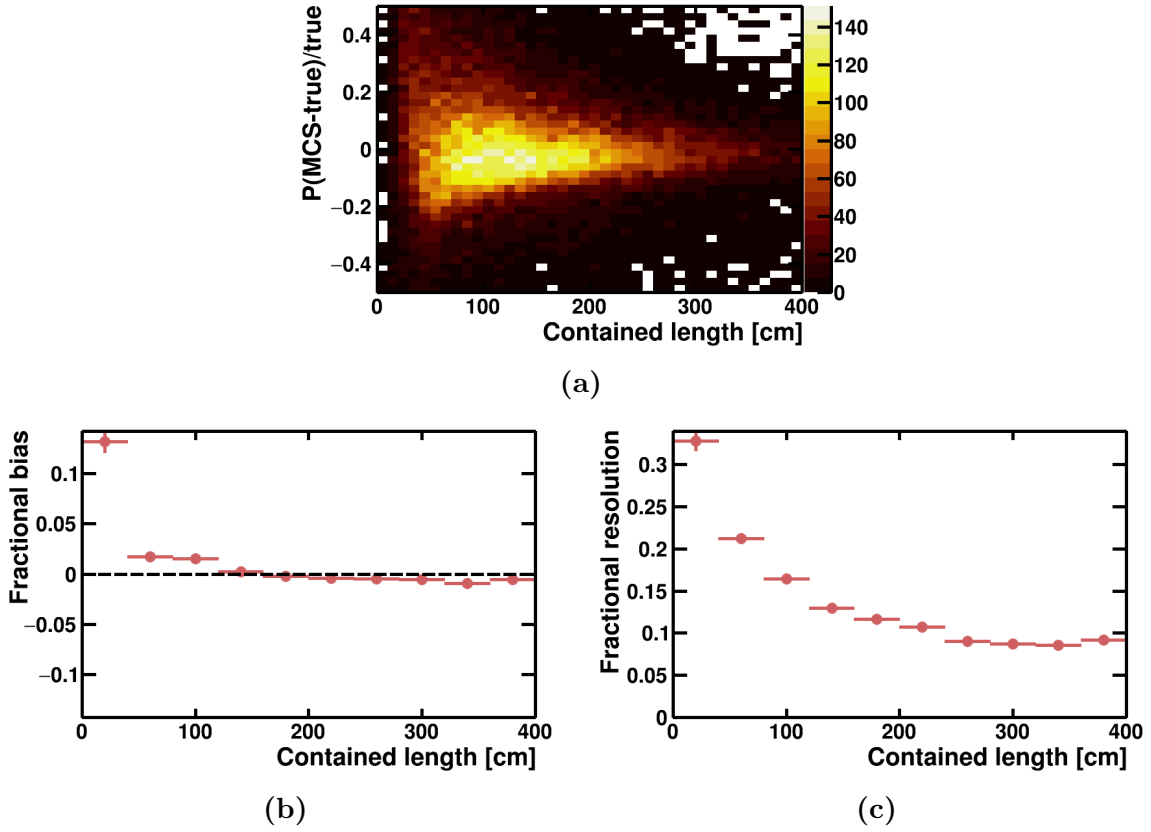
Figure 7.12: Fractional bias and resolution of the MCS based momentum estimation as a function of track length for exiting muons from ν_μ CC interactions in the TPC.

tional bias and resolution of the MCS method were parametrised in terms of contained track length, shown in Figure 7.12, and used to smear the true momentum.

7.3.5 Efficiency comparison

The efficiency of selecting ν_μ CC interactions in the fiducial volume was then directly compared to the efficiency obtained through full reconstruction to check that this method was likely to provide a reasonable approximation of the current reconstruction and selection performance. The efficiencies in both muon momentum and $\cos\theta$ are shown in Figure 7.13. The overall agreement is reasonable, with some deviations in regions with higher statistical uncertainty. This is not unexpected given the binning used.
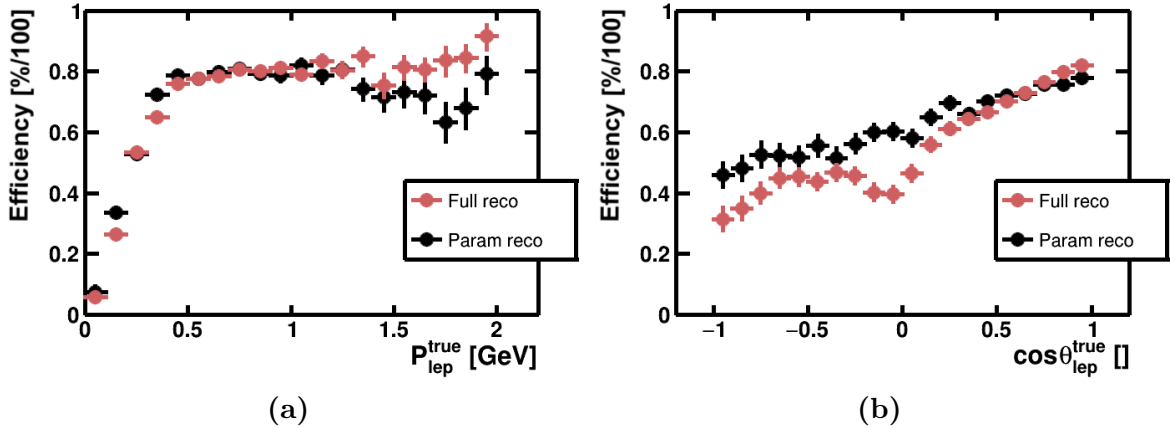
Figure 7.13: Full and parametrised reconstruction efficiency as a function of (a) P_μ and (b) $\cos\theta_\mu$. The dip is not reproduced by the parametrised reconstruction as the binning in this region is too large with the current statistics.

7.3.6   External background rates

External backgrounds are more difficult to predict with this method of parametrising the reconstruction as their contributions to the selected distributions tend to arise from the reconstruction failing in unpredictable ways. This cannot be modelled precisely on an event by event basis. The expected background rates at full exposure were estimated in Section 6.1.1. The contribution from external backgrounds was assumed to already be subtracted from the measured rate in the distributions provided in the next section and the uncertainties from this subtraction will be explored in Section 7.4.

7.3.7   Expected rate distributions

With the parametrised selection and reconstruction it was possible to compare the expected reconstructed rates for different models in the detector. Here, the interaction rates of selected ν_μ CC interactions with the full expected POT as predicted by GENIE v3 are shown in reconstructed muon momentum and $\cos\theta$, Figure 7.14.

The choice of binning took into account both the statistics per bin and the measurement resolution of the kinematic variables to minimise bin migration. The minimum bin width for $\cos\theta$ was set as 0.08 and for momentum it was set to 100 MeV. To account for bins with low statistics bin edges were removed until the statistical uncertainty on each bin
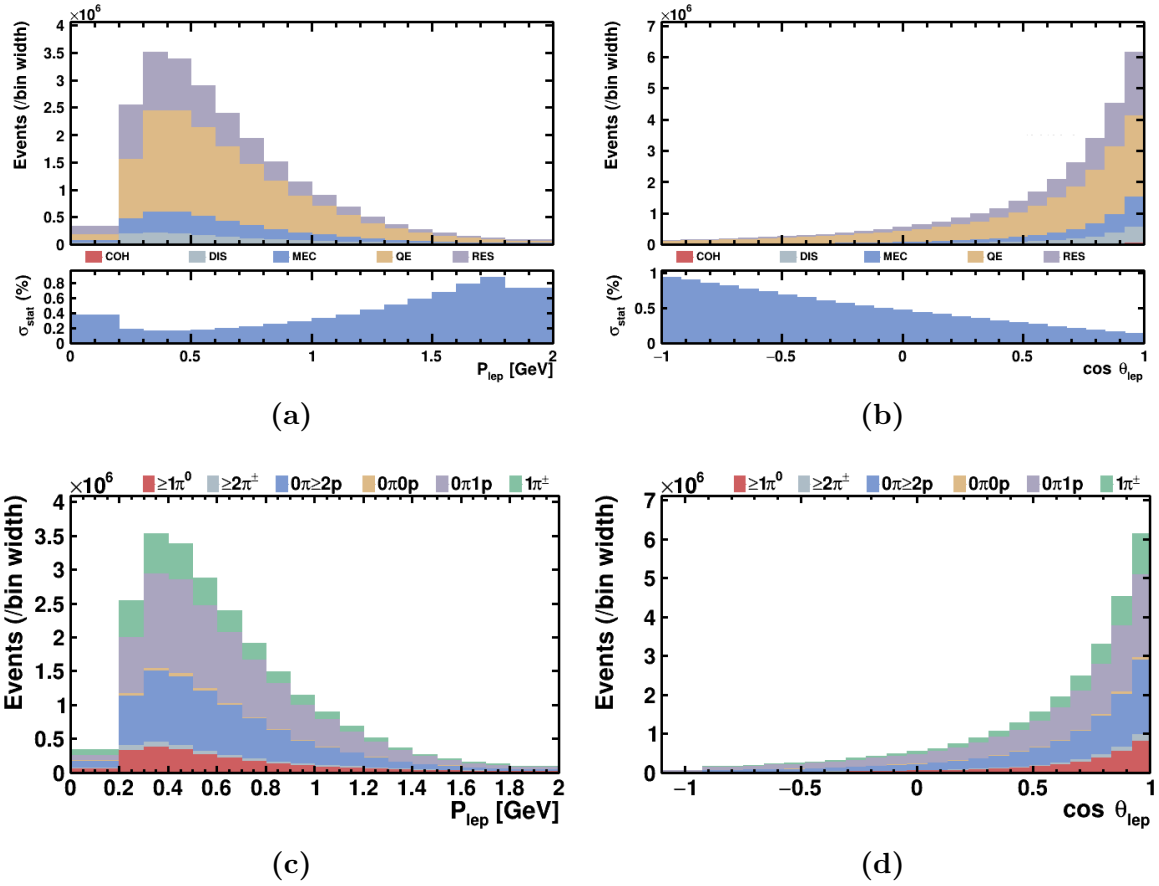
Figure 7.14: 1D rate distributions in reconstructed (a)&(c) P_μ and (b)&(d) $\cos\theta_\mu$ with statistical uncertainties displayed as a percentage of the bin contents. (a)&(b) show the distributions broken down by the true interaction type and (c)&(d) show the contribution from each final state topology.

was less than 1%.

A similar process was used for the two dimensional binning with the proviso that it be possible to slice the two dimensional histogram in one of the variables. The one dimensional projections were first binned with a maximum statistical uncertainty of 0.34% using the same minimum bin widths. The lower statistical uncertainty was used to ensure the binning was not too fine in one dimension. One variable was chosen to slice in and for each slice the other variable was rebinned with a maximum uncertainty of 1%. Figure 7.15 shows the result of this process with the momentum chosen as the slicing variable.
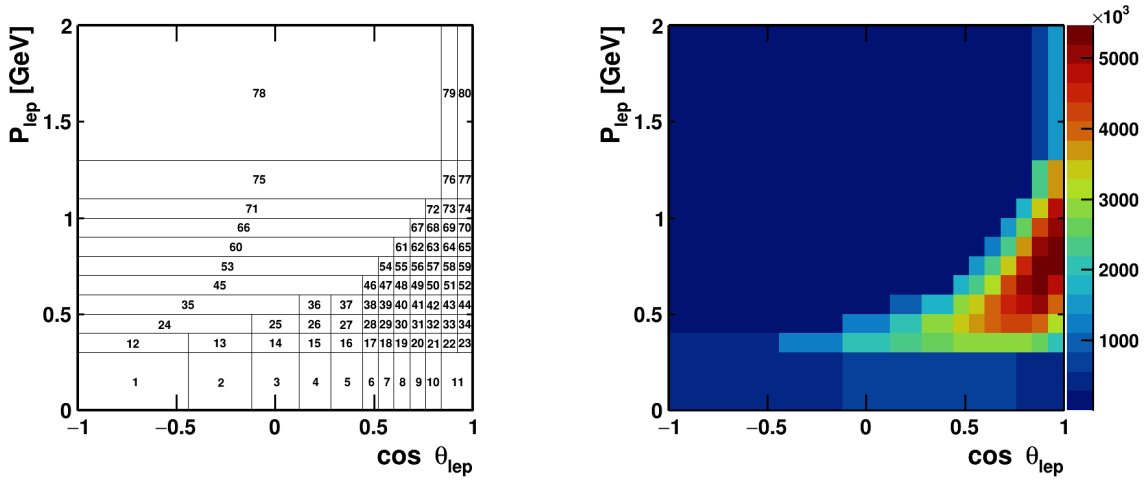
Figure 7.15: Two dimensional rate distribution in reconstructed P_μ and $\cos\theta_\mu$. The momentum binning was constant in $\cos\theta$ so that slices could be easily extracted, the $\cos\theta_\mu$ binning was varied for every momentum bin.

7.4   Systematic uncertainties

As can be seen in Figure 7.14, the full statistics of ν_μ CC interactions results in small statistical uncertainties. However, the systematic uncertainties in the cross section model, flux, and detector response must be considered when presenting a cross section measurement and using the data to compare between different models. It is difficult to perform a comprehensive study of all of the possible systematic effects without data being available. Nevertheless, it was possible to use the event rate prediction tool presented above to estimate the main sources of uncertainty we would expect given a specific model configuration.

For brevity, only the one-dimensional distributions will be shown when evaluating the individual sources of systematic uncertainty. The total covariance and correlation matrices for all distributions are shown in Section 7.4.6.

7.4.1 Reweighting

When evaluating the flux and cross section modelling, it is possible to estimate the effect of systematic changes to physics parameters on the expected measurements without producing hundreds of varied simulations. One large sample can be simulated with the most probable parameter values and then variations can be propagated to weights that can be applied to individual neutrino interactions, in a process called reweighting [91]. Each parameter modification is referred to as a toy universe, and the same parameter modification must be applied to all events within that universe.

Reweighting takes advantage of the properties of Monte Carlo generators discussed in Section 5.1.1, specifically that events are generated randomly and then kept based on a probability calculated by the cross section model. Each event is given a weight proportional to its probability of occurring. If the model parameters are changed, the probability of the event occurring is also often different and so its weight can be modified without having to regenerate new events [184].

One of the caveats of this is that the sample that is reweighted must be sufficiently large enough to cover the entire possible phase space. Reweighting cannot be used to generate events with different kinematic variables to those simulated. For this reason, reweighting was not used for the smaller fully reconstructed sample as it may have resulted in misleading uncertainties.

An event reweighting framework that was first developed by MiniBooNE and then adapted for use in a LArTPC by MicroBooNE was used to reweight both the flux and GENIE parameters. The framework acts as an interface to the native GENIE reweighting tools [91].

7.4.2 Flux

One of the benefits of using the same neutrino beam as other experiments, namely Mini-BooNE and MicroBooNE, is that detailed studies of the neutrino flux and associated uncertainties have been performed [105, 136]. As described by the MicroBooNE collabo-

ration in [136] there are a number of different uncertainties that contribute to the overall flux uncertainty. These were all re-evaluated for the SBND flux.

A summary of the parameters that were varied in the flux reweighting is given in Table 7.2. The different parameters were:

- **Horn current**: The magnetic focusing horn is pulsed with a current in sync with proton delivery, this current has some variation around the central value of 174 kA [105].

- **Skin depth**: The skin effect results in some of the pulsed current in the horn penetrating the conductive surface. This causes electromagnetic currents within the conductor and can lead to large uncertainties at high neutrino energies. The effect was modelled as an exponential decay of current density to a depth of 1.4 mm [105].

- σ_{π^+}, σ_{π^-}: Pion production cross section uncertainties.

- σ_{K^+}, σ_{K^0}, σ_{K^-}: Kaon production cross section uncertainties.

- σ_{inel}^{π}, σ_{QE}^{π}, σ_{total}^{π}: Pion-beryllium/aluminium inelastic scattering, QE scattering and total cross section uncertainties. Beryllium is the material of the target and the horn is mostly composed of aluminium.

- σ_{inel}^{N}, σ_{QE}^{N}, σ_{total}^{N}: Nucleon-beryllium/aluminium inelastic scattering, QE scattering and total cross section uncertainties.

- **POT**: Uncertainty on the delivery of protons in each spill.

The method used to originally determine the simulated flux model parameters often determined how the parameters were reweighted, there were several different reweighting methods used:

- **Flux Unisim (FU)**: Physics parameters were varied around their central values in different universes using either a Gaussian distribution or single values at $\pm 1\sigma$, the new parameters were then used to recalculate event weights.

Table 7.2: Flux reweighting parameters varied in the systematic uncertainty estimation. The pion production uncertainties contribute to the inclusive muon channel the most, as can be seen in Table 3.2.

Parameter	Method	Uncertainty
Horn current	FU	± 1 kA
Skin depth	FU	On/Off
σ_{π^+}	CSV	[105]
σ_{π^-}	CSV	[105]
σ_{K^+}	FS	[105]
σ_{K^0}	SW	[105]
σ_{K^-}	N	100%
σ_{inel}^{π} (Be/Al)	FU	$\pm 10/\pm 20$ mb
σ_{QE}^{π} (Be/Al)	FU	$\pm 11.2/\pm 25.9$ mb
σ_{total}^{π} (Be/Al)	FU	$\pm 11.9/\pm 28.7$ mb
σ_{inel}^{N} (Be/Al)	FU	$\pm 5/\pm 10$ mb
σ_{QE}^{N} (Be/Al)	FU	$\pm 20/\pm 45$ mb
σ_{total}^{N} (Be/Al)	FU	$\pm 15/\pm 25$ mb
POT	N	2% [136]

- **Central spline variation (CSV)**: Ratios of the central value prediction to varied spline fits of the smeared pion cross section data were used to generate weights for interactions, this was applied based on the parent particle of the neutrino [105].

- **Feynman scaling (FS)**: Kaon cross section measurements were extrapolated to regions where there is little experimental data using Feynman scaling [134]. The coefficients used in the scaling were varied within their correlated uncertainties and then the cross section was recalculated to generate a new weight.

- **Sanford Wang (SW)**: Parameters in Sanford Wang fit to data were smeared and new cross sections are recalculated to give event weights [105].

- **Normalisation (N)**: A normalisation uncertainty was applied to a process and propagated to event weights.

For each parameter, 100 different universes were generated with the variations distributed according to the methods in Table 7.2. Every neutrino interaction was given a weight in every universe, if the parameter variation did not change then the interaction

probability weight was one. The flux simulation parameters are uncorrelated with one another and so to estimate the overall flux uncertainty it was possible to take the product of the weights within each universe. A new rate histogram was filled for each universe and the standard deviation of the bin contents across all universes was used as the systematic uncertainty for that bin. The flux systematic uncertainties can be seen in Figure 7.16.

To study the variance of the bin values in relation to other bins with flux parameter variations, a covariance matrix was constructed. For the rate predictions, the covariance matrix is given by

$$Cov_{ij} = \frac{1}{U} \sum_{n=1}^{U} \left(N_i^n - N_i^{cv} \right) \left(N_j^n - N_j^{cv} \right) \tag{7.16}$$

where U is the number of reweighting universes simulated, N_i^n is the predicted rate in bin i and N_i^{cv} is the central value in bin i.

It is often more visually interpretable to show the correlation matrix, the covariance matrix of the bin contents normalised by the standard deviation of the bins, defined as

$$Corr_{ij} = \frac{Cov_{ij}}{\sqrt{Cov_{ii}}\sqrt{Cov_{jj}}} = \frac{Cov_{ij}}{\sigma_i \sigma_j} \tag{7.17}$$

where $\sigma_i = \sqrt{Cov_{ii}}$ is the standard deviation of bin i. The correlation matrix for the flux systematic uncertainties can be seen in Figure 7.16.

7.4.3 GENIE

The GENIE generator provides a package for performing event reweighting [91] which contains tools for modifying and propagating uncertainties in cross section models, rescattering, hadronisation and decays. A physics parameter, P, which may be a single quantity or a function, can be modified by a Gaussian distributed multiplier, x_P, to the standard deviation of that parameter, σ_P, so that

$$P \rightarrow P' = P \left(1 + x_P \times \frac{\sigma_P}{P} \right). \tag{7.18}$$
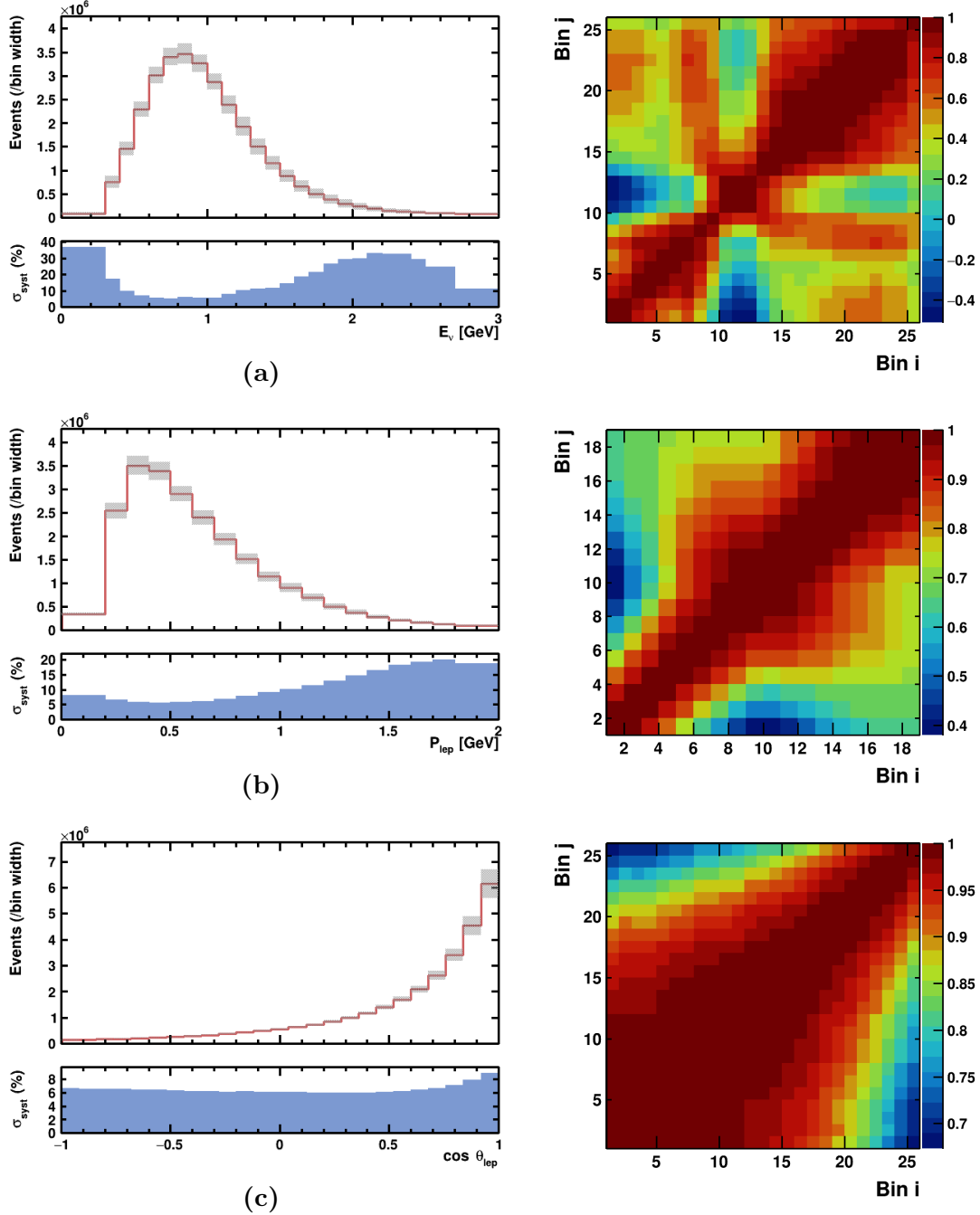
Figure 7.16: The contribution of the flux systematic uncertainties to the total rate distributions and corresponding bin correlation matrices for (a) true neutrino energy, (b) reconstructed P_μ and (c) reconstructed $\cos\theta_\mu$. The peak flux uncertainty is smaller than the total uncertainty in Table 3.2 as the large low energy uncertainties do not contribute to the rate uncertainty due to the small interaction cross sections in this region.

Table 7.3: GENIE cross section reweighting parameters. Table adapted from [91]. The uncertainties on the axial mass for CCQE contribute most to the inclusive sample as it is dominated be CCQE interactions, as can be seen in Figure 7.14.

x_P	Description	σ_P/P
$x_{M_A^{NCEL}}$	Axial mass for NC elastic	$\pm 25\%$
$x_{\eta^{NCEL}}$	Strange axial form factor η for NC elastic	$\pm 30\%$
$x_{M_A^{CCQE}}$	Axial mass for CCQE	-15%+25%
$x_{CCQE-PauliSup}$	CCQE Pauli Suppression	$\pm 35\%$
$x_{M_A^{CCRES}}$	Axial mass for CCRES	$\pm 20\%$
$x_{M_V^{CCRES}}$	Vector mass for CCRES	$\pm 10\%$
$x_{M_A^{NCRES}}$	Axial mass for NCRES	$\pm 20\%$
$x_{M_V^{CCRES}}$	Vector mass for NCRES	$\pm 10\%$
$x_{M_A^{COH}}$	Axial mass for CC and NC COH	$\pm 50\%$
$x_{R_0^{COH}}$	π absorption in RS model	$\pm 10\%$
$x_{R_{bkg}^{\nu p, CC1\pi}}$	Non-resonance background in νp CC1π reactions	$\pm 50\%$
$x_{R_{bkg}^{\nu p, CC2\pi}}$	Non-resonance background in νp CC2π reactions	$\pm 50\%$
$x_{R_{bkg}^{\nu n, CC1\pi}}$	Non-resonance background in νn CC1π reactions	$\pm 50\%$
$x_{R_{bkg}^{\nu n, CC2\pi}}$	Non-resonance background in νn CC2π reactions	$\pm 50\%$
$x_{R_{bkg}^{\nu p, NC1\pi}}$	Non-resonance background in νp NC1π reactions	$\pm 50\%$
$x_{R_{bkg}^{\nu p, NC2\pi}}$	Non-resonance background in νp NC2π reactions	$\pm 50\%$
$x_{R_{bkg}^{\nu n, NC1\pi}}$	Non-resonance background in νn NC1π reactions	$\pm 50\%$
$x_{R_{bkg}^{\nu n, NC2\pi}}$	Non-resonance background in νn NC2π reactions	$\pm 50\%$

The physics parameters that were varied in this analysis are summarised in Tables 7.3, 7.4, and 7.5.

Given the large number of parameters in the comprehensive model built by GENIE and the inclusion of more theoretically motivated models that may not lend themselves to reweighting, the parameters in the tables above do not cover all of the possible uncertainties. While these parameter variations do not represent the full cross section model systematic uncertainty, the included modifications should provide a reasonable approximation for the CC inclusive channel.

The GENIE systematic uncertainties were all varied together over 100 universes and propagated to weights [91]. The process for obtaining the uncertainties from the universe

Table 7.4: GENIE rescattering reweighting parameters. Table adapted from [91].

x_P	Description	σ_P/P
x_{mfp}^N	Nucleon mean free path	$\pm 20\%$
x_{cex}^N	Nucleon charge exchange probability	$\pm 50\%$
x_{inel}^N	Nucleon inelastic reaction probability	$\pm 40\%$
x_{abs}^N	Nucleon absorption probability	$\pm 20\%$
x_{π}^N	Nucleon pion production probability	$\pm 20\%$
x_{mfp}^π	Pion mean free path	$\pm 20\%$
x_{cex}^π	Pion charge exchange probability	$\pm 50\%$
x_{inel}^π	Pion inelastic reaction probability	$\pm 40\%$
x_{abs}^π	Pion absorption probability	$\pm 20\%$
x_{π}^π	Pion pion production probability	$\pm 20\%$

Table 7.5: GENIE hadronisation and decay reweighting parameters. The blank σ_P/P refers to parameter variations that cannot be expressed as a single number. Table adapted from [91].

x_P	Description	σ_P/P
$x_{AGKY}^{pT1\pi}$	Pion transverse momentum for $N\pi$ states in AGKY	-
$x_{AGKY}^{pF1\pi}$	Pion Feynman x for $N\pi$ states in AGKY	-
x_{fz}	Hadron formation zone	$\pm 50\%$
$x_{\theta_\pi}^{\Delta \to \pi N}$	Pion angular distribution in $\Delta \to \pi N$	-
$x_{BR}^{R \to X+1\gamma}$	Branching ratio for radiative resonance decays	$\pm 50\%$

variations was the same as for the flux, shown in Figure 7.17.

7.4.4 Detector

There will be a number of uncertainties in the modelling of the detector response that contribute to systematic uncertainties on a cross section measurement. Event reweighting is not appropriate here as the detector modelling does not change the probability of an interaction occurring.

The uncertainties will be evaluated by producing multiple full simulations with modifications to detector simulation parameters and with the same neutrino interaction inputs. The entire reconstruction and analysis chain will be run on the modified universes and the cross section bins compared between simulations. This is a time and resource expensive process that is only worthwhile when confident that the detector is well modelled and the uncertainties understood.

The main predicted sources of uncertainty are discussed below and the work of Chapter 4 was used to inform predictions on how these uncertainties may propagate to the CC inclusive measurement.

There are several ways that variations in detector performance and physics may affect measurements. Firstly, entire neutrino interactions may or may not be reconstructed, predominantly at low energy, this could affect both the shape and normalisation of the measured distributions. Secondly, the performance of external and internal background reconstruction may be affected, also changing the shape and normalisation of measured distributions if not accounted for by control samples. Thirdly, differences in the reconstruction performance may affect the particle identification and the smearing of the measured kinematic variables, this can change the shape of measured distributions if migration between bins is high.

The expected sources of detector uncertainties relevant to this analysis are:

- **Space charge:** A build up of positive ions will modify the electric field inside the detector and alter the electron drift [147]. This is not included in this analysis
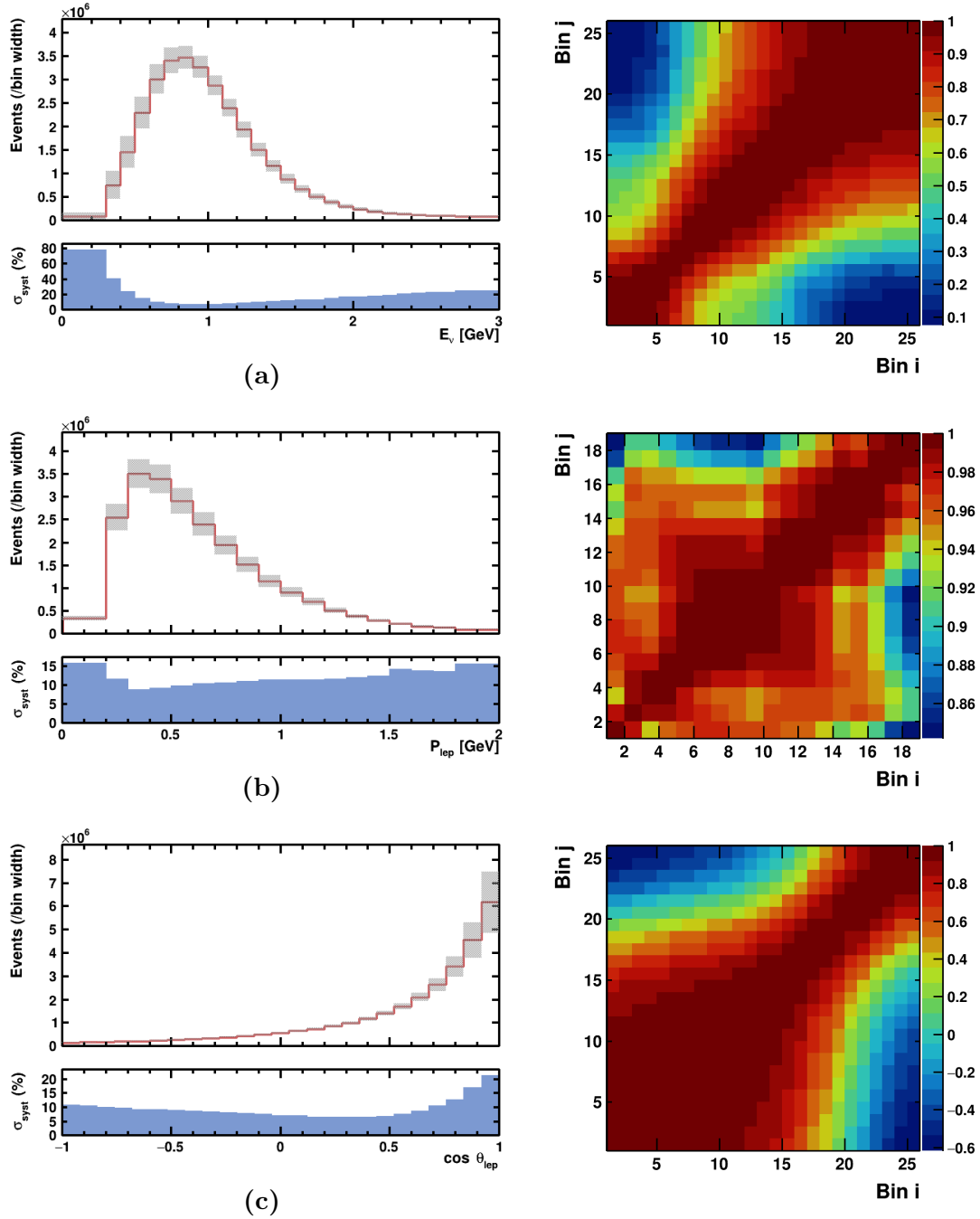
Figure 7.17: The contribution of the cross section, rescattering, hadronisation and decay systematic uncertainties to the total rate distributions and corresponding bin correlation matrices for (a) true neutrino energy, (b) reconstructed P_μ and (c) reconstructed $\cos\theta_\mu$.

but must be corrected for to get the true particle trajectories. Uncertainties in the modelling have the potential to modify the observed muon angle and momentum distributions as well as background predictions.

- **Prediction:** Electric field decrease from +5% to -2% from cathode to anode.

- **Total systematic uncertainty (expected):** 1-2%.

- **APA gap:** The behaviour of drifted electrons around the gap between APAs is not well defined, they may enter the gap or be detected by wires either side. Provided that the fiducial volume excludes vertices sufficiently close to the gap the effect on event reconstruction and muon kinematic measurements should be negligible.

  - **Prediction:** 18 mm gap between APAs.

  - **Total systematic uncertainty (expected):** < 1%.

- **Electronics response:** The response of the TPC channels to drifted charge [170] and the PMT and CRT channels to photons will affect the calorimetry and triggering. This will require careful calibration to data as it can be hard to predict how different components will affect each other until the entire system is in place. Two dimensional deconvolution will significantly reduce the dominant systematic uncertainties from dynamic induced charge [170].

  - **Total systematic uncertainty (expected):** 2-3%.

- **Diffusion:** The time and spatial dependence of the longitudinal and transverse spread of drifted electron clouds will affect the calorimetry if the spread is on the order of the wire gaps. The effect is not expected to be large enough to significantly affect the performance of the track or momentum reconstruction.

  - **Prediction:** 6.82 cm^2/s longitudinal and 13.16 cm^2/s transverse [146].

  - **Total systematic uncertainty (expected):** < 1%.

- **Electron lifetime:** As discussed in Section 4.2.1, the purity changes the charge loss as a function of distance and can affect the calorimetry and track reconstruction. Provided the electron lifetime is sufficiently high (around 3 ms) and well calibrated

the inclusive cross section measurements should not be sensitive to slight differences between data and simulation.

- **Prediction:** Greater than 10 ms [148].

- **Total systematic uncertainty (expected):** $< 1\%$.

- **APA alignment:** A misalignment between two joined APAs has the potential to break up or alter the trajectory of long muon tracks. It was shown in Section 4.2.3 that we have the ability to measure and correct any misalignment to a high degree of precision and accuracy.

  - **Prediction:** Translation in x < 0.5 mm, rotation in y < 0.12 degrees.

  - **Total systematic uncertainty (expected):** $< 1\%$.

- **Wire continuity:** Faulty connections between wires joined across the APA could reduce sensitivity in areas of the detector altering event rates and kinematic reconstruction. Provided that any faulty connections are modelled this can be corrected for with simulations but there will be uncertainties involved. The strategies discussed in Section 4.1.2 should help to prevent any faults during installation.

  - **Prediction:** All wires continuous, any faults detected and corrected for.

  - **Total systematic uncertainty (expected):** $< 1\%$.

- **Wire tension:** Significant reductions in tension could alter the measured particle trajectories or cause electrical shorts between wires, reducing coverage. If the method outlined in Section 4.1.1 was to be implemented in SBND, the wire tensions could be continuously monitored during installation and operation.

  - **Prediction:** All wires > 5 N [153].

  - **Total systematic uncertainty (expected):** $< 1\%$.

- **Detector system alignment:** An accurate mapping of the locations of the TPC, PDS and CRT relative to each other and the BNB is required. Uncertainties have the potential to alter the observed neutrino flux away from the prediction and could affect triggering and cosmic background removal.

Table 7.6: Detector uncertainty systematic variations predicted based on the current selection performance and possible contributions from different detector effects. Variations in efficiency refer to a systematic shift in the the overall efficiency. Variations in resolutions refer to a percentage change to the binned fractional resolution, e.g. a +5% change to a 50% fractional resolution would be 52.5%.

Quantity	Variation
Muon reconstruction efficiency	±4%
Pion reconstruction efficiency	±6%
Proton reconstruction efficiency	±5%
Proton identification efficiency	±5%
Muon selection efficiency	±4%
Pion selection efficiency	±12%
Proton selection efficiency	±8%
MCS momentum fractional resolution	±5%

- **Prediction:** Relative position of TPC-CRT known within 1 cm, relative position of TPC-PDS known with 1 mm.

- **Total systematic uncertainty (expected):** 1-2%.

While it was not possible to test all of these individual effects, the parametrised reconstruction allowed for variations in high level reconstruction performance as a simple estimator of detector systematics. This should provide an estimate to how robust the selection is to detector variations although the correlations between them are unlikely to be representative of actual uncertainties in detector modelling.

The reconstruction, particle identification and kinematic variable measurement performances were varied independently over 50 universes according to Table 7.6 in order to estimate detector modelling uncertainties. It was assumed that there will be a constant 1% uncertainty in the normalisation due to uncertainty in the external background misidentification rate.

7.4.5 External background subtraction

As the background predictions are subtracted from the total event rate the systematic uncertainties on those predictions must be considered. In the final measurement, over-

(a)

(b)
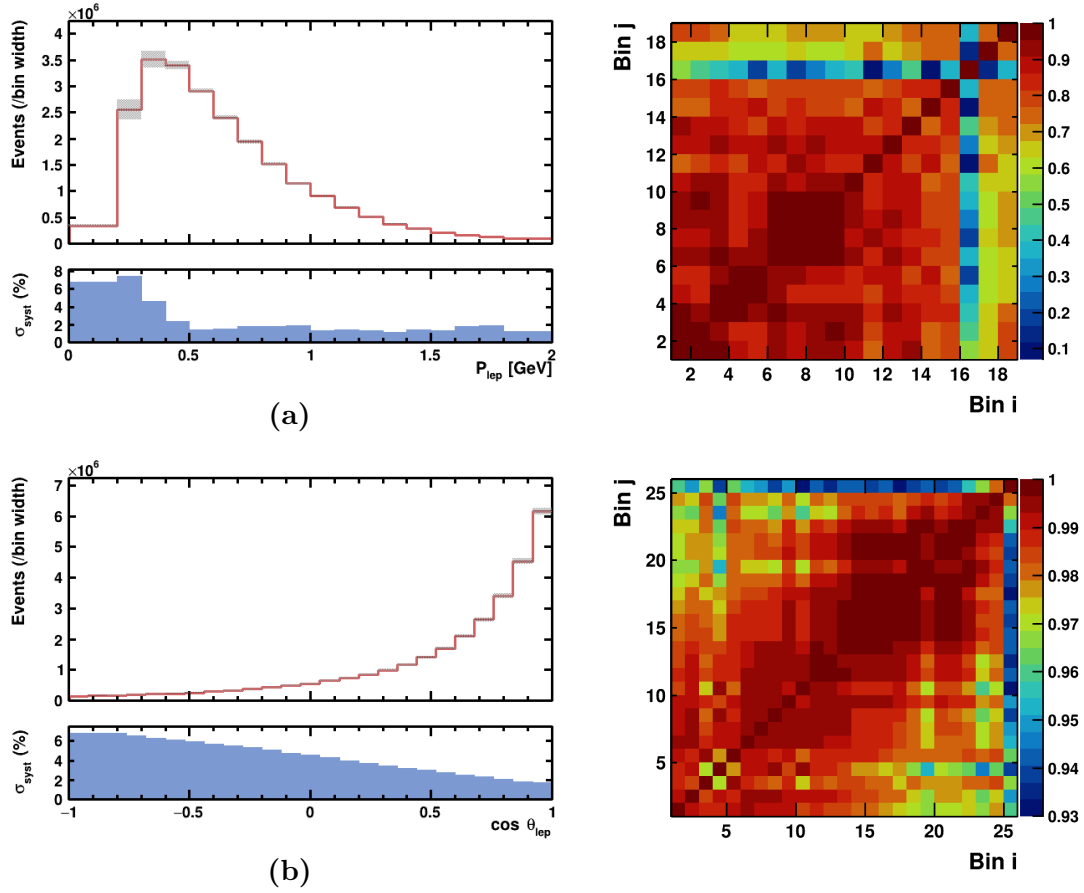
Figure 7.18: The contribution of the parametrised detector systematic uncertainties to the total rate distributions and corresponding bin correlation matrices for reconstructed (a) P_μ and (b) $\cos\theta_\mu$. The muon reconstruction and selection efficiencies contribute to the overall systematics the most.
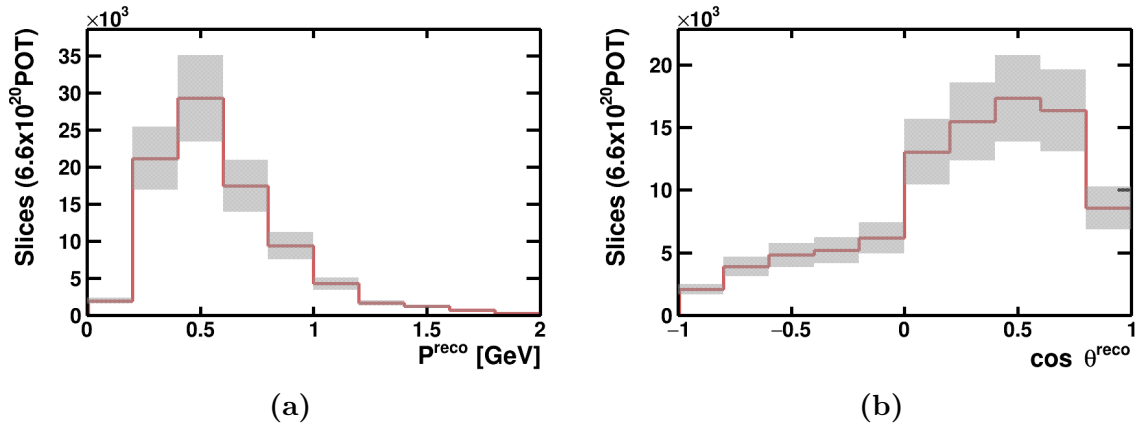
Figure 7.19: Scaled cosmic ray muon contributions to one dimensional reconstructed (a) P_μ and (b) $\cos\theta_\mu$ rate distributions with statistical and systematic uncertainties.

lays of real cosmic data will be used in the place of simulations and so uncertainties in the modelling of the cosmic ray interactions should not contribute. There may however be systematic uncertainties associated to the overlaying process and any difference in operational conditions between taking the overlaid cosmic data and the beam data.

Cosmic ray interactions were not included in the full POT sample due to memory constraints and so the selected kinematic distributions from the fully reconstructed sample in Chapter 6 were scaled. As with the detector uncertainties, it is difficult to predict the exact form of the uncertainties and so a conservative 20% uncorrelated uncertainty on each bin was used. The off-beam and on-beam cosmic ray muon contributions were treated together, shown in Figure 7.19.

The other external backgrounds will arise from neutrino interactions outside the fiducial volume and so will be subject to many of the same cross section, flux and detector systematic uncertainties as the signal events. Dirt interactions were also not included in the full POT sample and so the uncertainties could not be predicted in the same way, especially as the reconstructed kinematics are often not correlated with the true kinematics due to incomplete reconstruction. The selected dirt background estimation from Section 6.5 was scaled to the predicted POT and a constant 50% systematic uncertainty was used for each bin along with the scaled statistical uncertainty, shown in Figure 7.20.

The reconstructed rate distributions with the predicted statistical and systematic uncertainties from external background removal are shown in Figure 7.21. The uncertainties
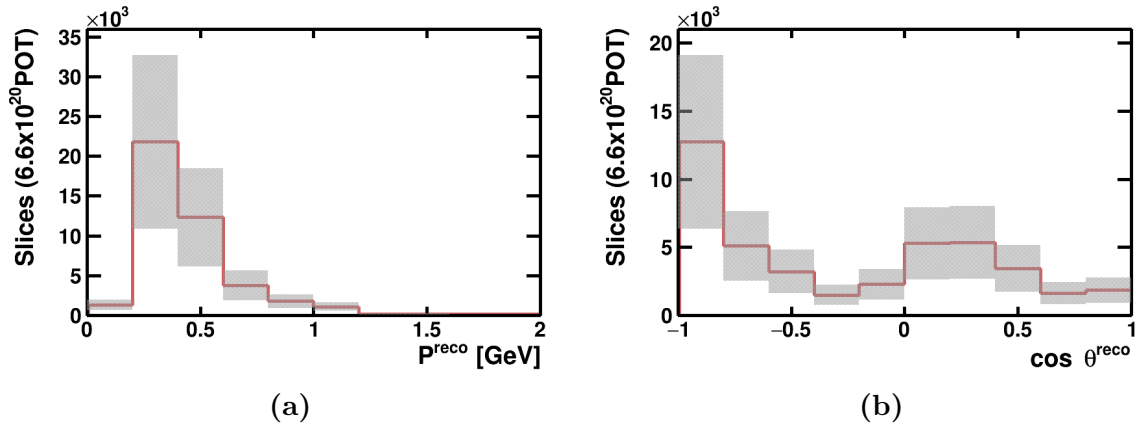
Figure 7.20: Scaled dirt contributions to one dimensional reconstructed (a) P_μ and (b) $\cos\theta_\mu$ rate distributions with statistical and systematic uncertainties.
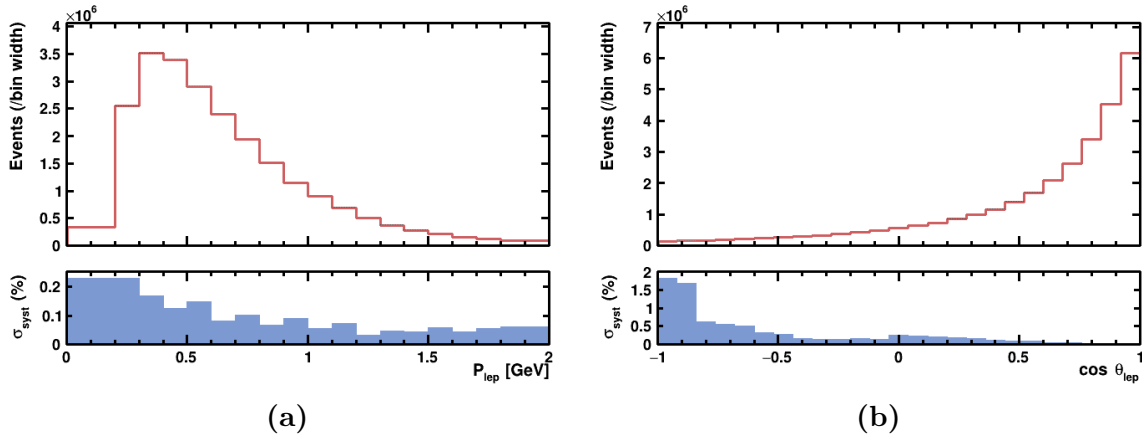
Figure 7.21: Reconstructed P_μ and $\cos\theta_\mu$ rate distributions with external background subtraction uncertainties.

were propagated to the rate bins by determining the corresponding background bins from Figures 7.19 and 7.20. The expected number of background events were scaled by the relative bin widths and the percentage uncertainties on the bins were used to calculate the uncertainties on the rate bins. This process was also used for two dimensional measurements but with courser binning, a percentage uncertainty of 0.1% was used for unpopulated bins.

7.4.6   Summary

The predicted systematic uncertainties on the selected rate of muon neutrino CC interactions with external backgrounds subtracted are presented in Table 7.7. The overall

Table 7.7: Summary of systematic uncertainties on the expected total rate of reconstructed and selected ν_μ CC interactions in the fiducial volume.

Source of uncertainty	Percentage
Flux	6.88%
GENIE modelling	10.55%
Detector performance	2.77%
External background subtraction	0.63%
Cosmic misidentification	1.00%
POT counting	2.00%
Total systematic	13.10%
Total statistical	0.06%
Total	**13.10%**

systematic uncertainty on the total rate prediction given the current analysis strategy and the GENIE v3 cross section model is expected to be 13.1%.

The total reconstructed and selected event rate predictions and associated systematic uncertainties that would be expected in SBND given the combination of models in Table 5.1 are shown for one dimensional distributions of P_μ and $\cos\theta_\mu$ in Figures 7.22 and 7.23. The two dimensional distribution is shown in Figure 7.24. The response, Equation 7.14, covariance, Equation 7.16, and correlation, Equation 7.17, matrices associated with each distribution are also shown.

Table 7.7 demonstrates that the selection procedure is able to reduce the external backgrounds to such a level that even large uncertainties on the subtraction procedure are only small contributions to the total uncertainty. Flux and GENIE uncertainties dominate, although, as discussed later in Section 7.6, there are reasons to believe that the GENIE uncertainties evaluated with this reweighting scheme are inflated. The detector systematics are small in comparison with the first MicroBooNE cross section paper [125], the majority of this large uncertainty was from induced charge from other wires [170], this is significantly reduced by two dimensional deconvolution, bringing the total detector uncertainty down to the 3% level.

(a)

(b)

(c)

(d)
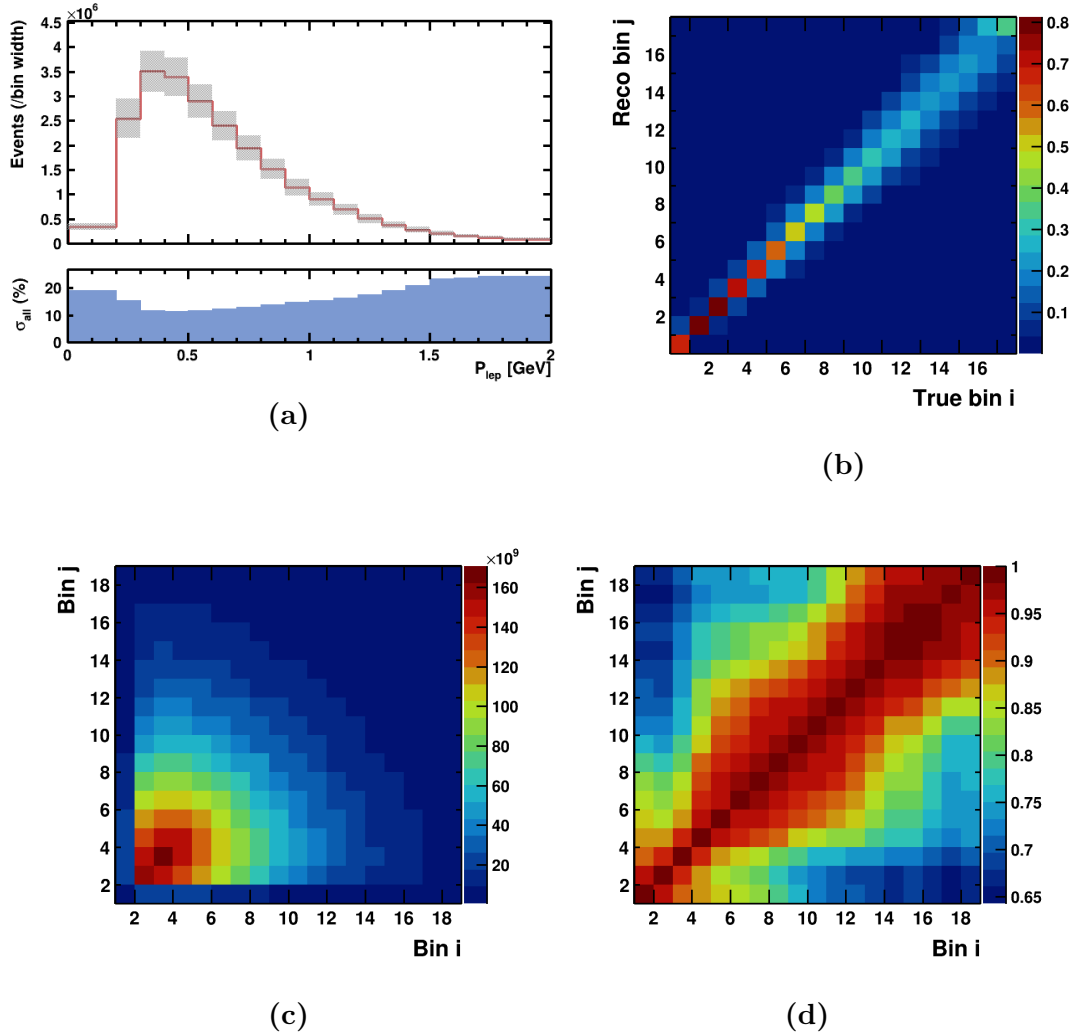
Figure 7.22: (a) Event rate prediction in P_μ with statistical and systematic uncertainties. (b) Response matrix for all reconstructed events. (c) & (d) Covariance and correlation matrices.

(a)

(b)

(c)

(d)
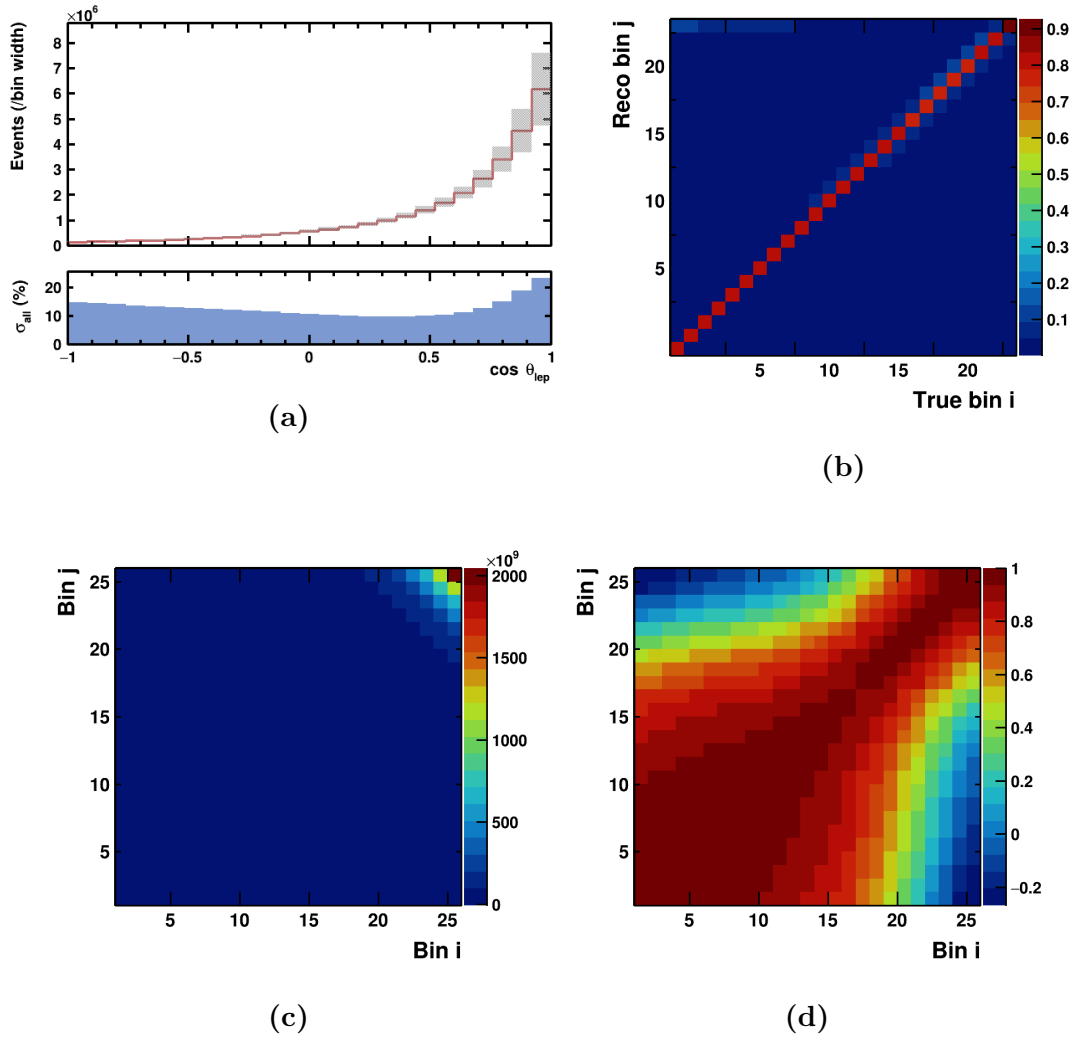
Figure 7.23: (a) Event rate prediction in $\cos\theta_\mu$ with statistical and systematic uncertainties. (b) Response matrix for all reconstructed events. (c) & (d) Covariance and correlation matrices.
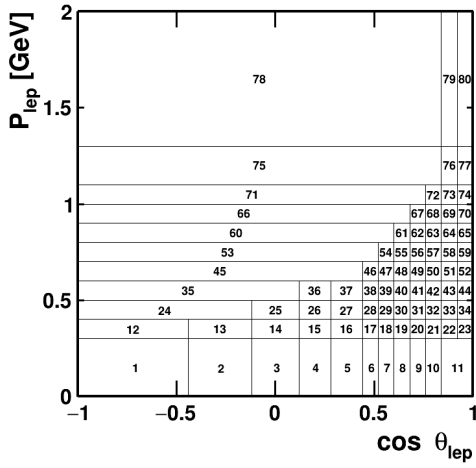
(a)
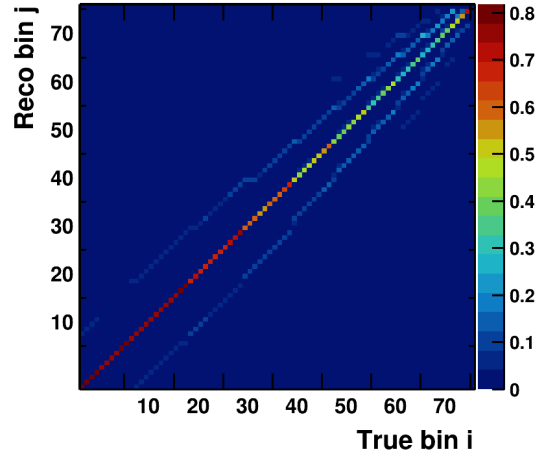
(b)
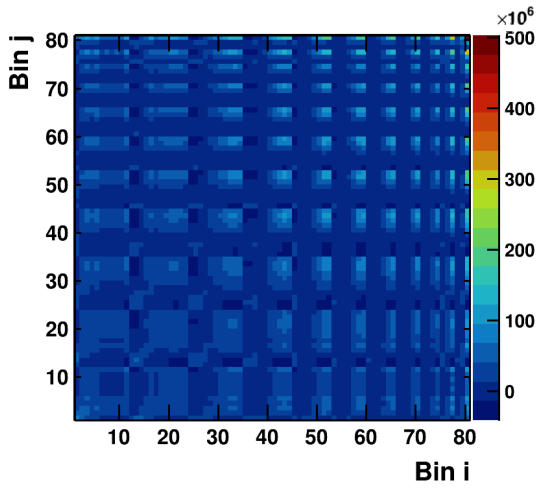
(c)
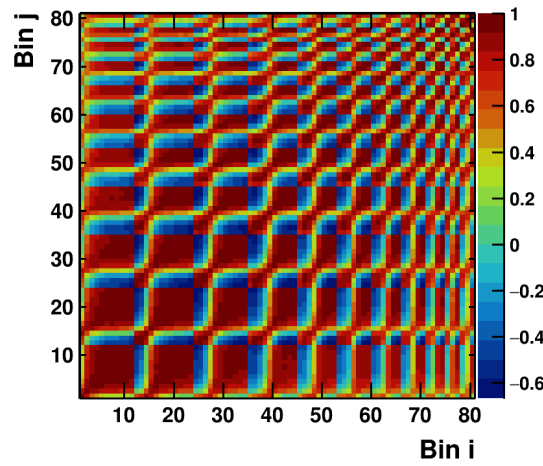
(d)

Figure 7.24: (a) Two dimensional binning scheme. (b) Response matrix prediction for predicted reconstructed event rate in P_μ and $\cos\theta_\mu$. (c) & (d) Covariance and correlation matrices.

7.5   Cross section systematics

The systematic uncertainties presented in the previous section are on the total expected rate in the detector and are not the same as the expected uncertainties on a cross section measurement. For a rate measurement, the data does not have any associated uncertainties because it has been measured with the true flux, cross section and detector response. The uncertainties on modelling these components only affect the predictions.

For the cross section measurement, a number of model dependent corrections are made to the rate and each of these will have an associated uncertainty. If we take, for example, the flux-integrated inclusive differential cross section in reconstructed momentum from Equation 7.10 and evaluate the flux systematic uncertainties, in every universe, n, we have,

$$\left(\frac{d\sigma}{dP_\mu^{reco}}\right)_i^n = \frac{N_i - B_i^n}{\zeta_i^n \cdot n_T \cdot \Phi^n \cdot (\Delta P_\mu^{reco})_i}, \tag{7.19}$$

where the superscript n denotes a quantity that must be re-evaluated for that universe. This is also true for the GENIE and detector uncertainties with the exception that Φ does not change. The measured rate N_i is constant for every universe.

The measure of covariance then becomes

$$Cov_{ij} = \frac{1}{U}\sum_{n=1}^{U}\left(\left(\frac{d\sigma}{dP_\mu^{reco}}\right)_i^n - \left(\frac{d\sigma}{dP_\mu^{reco}}\right)_i^{cv}\right)\left(\left(\frac{d\sigma}{dP_\mu^{reco}}\right)_j^n - \left(\frac{d\sigma}{dP_\mu^{reco}}\right)_j^{cv}\right), \tag{7.20}$$

and the correlation matrix is the same as Equation 7.17.

To predict the systematic uncertainties on a cross section measurement in SBND, the simulated rate was taken as the fixed measured rate and universe variations were made as in Section 4.2.1. The cross sections were calculated for each universe and the covariances and correlations were evaluated. The predicted systematic uncertainties on the cross section are summarised in Table 7.8. The plots showing the systematic uncertainties on the single and double differential cross sections are available in Appendix A.

The total systematic uncertainties on the rate prediction and cross section measurement were similar but the individual contributions differed. In particular, there is a much

Table 7.8: Summary of the expected systematic uncertainties on a measurement of the total ν_μ CC inclusive cross section as predicted by GENIE v3.

Source of uncertainty	Percentage
Flux	11.36%
GENIE modelling	0.98%
Detector performance	2.93%
External background subtraction	0.63%
Cosmic misidentification	1.00%
POT counting	2.00%
Total systematic	12.00%
Total statistical	0.05%
Total	**12.00%**
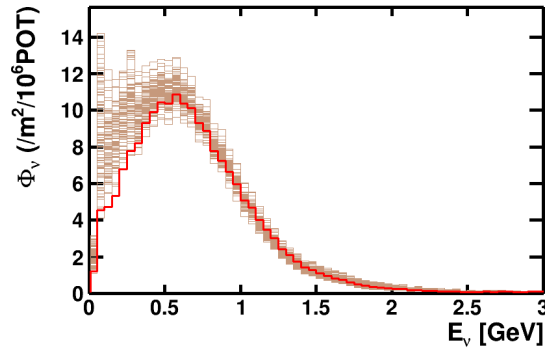
Figure 7.25: Systematic universe variations to the muon neutrino flux. Large differences between the pion cross section parametrisation and spline fits at low hadron momentum correspond to large universe differences at low neutrino energy.

greater flux uncertainty on the cross section measurement due to the integrated flux normalisation. The cause of this difference was the way the systematic uncertainties were evaluated for the HARP pion production cross sections [131] used in the beam simulation. The spline fits at low hadron momentum did not correspond to realistic uncertainties on the Sanford Wang parametrisation. The large uncertainties are reasonable in the regions not covered by the HARP data, but the errors on the low energy data do not cover the parametrisation at all. The ν_μ flux universe variations demonstrating this effect can be seen in Figure 7.25.

The Sanford Wang parametrisation underestimates the data at low hadron momentum and the spline fits do not correspond to realistic uncertainties resulting in the universe

variations not being centred around the simulated value. This adds an extra bias term to the covariance matrix which may result in an overly conservative estimation of the uncertainty. This suggests that either the pion cross section predictions or their uncertainties are unrealistic at low hadron momentum and the simulated central value or spline fits should be updated for future analyses.

This large uncertainty is reduced when considering the rate prediction as the neutrino-argon cross section decreases with neutrino energy, limiting the contribution of the large pion cross section uncertainties. The large integrated flux normalisation uncertainties suggests that a rate measurement may be better for testing cross section models. The total GENIE modelling uncertainties are low because of the high purity of the selection but increase when considering differential cross sections because of the effect of the response matrix and efficiency predictions.

7.6 Model comparisons

In the current era of precision oscillation measurements, cross section measurements are used to test the limits of applicability of models in various neutrino energy regimes and on different nuclear targets. The direct comparisons between models and data can aide their improvement and the reduction of uncertainties. Furthermore, they can be used to tune model parameters in areas of disagreement [118]. The ability to compare different models to our data will be a crucial part of this.

To investigate the sensitivity of SBND to different cross section models, another large sample of neutrino interactions was generated with the model configuration shown in Table 7.9. These interactions were passed through the parametrised reconstruction and the systematics were evaluated in the same way. The separation between model predictions of forward folded, flux integrated cross sections in SBND was investigated, although it is challenging to make definitive statements on sensitivity in the absence of data.

The two samples, while being produced by the same generator, had significant differences in the predicted rates, as can be seen in Figure 7.26. GENIE v2 predicted a higher overall

Table 7.9: Cross section models used in GENIE v2.12.10 tune DefaultPlusMECWithNC.

Component	Model
Nuclear model	Bodek-Ritchie RFG [185]
Meson exchange currents (MEC)	Dytman Empirical [91]
Coherent pion production (COH)	Rein-Seghal [87]
Quasi-elastic scattering (QE)	Llewellyn-Smith [60]
Resonant pion production (RES)	Rein-Seghal [89]
Deep inelastic scattering (DIS)	Bodek-Yang [94]
Final state interactions (FSI)	INTRANUKE hA2015 [91]

normalisation in all channels around the peak of the lepton momentum distribution with the biggest differences being in the MEC and DIS channels. There was also a significant shape difference in the MEC channel, likely the result of the more theoretically motivated model used in GENIE v3.

The systematic uncertainties were also evaluated for the GENIE v2 rate predictions, shown in Appendix B, with the total rate uncertainties given in Table 7.10. Most sources of systematic uncertainties were consistent but there was significant difference in the GENIE uncertainties. The cause for this becomes apparent when the GENIE universe variations are plotted, Figure 7.27. There was a bias in the simulated value away from the mean of the universe variations for GENIE v3. It is unlikely that the model uncertainties have increased, but it may be the case that the reweighting parameters have not been fully verified for GENIE version 3. It is possible that Gaussian variations of the parameters result in non-Gaussian uncertainties on the cross section, but given the large differences between the uncertainties on the two model configurations this is unlikely.

To investigate the model separation, one model was treated as data, and the statistical and systematic uncertainties were used to generate covariance matrices for single and double differential cross section measurements, as in Appendix A. The other model was treated normally as a Monte Carlo prediction.

The fake data and Monte Carlo prediction were then compared through a χ^2 test statistic
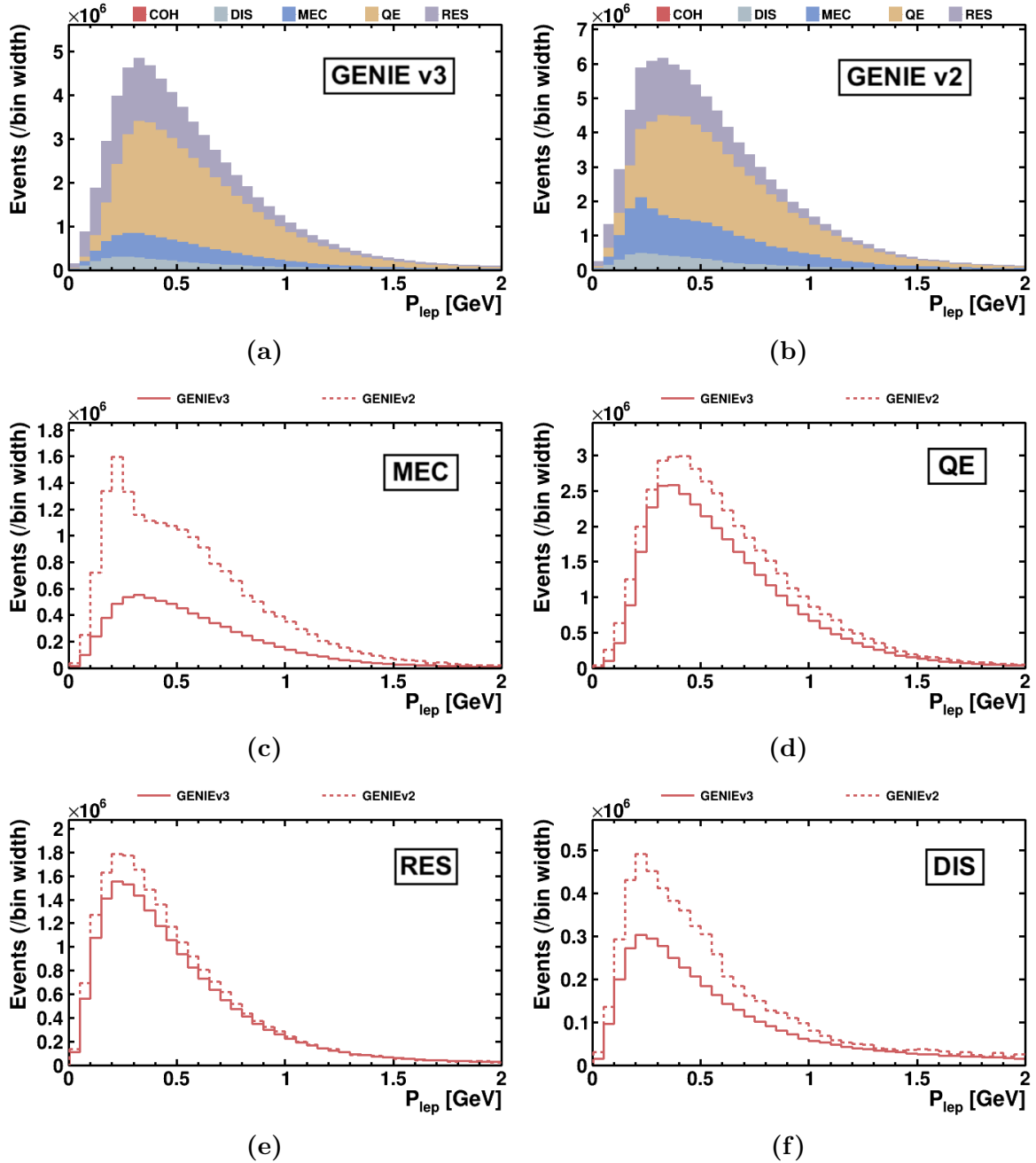
Figure 7.26: (a) GENIE v2 and (b) v3 predicted event rates in true muon momentum. The event rates are further separated into (c) meson exchange currents, (d) quasi-elastic scattering, (e) resonant pion production and (f) deep inelastic scattering channels.

Table 7.10: Summary of systematic uncertainties on the expectation of the total rate of reconstructed and selected ν_μ CC interactions in the fiducial volume predicted by the GENIE v2 model configuration.

Source of uncertainty	Percentage
Flux	6.61%
GENIE modelling	5.48%
Detector performance	2.71%
External background subtraction	0.47%
Cosmic misidentification	1.00%
POT counting	2.00%
Total systematic	9.29%
Total statistical	0.06%
Total	**9.29%**

(a)   (b)
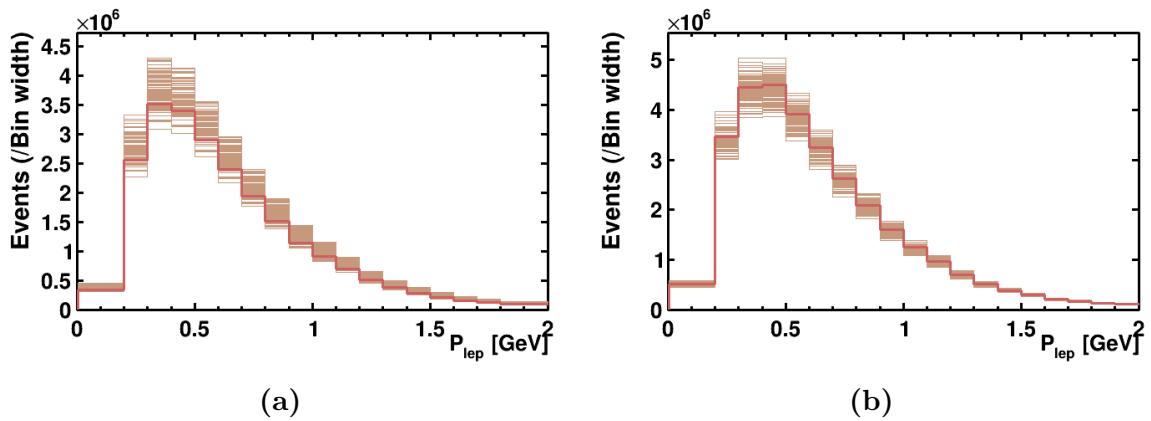
Figure 7.27: GENIE systematic universe variations to the reconstructed muon momentum rate for (a) GENIE v3 and (b) GENIE v2.

Table 7.11: P values from χ^2 test for comparisons between GENIE model configurations with systematic uncertainties. GENIE version 3 (Gv3) was used to generate the fake data.

	χ^2	$ndof$	p value
P_μ	71.3	17	1.26×10^{-8}
$\cos\theta_\mu$	105.1	24	4.06×10^{-12}
$P_\mu, \cos\theta_\mu$	2513.8	79	0

that accounts for correlated variables,

$$\chi^2 = \sum_{ij} (\sigma_i - \mu_i) \cdot Cov_{ij}^{-1} \cdot (\sigma_j - \mu_j) \tag{7.21}$$

where σ_i is the measured single or double differential cross section in bin i, μ_i is the predicted cross section and Cov^{-1} is the inverse of the covariance matrix defined in Equation 7.20.

The predictions of the two models in reconstructed muon momentum and $\cos\theta$ can be seen in Figure 7.28. The GENIE v3 prediction treated as data is shown with the expected systematic and statistical uncertainty at the full 6.6×10^{20} POT. The results of the χ^2 test are given in Table 7.11. The one dimensional binning was the same as in Figure 7.14 and the two dimensional binning as in Figure 7.15.

The p values appear to show that SBND would have a very strong distinguishing power between the two model configurations. This is slightly misleading because it does not account for the systematic uncertainties in the model predictions. There are several options for including model systematics in p value calculations [186] but this is additionally complicated by the fact that many of the uncertainties are correlated between the measurement and prediction. This is not the case when studying the rate as no model dependent corrections have been applied and so direct rate comparisons with models may provide a better statistical test [182].

(a)

(b)

(c)

(d)
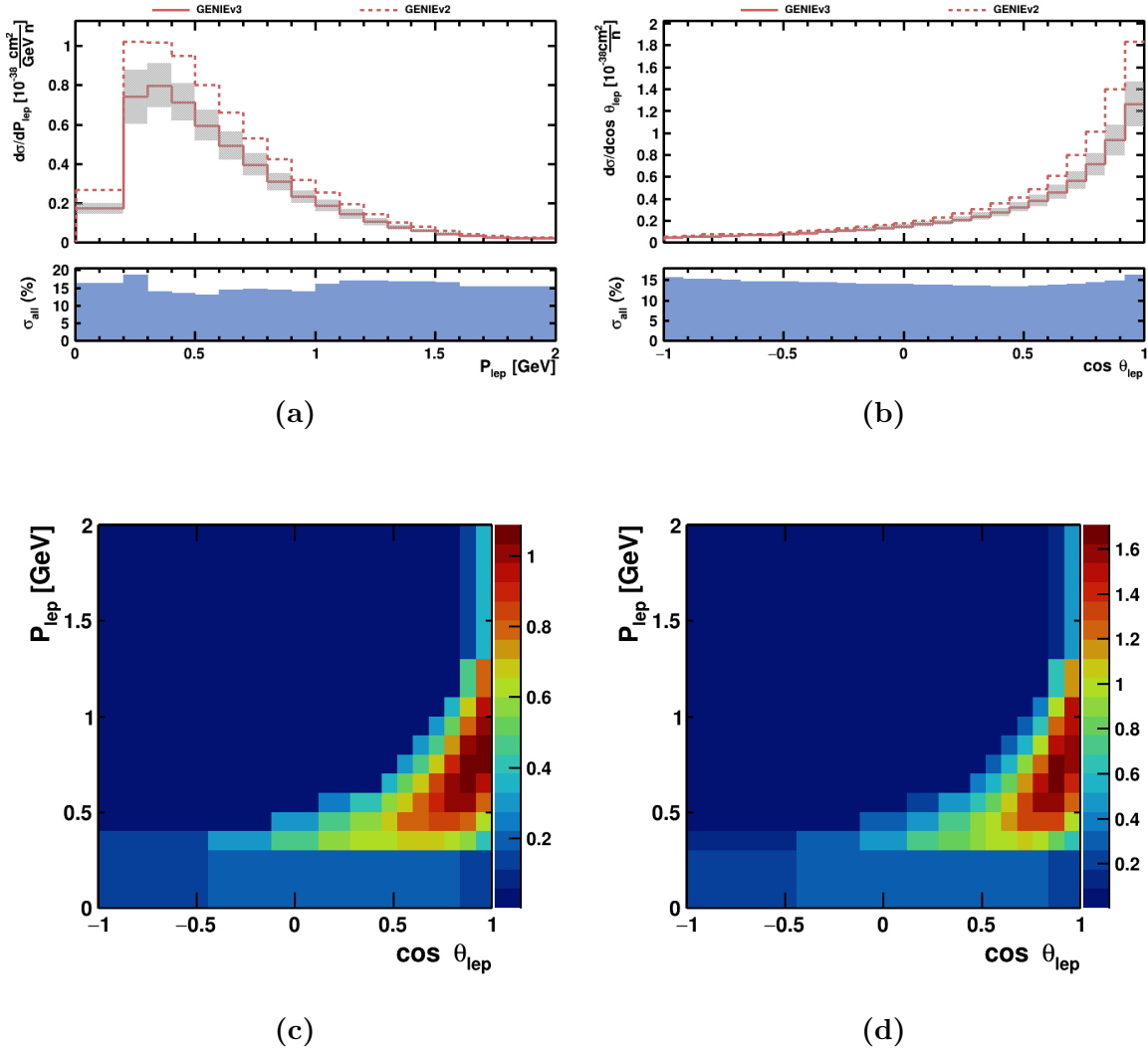
Figure 7.28: Comparison of expected measured cross sections from GENIE v2 and v3 model configurations in reconstructed (a) P_μ, (b) $\cos\theta_\mu$ and $P_\mu, \cos\theta_\mu$ for (c) v3 and (d) v2. The v3 prediction was treated as data with statistical and systematic uncertainties shown on the single differential cross section plot. The 2D slice comparisons are shown in Appendix C.

Chapter 8

Conclusions

SBND has the potential to make an important contribution to the field of neutrino-nucleus cross section modelling thanks to its high event rate, wide acceptance and millimetre level position resolution. This thesis has provided an in-depth report on the status of construction and calibration tools, the procedure that will be used for performing an muon neutrino charged current inclusive selection, and an estimate of the model separation in this channel at the expected POT of SBND.

The majority of the cross section model uncertainties arise from the treatment of the nuclear target and this will have direct consequences for future oscillation experiments such as DUNE. It is inadvisable to attempt to directly measure nuclear and cross section model parameters through the inclusive scattering channel. This is due to large flux uncertainties, unknown momentum transfers and complicated final state interactions. However, it is the work that goes into the rejection of backgrounds and understanding the detector when doing an inclusive measurement that provides a gateway to more exclusive channels.

It is the exclusive channels where SBND comes in to its own. The ability to reconstruct protons emerging from the nucleus, potentially down to kinetic energies of a few 10s of MeV [121, 187], will provide stringent tests of np-nh models. The charged current channel with one proton also allows for a less biased reconstruction of the incoming neutrino energy [188]. It will also allow the study of transverse variables where the contribution of less well understood effects may be enhanced [120].

There is also an opportunity to compare the measured neutrino-argon cross sections with neutrino-oxygen cross sections from the ANNIE detector [189] currently running in an adjacent building. The two detectors will be exposed to a nearly identical neutrino flux, and, as in an oscillation analysis, many systematic uncertainties would cancel. A joint analysis would help to reduce uncertainties and maximise the physics sensitivity when potentially combining DUNE [7] and Hyper-K [50] results in the future.

With all of its cross section measurements, SBND has a duty to present them in a way that maximises their usefulness to both the experimental and theoretical communities. Therefore, for the sake of being able to quickly compare to past theoretical predictions, the unfolded cross sections in true kinematic variables can be presented. To preserve the value of the data for future model builders, the data should also be presented in a way that minimises the dependence on any cross section models.

One way of doing this is to provide cross sections in terms of reconstructed variables, as in Section 7.2, and a response matrix that can be applied to model predictions. This method removes the bias incurred by unfolding [167], and the response matrix can be constructed with minimal model dependencies by having a much finer binning in all of the true variables that affect the reconstruction [182].

It is also possible to take this one step further and publish the rate measured in the detector along with a response matrix that includes truth binning for background processes [182]. This may be preferable for some channels as the main sources of backgrounds arise from other neutrino interactions, so both the signal and background predictions are able to evolve with improved modelling.

However the measurements are eventually presented, the SBND ν_μ CC inclusive selection is in a good position to be quickly calibrated and then applied to data when the detector becomes operational. The main source of backgrounds, cosmic ray muons, can be reduced by 99.96%, and the total efficiency of selecting signal events in the defined fiducial volume is expected to be 67% with a purity of 90%. The huge reduction in external backgrounds means the measurement will be less sensitive to the often large systematic uncertainties that are associated with them.

The large uncertainties on the neutrino flux are a limiting factor to the sensitivity as it can be difficult to disentangle whether deviations between predictions and data are from flux or cross section modelling. This work has shown that the flux uncertainty on the predicted rates are 4.5% smaller than on flux-integrated cross section measurements. The high event rate can also be used to reduce these uncertainties further through the measurement of neutrino electron scattering [190]. In the absence of FSI the neutrino energy can be reconstructed from final state kinematics and the flux can be constrained.

There are several areas in both the selection and cross section analysis that have the potential to be optimised or improved. The usage of the PDS is still in its infancy and only a fraction of the available information has been used in this analysis. More advanced flash matching methods will reduce the external background further while keeping more neutrino events. The inclusion of additional light information could also be used to improve the track and calorimetry reconstruction.

The tools developed for identifying the primary muon could be input to an MVA to identify other track-like particles for exclusive channel measurements. There is also potential for using deep learning techniques at different stages of the analysis given the volume of data available from a LArTPC.

Biases between the simulated values and means of the GENIE and flux systematic variation universes artificially increase the uncertainty on both the rate and cross section measurements. The simulated parameters could be modified to better align with the most probable values or the variations could be modified to be more representative of the true uncertainties. This will reduce the systematic uncertainties and make the comparisons between models and data more statistically meaningful [167].

In summary, SBND is well placed to begin calibrating and producing charged current muon neutrino cross section measurements. The high efficiency and purity of the inclusive measurement along with studies into the identification of other track-like particles should allow branching into exclusive channels to be done consistently and easily. The tooling developed to investigate the sensitivity of SBND to different model configurations already supports exclusive channels, and could be easily adapted to become the interface between

models and data.

There is great need for more neutrino-nucleus interaction measurements in the precision era of neutrino oscillation physics, and this need may only grow further if the neutrino reveals more unexpected properties in the future. SBND will form an integral part of this, both through studies of short-baseline oscillations and through the largest sample of neutrino-argon interactions to date.

Bibliography

[1] W. Pauli, "Dear radioactive ladies and gentlemen", *Phys. Today* 31N9 (1979), p. 27.

[2] C. L. Cowan et al., "Detection of the free neutrino: A confirmation", *Science.* 124.3212 (1956), pp. 103–104, DOI: `10.1126/science.124.3212.103`.

[3] Andrej Dmitrievich Sakharov, "Violation of CP invariance, C asymmetry, and baryon asymmetry of the universe", *JETP Lett.* 5 (1967), pp. 24–27.

[4] Pablo F. de Salas et al., "Neutrino Mass Ordering from Oscillations and Beyond: 2018 Status and Future Prospects", *Front. Astron. Sp. Sci.* 5 (2018), DOI: `10.3389/fspas.2018.00036`, arXiv: `1806.11051`.

[5] O. G. Miranda et al., "Exploring the potential of short-baseline physics at Fermilab", *Phys. Rev. D* 97.9 (2018), DOI: `10.1103/PhysRevD.97.095026`, arXiv: `1802.02133`.

[6] L. Alvarez-Ruso et al., "NuSTEC White Paper: Status and challenges of neutrino-nucleus scattering", *Prog. Part. Nucl. Phys.* 100 (2018), pp. 1–68, DOI: `10.1016/j.ppnp.2018.01.006`, arXiv: `1706.03621`.

[7] B. Abi et al., "The DUNE Far Detector Interim Design Report Volume 1: Physics, Technology and Strategies" (2018), arXiv: `1807.10334`.

[8] C. Rubbia, "The Liquid Argon Time Projection Chamber: A New Concept For Neutrino Detectors", *CERN-EP-INT-77-08* (1977).

[9] K. Abe et al., "The T2K experiment", *Nucl. Instruments Methods Phys. Res. Sect. A Accel. Spectrometers, Detect. Assoc. Equip.* 659.1 (2011), pp. 106–135, DOI: `10.1016/J.NIMA.2011.06.067`.

[10] L. Aliaga et al., "Design, calibration, and performance of the MINERvA detector", *Nucl. Instruments Methods Phys. Res. Sect. A Accel. Spectrometers, Detect. Assoc. Equip.* 743 (2014), pp. 130–159, DOI: `10.1016/j.nima.2013.12.053`, arXiv: `1305.5199`.

Bibliography

[11] R. Acciarri et al., "A Proposal for a Three Detector Short-Baseline Neutrino Oscillation Program in the Fermilab Booster Neutrino Beam" (2015), arXiv: 1503.01520.

[12] Diego Garcia-Gamez et al., "A novel electrical method to measure wire tensions for time projection chambers", *Nucl. Instruments Methods Phys. Res. Sect. A Accel. Spectrometers, Detect. Assoc. Equip.* 915 (2019), pp. 75–81, DOI: 10.1016/j.nima.2018.09.031, arXiv: 1804.05941.

[13] J. Chadwick, "The intensity distribution in the magnetic spectrum of beta particles from radium (B+ C)", *Verh. Phys. Gesell* 16 (1914), p. 383.

[14] E. Fermi, "Versuch einer Theorie der β-Strahlen. I", *Zeitschrift für Phys.* 88.3-4 (1934), pp. 161–177, DOI: 10.1007/BF01351864.

[15] G. Danby et al., "Observation of high-energy neutrino reactions and the existence of two kinds of neutrinos", *Phys. Rev. Lett.* 9.1 (1962), pp. 36–44, DOI: 10.1103/PhysRevLett.9.36.

[16] M. L. Perl et al., "Evidence for anomalous lepton production in $e^+ - e^-$ annihilation", *Phys. Rev. Lett.* 35.22 (1975), pp. 1489–1492, DOI: 10.1103/PhysRevLett.35.1489.

[17] K. Kodama et al., "Observation of tau neutrino interactions", *Phys. Lett. Sect. B Nucl. Elem. Part. High-Energy Phys.* 504.3 (2001), pp. 218–224, DOI: 10.1016/S0370-2693(01)00307-0, arXiv: 0012035 [hep-ex].

[18] D. DeCamp et al., "Determination of the number of light neutrino species", *Phys. Lett. B* 231.4 (1989), pp. 519–529, DOI: 10.1016/0370-2693(89)90704-1.

[19] J. A. Bagger et al., "Precision electroweak measurements on the Z resonance", *Phys. Rep.* 427.5-6 (2006), pp. 257–454, DOI: 10.1016/j.physrep.2005.12.006, arXiv: 0509008 [hep-ex].

[20] Emmy Noether, "Invariant Variation Problems", *Transp. Theory Stat. Phys.* 1.3 (1971), pp. 186–207, DOI: 10.1080/00411457108231446, arXiv: 0503066 [physics].

[21] T. D. Lee and C. N. Yang, "Question of Parity Conservation in Weak Interactions", *Phys. Rev.* 104.1 (1956), pp. 254–258, DOI: 10.1103/PhysRev.104.254.

[22] C. S. Wu et al., "Experimental Test of Parity Conservation in Beta Decay", *Phys. Rev.* 105.4 (1957), pp. 1413–1415, DOI: 10.1103/PhysRev.105.1413.

[23] M. Goldhaber, L. Grodzins, and A. W. Sunyar, "Evidence for Circular Polarization of Bremsstrahlung Produced by Beta Rays", *Phys. Rev.* 106.4 (1957), pp. 826–828, DOI: 10.1103/PhysRev.106.826.

[24] H. A. Bethe, "Energy Production in Stars", *Phys. Rev.* 55.5 (1939), pp. 434–456, DOI: 10.1103/PhysRev.55.434.

[25]   Raymond Davis, Don S. Harmer, and Kenneth C. Hoffman, "Search for Neutrinos from the Sun", *Phys. Rev. Lett.* 20.21 (1968), pp. 1205–1209, DOI: 10.1103/PhysRevLett.20.1205.

[26]   B. Pontecorvo, "Inverse Beta Processes and Nonconservation of Lepton Chare", *J. Exptl. Theor. Phys.* 34 (1958), pp. 247–249.

[27]   B. Pontecorvo, "Neutrino Experiments and the Problem of Conservation of Leptonic Charge", *Sov. J. Exp. Theor. Phys.* 26 (1968), p. 984.

[28]   Ziro Maki, Masami Nakagawa, and Shoichi Sakata, "Remarks on the Unified Model of Elementary Particles", *Prog. Theor. Phys.* 28.5 (1962), pp. 870–880, DOI: 10.1143/ptp.28.870.

[29]   Michael Edward Peskin and Daniel V. Schroeder, *An Introduction To Quantum Field Theory*, Westview Press, 1995.

[30]   T. J. Haines et al., "Calculation of Atmospheric Neutrino-Induced Backgrounds in a Nucleon-Decay Search", *Phys. Rev. Lett.* 57.16 (1986), pp. 1986–1989, DOI: 10.1103/PhysRevLett.57.1986.

[31]   Masayuki Nakahata et al., "Atmospheric Neutrino Background and Pion Nuclear Effect for KAMIOKA Nucleon Decay Experiment", *J. Phys. Soc. Japan* 55.11 (1986), pp. 3786–3805, DOI: 10.1143/JPSJ.55.3786.

[32]   Y. Fukuda et al., "Evidence for oscillation of atmospheric neutrinos", *Phys. Rev. Lett.* 81.8 (1998), pp. 1562–1567, DOI: 10.1103/PhysRevLett.81.1562, arXiv: 9807003 [hep-ex].

[33]   Q. R. Ahmad et al., "Measurement of the rate of $\nu_e + d \rightarrow p + p + e^-$ interactions produced by 8B solar neutrinos at the sudbury neutrino observatory", *Phys. Rev. Lett.* 87.7 (2001), pp. 71301–1–71301–4, DOI: 10.1103/PhysRevLett.87.071301, arXiv: 0106015 [nucl-ex].

[34]   S. M. Bilenky and J. Hošek, "Glashow-Weinberg-Salam theory of electroweak interactions and the neutral currents", *Phys. Rep.* 90.2 (1982), pp. 73–157, DOI: 10.1016/0370-1573(82)90016-3.

[35]   Paul Langacker, Jens Erler, and Eduardo Peinado, "Neutrino physics", *J. Phys. Conf. Ser.* 18.1 (2005), pp. 154–187, DOI: 10.1088/1742-6596/18/1/004, arXiv: 0506257 [hep-ph].

[36]   Peter W. Higgs, "Broken symmetries and the masses of gauge bosons", *Phys. Rev. Lett.* 13.16 (1964), pp. 508–509, DOI: 10.1103/PhysRevLett.13.508.

[37]   Ettore Majorana, "Teoria simmetrica dell'elettrone e del positrone", *Nuovo Cim.* 14.4 (1937), pp. 171–184, DOI: 10.1007/BF02961314.

Bibliography

[38] T. Yanagida, "Horizontal Symmetry and Masses of Neutrinos", *Prog. Theor. Phys.* 64.3 (1980), pp. 1103–1105, DOI: 10.1143/ptp.64.1103.

[39] V. N. Aseev et al., "Upper limit on the electron antineutrino mass from the Troitsk experiment", *Phys. Rev. D - Part. Fields, Gravit. Cosmol.* 84.11 (2011), p. 112003, DOI: 10.1103/PhysRevD.84.112003.

[40] P. Hernández, "Neutrino physics", *2015 Cern. Sch. High-Energy Physics, Proc.* Vol. 2015-March, CERN, 2016, pp. 85–142, DOI: 10.5170/CERN-2016-005.85, arXiv: 1708.01046.

[41] R.N. Mohapatra and P.B. Pal, "Massive neutrinos in physics and astrophysics. Second edition", *World Sci.Lect.Notes Phys.* 60 (1998), pp. 1–451.

[42] Ivan Esteban et al., "Global analysis of three-flavour neutrino oscillations: synergies and tensions in the determination of θ 23 , δ CP , and the mass ordering", *J. High Energy Phys.* 2019.1 (2019), DOI: 10.1007/JHEP01(2019)106, arXiv: 1811.05487.

[43] L. Wolfenstein, "Neutrino oscillations in matter", *Phys. Rev. D* 17.9 (1978), pp. 2369–2374, DOI: 10.1103/PhysRevD.17.2369.

[44] S. P. Mikheyev and A. Yu Smirnov, "Resonant amplification of ν oscillations in matter and solar-neutrino spectroscopy", *Nuovo Cim. C* 9.1 (1986), pp. 17–26, DOI: 10.1007/BF02508049.

[45] M. Tanabashi et al., "Review of Particle Physics", *Phys. Rev. D* 98.3 (2018), p. 030001, DOI: 10.1103/PhysRevD.98.030001.

[46] I. Girardi, S. T. Petcov, and A. V. Titov, "Predictions for the Majorana CP violation phases in the neutrino mixing matrix and neutrinoless double beta decay", *Nucl. Phys. B* 911 (2016), pp. 754–804, DOI: 10.1016/j.nuclphysb.2016.08.019, arXiv: 1605.04172.

[47] S.M. Bilenky, J. Hošek, and S.T. Petcov, "On the oscillations of neutrinos with Dirac and Majorana masses", *Phys. Lett. B* 94.4 (1980), pp. 495–498, DOI: 10.1016/0370-2693(80)90927-2.

[48] M. A. Acero et al., "New constraints on oscillation parameters from ν e appearance and ν μ disappearance in the NOvA experiment", *Phys. Rev. D* 98.3 (2018), p. 032012, DOI: 10.1103/PhysRevD.98.032012.

[49] K. Abe et al., "Search for CP Violation in Neutrino and Antineutrino Oscillations by the T2K Experiment with 2.21021 Protons on Target", *Phys. Rev. Lett.* 121.17 (2018), DOI: 10.1103/PhysRevLett.121.171802, arXiv: 1807.07891.

[50] K. Abe et al., "Letter of Intent: The Hyper-Kamiokande Experiment — Detector Design and Physics Potential —" (2011), arXiv: 1109.3262.

[51] Marco Drewes, "The phenomenology of right handed neutrinos", *Int. J. Mod. Phys. E* 22.8 (2013), DOI: `10.1142/S0218301313300191`, arXiv: `1303.6912`.

[52] A. Aguilar et al., "Evidence for neutrino oscillations from the observation of $\bar{\nu}_e$ appearance in a $\bar{\nu}_\mu$ beam", *Phys. Rev. D* 64.11 (2001), p. 112007, DOI: `10.1103/PhysRevD.64.112007`.

[53] A. A. Aguilar-Arevalo et al., "Significant Excess of Electronlike Events in the MiniBooNE Short-Baseline Neutrino Experiment", *Phys. Rev. Lett.* 121.22 (2018), p. 221801, DOI: `10.1103/PhysRevLett.121.221801`.

[54] G. Mention et al., "Reactor antineutrino anomaly", *Phys. Rev. D* 83.7 (2011), p. 073006, DOI: `10.1103/PhysRevD.83.073006`.

[55] Mario A. Acero, Carlo Giunti, and Marco Laveder, "Limits on ν_e and $\bar{\nu}_e$ disappearance from Gallium and reactor experiments", *Phys. Rev. D* 78.7 (2008), p. 073009, DOI: `10.1103/PhysRevD.78.073009`.

[56] Mona Dentler et al., "Updated global analysis of neutrino oscillations in the presence of eV-scale sterile neutrinos", *J. High Energy Phys.* 2018.8 (2018), DOI: `10.1007/JHEP08(2018)010`, arXiv: `1803.10661`.

[57] M. G. Aartsen et al., "Searches for Sterile Neutrinos with the IceCube Detector", *Phys. Rev. Lett.* 117.7 (2016), p. 071801, DOI: `10.1103/PhysRevLett.117.071801`.

[58] P. Adamson et al., "Search for Sterile Neutrinos in MINOS and MINOS+ Using a Two-Detector Fit", *Phys. Rev. Lett.* 122.9 (2019), DOI: `10.1103/PhysRevLett.122.091803`, arXiv: `1710.06488`.

[59] Teppei Katori and Marco Martini, "Neutrino-nucleus cross sections for oscillation experiments", *J. Phys. G Nucl. Part. Phys.* 45.1 (2018), DOI: `10.1088/1361-6471/aa8bf7`, arXiv: `1611.07770`.

[60] C. H. Llewellyn Smith, "Neutrino reactions at accelerator energies", *Phys. Rep.* 3.5 (1972), pp. 261–379, DOI: `10.1016/0370-1573(72)90010-5`.

[61] Robert Hofstadter, "Electron scattering and nuclear structure", *Rev. Mod. Phys.* 28.3 (1956), pp. 214–254, DOI: `10.1103/RevModPhys.28.214`.

[62] Jouni T. Suhonen, "Value of the axial-vector coupling strength in β and $\beta\beta$ decays: A review", *Front. Phys.* 5.NOV (2017), p. 55, DOI: `10.3389/fphy.2017.00055`, arXiv: `1712.01565`.

[63] J. R. Dunning et al., "Quasi-elastic electron-deuteron scattering and neutron form factors", *Phys. Rev.* 141.4 (1966), pp. 1286–1297, DOI: `10.1103/PhysRev.141.1286`.

[64] Bhubanjyoti Bhattacharya, Richard J. Hill, and Gil Paz, "Model-independent determination of the axial mass parameter in quasielastic neutrino-nucleon scattering", *Phys. Rev. D - Part. Fields, Gravit. Cosmol.* 84.7 (2011), DOI: `10.1103/ PhysRevD.84.073006`, arXiv: `1108.0423`.

[65] Omar Benhar et al., "Electron- and neutrino-nucleus scattering in the impulse approximation regime", *Phys. Rev. D - Part. Fields, Gravit. Cosmol.* 72.5 (2005), DOI: `10.1103/PhysRevD.72.053005`, arXiv: `0506116 [hep-ph]`.

[66] V.R. Pandharipande, "Many-body theory of electron-nucleus scattering", *Nucl. Phys. B - Proc. Suppl.* 112.1-3 (2003), pp. 51–56, DOI: `10.1016/s0920-5632(02) 01762-0`.

[67] Taber De Forest, "Off-shell electron-nucleon cross sections. The impulse approximation", *Nucl. Physics, Sect. A* 392.2-3 (1983), pp. 232–248, DOI: `10.1016/0375-9474(83)90124-0`.

[68] Gerald A. Miller, "Fermi Gas Model", *Nucl. Phys. B - Proc. Suppl.* 112.1-3 (2003), pp. 223–225, DOI: `10.1016/s0920-5632(02)01786-3`.

[69] Carlos A. Bertulani, *Nuclear physics in a nutshell*, Princeton University Press, 2007, p. 473.

[70] Joanna Ewa Sobczyk, "Accuracy of the lepton-nucleus scattering models in the quasielastic region", *Phys. Rev. C* 96.4 (2017), DOI: `10.1103/PhysRevC.96. 045501`, arXiv: `1706.06739`.

[71] J. Nieves, J. E. Amaro, and M. Valverde, "Inclusive quasielastic charged-current neutrino-nucleus reactions", *Phys. Rev. C - Nucl. Phys.* 70.5 (2004), DOI: `10.1103/ PhysRevC.70.055503`, arXiv: `0408005 [nucl-th]`.

[72] H. Hassanabadi, A. Armat, and L. Naderi, "Relativistic Fermi-Gas Model for Nucleus", *Found. Phys.* 44.11 (2014), pp. 1188–1194, DOI: `10.1007/s10701-014-9836-7`.

[73] D. R. Hartree, "The Wave Mechanics of an Atom with a Non-Coulomb Central Field. Part II. Some Results and Discussion", *Math. Proc. Cambridge Philos. Soc.* 24.1 (1928), pp. 111–132, DOI: `10.1017/S0305004100011920`.

[74] P G Reinhard, "The relativistic mean-field description of nuclei and nuclear dynamics", *Reports Prog. Phys.* 52.4 (1989), pp. 439–514, DOI: `10.1088/0034-4885/52/4/002`.

[75] R. Subedi et al., "Probing cold dense nuclear matter", *Science.* 320.5882 (2008), pp. 1476–1478, DOI: `10.1126/science.1156675`.

Bibliography

[76] M. Chemtob and M. Rho, "Meson exchange currents in nuclear weak and electromagnetic interactions", *Nucl. Physics, Sect. A* 163.1 (1971), pp. 1–55, DOI: 10.1016/0375-9474(71)90520-3.

[77] R. Machleidt and D. R. Entem, "Chiral effective field theory and nuclear forces", *Phys. Rep.* 503.1 (2011), pp. 1–75, DOI: 10.1016/j.physrep.2011.02.001, arXiv: 1105.2919.

[78] David Pines and David Bohm, "A collective description of electron interactions: II. Collective vs individual particle aspects of the interactions", *Phys. Rev.* 85.2 (1952), pp. 338–353, DOI: 10.1103/PhysRev.85.338.

[79] D. J. Thouless, "Vibrational states of nuclei in the random phase approximation", *Nucl. Phys.* 22.1 (1961), pp. 78–95, DOI: 10.1016/0029-5582(61)90364-9.

[80] J. A. Formaggio and G. P. Zeller, "From eV to EeV: Neutrino cross sections across energy scales", *Rev. Mod. Phys.* 84.3 (2012), pp. 1307–1341, DOI: 10.1103/RevModPhys.84.1307.

[81] Ulrich Mosel, "Neutrino event generators: foundation, status and future", *J. Phys. G Nucl. Part. Phys.* 46.11 (2019), p. 113001, DOI: 10.1088/1361-6471/ab3830, arXiv: 1904.11506.

[82] J. Nieves, I. Ruiz Simo, and M. J.Vicente Vacas, "Inclusive charged-current neutrino-nucleus reactions", *Phys. Rev. C - Nucl. Phys.* 83.4 (2011), DOI: 10.1103/PhysRevC.83.045501, arXiv: 1102.2777.

[83] R. Gran et al., "Neutrino-nucleus quasi-elastic and 2p2h interactions up to 10 GeV", *Phys. Rev. D - Part. Fields, Gravit. Cosmol.* 88.11 (2013), DOI: 10.1103/PhysRevD.88.113007, arXiv: 1307.8105.

[84] J. E. Amaro et al., "Using electron scattering superscaling to predict charge-changing neutrino cross sections in nuclei", *Phys. Rev. C - Nucl. Phys.* 71.1 (2005), DOI: 10.1103/PhysRevC.71.015501, arXiv: 0409078 [nucl-th].

[85] M. Martini et al., "Unified approach for nucleon knock-out and coherent and incoherent pion production in neutrino interactions with nuclei", *Phys. Rev. C - Nucl. Phys.* 80.6 (2009), DOI: 10.1103/PhysRevC.80.065501, arXiv: 0910.2622.

[86] V. Pandey et al., "Impact of low-energy nuclear excitations on neutrino-nucleus scattering at MiniBooNE and T2K kinematics", *Phys. Rev. C* 94.5 (2016), DOI: 10.1103/PhysRevC.94.054609, arXiv: 1607.01216.

[87] D. Rein and L. M. Sehgal, "Coherent production of photons by neutrinos", *Phys. Lett. B* 104.5 (1981), pp. 394–398, DOI: 10.1016/0370-2693(81)90706-1.

[88]   D. Rein and L. M. Sehgal, "PCAC and the deficit of forward muons in $\pi+$ production by neutrinos", *Phys. Lett. Sect. B Nucl. Elem. Part. High-Energy Phys.* 657.4-5 (2007), pp. 207–209, DOI: 10.1016/j.physletb.2007.10.025, arXiv: 0606185 [hep-ph].

[89]   Dieter Rein and Lalit M Sehgal, "Neutrino-excitation of baryon resonances and single pion production", *Ann. Phys. (N. Y).* 133.1 (1981), pp. 79–153, DOI: 10.1016/0003-4916(81)90242-6.

[90]   R. P. Feynman, M. Kislinger, and F. Ravndal, "Current matrix elements from a relativistic quark model", *Phys. Rev. D* 3.11 (1971), pp. 2706–2732, DOI: 10.1103/PhysRevD.3.2706.

[91]   Costas Andreopoulos et al., "The GENIE Neutrino Monte Carlo Generator: Physics and User Manual" (2015), arXiv: 1510.05494.

[92]   Ch. Berger and L. M. Sehgal, "Lepton Mass Effects in Single Pion Production by Neutrinos", *Phys. Rev. D - Part. Fields, Gravit. Cosmol.* 76.11 (2007), DOI: 10.1103/PhysRevD.76.113004, arXiv: 0709.4378.

[93]   Ch Berger and L. M. Sehgal, "Partially conserved axial vector current and coherent pion production by low energy neutrinos", *Phys. Rev. D - Part. Fields, Gravit. Cosmol.* 79.5 (2009), DOI: 10.1103/PhysRevD.79.053003.

[94]   A. Bodek and U. K. Yang, "Higher twist, ζw scaling, and effective LO PDFs for lepton scattering in the few GeV region", *J. Phys. G Nucl. Part. Phys.* Vol. 29, 8, 2003, pp. 1899–1905, DOI: 10.1088/0954-3899/29/8/369, arXiv: 0210024 [hep-ex].

[95]   Tomasz Golan, Cezary Juszczak, and Jan T. Sobczyk, "Effects of final-state interactions in neutrino-nucleus interactions", *Phys. Rev. C - Nucl. Phys.* 86.1 (2012), DOI: 10.1103/PhysRevC.86.015505, arXiv: 1202.4197.

[96]   N. Metropolis et al., "Monte Carlo Calculations on Intranuclear Cascades. I. Low-Energy Studies", *Phys. Rev.* 110.1 (1958), pp. 185–203, DOI: 10.1103/PhysRev.110.185.

[97]   O. Buss et al., "Transport-theoretical description of nuclear reactions", *Phys. Rep.* 512.1-2 (2012), pp. 1–124, DOI: 10.1016/j.physrep.2011.12.001, arXiv: 1106.1344.

[98]   C. Andreopoulos et al., "The GENIE Neutrino Monte Carlo Generator", *Nucl. Instruments Methods Phys. Res. Sect. A Accel. Spectrometers, Detect. Assoc. Equip.* 614.1 (2009), pp. 87–104, DOI: 10.1016/j.nima.2009.12.009, arXiv: 0905.2517.

[99]   W. A. Mann et al., "Study of the Reaction $\nu_\mu + n \rightarrow \mu^- + p$", *Phys. Rev. Lett.* 31.13 (1973), pp. 844–847, DOI: 10.1103/PhysRevLett.31.844.

[100] S. J. Barish et al., "Study of neutrino interactions in hydrogen and deuterium: Description of the experiment and study of the reaction $\nu_\mu + d \to \mu^- + p + p_s$", *Phys. Rev. D* 16.11 (1977), pp. 3103–3121, DOI: `10.1103/PhysRevD.16.3103`.

[101] N. J. Baker et al., "Quasielastic neutrino scattering: A measurement of the weak nucleon axial-vector form factor", *Phys. Rev. D* 23.11 (1981), pp. 2499–2505, DOI: `10.1103/PhysRevD.23.2499`.

[102] T. Kitagaki et al., "High-energy quasielastic $\nu_\mu n \to \mu^- p$ scattering in deuterium", *Phys. Rev. D* 28.3 (1983), pp. 436–442, DOI: `10.1103/PhysRevD.28.436`.

[103] Véronique Bernard, Latifa Elouadrhiri, and Ulf G. Meißner, "Axial structure of the nucleon", *J. Phys. G Nucl. Part. Phys.* 28.1 (2002), DOI: `10.1088/0954-3899/28/1/201`, arXiv: `0107088 [hep-ph]`.

[104] A. A. Aguilar-Arevalo et al., "The MiniBooNE detector", *Nucl. Instruments Methods Phys. Res. Sect. A Accel. Spectrometers, Detect. Assoc. Equip.* 599.1 (2009), pp. 28–46, DOI: `10.1016/j.nima.2008.10.028`, arXiv: `0806.4201`.

[105] A. A. Aguilar-Arevalo et al., "Neutrino flux prediction at MiniBooNE", *Phys. Rev. D - Part. Fields, Gravit. Cosmol.* 79.7 (2009), DOI: `10.1103/PhysRevD.79.072002`, arXiv: `0806.1449`.

[106] A. A. Aguilar-Arevalo et al., "First measurement of the muon neutrino charged current quasielastic double differential cross section", *Phys. Rev. D* 81.9 (2010), p. 092005, DOI: `10.1103/PhysRevD.81.092005`.

[107] Luis Alvarez-Ruso, "Neutrino interactions: Challenges in the current theoretical picture", *Nucl. Phys. B - Proc. Suppl.* 229-232 (2012), pp. 167–173, DOI: `10.1016/j.nuclphysbps.2012.09.027`, arXiv: `1012.3871`.

[108] K. Abe et al., "T2K neutrino flux prediction", *Phys. Rev. D - Part. Fields, Gravit. Cosmol.* 87.1 (2013), DOI: `10.1103/PhysRevD.87.012001`, arXiv: `1211.0469`.

[109] L. Aliaga et al., "Neutrino flux predictions for the NuMI beam", *Phys. Rev. D* 94.9 (2016), DOI: `10.1103/PhysRevD.94.092005`, arXiv: `1607.00704`.

[110] T2K Collaboration et al., "Measurement of inclusive double-differential ν_μ charged-current cross section with improved acceptance in the T2K off-axis near detector", *Phys. Rev. D* 98.1 (2018), DOI: `10.1103/PhysRevD.98.012004`, arXiv: `1801.05148`.

[111] A. Filkins et al., "Double-Differential Inclusive Charged-Current ν_μ Cross Sections on Hydrocarbon in MINERvA at $\langle E_\nu \rangle \sim 3.5$ GeV" (2020), arXiv: `2002.12496`.

[112] Callum Wilkinson et al., "Reanalysis of bubble chamber measurements of muon-neutrino induced single pion production", *Phys. Rev. D - Part. Fields, Gravit. Cosmol.* 90.11 (2014), DOI: `10.1103/PhysRevD.90.112017`, arXiv: `1411.4482`.

Bibliography

[113] B. Eberly et al., "Charged pion production in $\nu\mu$ interactions on hydrocarbon at $\langle E_\nu \rangle$=4.0 GeV", *Phys. Rev. D - Part. Fields, Gravit. Cosmol.* 92.9 (2015), DOI: 10.1103/PhysRevD.92.092008, arXiv: 1406.6415.

[114] Olga Lalakulich and Ulrich Mosel, "Pion production in the MiniBooNE experiment", *Phys. Rev. C - Nucl. Phys.* 87.1 (2013), DOI: 10.1103/PhysRevC.87.014602, arXiv: 1210.4717.

[115] Jakub Zmuda and Krzysztof M. Graczyk, "Electroweak single pion production and form factors of the $\Delta(1232)$ resonance", *AIP Conf. Proc.* Vol. 1680, 2015, DOI: 10.1063/1.4931872, arXiv: 1501.03086.

[116] U. Mosel and K. Gallmeister, "Muon-neutrino-induced charged-current pion production on nuclei", *Phys. Rev. C* 96.1 (2017), DOI: 10.1103/PhysRevC.96.015503.

[117] R. González-Jiménez, K. Niewczas, and N. Jachowicz, "Pion production within the hybrid relativistic plane wave impulse approximation model at MiniBooNE and MINERvA kinematics", *Phys. Rev. D* 97.1 (2018), DOI: 10.1103/PhysRevD.97.013004.

[118] P. Stowell et al., "Tuning the genie pion production model with MINERvA data", *Phys. Rev. D* 100.7 (2019), DOI: 10.1103/PhysRevD.100.072005, arXiv: 1903.01558.

[119] K. Abe et al., "Measurement of the muon neutrino charged-current single π^+ production on hydrocarbon using the T2K off-axis near detector ND280", *Phys. Rev. D* 101 (2019), DOI: 10.1103/PhysRevD.101.012007, arXiv: 1909.03936.

[120] Stephen Dolan, "Exploring Nuclear Effects in Neutrino-Nucleus Interactions Using Measurements of Transverse Kinematic Imbalance from T2K and MINERvA" (2018), arXiv: 1810.06043.

[121] R. Acciarri et al., "Detection of back-to-back proton pairs in charged-current neutrino interactions with the ArgoNeuT detector in the NuMI low energy beam line", *Phys. Rev. D - Part. Fields, Gravit. Cosmol.* 90.1 (2014), DOI: 10.1103/PhysRevD.90.012008, arXiv: 1405.4261.

[122] C. Anderson et al., "The ArgoNeuT detector in the NuMI low-energy beam line at Fermilab", *J. Instrum.* 7.10 (2012), DOI: 10.1088/1748-0221/7/10/P10019, arXiv: 1205.6747.

[123] R. Acciarri et al., "Measurements of inclusive muon neutrino and antineutrino charged current differential cross sections on argon in the NuMI antineutrino beam", *Phys. Rev. D - Part. Fields, Gravit. Cosmol.* 89.11 (2014), DOI: 10.1103/PhysRevD.89.112003, arXiv: 1404.4809.

[124] R. Acciarri et al., "Design and construction of the MicroBooNE detector", *J. Instrum.* 12.2 (2017), DOI: 10.1088/1748-0221/12/02/P02017, arXiv: 1612.05824.

[125] C. Adams et al., "First Measurement of Inclusive Muon Neutrino Charged Current Differential Cross Sections on Argon at $E_\nu \sim 0.8$ GeV with the MicroBooNE Detector" (2019), arXiv: 1905.09694.

[126] N. Canci, "The ICARUS T600 Detector at LNGS Underground Laboratory", *Phys. Procedia*, vol. 37, Elsevier, 2012, pp. 1257–1265, DOI: 10.1016/j.phpro.2012.02.466.

[127] DUNE Collaboration et al., "The DUNE Far Detector Interim Design Report, Volume 2: Single-Phase Module" (2018), arXiv: 1807.10327.

[128] B. Abi et al., "The Single-Phase ProtoDUNE Technical Design Report" (2017), arXiv: 1706.07081.

[129] D. I. Britton et al., "Measurement of the branching ratio", *Phys. Rev. Lett.* 68.20 (1992), pp. 3000–3003, DOI: 10.1103/PhysRevLett.68.3000.

[130] G. Amelino-Camelia et al., "Physics with the KLOE-2 experiment at the upgraded DAΦNE", *Eur. Phys. J. C* 68.3 (2010), pp. 619–681, DOI: 10.1140/epjc/s10052-010-1351-1, arXiv: 1003.3868.

[131] M. G. Catanesi et al., "Measurement of the production cross-section of positive pions in the collision of 8.9 GeV/c protons on beryllium", *Eur. Phys. J. C* 52.1 (2007), pp. 29–53, DOI: 10.1140/epjc/s10052-007-0382-8, arXiv: 0702024 [hep-ex].

[132] I. Chemakin et al., "Pion production by protons on a thin beryllium target at 6.4, 12.3, and 17.5 GeV/c incident proton momenta", *Phys. Rev. C - Nucl. Phys.* 77.1 (2008), DOI: 10.1103/PhysRevC.77.015209, arXiv: 0707.2375.

[133] G. Cheng et al., "Measurement of K+ production cross section by 8 GeV protons using high-energy neutrino interactions in the SciBooNE detector", *Phys. Rev. D - Part. Fields, Gravit. Cosmol.* 84.1 (2011), DOI: 10.1103/PhysRevD.84.012009, arXiv: 1105.2871.

[134] C. Mariani et al., "Improved Parameterization of K^+ Production in p-Be Collisions at Low Energy Using Feynman Scaling", *Phys. Rev. D* 84.11 (2011), p. 114021, DOI: 10.1103/PhysRevD.84.114021, arXiv: 1110.0417.

[135] S. Agostinelli et al., "Geant4a simulation toolkit", *Nucl. Instruments Methods Phys. Res. Sect. A Accel. Spectrometers, Detect. Assoc. Equip.* 506.3 (2003), pp. 250–303, DOI: 10.1016/S0168-9002(03)01368-8.

[136] Microboone Collaboration, "Booster Neutrino Flux Prediction at MicroBooNE", *MICROBOONE-NOTE-1031-PUB* (2018), pp. 1–7.

[137] Don Athula Abeyarathna Wickremasinghe, "HARP targets pion production cross section and yield measurements. Implications for MiniBooNE neutrino flux", PhD thesis, Batavia, IL (United States): Fermi National Accelerator Laboratory (FNAL), 2015, DOI: `10.2172/1223260`.

[138] NIST, "Thermophysical properties of fluid systems", *Natl. Inst. Stand. Technol.* (2017), pp. 2–3.

[139] M. Miyajima et al., "Average energy expended per ion pair in liquid argon", *Phys. Rev. A* 9.3 (1974), pp. 1438–1443, DOI: `10.1103/PhysRevA.9.1438`.

[140] Eido Shibamura et al., "Drift velocities of electrons, saturation characteristics of ionization and W-values for conversion electrons in liquid argon, liquid argon-gas mixtures and liquid xenon", *Nucl. Instruments Methods* 131.2 (1975), pp. 249–258, DOI: `10.1016/0029-554X(75)90327-4`.

[141] Donald E. Groom, Nikolai V. Mokhov, and Sergei I. Striganov, "Muon stopping power and range tables 10 MeV-100 TeV", *At. Data Nucl. Data Tables* 78.2 (2001), pp. 183–356, DOI: `10.1006/adnd.2001.0861`.

[142] P.V. Vavilov, "Ionization losses of high-energy heavy particles", *Zh.Eksp.Teor.Fiz.* 32 (1957), pp. 749–751.

[143] R. M. Sternheimer, "The Density Effect for the Ionization Loss in Various Materials", *Phys. Rev.* 88.4 (1952), pp. 851–859, DOI: `10.1103/PhysRev.88.851`.

[144] BNL, *Notes on Particle Passage*, https://lar.bnl.gov/properties/pass.html, 2020.

[145] R Acciarri et al., "A study of electron recombination using highly ionizing particles in the ArgoNeuT Liquid Argon TPC", *J. Instrum.* 8.08 (2013), P08005–P08005, DOI: `10.1088/1748-0221/8/08/P08005`.

[146] Yichen Li et al., "Measurement of longitudinal electron diffusion in liquid argon", *Nucl. Instruments Methods Phys. Res. Sect. A Accel. Spectrometers, Detect. Assoc. Equip.* 816 (2016), pp. 160–170, DOI: `10.1016/j.nima.2016.01.094`, arXiv: `1508.07059`.

[147] Michael Mooney, "The MicroBooNE Experiment and the Impact of Space Charge Effects" (2015), arXiv: `1511.01563`.

[148] M. Antonello et al., "Experimental observation of an extremely high electron lifetime with the ICARUS-T600 LAr-TPC", *J. Instrum.* 9.12 (2014), DOI: `10.1088/1748-0221/9/12/P12006`, arXiv: `1409.5592`.

[149] T. Heindl et al., "The scintillation of liquid argon", *EPL* 91.6 (2010), DOI: `10.1209/0295-5075/91/62002`, arXiv: `1511.07718`.

[150] Tadayoshi Doke et al., "Absolute scintillation yields in liquid argon and xenon for various particles", *Japanese J. Appl. Physics, Part 1 Regul. Pap. Short Notes Rev. Pap.* 41.3 A (2002), pp. 1538–1545, DOI: `10.1143/jjap.41.1538`.

[151] A. Neumeier et al., "Attenuation measurements of vacuum ultraviolet light in liquid argon revisited", *Nucl. Instruments Methods Phys. Res. Sect. A Accel. Spectrometers, Detect. Assoc. Equip.* 800 (2015), pp. 70–81, DOI: `10.1016/J.NIMA.2015.07.051`.

[152] Emily Grace et al., "Index of refraction, Rayleigh scattering length, and Sellmeier coefficients in solid and liquid argon and xenon", *Nucl. Instruments Methods Phys. Res. Sect. A Accel. Spectrometers, Detect. Assoc. Equip.* 867 (2017), pp. 204–208, DOI: `10.1016/j.nima.2017.06.031`, arXiv: `1502.04213`.

[153] R. Acciarri et al., "Construction of precision wire readout planes for the Short-Baseline Near Detector (SBND)" (2020), arXiv: `2002.08424`.

[154] A. A. Machado et al., "The X-ARAPUCA: An improvement of the ARAPUCA device", *J. Instrum.* Vol. 13, 4, 2018, DOI: `10.1088/1748-0221/13/04/C04026`, arXiv: `1804.01407`.

[155] L. Bartoszek et al., *Mu2e Technical Design Report*, tech. rep., 2014, arXiv: `1501.05241`.

[156] Martin Auger et al., "A Novel Cosmic Ray Tagger System for Liquid Argon TPC Neutrino Detectors", *Instruments* 1.1 (2017), p. 2, arXiv: `1612.04614`.

[157] Yoshimoto Hoshi, Minoru Satoh, and Masato Higuchi, "A simple method for measuring wire tension in drift tubes", *Nucl. Instruments Methods Phys. Res. Sect. A Accel. Spectrometers, Detect. Assoc. Equip.* 236.1 (1985), pp. 82–84, DOI: `10.1016/0168-9002(85)90129-9`.

[158] Bradley Brinkley, J. Busenitz, and Gyula Zilizi, "Wire tension measurement using voltage switching", *Nucl. Instruments Methods Phys. Res. Sect. A Accel. Spectrometers, Detect. Assoc. Equip.* 373.1 (1996), pp. 23–29, DOI: `10.1016/0168-9002(95)01489-6`.

[159] T. Ohama et al., "Electrical measurement of wire tension in a multi-wire drift chamber", *Nucl. Instruments Methods Phys. Res. Sect. A Accel. Spectrometers, Detect. Assoc. Equip.* 410.2 (1998), pp. 175–178, DOI: `10.1016/S0168-9002(98)00224-1`.

[160] Chance Elliott et al., "National Instruments LabVIEW: A Programming Environment for Laboratory Automation and Measurement", *J. Lab. Autom.* 12.1 (2007), pp. 17–24, DOI: `10.1016/j.jala.2006.07.012`.

[161]   Raffaele Persico, Andrea Cataldo, and Egidio De Benedetto, "Time-domain reflectometry: Current uses and new possibilities", *Innov. Near-Surface Geophys.* Elsevier, 2019, pp. 59–96, DOI: `10.1016/b978-0-12-812429-1.00003-9`.

[162]   J. Paley et al., "LArIAT: Liquid Argon In A Testbeam" (2014), arXiv: `1406.5560`.

[163]   K. S. Kölbig and B. Schorr, "A program package for the Landau distribution", *Comput. Phys. Commun.* 31.1 (1984), pp. 97–111, DOI: `10.1016/0010-4655(84) 90085-7`.

[164]   E.L. Snider and G. Petrillo, "LArSoft: toolkit for simulation, reconstruction and analysis of liquid argon TPC neutrino detectors", *J. Phys. Conf. Ser.* 898.4 (2017), p. 042057, DOI: `10.1088/1742-6596/898/4/042057`.

[165]   C Green et al., "The art framework", *J. Phys. Conf. Ser.* 396.2 (2012), p. 022020, DOI: `10.1088/1742-6596/396/2/022020`.

[166]   Rene Brun and Fons Rademakers, "ROOT An object oriented data analysis framework", *Nucl. Instruments Methods Phys. Res. Sect. A Accel. Spectrometers, Detect. Assoc. Equip.* 389.1-2 (1997), pp. 81–86, DOI: `10.1016/S0168-9002(97)00048-X`.

[167]   Glen Cowan, *Statistical data analysis*, Clarendon Press, 1998, p. 197.

[168]   D. Heck et al., "CORSIKA: A Monte Carlo Code to Simulate Extensive Air Showers", *Forschungszentrum Karlsruhe* FZKA 6019 (1998), pp. 1–90.

[169]   D. Garcia-Gamez, "Developing scintillation light readout simulation for the SBND experiment", *J. Instrum.* 11.1 (2016), DOI: `10.1088/1748-0221/11/01/C01080`.

[170]   C. Adams et al., "Ionization electron signal processing in single phase LArTPCs. Part I. Algorithm Description and quantitative evaluation with MicroBooNE simulation", *J. Instrum.* 13.7 (2018), DOI: `10.1088/1748-0221/13/07/P07006`, arXiv: `1802.08709`.

[171]   C. Adams et al., "Deep neural network for pixel-level electromagnetic particle identification in the MicroBooNE liquid argon time projection chamber", *Phys. Rev. D* 99.9 (2019), DOI: `10.1103/PhysRevD.99.092001`, arXiv: `1808.07269`.

[172]   Xin Qian et al., "Three-dimensional imaging for large LArTPCs", *J. Instrum.* 13.5 (2018), DOI: `10.1088/1748-0221/13/05/P05032`, arXiv: `1803.04850`.

[173]   R. Acciarri et al., "The Pandora multi-algorithm approach to automated pattern recognition of cosmic-ray muon and neutrino events in the MicroBooNE detector", *Eur. Phys. J. C* 78.1 (2018), DOI: `10.1140/epjc/s10052-017-5481-6`, arXiv: `1708.03135`.

[174]   P. Abratenko et al., "Determination of muon momentum in the MicroBooNE LArTPC using an improved model of multiple Coulomb scattering", *J. Instrum.* 12.10 (2017), DOI: `10.1088/1748-0221/12/10/P10010`, arXiv: `1703.06187`.

[175] Amy Williams et al., "An efficient and robust ray-box intersection algorithm", *ACM SIGGRAPH 2005 Courses, SIGGRAPH 2005* 10 (2005), p. 54, DOI: 10.1145/1198555.1198748.

[176] David H. Eberly, *3D game engine design : a practical approach to real-time computer graphics*, Elsevier Morgan Kaufmann, 2007, p. 1018.

[177] W. T. Eadie, *Statistical methods in experimental physics,* North-Holland Pub. Co, 1971, p. 296.

[178] G. D'Agostini, "A multidimensional unfolding method based on Bayes' theorem", *Nucl. Inst. Methods Phys. Res. A* 362.2-3 (1995), pp. 487–498, DOI: 10.1016/0168-9002(95)00274-X.

[179] Andreas Höcker and Vakhtang Kartvelishvili, "SVD approach to data unfolding", *Nucl. Instruments Methods Phys. Res. Sect. A Accel. Spectrometers, Detect. Assoc. Equip.* 372.3 (1996), pp. 469–481, DOI: 10.1016/0168-9002(95)01478-0, arXiv: 9509307 [hep-ph].

[180] Volker Blobel, "An Unfolding Method for High Energy Physics Experiments" (2002), arXiv: 0208022 [hep-ex].

[181] Robert D. Cousins, Samuel J. May, and Yipeng Sun, "Should unfolded histograms be used to test hypotheses?" (2016), arXiv: 1607.07038.

[182] Lukas Koch, "A response-matrix-centred approach to presenting cross-section measurements", *J. Instrum.* 14.9 (2019), DOI: 10.1088/1748-0221/14/09/P09013, arXiv: 1903.06568.

[183] Hans Bichsel, *A method to improve tracking and particle identification in TPCs and silicon detectors*, 2006, DOI: 10.1016/j.nima.2006.03.009.

[184] Luke Pickering, Patrick Stowell, and Jan Sobczyk, "Event reweighting with the NuWro neutrino interaction generator", *J. Phys. Conf. Ser.* Vol. 888, 1, Institute of Physics Publishing, 2017, DOI: 10.1088/1742-6596/888/1/012175.

[185] A. Bodek and J. L. Ritchie, "Further studies of Fermi-motion effects in lepton scattering from nuclear targets", *Phys. Rev. D* 24.5 (1981), pp. 1400–1402, DOI: 10.1103/PhysRevD.24.1400.

[186] Luc Demortier, "P Values: What They Are and How to Use Them", *CDF/MEMO /STATISTICS/PUBLIC/8662* (2007).

[187] R. Acciarri et al., "Demonstration of MeV-scale physics in liquid argon time projection chambers using ArgoNeuT", *Phys. Rev. D* 99.1 (2019), p. 012002, DOI: 10.1103/PhysRevD.99.012002, arXiv: 1810.06502.

[188] Andrew P. Furmanski and Jan T. Sobczyk, "Neutrino energy reconstruction from one-muon and one-proton events", *Phys. Rev. C* 95.6 (2017), DOI: 10.1103/PhysRevC.95.065501, arXiv: 1609.03530.

[189] A. R. Back et al., "Accelerator Neutrino Neutron Interaction Experiment (AN-NIE): Preliminary Results and Physics Phase Proposal" (2017), arXiv: 1707.08222.

[190] E. Valencia et al., "Constraint of the MINERvA Medium Energy Neutrino Flux using Neutrino-Electron Elastic Scattering", *Phys. Rev. D* 100.9 (2019), DOI: 10.1103/PhysRevD.100.092001, arXiv: 1906.00111.

Acronyms

ADC Analogue-to-Digital Converter. 53, 55, 91, 100

ANL Argonne National Laboratory. 30

APA Anode Plane Assembly. 46, 51, 52, 55, 59, 60, 64, 68–70, 75, 82, 83, 85, 124, 126, 127, 131, 174

ASIC Application Specific Integrated Circuit. 53

BNB Booster Neutrino Beam. 31, 38, 43–45, 117, 118, 135, 175

BSM Beyond the Standard Model. 15, 17, 41

BUU Boltzmann-Uehling-Uhlenbeck. 29

CC Charged Current. 18, 19, 25, 26, 30, 31, 33–36, 39, 86, 102, 107, 116, 117, 119–122, 126, 128, 141–144, 148–150, 153, 158, 159, 162–164, 170, 173, 178, 194

COH Coherent pion production. 26, 27

CP Charge-Parity. 14, 15

CPA Cathode Plane Assembly. 46, 51, 52, 70, 122

CRT Cosmic Ray Tagger. 47, 55, 69, 71, 73, 77, 83, 86, 91–93, 100, 101, 108, 109, 111, 112, 114, 122–124, 131, 174, 175

DAQ Data Aquisition. 53

DCA Distance of Closest Approach. 112–114, 123, 135, 141

DIS Deep Inelastic Scattering. 27, 28, 186

DUNE Deep Underground Neutrino Experiment. 2, 40, 41, 55, 192, 193

EM Electromagnetic. 19, 135

FEMB Front End MotherBoard. 53, 55

FNAL Fermi National Accelerator Laboratory. 2, 34, 38, 58, 77

FPGA Field Programmable Gate Array. 53

FSI Final State Interactions. 28, 33, 34, 36, 87, 194

GFG Global Fermi Gas. 21

IA Impulse Approximation. 20, 25

LArTPC Liquid Argon Time Projection Chamber. 2, 3, 36, 38, 39, 41, 46, 59, 60, 63, 77, 88, 93, 94, 165, 195

LFG Local Fermi Gas. 21, 26

LGC Landau-Gaussian Convolution. 71, 73

MCS Multiple Coulomb Scattering. 104, 105, 129, 135, 136, 141, 161

MEC Meson Exchange Currents. 23, 26, 32, 186

MIP Minimum Ionising Particle. 48, 69, 70, 92

MVA Multi-Variate Algorithm. 97, 127, 138, 139, 194

NC Neutral Current. 18, 19, 107, 117, 131

PDS Photon Detection System. 46, 47, 54, 55, 86, 90, 91, 98, 107, 125, 127, 131, 175, 194

PE Photo-Electrons. 55, 91, 92, 98–101, 107, 109, 117, 125, 126

PID Particle Identification. 105

PMT Photomultiplier Tube. 51, 54, 55, 91, 98, 99, 107, 125, 174

POT Protons On Target. 40, 45, 117–119, 149, 150, 155, 157, 163, 177, 178, 192

QCD Quantum Chromo-Dynamics. 20, 27, 28

QE Quasi-Elastic. 21, 25–27, 30, 31, 33–35, 166

QFT Quantum Field Theory. 19

RES Resonant pion production. 26, 27, 34

RFG Relativistic Fermi Gas. 21

RPA Random Phase Approximation. 23, 26

SBN Short-Baseline Neutrino. 2, 38–40, 43

SBND Short-Baseline Near Detector. 2, 3, 26, 37, 38, 40, 41, 43, 45, 47, 55, 58, 60, 61, 65, 68, 77, 78, 81, 83, 86, 88–90, 92, 95, 102, 104, 119, 125, 131, 133, 147, 151–153, 157, 166, 175, 179, 183, 184, 186, 189, 192–195

SF Spectral Function. 20, 22

SiPM Silicon Photomuiltiplier. 51, 54, 55, 57, 92, 100

SM Standard Model. 7, 9, 10, 15, 16

TPB TetraPhenyl Butadiene. 51, 54, 91, 99

TPC Time Projection Chamber. 46, 47, 51–53, 55, 57, 64, 77, 78, 82, 83, 89–91, 95, 96, 98, 99, 102, 105, 107–109, 111, 112, 114, 116–118, 120–127, 129, 131, 132, 139, 160, 174, 175

VST Vertical Slice Test. 77, 78, 81

VUV Vacuum Ultra-Violet. 50, 51

Appendices

Appendix A

Cross section measurement systematics

A.1 Flux

(a)

(b)

(c)

(d)
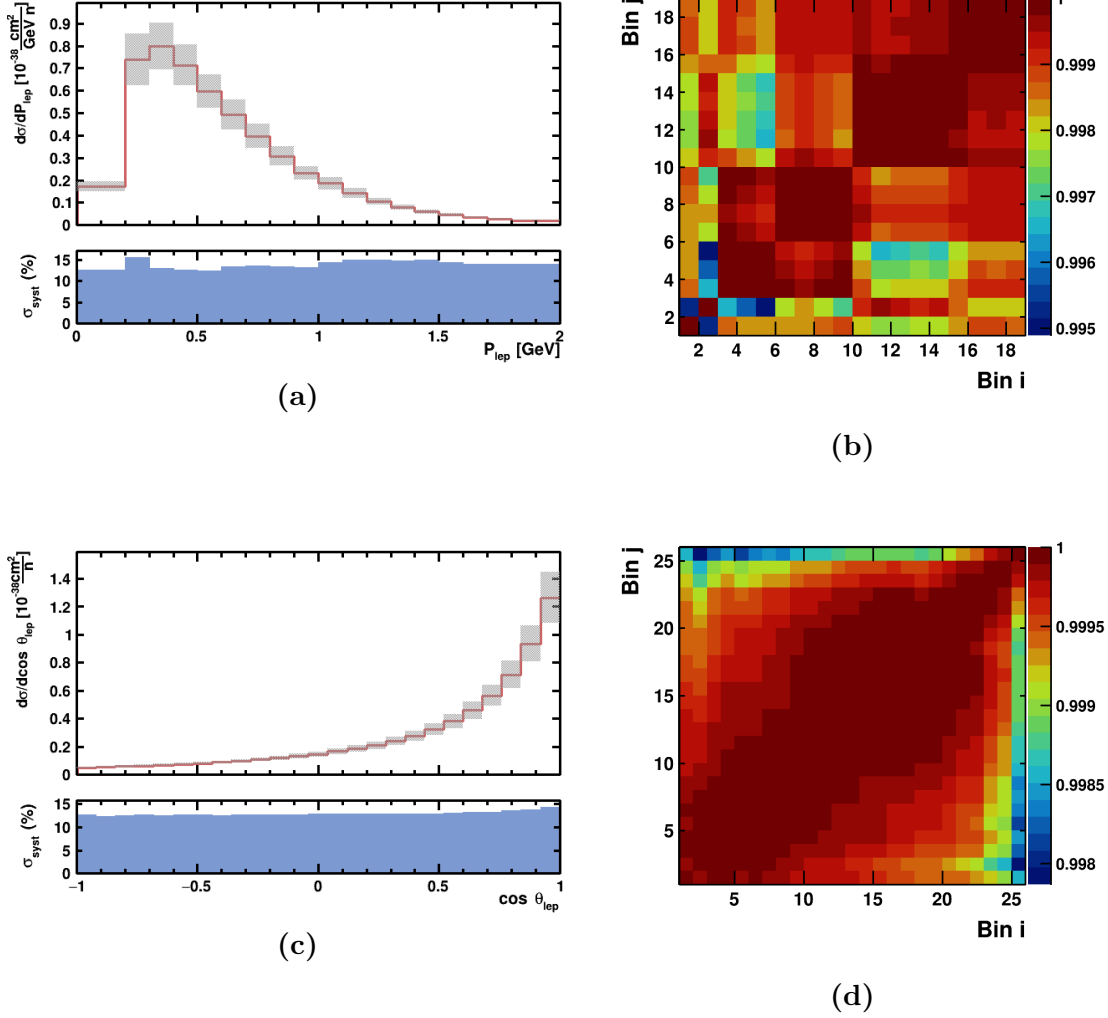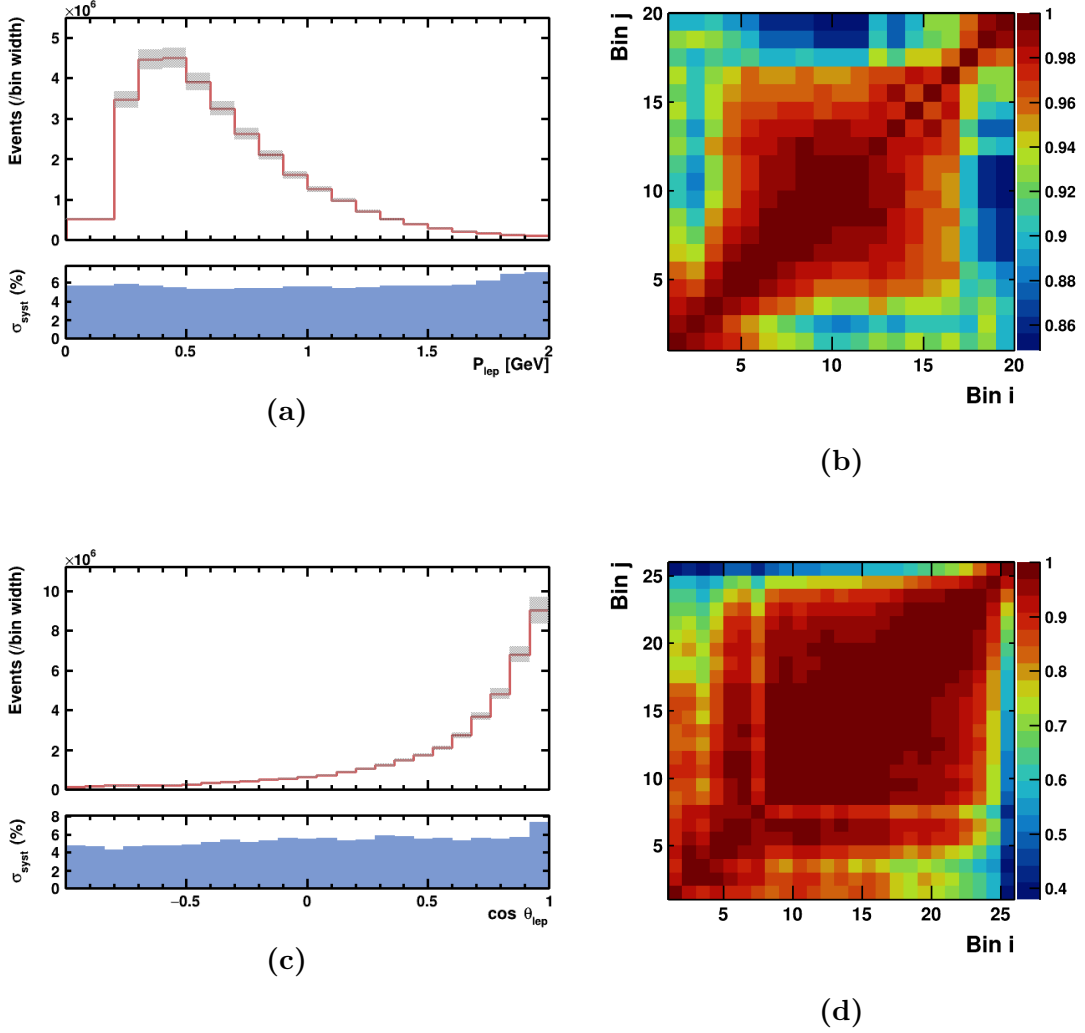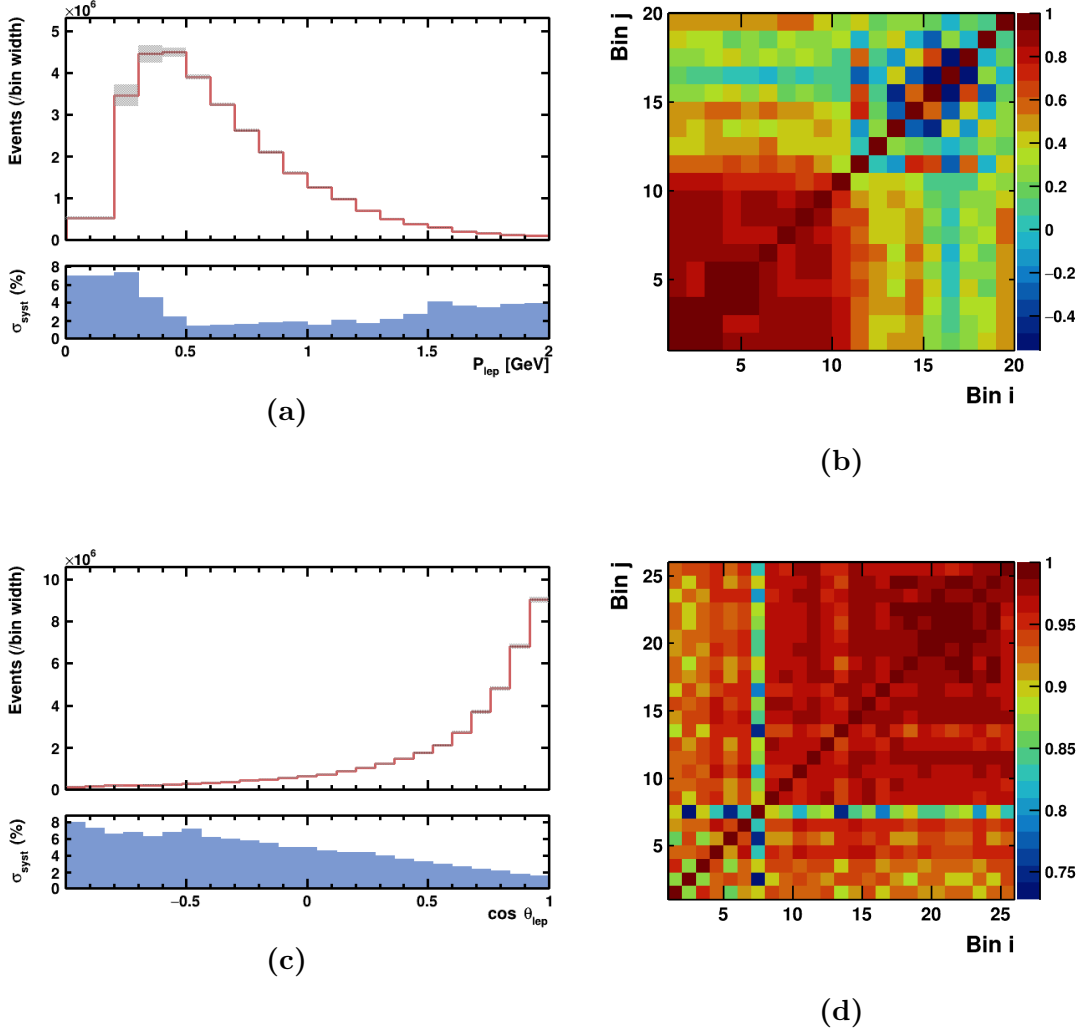
Figure A.1: The contribution of the flux systematic uncertainties to the single differential cross sections and corresponding bin correlation matrices for (a) & (b) reconstructed P_μ and (c) & (d) reconstructed $\cos\theta_\mu$.

A.2   GENIE

**(a)**

(b)

(c)

(d)
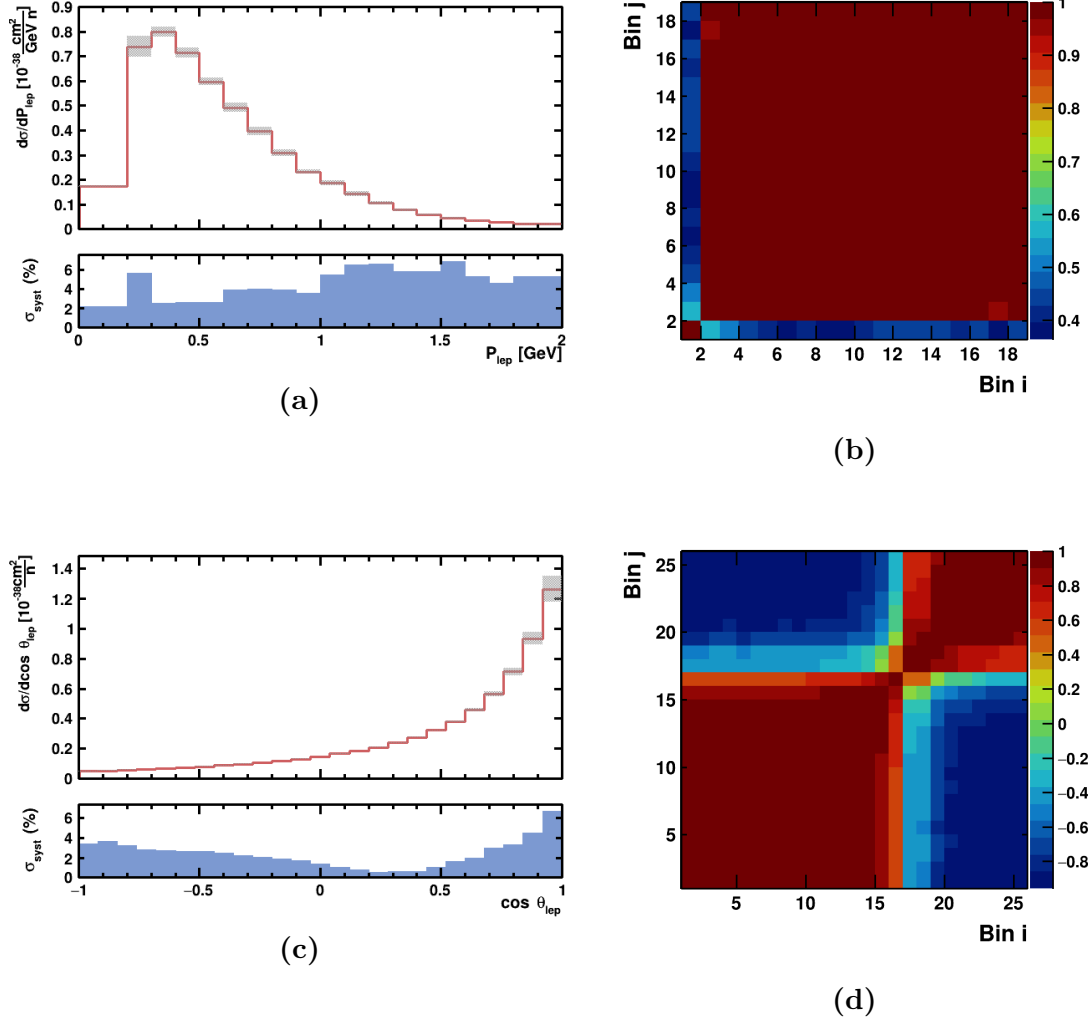
Figure A.2: The contribution of the cross section, rescattering, hadronisation and decay systematic uncertainties to the single differential cross sections and corresponding bin correlation matrices for (a) & (b) reconstructed P_μ and (c) & (d) reconstructed $\cos\theta_\mu$.

A.3 Detter

(a)


(b)

(c)

(d)
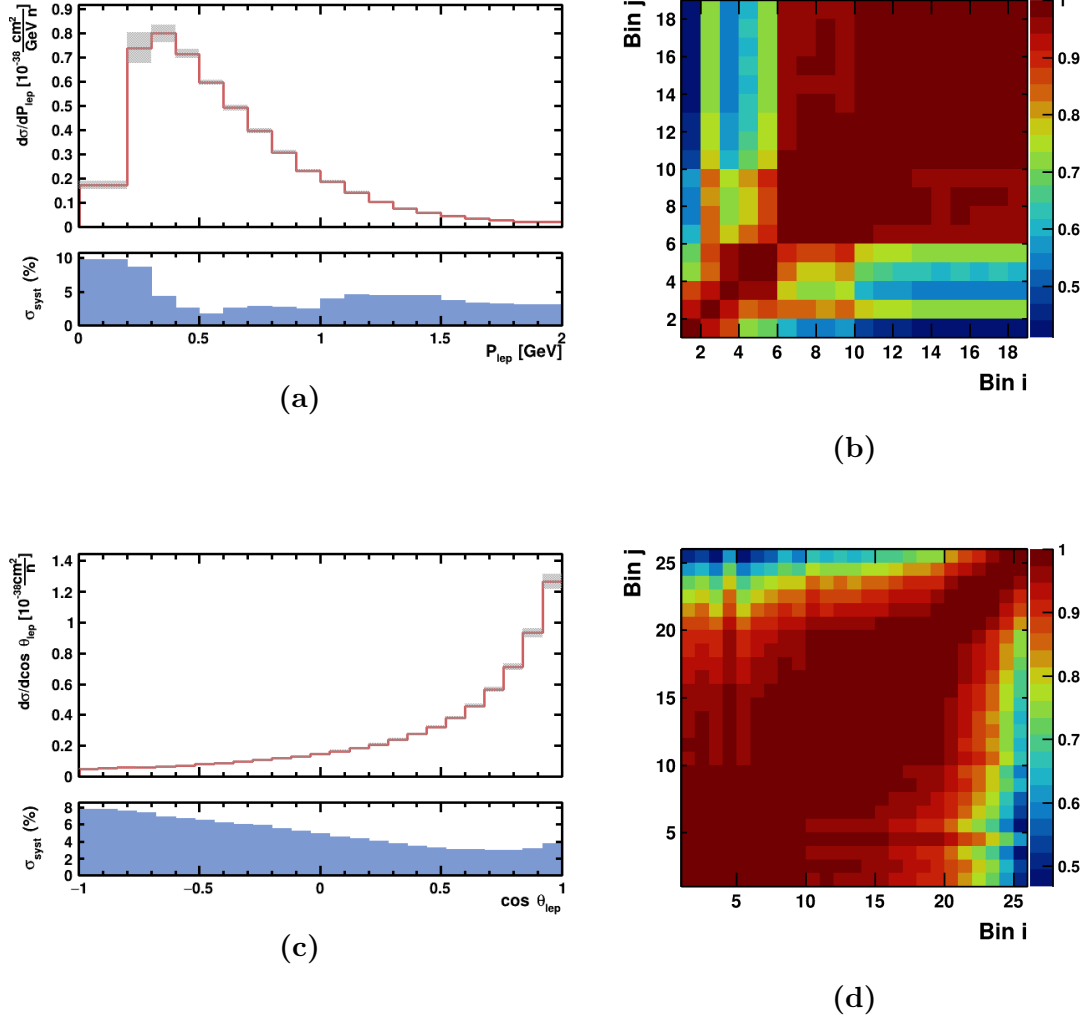
Figure A.3: The contribution of the parametrised detector systematic uncertainties to the single differential cross sections and corresponding bin correlation matrices for reconstructed (a) & (b) P_μ and (c) & (d) $\cos\theta_\mu$.
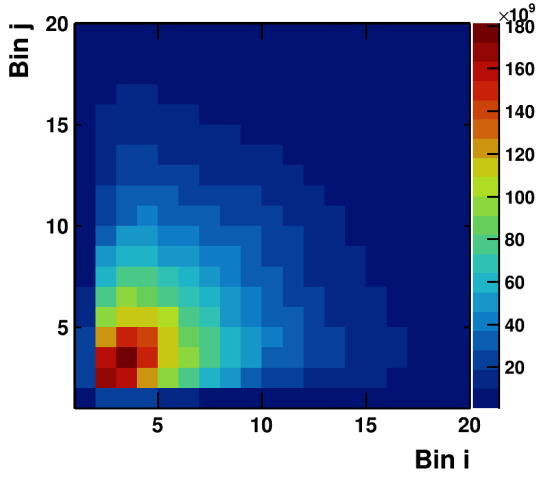
A.4 Total
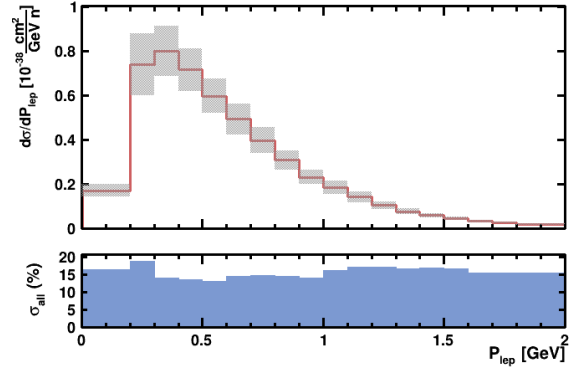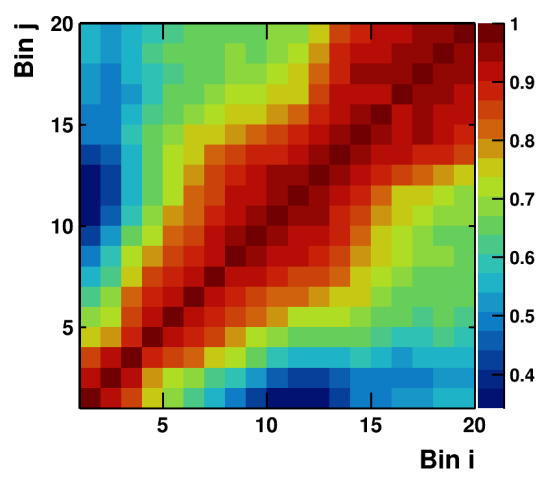

(a)
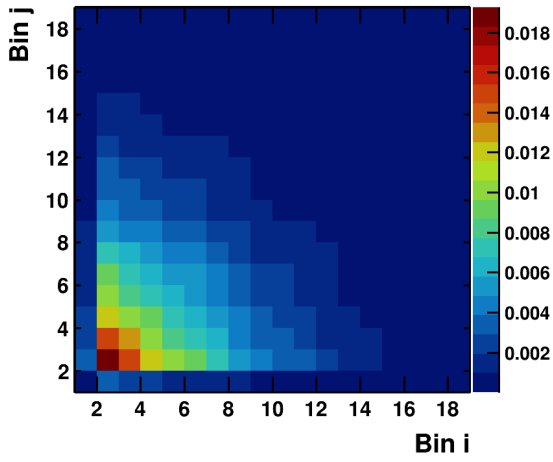
(b)
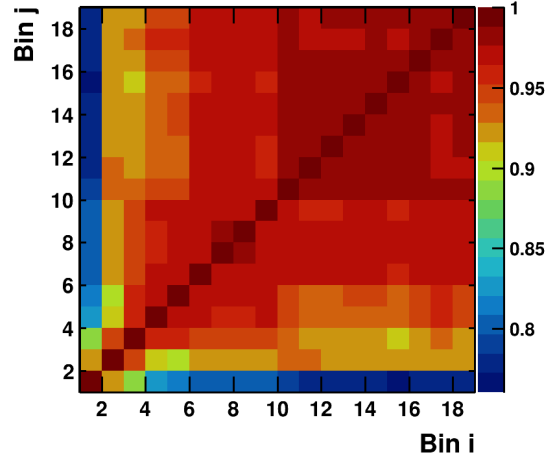
(c)

Figure A.4: (a) Reconstructed one dimensional muon momentum event rates with statistical and systematic uncertainties. (b) & (c) Covariance and Correlation matrices.

(a)

(b)

(c)

Figure A.5: (a) Reconstructed one dimensional muon $\cos\theta$ event rates with statistical and systematic uncertainties. (b) & (c) Covariance and Correlation matrices.
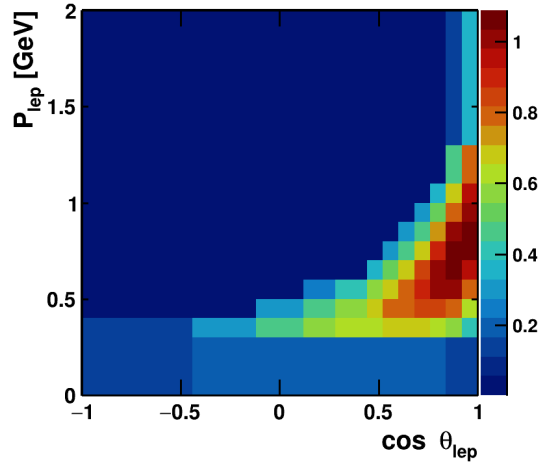
(a)
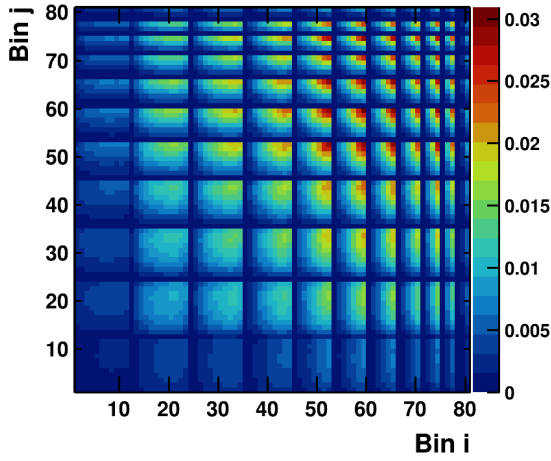
(b)
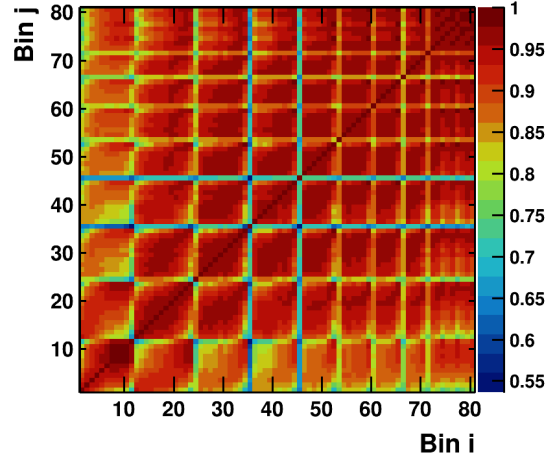
(c)

Figure A.6: (a) Response matrix for all reconstructed events in two dimensional P and $\cos\theta$ distribution. (b) & (c) Covariance and Correlation matrices.

Appendix B

GENIE v2 rate prediction systematics

B.1 Flux

(a)

(b)

(c)

(d)
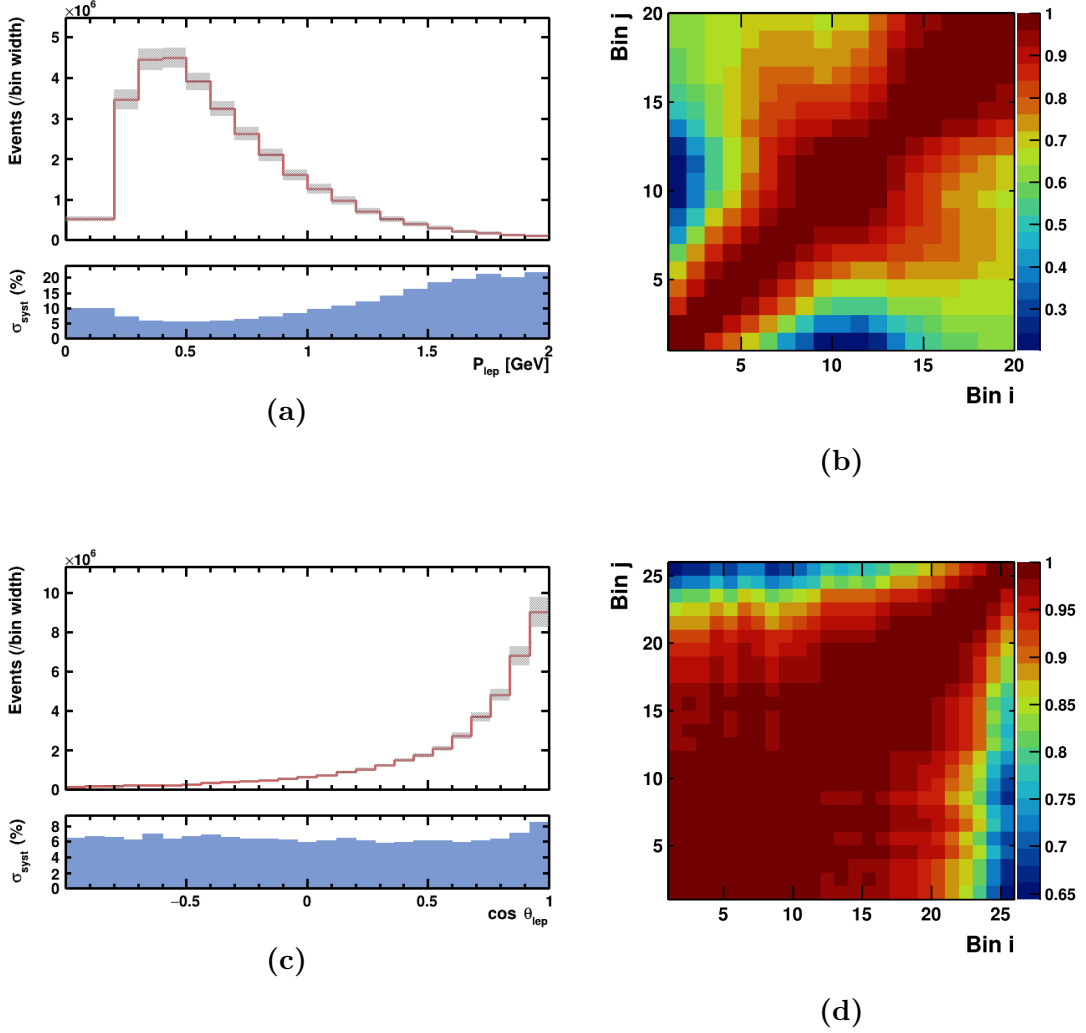
Figure B.1: The contribution of the flux systematic uncertainties to the single differential cross sections and corresponding bin correlation matrices for (a) & (b) reconstructed P_μ and (c) & (d) reconstructed $\cos\theta_\mu$.

B.2 GENIE

(a)

(b)

(c)

(d)

Figure B.2: The contribution of the cross section, rescattering, hadronisation and decay systematic uncertainties to the single differential cross sections and corresponding bin correlation matrices for (a) & (b) reconstructed P_μ and (c) & (d) reconstructed $\cos\theta_\mu$.

B.3   Detector

(a)

(b)

(c)

(d)

Figure B.3: The contribution of the parametrised detector systematic uncertainties to the single differential cross sections and corresponding bin correlation matrices for reconstructed (a) & (b) P_μ and (c) & (d) $\cos\theta_\mu$.

B.4   Total
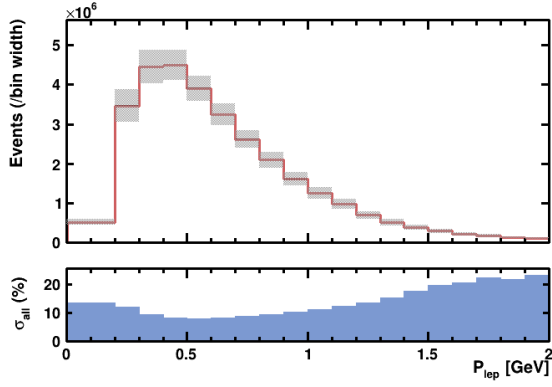
(a)
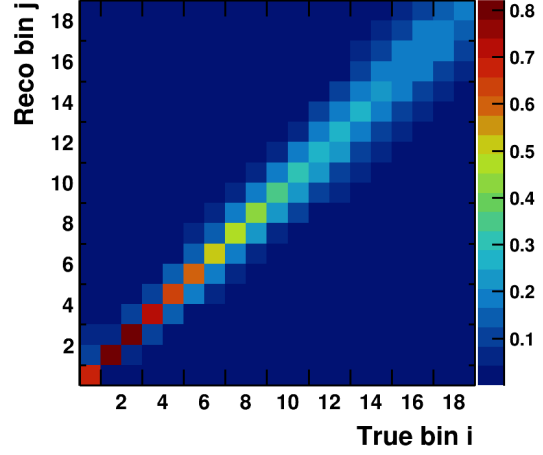
(b)

(c)

(d)

Figure B.4: (a) Reconstructed one dimensional muon momentum event rates with statistical and systematic uncertainties. (b) Response matrix. (c) & (d) Covariance and Correlation matrices.

(a)

(b)

(c)

(d)
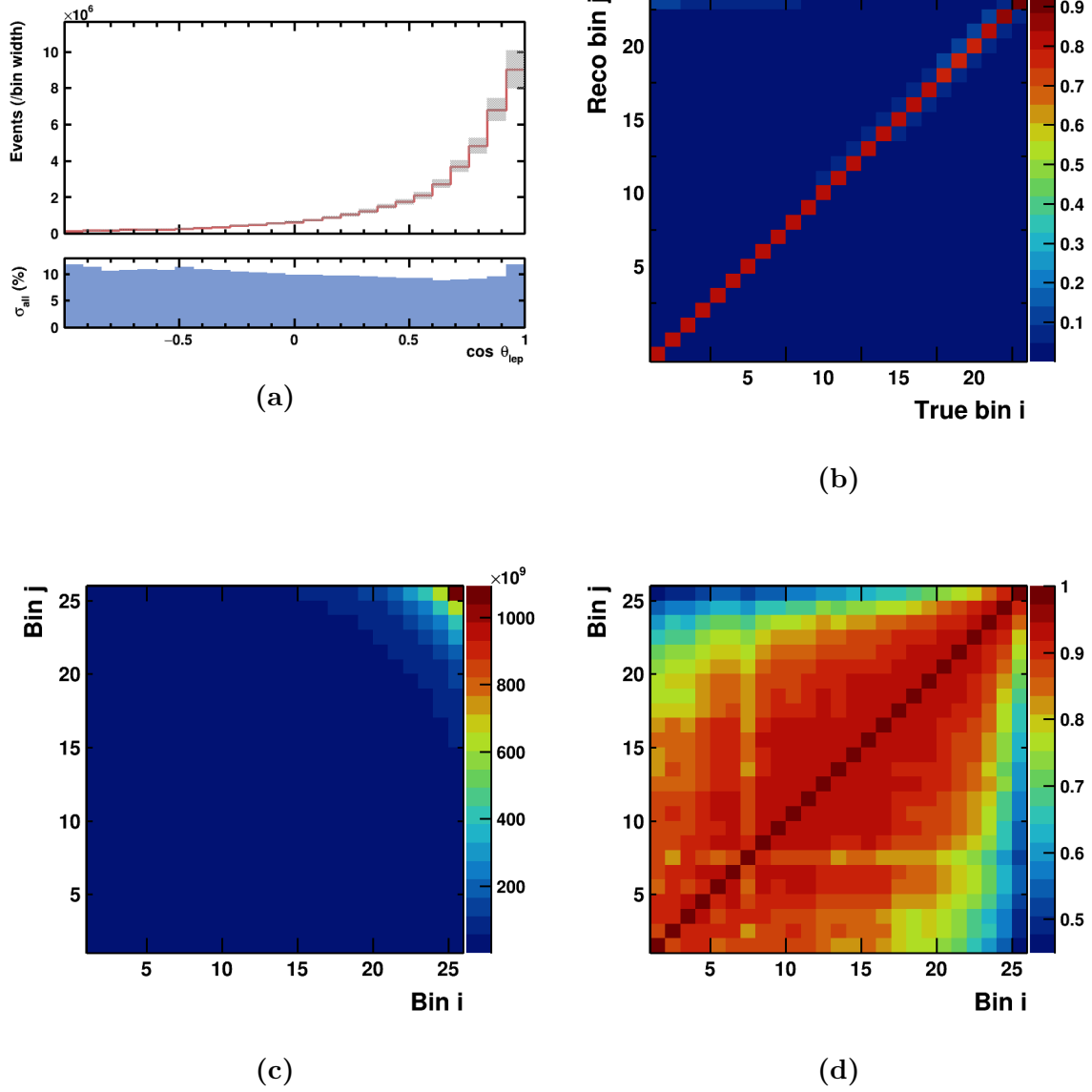
Figure B.5: (a) Reconstructed one dimensional muon $\cos\theta$ event rates with statistical and systematic uncertainties. (b) response matrix. (c) & (d) Covariance and Correlation matrices.
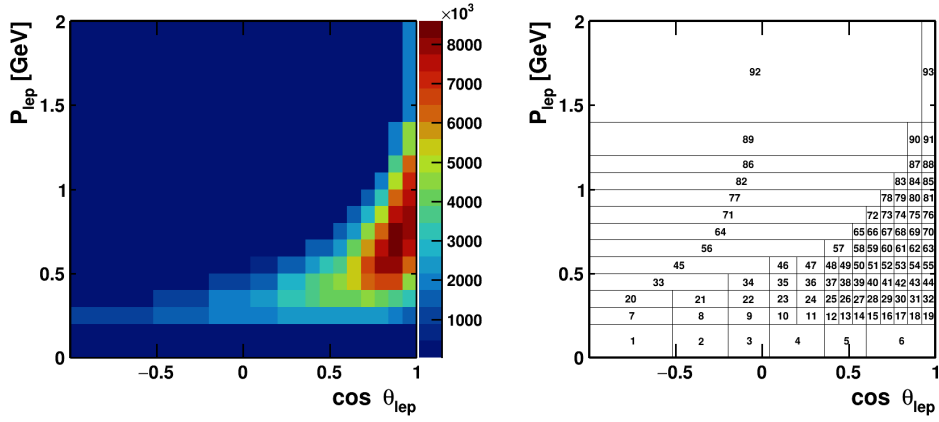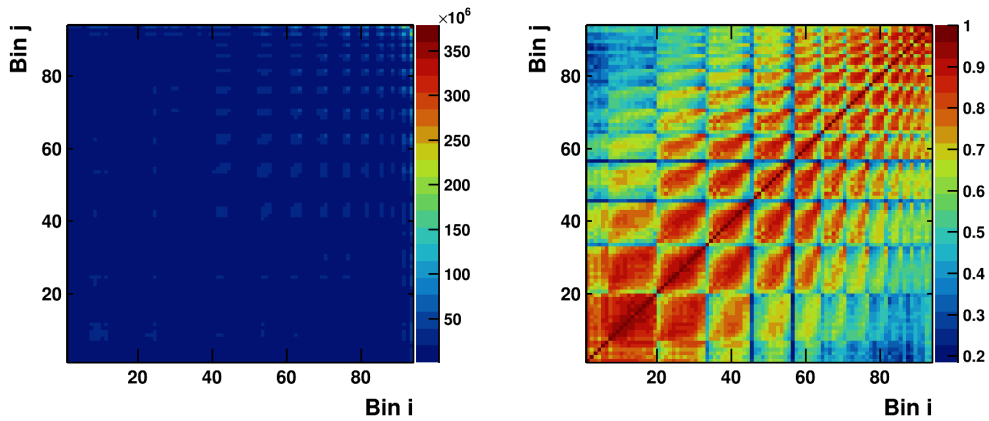
(a)

(b)
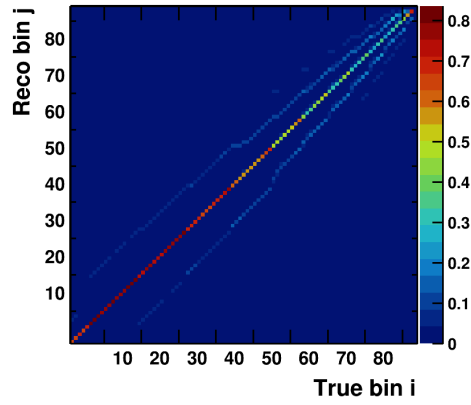
(c)

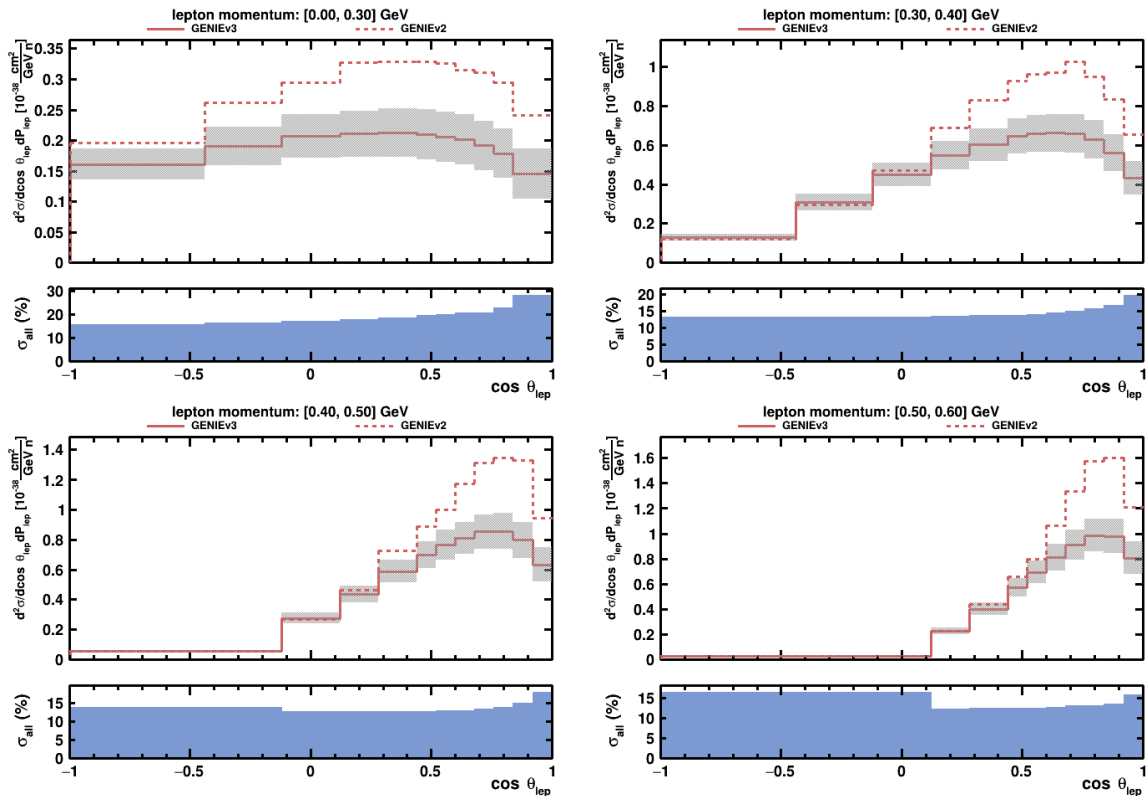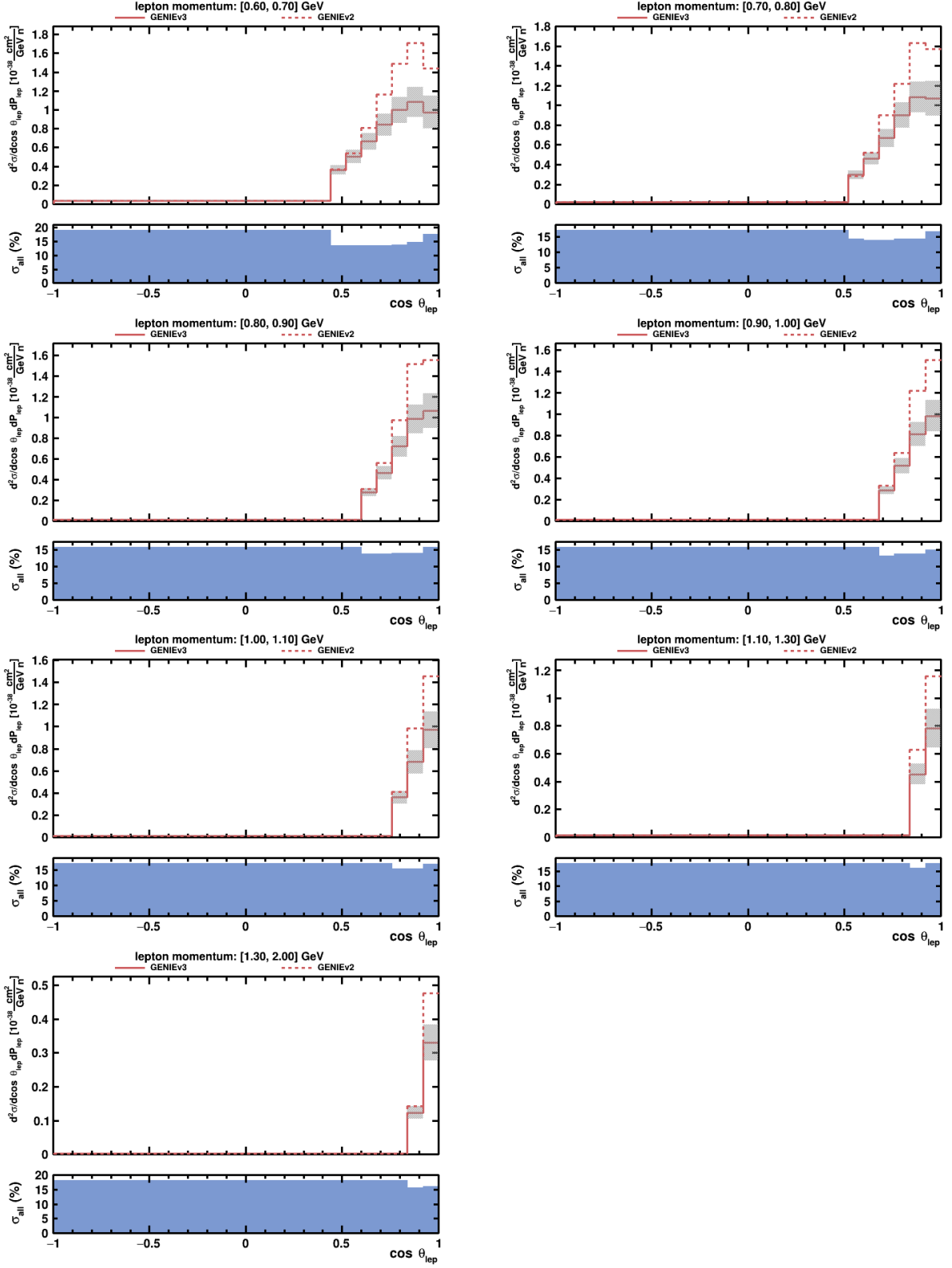(d)

(e)

Figure B.6: (a) Response matrix for all reconstructed events in two dimensional P and $\cos\theta$ distribution. (b) Bin definitions. (c) Response matrix. (d) & (e) Covariance and Correlation matrices.

Appendix C

Double differential cross section slices for model comparisons

Figure C.1: One dimensional momentum slices of the comparison of expected measured double differential cross sections from GENIE v2 and v3 model configurations in reconstructed P_μ and $\cos\theta_\mu$.